NASA Contractor Report 191060

NASA-CR-191060
19960011632

Laser Doppler Velocimeter Measurements and Laser Sheet Imaging in an Annular Combustor Model

Richard Dale Dwenger
Purdue University
West Lafayette, Indiana

December 1995

Prepared for
Lewis Research Center
Under Contract NAS3–24350

National Aeronautics and
Space Administration

LASER DOPPLER VELOCIMETER MEASUREMENTS AND LASER SHEET IMAGING IN AN ANNULAR COMBUSTOR MODEL

A Thesis

Submitted to the Faculty

of

Purdue University

by

Richard Dale Dwenger

In Partial Fulfillment of the

Requirements for the Degree

of

Master of Science in Aeronautics and Astronautics

August 1990

ACKNOWLEDGEMENTS

The author would like to thank Dr. John P. Sullivan for all his instruction, criticism, and patience during the course of this research.

Additional thanks to Dr. S.N.B. Murthy and Dr. W.A. Gustafson for their participation on the author's advisory committee.

Special thanks are in order for the technical staff Bob Sanders, Bill Bader, Jack Davis, Dave Reagan, and Robert Scott for equipment fabrication, repair, and service during this research, and Jeanne Figolah for her secretarial assistance. Additional thanks to my fellow graduate students for their input and help.

The author would like to thank NASA Lewis Research Center and Allison-Gas Turbine Division for the financial support of this research.

TABLE OF CONTENTS

Page

LIST OF TABLES

LIST OF FIGURES

Figure Page

Figure Page

Figure Page

Figure Page

Figure Page

Figure Page

Figure Page

Appendix
Figure

Appendix Figure

Appendix
Figure Page

Appendix
Figure Page

Appendix Figure

Appendix
Figure Page

Appendix
Figure Page

ABSTRACT

Dwenger, Richard Dale. M.S.A.A., Purdue University, August 1990. Laser Doppler Velocimeter Measurements and Laser Sheet Imaging in an Annular Combustor Model. Major Professor: Dr. John P. Sullivan

An experimental study was conducted in an annular combustor model to provide a better understanding of the flowfield. Combustor model configurations consisting of primary jets only, annular jets only, and a combination of annular and primary jets were investigated. The purpose of this research was to provide a better understanding of combustor flows and to provide a data base for comparison with computational models.

The first part of this research used a laser Doppler velocimeter to measure mean velocity and statistically calculate root-mean-square velocity in two coordinate directions. From this data, one Reynolds shear stress component and a two-dimensional turbulent kinetic energy term was determined. Major features of the flowfield included recirculating flow, primary and annular jet interaction, and high turbulence. The most pronounced result from this data was the effect the primary jets had on the flowfield. The primary jets were seen to reduce flow asymmetries, create larger recirculation zones, and higher turbulence levels.

The second part of this research used a technique called marker nephelometry to provide mean concentration values in the combustor. Results

showed the flow to be very turbulent and unsteady. All configurations investigated were highly sensitive to alignment of the primary and annular jets in the model and inlet conditions. Any imbalance between primary jets or misalignment of the annular jets caused severe flow asymmetries.

INTRODUCTION

Economic problems apply to everyone, and the aerospace industry is no exception. Rising development, production, and maintenance costs have driven the aerospace industry to use more efficient and longer lasting products. The area of propulsion is no exception. In the past, combustion chambers for gas turbine engines have mainly been designed by trial and error and evolved over many years. Improvements in combustor exit temperature profile, minimizing pollutants, increased combustor life, and complete mixing of fuel and air are benefits that could result with a better understanding of the combustion process.

The objective of this research was to provide a better understanding of the flow in the primary zone of a gas turbine combustor and to provide a data base that can be used to determine the accuracy and shortcomings of analytical models. Measurements were taken in a cold flow annular type combustor to simulate the primary zone of a gas turbine combustor. The primary zone of a combustor usually has three flows entering this region. These flows consist of: air from the discharge of a compressor through a swirler in a dome wall, fuel injection in the center of a swirler, and primary air jets normal to the mean flow in the combustor. The test model itself was of rectangular cross section and contained five pairs of opposing jets for the first case, five annular jets for the second case, and annular

and primary jets together for the third case. No fuel injection was simulated in this research.

To carry out these measurements a one-component laser Doppler velocimeter was used to provide mean and rms velocities in two components. These quantities allowed the calculation of the Reynolds shear stress in one plane and the two-dimensional turbulent kinetic energy. In addition, laser sheet imaging was used to provide scalar concentration measurements throughout the combustor model.

Major features of this model include primary jet cross-flow interaction and primary and annular jet flow interaction. Measurement results indicate flow recirculation zones with very high levels of turbulence intensity. The recirculation zones are the most important characteristic of the flowfield since they provide areas of fuel and air mixing and directly effect the combustor efficiency.

This thesis starts with a literature review of related work along with a description of the experimental apparatus and data acquisition system used. Next, LDV measurement results are presented for the primary jets only, the annular jets only, and annular and primary jets case. Presentation of the measurements are broken down into inlet conditions, mean velocities, and turbulent quantities. Following the measurement results, scalar concentration results will be presented in order to demonstrate the mixing occurring inside the test rig. Finally, a summary of the results will be made and conclusions will be drawn about the effectiveness of this study.

CHAPTER 1

EXPERIMENTAL OVERVIEW AND SETUP

1.1 Literature Review

1.1.1 LDV Literature Review

Several experimental studies on opposed jet configurations have been published. Khan and Whitelaw [1] published mean velocity and scalar concentration measurements on five pairs of opposing jets discharging normally into a crossflow. Measurements were taken downstream of the jets for pitch, distance between jet centerlines, to diameter ratios of two and four, in order to determine the influence of hole eccentricity. Flow asymmetries were seen to arise from geometric asymmetries. Larger asymmetries occurred at the lower pitch to diameter ratio.

Atkinson, Khan, and Whitelaw [2] reported measurements of mean velocity, turbulence characteristics, and scalar concentration in a rig similar to that used by Khan and Whitelaw. Measurements were taken using pitch to diameter ratios of two, four, and a limiting case of two opposing jets at different jet to freestream velocity ratios. Results for velocity ratios of unity and less show that the jets retain their identities downstream for all three pitch to diameter ratios. At higher velocity

ratios, the jets could bifurcate in several ways, depending on the jet spacing. In general, the authors concluded that turbulence characteristics are determined by the mean flow, which is controlled by pressure forces.

Flow characteristics of opposing rows of jets in a confined space were investigated by Sivasgaram and Whitelaw [3] by using flow visualization. The effects of angular misalignment, axial misalignment, and unequal mean jet velocities were investigated. The flows were seen to be very sensitive to rear wall placement, axial and angular jet misalignment, and jet velocity mismatch. The asymmetry of the flow was dominated by axial and angular jet misalignment. In addition, sensitivity of flow asymmetries were observed to be magnified at larger pitch to diameter ratios. The work done by Kahn and Whitelaw [1] contradicts this result as their results indicate that asymmetries were larger at smaller pitch to diameter ratios when jets were in crossflow.

Miau and Sun [4,5] used particle tracer visualization to provide qualitative results on the flowfield in a side inlet square duct. A jet flapping motion in the stagnation region of the impinging flow was observed. Unsteady vortex structures were seen to form upstream of the jets, while two recirculation regions formed on the side walls downstream of the jets. Violent reattachment processes were seen occurring along the side walls, where in some cases the flow would reattach and then be reflected from the wall. In addition, a physical model of the flow was proposed.

Experimental studies have been conducted at Purdue University using the apparatus used for the present research, references [6,7,8]. Studies conducted by Barron [6] and Seal [7] investigated the use of sixty degree annular swirlers with and without primary jets. Three mean velocity components and their fluctuating components were measured. Primary jets were found to have a very strong effect of the mean and turbulent flowfields. The cross jets reduced the overall swirl in the test section to negligible levels and also drove a four-celled vortex-type motion near the cross jet injection plane.

Ko and Chan [22] investigated the flow structure in the inner region of three annular jets. Mean velocity, static pressure, and pressure fluctuations and their spectra were presented. Annular jets investigated included a basic annular jet, and two annular jets with conical and ellipsoidal center bodies extending downstream a distance of 1.5 times the outer diameter of the annular jet. The outer mixing region of all three annular jets and a single jet showed similarity in mean velocity and turbulence intensity profiles. In the inner region of the basic annular jet, an inner mixing region and internal recirculating region immediately downstream of the nozzle exit exists. The inner region for the annular jets with center bodies had no internal recirculating region, but wake vortices formed in the boundary layer of the surface of these center bodies.

Kuhlman [23] made measurements of mean velocity distributions for axisymmetric circular and annular jets, from which centerline velocity decay and jet width growth data was presented. All jets showed a linear width growth and

inverse centerline velocity decay in the far-field. Annular jets had an enhanced near-field mixing, far-field centerline velocity decay and more rapid jet width growth than plane circular jets. Far-field entrainment rates for some annular jets increased by more than 40% relative to circular jets.

1.1.2 Scalar Concentration Literature Review

The optical technique of measuring concentration in a flow, called marker nephelometry, was established by Rosensweig, Hottel, and Williams [13] in 1961. This initial study established the feasibility of the technique by investigating a turbulent jet discharging into ambient air. Becker, Hottel, and Williams [14] refined the method and performed additional measurements. A through review of this technique is presented by Becker [16].

Shaughnessy and Morton [17] used this technique to measure the concentration downstream of a turbulent jet exhausting into a secondary air stream. An argon-ion laser was used as the light source, instead of a bright lamp as used in earlier experiments. Electronic shot noise present in previous studies was negligible due to the high beam intensity of the laser.

Early studies, focused light to a point in the flow and collected the scattered light with a photomultiplier tube. Photomultiplier tube output was proportional to the concentration of seed particles at a single point. Long, Chu, and Chang [18] focused a laser sheet into the flow and used a TV camera to record the scattered light intensity. This allowed a two-dimensional section of the flow to be recorded rather than a single point.

Morgan [8] used laser induced fluorescence dye in a water flow apparatus of identical geometry to the current apparatus to provide scalar concentration measurements of the flowfield. Mean and fluctuating concentrations were obtained for opposing primary jets and a combination of annular jets and primary jets. Seal [7] used ethyl alcohol and fog juice to seed the flow of a swirling jet. Qualitative results of the jet concentration were presented. For both studies a laser sheet was set up in the desired region of the flow and light was scattered with marker particles. A video camera and VCR were used to record images that were later processed with computer software.

1.2 Experimental Apparatus

In an ideal annular combustor, geometric symmetry exists between annular jets. The volume between these annular jets, or cells, extend downstream of the combustor inlet. The flowfield between cells will be the same because of this geometric similarity. Therefore, measurements would only need to be taken for one cell to obtain the entire flowfield within the combustor.

The annular combustor model, figure 1.1, was designed to simulate the cold flow characteristics of current gas turbine combustors. Five cells were used in its construction in order to allow for any interaction between cells and remove wall effects. The primary zone of a combustor usually has three flows entering this region. These flows consist of: air from the discharge of a compressor through swirlers in a dome wall, fuel injection through the center of the swirler, and primary air jets normal to the mean flow in the combustor. Figure 1.2 shows a cross

section of an annular combustor with fuel nozzles and swirlers. No fuel injection was used in this research.

The cross section was 15 inches wide with a 3 inch height. The test section extended downstream a distance of 30 inches. Each cell contained one pair of primary jets located 1.5 inches downstream of the end plate, mounted normal to the flow from the annular jets.

Figure 1.3 shows a drawing on both annular and primary jets. Both annular and primary jets were constructed of aluminum. The annular and primary jets were designed with a contraction in order to provide a flat velocity profile upon entrance into the test section. The annular jet had an inlet diameter of 2.543 inches and diameter of 1.459 inches at the test section entrance. The center portion of the annular jet had a diameter of 1.084 inches at the test section entrance. This results in an annular gap of 0.1875 inches and entrance area of 0.7489 square inches. The primary jets were 1.375 inches in length with an inlet diameter of 1.0 inch and diameter of 0.43 inches at the test section entrance. This results in an inlet area of 0.1452 square inches for each primary jet.

In order to damp out disturbances and allow uniform mixing of the seed particles before entrance into the test section, tubing was attached to the primary and annular jets. Tubes extending 10.5 inches above the machined jets were connected to all ten primary jets. Preliminary flow visualization indicated that these tubes helped reduce unsteady displacement of the jet stagnation point. Tubes

extending 9.75 inches in front of the annular jets were used mainly to provide adequate length to allow mixing of the smoke.

The exit of the combustor model was connected to a plenum chamber, which was connected to a fan. A centrifugal blower was used to draw air through the test section. Previous work preformed on this model indicated that large scale feedback from the fan existed. To eliminate these large disturbances screens and foam were placed in the last 9.5 inches of the combustor model.

1.3 Laser Doppler Velocimetry Optics

The laser Doppler velocimetry system used in this experiment incorporated a Spectra Physics model 165 Argon-ion laser. It was configured to measure a single component of velocity using the wavelength of 4880 Angstroms, blue. Figure 1.4 is a schematic of the LDV system used.

The transmitting optics used were made up of the DISA 55X components. In the first stage of the transmitting optics the beams entered a beam waist. The beam waist was used to adjust the beam diameters to a minimum at the probe volume. This was necessary because when the beams have a minimum diameter the wavefronts are planar. The interference pattern produced by the intersection of planar waves produces an evenly spaced interference pattern across the probe volume. If the wave fronts were spherical, the resulting fringe surfaces would be distorted and an evenly spaced interference pattern would not be produced. Particles with the same velocity, but crossing different parts of the probe volume, would produce different Doppler frequencies when spherical wave fronts intersect.

A beam splitter is used next to split the single beam into two equal intensity beams. One beam stayed along the optical axis, while the second beam was translated approximately 30 mm from the optical axis.

The frequency of the beam along the optical axis was acousto-optically shifted by 40 MHz using a Bragg cell. The Bragg cell causes the fringes in the probe volume to move at 40 MHz. With fringe movement in the probe volume, the velocity directions of the particles crossing the probe volume can be detected. A frequency of 40 MHz plus the Doppler frequency resulted when particles were moving in the opposite direction of fringe movement and a frequency of 40 MHz minus the Doppler frequency for particles moving with the fringe movement. In addition to detection of velocity directions, the Bragg cell helps correct for angle or fringe bias in the velocity measurements.

The final set of optics in the transmitting optics package was the beam translator. The beam translator moves the off axis beam back towards the optical axis. This was necessary in order to allow entrance into the beam expander. Also, adjustments in the beam translator allowed the beams to be focused to a common intersection point.

Upon exit from the beam translator, a beam expander is used to increase the beam diameters by a ratio of 3.75 to 1. The purpose of increasing the beam diameters was to reduce the size of the probe volume. With a smaller probe volume, gradient bias is reduced and greater resolution of the flowfield can be

obtained by using smaller grid spacing. The radius and length of the probe volume is given by equations 1.1 & 1.2.

$$b_o = \frac{f \cdot \lambda}{b \cdot \pi} \tag{1.1}$$

$$l = \frac{2b_o}{\sin(\frac{\Theta_B}{2})} \tag{1.2}$$

where:

b = radius of input beam

f = focal length of field lens

λ = wavelength of laser beam

θ_b = angle between beams

A field lens focused the two incoming beams to a common point. The field lens used was actually made up of two lenses. Focal lengths for each lens was f_1= 30 inches and f_2=48 inches. From lens theory, the effective focal length of the two lenses can be expressed by equation 1.3.

$$f = \frac{1}{\left[\frac{1}{f_1} + \frac{1}{f_2}\right]} \tag{1.3}$$

Therefore, the field lens had a focal length of 18.46 inches. Table 1.1 lists parameter settings of the LDV system used for this research.

The receiving optics used consisted of different elements made by DISA. The optics were used in forward scatter, which ensures a stronger signal than in back scatter. Scattered light from the probe volume was focused to a point by a receiving lens. Next, a beam expander working in reverse reduced the diameter of the light from the receiving lens allowing entrance into a spatial filter.

In order to reduce extra light from reflections, room light, or scattered light not from the probe volume a spatial filter is used. This filter is the same size as the probe volume. The light passing through the spatial filter enters a photomultiplier. The photomultiplier is used to convert light intensities into electrical signals proportional to the intensity of the light. The output of the photomultiplier was then sent to a signal processing unit.

1.4 Data Acqustition System

1.4.1 Laser Doppler Velocimeter System

The output signal from the photomultiplier contains a signal that has been shifted by 40 MHz plus or minus the Doppler frequency from a measurement. This signal must first be frequency shifted to allow the processing electronics to handle the signal. A DISA 55N12 frequency mixer was used to mix the signal with a frequency between 31 MHz to 49 MHz. See figure 1.5 for a schematic of the data acquisition system.

After frequency mixing, the signal was sent to a TSI model 1980 counter type signal processor. This signal first entered a model 1984 input conditioner

where high and low pass filtering occurred to remove the "pedestal" or DC component from the signal and remove any high frequency noise. In addition, gain adjustment and minimum cycles/burst settings were set in the input conditioner. The cycles/burst setting is used to determine the number of fringes a particle must traverse in the probe volume before that signal is accepted by the processing electronics as a valid data point. A setting of 16 cycles/burst was used for all measurements. This eliminated data from particles that passed through the edge of the probe volume and crossed only a few fringes. The filtered output jack was connected to a Hewlett Packard Spectrum Analyzer to monitor the Doppler frequency of the signal.

Output of the input conditioner was sent to a model 1985 timer for further analysis. A percent comparison setting is used to make a comparison between the time for N cycles and N/2 cycles. Measurements were made with a 1 % setting, which ensured an actual .8 % comparison between N and N/2 cycles. (The time for 16 and 8 cycles must be within .8 % for the data point to be accepted.) Additionally, settings for the exponent and setting manual/auto ranging on the exponent was available. The data ready jack, provided a 0.6 microsecond pulse every time a new data point is validated. This was connected to a counter to determine the data rate. A monitor output jack is connected to a Tektronix 215A oscilloscope in order to observe validated data.

Data was output to a PC's Limited microcomputer through digital outputs on the timer unit. In addition to processing the data, the computer controlled the

position of the probe volume within the test rig via a Metrobyte Das20 A/D board. Table movement commands were carried out by three stepper motors allowing three dimensional movement of the probe volume. A laser table contained two directions of movement, where the third direction of movement was accomplished by movement of the field lens. Probe volume position in the test rig was read into the computer by using an Acu-Rite III digital readout system. A scale attached to each axis of the table provided position information. Each scale had an accuracy of .0005 inches, which facilitated accurate repositioning of the probe volume for repeated runs.

Velocity bias is caused by the arrival rate of particles in the probe volume being dependent on the flow velocity. A burst mode signal processor was used in this research, which operates on the signals generated by single particles passing through the probe volume. Therefore, particles will pass through the probe volume more often when the flow velocity is high and less often when the flow velocity is low. The result of simply averaging these signals would cause the mean velocity to be biased high and the rms velocity to be biased low.

Many different methods are presently used to correct for velocity bias. Equal time sampling was used to eliminate the velocity bias for this research. Roesler [9] presents a study done on velocity bias and shows that this velocity bias may be eliminated by using equal time sampling. Data rates of 100 times the sampling rate were recommended to ensure equal time sampling, however it was shown that data rates of 10 times the sampling rate provided equal time sampling.

Data rates between 10,000 to 90,000 samples per second were present for this study, with average rates of 45,000 samples per second. A sampling rate of 1,000 Hz was used providing data rates 10 to 90 times the sampling rate. With these data rates, equal time sampling should exist between samples. A total of 10,000 samples were used to determine mean velocities for each point. Additional information on measurements and errors are in Appendices A and B.

1.4.2 Scalar Concentration Measurements

The beam from the Spectra Physics argon-ion laser was passed through a pair of focusing lenses and then through a cylindrical lens to produce a laser sheet of light. This sheet of light was then aligned within the combustor model at the desired measurement location. See figure 1.6 for a schematic of the laser sheet system.

Light scattered by marker particles was collected by a Panasonic WV-D5000 video camera. The camera, operated in normal shutter mode, recorded each field at 60 Hz and each frame at 30 Hz. Two fields are interlaced to produce each frame.

Output of the camera was recorded by a JVC Super VHS video recorder. These recorded images were digitized using an IBM PC/AT using Data-Translations DT-IRIS image processing hardware and software. These images were divided into 512 X 512 pixels and assigned a value between 0 and 255 to represent the relative concentration level of each pixel in the image. Software

averaging of multiple frames was done to obtain an average concentration level, for a particular location.

The DT-IRIS hardware/software pseudo-colors the images from the camera by mapping intensity levels to colors. Combinations of the colors red, green, and blue represent concentration levels. Pink indicates the highest concentration and dark blue the lowest concentration.

To eliminate any reflections occurring at the walls or in the background, an image called a dark image was subtracted from each image produced. A dark image was an image taken when no seed particles were in the test section. The resulting image represented the concentration of seed particles in the flow.

1.5 Particle Seeding

In order for a LDV system to operate particles must be mixed with the flow to determine the fluid velocity. Particles chosen for seeding must have several characteristics.

1) Must accurately follow the flow
2) Scatter light
3) Non-toxic
4) Inexpensive

The ability of the particles to follow the flow is most important. If a particle does not follow the flow, measured fluid velocities would be inaccurate. Particles in the flow must also scatter light since the LDV operates on the principle of

scattered light to detect the particle velocity. The use of non-toxic and inexpensive material is necessary for safety and economical reasons respectively.

The liquid chosen for use in these measurements was propylene glycol. This is a desirable liquid since it is non-toxic and completely water-soluble. In addition, droplets of propylene glycol are harmless to the respiratory system and is often used in many foods and domestic goods.

A TSI model 9306 six jet atomizer was used to produce uniform seed particles. Particles were approximately 2 microns in diameter. These particles caused little problems with condensation on the walls of the rig, as this would disrupt data acquisition. Cleaning of the rig had to be done occasionally in order to keep the condensation from disrupting the measurements.

Table 1.1 LDV Parameter Settings

OPTICAL SYSTEM SETTINGS

Wavelength	: 488 nm = 1.601 x 10^{-6} feet
Focal Length of Lens	: 18.46 inches
Diameter of Input Beam	: 0.175 in.
Angle Between Beams (avg.)	: 5 degrees
Length of Probe Volume (avg.)	: 0.056 in.
Diameter of Probe Volume (avg.)	: 0.0027 in.
Frequency Shift	: 40 MHz

DATA COLLECTION SETTINGS

Mode of Operation	: N burst mode
Filter Settings	: 20 MHz low pass 2 MHz high pass
Number of Fringes per Signal	: 16
Comparator	: 1 %
Sample Size	: 10,000 samples
Data Rate	: 10,000 to 90,000 samples/sec
Sample Rate	: 1000 samples/sec

FLOW SYSTEM PARAMETERS

Velocity Range	: -35 ft/sec ≤ U ≤ 35 ft/sec
Seed Particles	: Propylene Glycol
Seed Particle Size (avg.)	: 2 microns

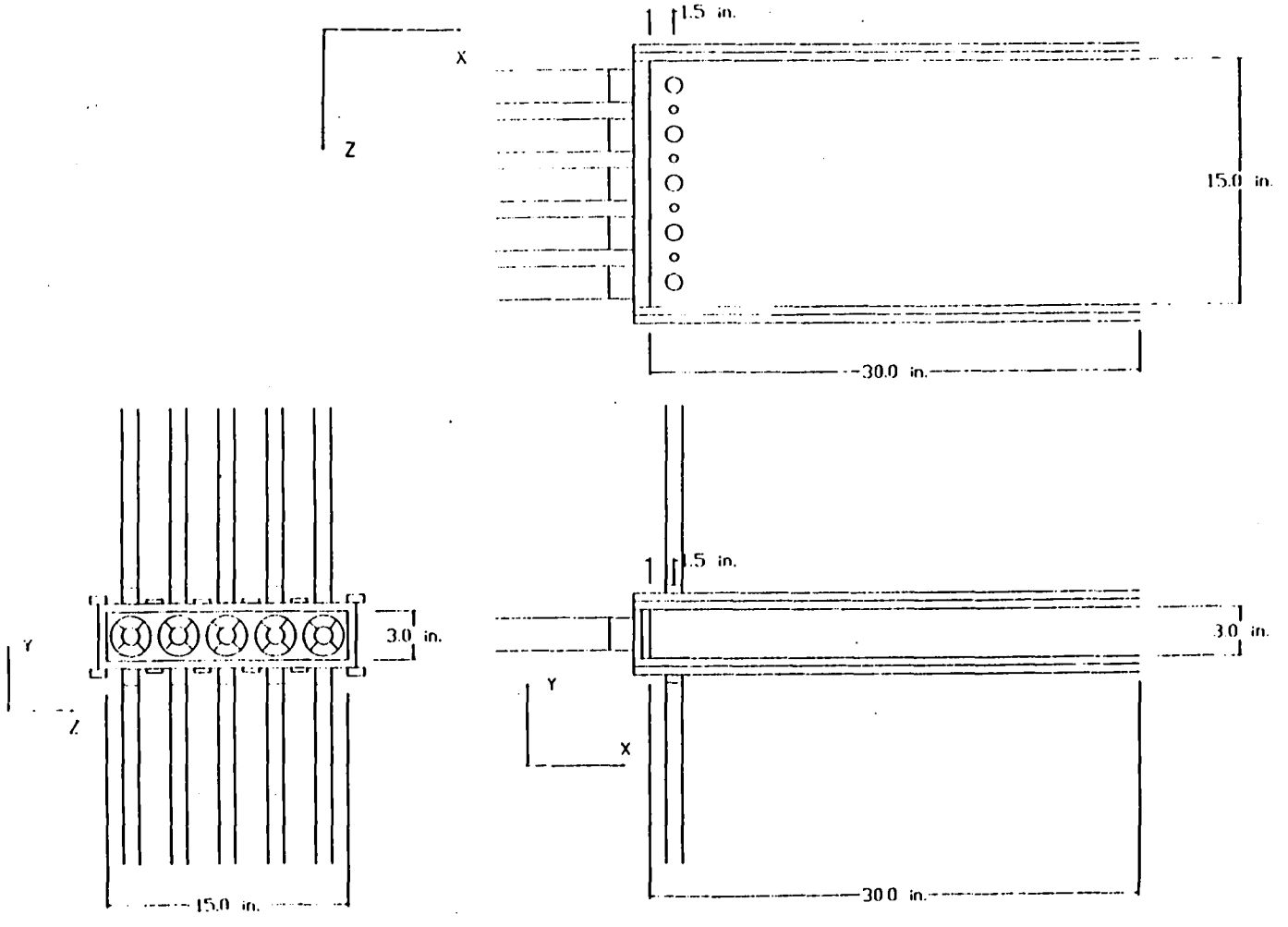

Figure 1.1 Three View Drawing of Annular Combustor Model

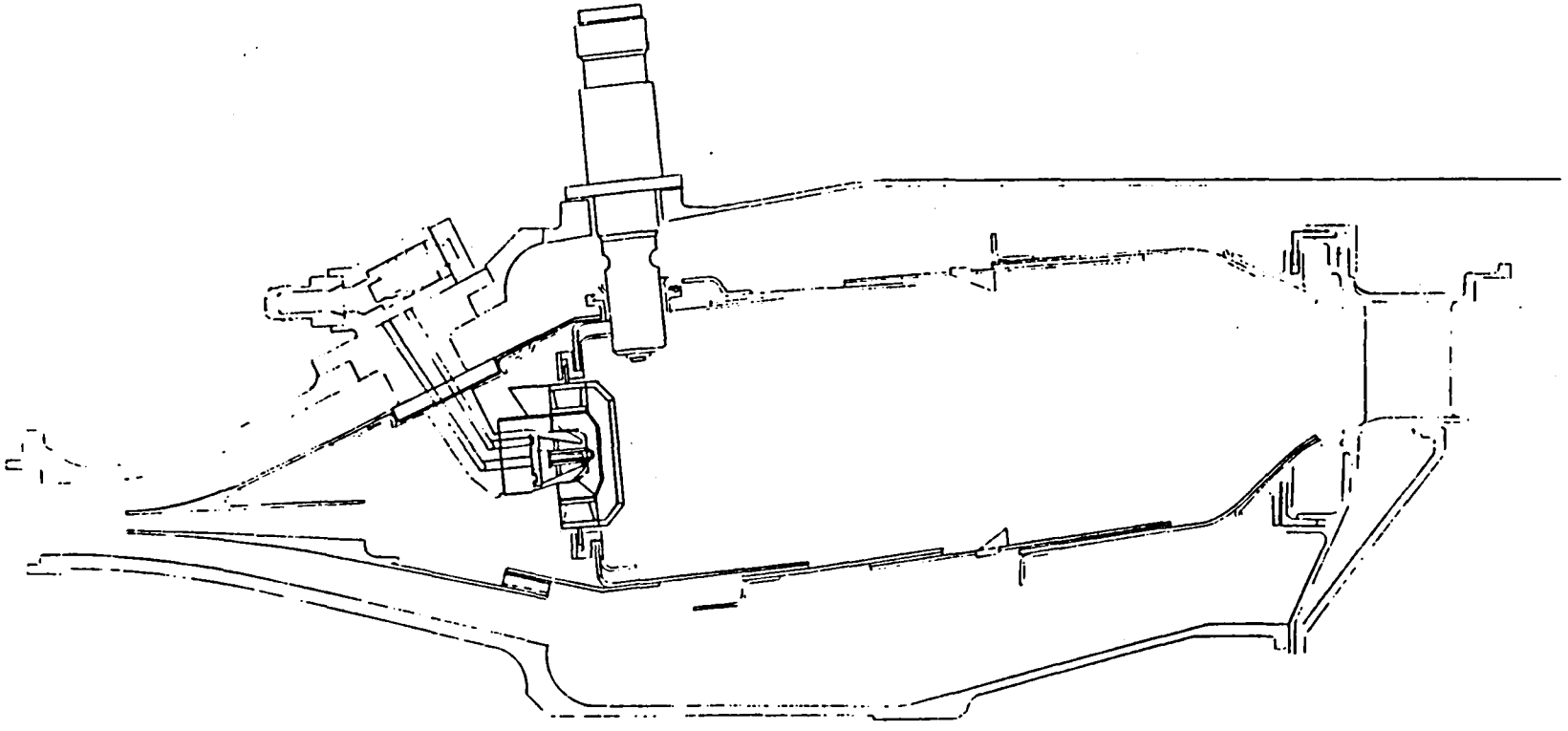

Figure 1.2 Cross Section of Allison's 570-K Annular Combustor

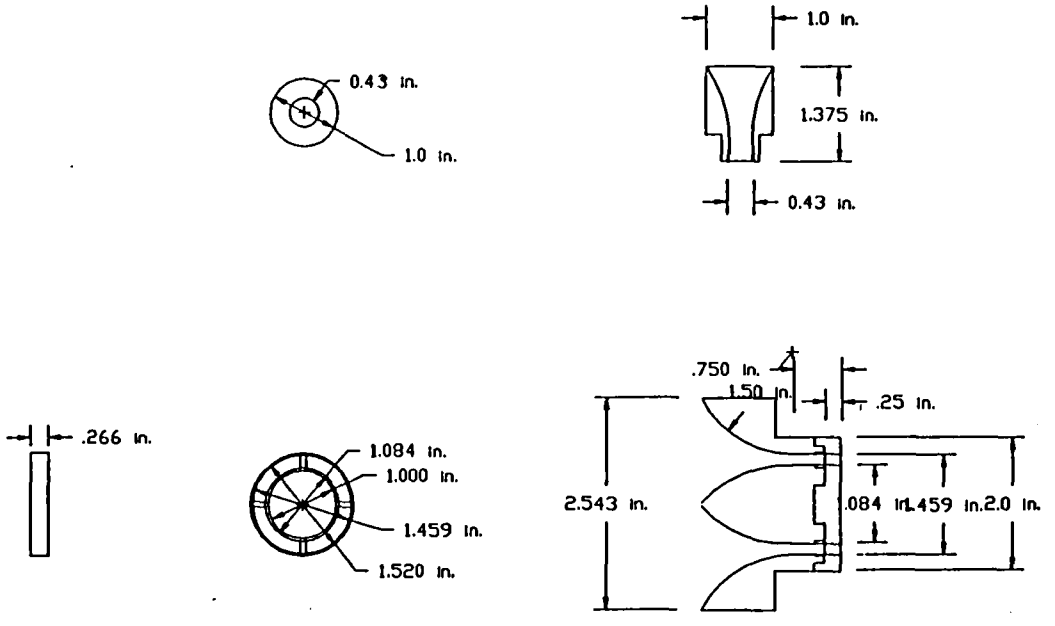

Figure 1.3 Primary and Annular Jet Drawing

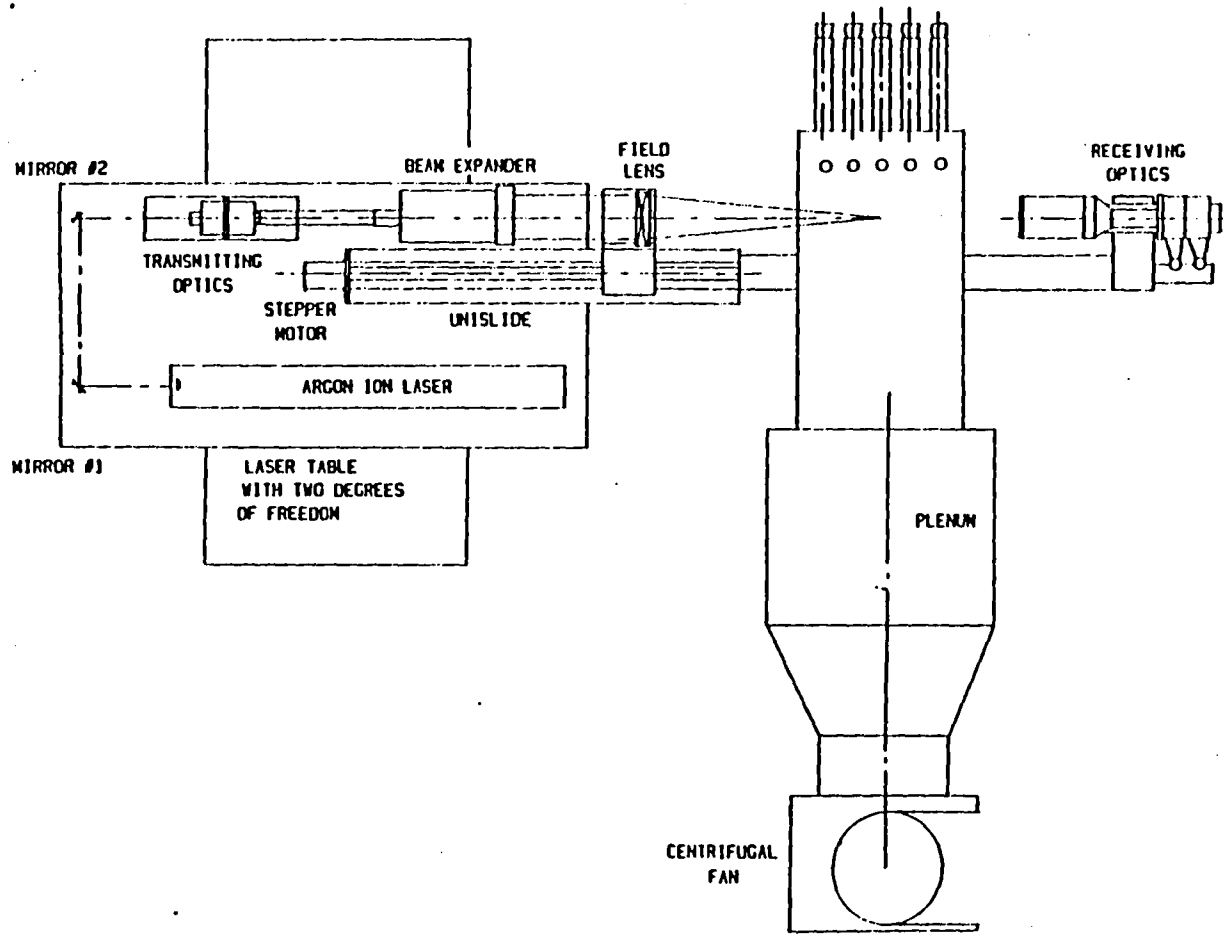

Figure 1.4 LDV Optics and Rig Setup (After Barron [6])

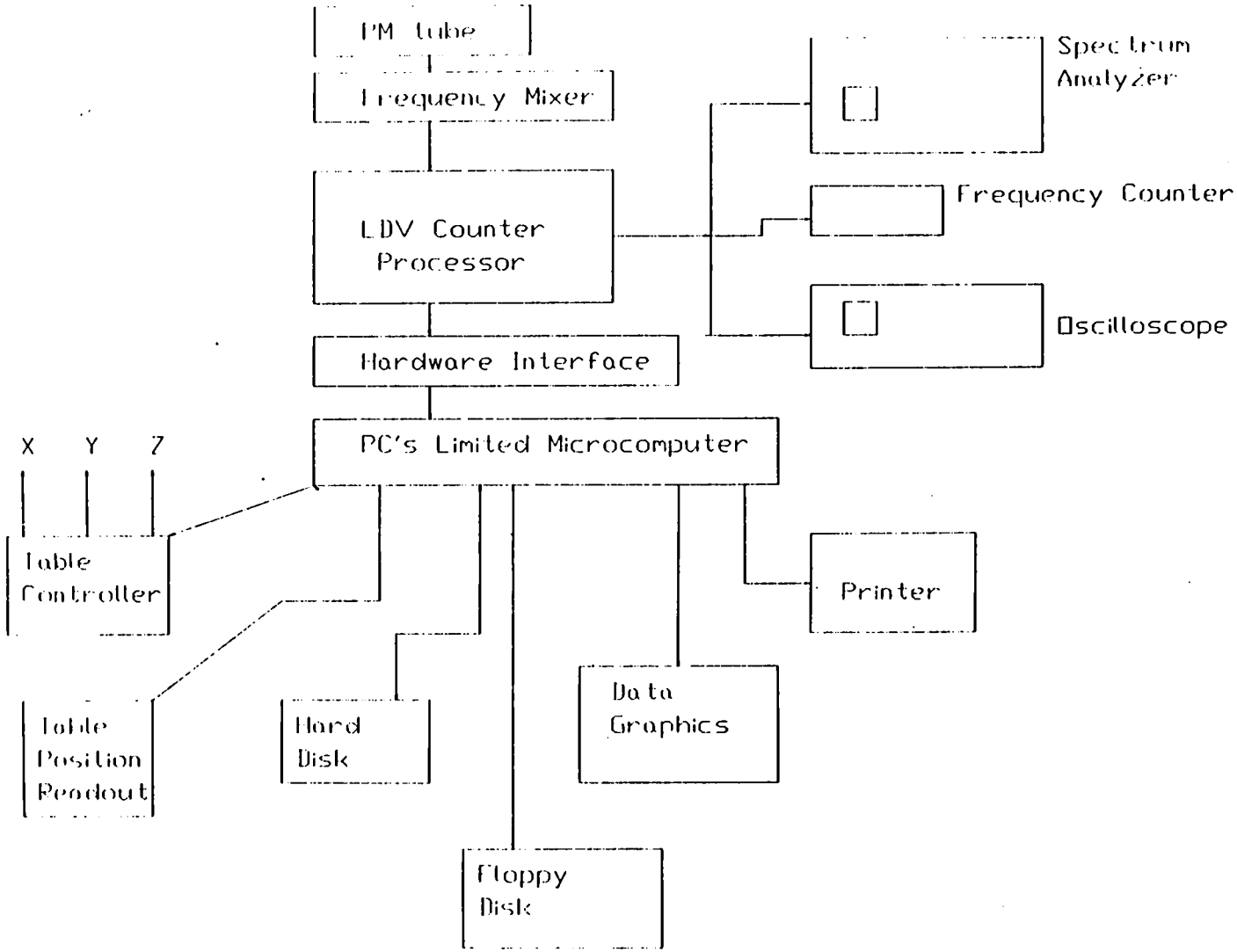

Figure 1.5 Schematic of LDV Data Acquisition System

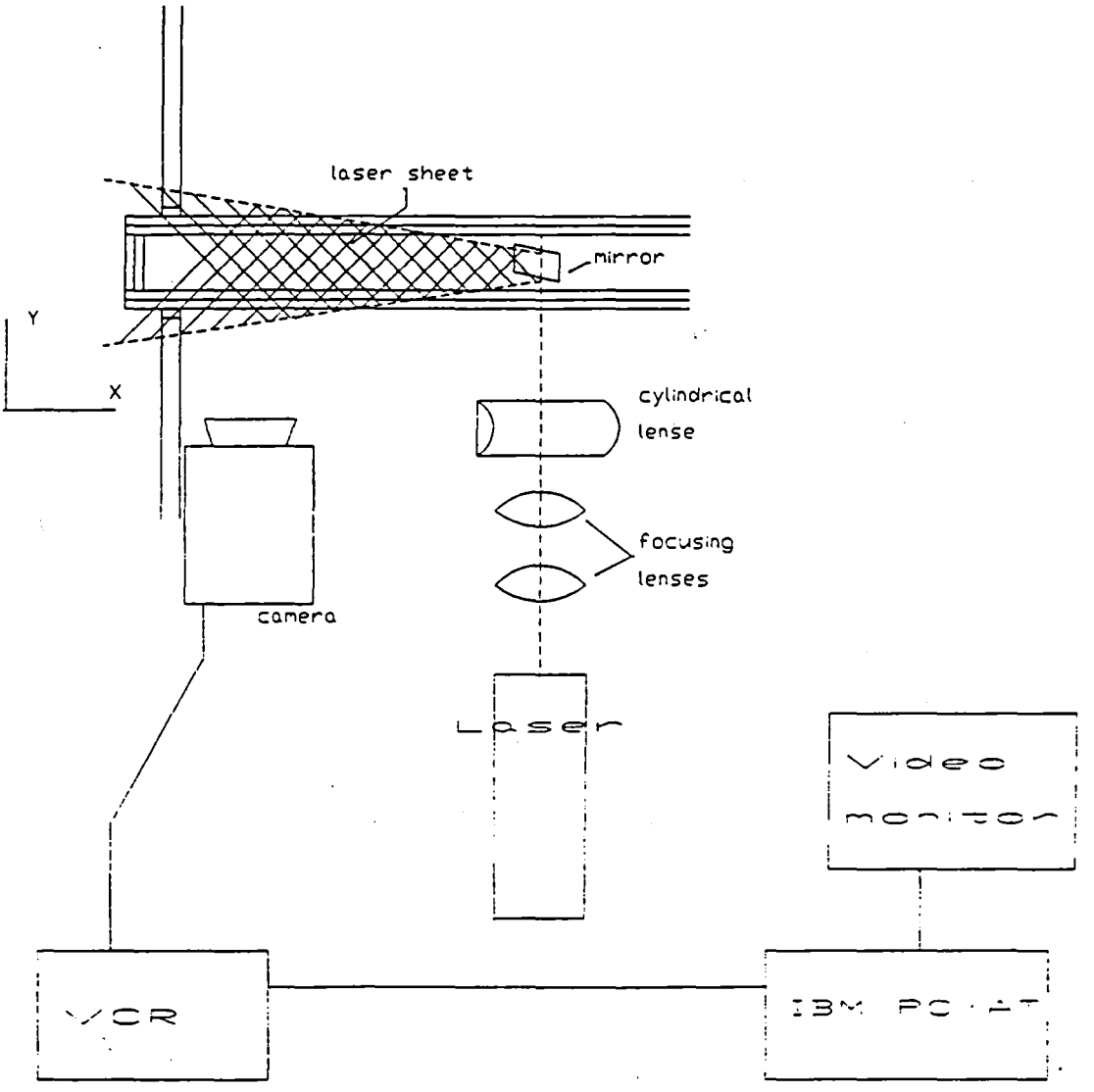

Figure 1.6 Schematic of Scalar Concentration Measurement System

CHAPTER 2

LASER DOPPLER VELOCIMETER MEASUREMENTS

A single component laser Doppler velocimeter system was used to obtain two-dimensional velocity measurements in the combustor model. Measurements include mean velocities, $\bar{U}$ and $\bar{V}$, root-mean-square velocities, U' and V', Reynolds shear stress component U'V', and a two-dimensional turbulent kinetic energy term. The turbulent kinetic energy term presented uses only the two fluctuating components measured in its evaluation. Details on all velocity measurements and the calculation of the statistics can be found in Appendix A.

Measurement grids for the various cases were mainly dependent on the type of flow being measured. A finer grid was necessary in regions of high velocity gradients in order to provide enough resolution to capture the details of the flow. In addition, probe volume must not overlap between data points so the probe volume length and radius must be taken into account.

All velocity measurements for the three different cases were taken in the XY plane. The sampling grids for the three cases are shown in figures 2.1-2.3. Measurements in the X-direction were taken at .5 inch intervals for the first four inches in the axial direction and at larger intervals downstream. Measurement ranges in the Y-direction (vertical) were determined by the limits of laser beam

access in the rig. Beam geometry allowed measurements for .5 in. ≤ Y ≤ 2.5 in.. Z-direction measurements, traverse, were confined to one cell of the combustor rig since symmetry was assumed between cells. Therefore, measurements in the Z-direction were between Z=6.0 in. Z=9.0 in..

2.1 Primary Jets Only

A set of five pairs of opposing primary jets centered 1.5 inches downstream of the rig end plate were used as the first case. The annular jet endplate was replaced with a solid one inch thick aluminum plate for this case. Figure 1.1 shows a drawing of the rig when annular jets are used in conjunction with the primary jets.

2.1.1 Inlet Conditions

To establish inlet conditions, velocity measurements of the primary jets were conducted. An extensive measurement of the lower primary jet was performed to observe the development of the jet as it enters the combustor model. A series of XY plane scans using the grid in figure 2.4 were performed. These scans were taken at .05 in. intervals in the Z-direction resulting in the XZ plane grid shown in figure 2.5. Since the average probe volume length was .05 in., the probe volume should not overlap between data points. Additionally, a measurement was taken of the upper and lower jets to determine the relative strengths of the two primary jets.

The mean and rms plots of the lower jet are presented in figures 2.6-2.12. Figure 2.6 shows the axial velocity, $\bar{V}$, distribution of the lower jet at Y=0.1 inches.

From this plot it is evident that the entrance velocity has a flat top profile with mean velocity of 27.9 ft/sec. This yields a Reynolds number of 6,392 based on the jet diameter. The axial fluctuating velocity, V_{rms}, in figure 2.6 indicates peak values along the edges of the jet at Z=7.7 and Z=7.3 inches and lower values at the edges of the jet at X=1.3 and X=1.7 inches. This is caused by the length of the probe volume being approximately the same size as the grid spacings.

Measurements taken at Y=0.25, 0.5, 0.75, 1.0, and 1.25 inches, figures 2.7-2.11, shows that the maximum velocity at the center of the jet starts to gradually decrease and spread as more fluid is entrained into the jet and it nears the oppositely opposed jet. Also, the jet is seen to have a slight bend downstream due to the crossflow in the rig. The V_{rms} plots indicate that larger fluctuations occur at the jet edges as the jet emerges into the more turbulent flow. The upstream edge of the jet, X=1.3 in., shows larger fluctuations than any other part of the jet due to recirculating flow upstream of the jet entrance.

The plane at Y=1.5 inches is at the center of the combustor model, figure 2.12. Velocity fluctuations of 6 to -10 ft/sec are a result of the fluctuating stagnation point of the two opposing jets. Higher rms values due to increased turbulent mixing is also evident. Flow visualization revealed that the stagnation point of the two jets oscillated about the midpoint.

The velocity distribution .6 inches from the primary jet inlets is plotted in figure 2.13, showing a comparison between the upper and lower primary jets. Approximately a 3% difference between the upper and lower jet maximum velocity

is present. The rms values indicate that the upstream side of the jet has a slightly higher turbulence level due to recirculating flow.

2.1.2 Mean Flowfield Results

Perhaps the most helpful form of data presentation of the mean flow are XY plane vector plots. Vector plots at the various Z locations provide a quick and informative view of the flow. With the addition of streamlines to the vector plots, recirculation zones and symmetry about the rig centerline is evident. Figures 2.14-2.18 show vector plots for $7.1 \leq Z \leq 7.9$ inches. Symmetry should exist between upper and lower halves of the rig and between planes equal distance from the centerplane (Z=7.5 in.).

Figure 2.14 shows the vector plot for the rig centerplane (Z=7.5 in.). Clearly evident is the upper rear recirculation zone centered about X=3.5 in. and Y=2.2 in.. A lower recirculation zone also exists at approximately X=3.5 in. and Y=0.75 in.. Asymmetry between upper and lower halves is clear as the flow at the centerline tends toward the lower wall resulting in a reattachment point of the lower recirculation zone farther upstream than the upper zone. This reattachment point will cause the upper recirculation zone to be larger than the lower recirculation zone. A larger recirculation zone will allow the flow to diffuse faster and cause the stagnation point of the recirculation zone to occur farther upstream.

Plots at the planes of Z=7.4 and Z=7.6 inches (figure 2.15) should be the same due to symmetry of the rig. These two plots show the center of the upper and lower rear recirculation zones occur at X=3.5, Y=2.1 inches and X=3.75, Y=0.7

inches respectively for Z=7.6 inches. The same points for Z=7.4 inches are at X=3.45, Y=2.2 inches and X=3.75, Y=0.7 inches respectively. Here symmetry between planes was seen to exist, while symmetry between upper and lower halves of the rig does not exist.

Comparison of the two planes at Z=7.7 in. and Z=7.3 in. (figure 2.16) shows that the recirculation zones in the Z=7.3 in. plane are centered slightly forward of the zones in the Z=7.7 in. plane. In addition, the recirculation zones in the Z=7.3 in. plane entrains fluid immediately downstream of the jet stagnation point, while in the Z=7.7 in. plane the fluid immediately downstream of the jet stagnation point is allowed to move with the axial flow.

Different features of the flowfield are seen at the Z=7.2 and Z=7.8 in. planes. In figure 2.17, flow forward of the jet inlet point, X=1.5 in., is not all entrained into the forward recirculation zones. Since the primary jets have a diameter of .43 in., the planes here are outside the boundaries of the jet. Thus, fluid is able to flow downstream and be entrained into the rear recirculation zones. Comparison between the two planes show definite asymmetries. The rear recirculation zones in the Z=7.2 in. plane are offset due to the reattachment point of the lower recirculation zone being farther upstream than the upper zone. While both planes see a bending of the flow toward the lower wall, only the plane at Z=7.2 in. shows the dramatic offset of recirculation zones.

Figure 2.18 shows plots at Z=7.1 and Z=7.9 inches respectively. The plane at Z=7.1 in. seems fairly symmetric with rear recirculation zones at approximately

X=3.5 in.. The flow between upper and lower halves of the rig is symmetrical as the fluid continues downstream. The plane at Z=7.9 in. shows offset rear recirculation zones with the upper and lower zones centered around X=3.4 and 3.2 in. respectively. In addition, forward recirculation zones begin to become visible within the measured portion of the flow.

Additional vector plots of the flow between the planes Z=6.0 and 7.0 in. and Z=8.0 and Z=9.0 in. are presented in figures C1-C11 in Appendix C. Table 2.1 presents approximate forward and rear recirculation zone locations for the planes 6.5 in. $\leq Z \leq$ 8.6 in.. Some general trends of the recirculation zones can be seen from this table. Forward recirculation zones move downstream and toward the upper and lower walls farther away from the rig centerplane. Also, the forward recirculation zones tend to be fairly symmetric between upper and lower portions of the rig. These recirculation zones are clearly visible between the planes Z=6.5 and 7.0 in. and Z=8.0 and 8.5 in..

The center of the rear recirculation zones tend to move upstream and toward the upper and lower walls the farther away from the rig centerplane, Z=7.5 inches. Asymmetry between upper and lower recirculation zones is present in many of the plots. In addition, there seems to be a lot of variation in the occurrence of the recirculation zone centers between planes on different sides of the rig centerplane. Another very noticeable aspect in all the plots is the trend for the streamlines to bend quicker toward the lower wall of the rig. Reverse flow upstream of the jet entrance is evident even to the cell boundaries at Z=6.0 and 9.0 in., indicating how influential the primary jets are throughout the cell.

2.1.3 Turbulent Flowfield Results

To verify turbulence quantities, a close comparison to turbulent jet data from Sami [20] should exist. A comparison of Sami's data for both the Reynolds shear stress and axial rms quantities at a Reynolds number of 220,000, to data from the present experiment at Y=0.5 inches from the lower primary jet can be seen in figure 2.19. The data from Sami and from this study are both nondimensionalized by the maximum jet velocity. From figure 2.19, maximum values of Reynolds stress occur at the jet edge. The maximum value for the combustor model is 1.3 times larger than the maximum value obtained by Sami, but the difference could be larger due to the poor resolution of the measurement grid compared to Sami.

The turbulence intensity comparison in figure 2.19 shows peak turbulence intensity at the jet edge with maximum values of 18 % for Sami and 20 % for the combustor model. The difference between the two data sets is mainly due to the effect of the opposing jet and the main flow in the combustor model. Both comparisons provide confidence in the data reduction method used to obtain the turbulence quantities with in the combustor model.

Figures 2.20-2.23 present the axial fluctuating , U_{rms}, and the vertical fluctuating, V_{rms}, velocities in the YZ plane. At stations X=0.5 and X=1.0 inches peak values of the fluctuating components are seen at the center portion of the rig. The magnitudes of these quantities are seen to increase at station X=1.0 inches due to the measurements being closer to the impinging jets. The maximum value of the U_{rms} term is seen to be more and more concentrated in the center portion

to the rig at X=1.0 in. than at X=0.5 in. The V_{rms} term seems to diffuse and spread out at the X=1.0 in. station while the magnitudes of the fluctuations in the center portion of the rig nearly doubles.

At the entrance of the primary jets, X=1.5 in., the influence of the primary jets can clearly be seen. In figure 2.22, the U_{rms} velocity is seen to have a large decrease in magnitude between the upper and lower walls of the rig at Z=7.5 in. indicating very low turbulence in this region. Two peaks can be seen on both sides of this dip, at Z=6.6 in. and Z=8.4 in., indicating increased turbulence in these regions due to the fluid flow accelerating around the jets downstream.

The V_{rms} plot at X=1.5 in. shows a decrease in the V_{rms} velocity at the jet centerplane. However, this decrease in magnitude doesn't span the entire height of the rig. Peak values are seen at the middle of the rig at Y=1.5 in., Z=7.5 in.. This is caused by increased turbulence due to the fluctuation of the jet stagnation point about Y=1.5 in.

Downstream of the primary jet entrance, at X=2.0 inches, the magnitude of the U_{rms} plot increases due to the acceleration of fluid from the jet stagnation point between the upper and lower recirculation zones. The V_{rms} term shows a decrease and diffusing of magnitudes toward the walls and cell boundaries. Similar results are seen at stations X=2.5, 3.0, 3.5, 4.0, and 6.0 inches, see Appendix C figures C12-C16.

Figures 2.24 & 2.25 show line plots of the U_{rms} and V_{rms} velocities at measurement locations between X=0.5 and 6.0 inches for planes at Z=7.0, 7.5,

and 8.0 inches. The largest fluctuations in the U_{rms} term occur immediately upstream and downstream of the jet stagnation point. The largest V_{rms} fluctuations occur at the jet stagnation point, X=1.5 inches. The U_{rms} and V_{rms} magnitudes decrease and diffuse downstream and farther from the rig centerline until nearly uniform magnitudes at X=6.0 inches.

An alternate way to view the previous terms is through the two-dimensional turbulent kinetic energy term. Figures 2.26 & 2.27 show the results of the YZ plane plots for K'. At station X=0.5 inches, a central peak is observed in the middle regions of the rig indicating higher levels of turbulence than other regions of the flow. Similar results are seen at X=1.0 in. where the magnitude of K' increases due to the acceleration of the fluid from the jet stagnation point between the forward recirculation zones.

The greatest magnitude of turbulence energy occurs at the primary jet impingement, figure 2.27. A reduced magnitude of turbulence energy exists at Z=7.5 in., where the primary jets enter, and larger peaks on either side due to jet entraining fluid within the rig. Also visible are the two peaks either side of the rig midpoint, see figure 2.22 for the U_{rms} profile. Again, acceleration of fluid around the primary jets causes this increased turbulence.

Results at X=[illegible]es indicate a spreading of the turbulence energy in the Z direction. Increased [illegible] around the primary jets and downstream are responsible for this. Simil[illegible]s downstream are present in Appendix C in figures C17-C19.

Figure 2.28 represents line plots of K' at the Z planes of 7.0, 7.5, and 8.0 inches. It can be seen that the highest turbulence levels are around the stagnation region of the two jets. Turbulence levels decrease and spread towards the upper and lower walls of the rig as the flow continues downstream. Uniform turbulence is present by the time the flow is at X=6.0 inches.

Figures 2.29 & 2.30 represent YZ plane contour plots of the Reynolds shear stress component in the XY plane. Higher magnitudes of Reynolds stress occur in areas of higher velocity gradients where large momentum transfer occur. At the X=0.5 in. station peak values occur between Z=6.7 in. and Z=8.3 in.. In addition, the sign of the Reynolds stress changes at the midpoint of the rig, Y=1.5 in.. These peak values occur in the regions where the forward recirculation zones occur. A similar plot is seen at the X=1.0 in. station. Only differences between this plot and at X=0.5 in. is that the magnitudes have increased.

A very different plot is seen at X=1.5 in. in figure 2.30. Peak negative values occur at the Z=7.5 in. plane where the primary jets enter. This indicates a large amount of momentum transfer taking place due to the fluid being entrained into the entering jet. Maximum positive values occur in the center of the rig on either side of the centerplane. Here, the stagnation point of the two jets result in large amount of shear stress and higher turbulence as the stagnation point fluctuates.

The plot at X=2.0 inches shows negative values of shear stress now occur on the lower half of the rig, while positive values occur on the upper half of the rig.

Peak values can be seen to occur between Z=6.7 and Z=8.3 inches due to the recirculation zones in these regions. Additional plots downstream have similar trends and can be seen in figures C20-C22 in Appendix C.

Figure 2.31 shows the Reynolds shear stress distribution in the planes at Z=7.0, 7.5, and 8.0 inches. Peak values occur at the jet stagnation region. Magnitudes are seen to decrease the farther away from the centerplane and a uniform distribution between upper and lower walls develops at X=6.0 inches.

2.2 Annular Jets only

In the second case, five annular jets were investigated. The three-view drawing in figure 1.1 shows the configuration of the model except all primary jets were removed and replaced with plugs.

2.2.1 Inlet Conditions

To establish inlet conditions of the annular jets, velocity scans were made at four edges of the center annular jet. Figure 2.32 shows a sketch of where the data was taken with respect to the center annular jet.

Figure 2.33 show mean and rms velocities at 0.08 inches from the annular jet exit. The results are plotted versus the radius of the annular jet. The mean velocity has a relatively flat profile across the annular gap and agreement between data taken at the different edges. A mean velocity of 23.2 ft/sec exists in the gap. The rms velocity shows larger values for the right and left annular jet edges than the top and bottom edges. This is due to the finite size of the probe volume. The

probe volume length was oriented across the annular gap for these two measurements. This will cause gradient bias to occur due to the existence of a wide range of velocities across the probe volume.

2.2.2 Mean Flowfield Results

The vector plots for the annular jets only case are seen in figures 2.34-2.37. Figure 2.34 shows the rig centerplane vector plot with streamlines. Two regions of high velocity are seen as the fluid discharges into the rig through the annular jets. These peaks spread out and entrain more fluid as the annular jet of fluid develops into the rig. A portion of the fluid from the upper and lower section of the annular jet sets up a pair of counter rotating vortices within the center portion of the annular jet. The main portion of the fluid can be seen converging at the middle of the rig and accelerating as the flow is squeezed between recirculation regions of flow along the upper and lower walls of the rig. Downstream, the main flow then decelerates as the recirculation zones are passed.

Recirculating flow along the upper and lower walls of the rig has been observed through flow visualization studies and will be presented in a later chapter. The vector plot at Z=7.5 inches shows some indication of these recirculation zones by the slight turning of the flow at the upper and lower data limits.

Results similar to those at Z=7.5 inches are seen at Z=7.4 and 7.6 inches, figure 2.35. A recirculation zone along the upper wall in the Z=7.6 in. plot is more evident than the previous two plots demonstrating asymmetries in the flow. The existence of recirculating flow in the center annular jet region and the convergence

and acceleration of the main flow between the recirculating flow along the upper and lower walls still exist.

Similar results are seen farther away from the centerplane between 6.8 in. $\leq Z \leq$ 8.2 in., see Appendix C figures C23-C34 for planes $Z <$ 7.2 inches and $Z >$ 7.8 inches. Several general trends can be observed from these figures. First, the movement of the two velocity peaks at the annular jet exit toward the centerline and the disappearance of the recirculation zone behind the center of the annular jet. The cause of both of these is due to the annular jet curvature. Second, the widening of the recirculation zones along the upper and lower walls. Both recirculation zones are clearly evident farther away from the rig centerplane. Third, a decrease in the main flow velocity along the centerline is seen. The flow is still seen to accelerate between the upper and lower recirculation zones but with decreased velocities.

At planes outside of the annular jet, 6.0 in. $\leq Z \leq$ 6.7 in. and 8.3 in. $\leq Z \leq$ 9.0 in., there is a breakdown of any real organized pattern of flow. Some general trends are still noticeable in the plots. First, downstream flow is reduced and completely disappears by the time the planes at Z=6.3 in. and Z=8.7 in. are reached. Regions of backflow along upper and lower walls gradually converge at the center of the rig eliminating flow downstream. Second, larger regions of backflow seem to exist along the lower wall of the rig. Initial measurements showed the flow in the rig was very sensitive to the annular jet endplate position. If the plate was not perfectly perpendicular to all the rig walls asymmetries would arise.

No well defined recirculation zone can be seen in any of the previous plots. Sometimes very random, perhaps chaotic, flow velocities are seen in the recirculating flow. The flow was observed to be extremely unsteady during the flow visualization study. Still, general trends in the flow can be discerned.

2.2.3 Turbulent Flowfield Results

The YZ plane U_{rms} and V_{rms} plots for the annular jets only case can be seen in figures 2.38-2.39. Plots at X=0.5 inches, figure 2.38, show larger fluctuations in the annular gap of the annular jet with decreased fluctuations in the inner portion of the annular jet and outside the annular jet, Z < 6.8 inches. Larger turbulence levels occur at the exit of the annular jet due to the mixing of the fluid in the rig with that entering the rig. Larger turbulent fluctuations can also be seen at Z > 8.2 inches in both U_{rms} and V_{rms} plots. Since these levels are not present on the opposite side of the cell, these values may be in error.

At X=1.0 inches similar results are seen. Increased magnitudes are evident in the inner portion of the annular jet and a spreading of the turbulence due to the entraining of more fluid by the annular jet. The V_{rms} plot is seen to be spread out over a larger area than the Urms plot and have less defined fluctuations in the annular jet region. Plots on downstream show similar development of U_{rms} and V_{rms} profiles in the rig, see figures C35-C42 in Appendix C.

Figures 2.40 & 2.41 show the U_{rms} and V_{rms} velocities as they develop downstream of the annular jet in the planes at Z=7.0, 7.5, and 8.0 inches. The largest U_{rms} fluctuations occur at the annular jet entrance, while smaller fluctuations

are present in the center of the annular jet. For the V_{rms} plots, peak values can be seen behind the center of the annular jet. The turbulence spreads toward the upper and lower walls and the cell boundaries with decreasing magnitude the farther downstream. Uniform turbulence can be observed at X=6.0 inches. But, magnitudes are much greater than zero unlike values for the primary jets only case.

The two-dimensional turbulent kinetic energy plots are presented in figure 2.42. Trends existing in the U_{rms} and V_{rms} plots are also seen to occur here. Similar plots are seen at X=0.5 in. and X=1.0 in.. Most of the turbulent energy can be seen concentrated at the annular jet exit due to larger velocity gradients in this area because of annular jet flow mixing with the flow already in the rig. At X=1.0 in., the turbulent energy can be seen to spread out more and increases magnitude in the inner annular jet region. Regions of peak turbulence energy can be seen at Z > 8.2 in., where peaks existed in the rms plots. Similar results can be seen at downstream stations X=1.5 to 9 in. in figures C43-C46 in Appendix C.

Figure 2.43 shows line plots of the K' distribution as it develops downstream for planes at Z=7.0, 7.5, and 8.0 inches. The greatest turbulence energy can be seen at the annular jet exit, as was seen from the contour plots. Planes at Z=7.0 and 8.0 inches have peak values at the rig center, while at Z=7.5 inches two peaks are seen on both sides of the rig center. Peak magnitudes diffuse on downstream, but the K' distribution is not quite uniform at X=6.0 inches.

YZ plane plots of the XY plane Reynolds shear stress are in figure 2.44. The U'V' distribution at X=0.5 inches indicates that the largest magnitude occurs in the annular jet exit region and near the cell edges at Z > 8.5 inches. Peak fluctuations in the annular jet region occur at the edges of the annular gap where the largest turbulent friction exists due to fluid mixing between fluid entering through the annular jet and the fluid within the rig. Another flat profile can be seen outside the annular jet region, indicating that very little momentum transfer is occurring. Peak fluctuations at Z > 8.5 in. may be caused by error in measurement. Similar results are seen between X=1.0 in. and X=9.0 in.. Additional plots for downstream locations are in figures C47-C50 in Appendix C.

Figure 2.45 shows Reynolds shear stress distributions in planes at Z=7.0, 7.5, and 8.0 inches. Largest magnitudes and variations occur immediately downstream of the annular jet, where large velocity gradients and recirculation zones are present. Downstream, the shear stress spreads toward the rig boundaries with decreasing magnitudes. Positive values of U'V' occur in the upper portion of the rig and negative values in the lower portion of the rig.

2.3 Annular and Primary Jets

For the third case, annular and primary jets were used together. Figure 1.1 represents the three view drawing for this case. The five pair of primary jets were centered 1.5 inches downstream of the annular jet entrance.

2.3.1 Inlet Conditions

To establish inlet conditions for this case the same type of measurements made on the primary jets for the primary jets only case were performed along with measurements of the annular jet described earlier. Figures 2.46-2.52 present contour plots of the mean and rms velocity of the lower primary jet. Figure 2.46 shows the mean velocity distribution at Y=0.1 inches above the lower primary jet. Again, a flat top profile similar to the primary jets only results are seen. A mean velocity of 15.4 ft/sec is present resulting in a Reynolds number of 3,528. The rms velocity shows peak values along the edges of the jet at Z=7.7 in. and Z=7.35 in. and lower peaks along edges at X=1.35 in. and X=1.7 in.. Error due to probe volume length and the grid spacing produces this result. In addition, higher fluctuations occur on the upstream side of the jet, X < 1.3 in., than on the downstream side due to a recirculation zone at this edge of the jet.

Measurements taken in the planes at Y=0.25, 0.5, 0.75, 1.0, and 1.25 inches, figures 2.47-2.51, show the development of this jet as it enters the combustor model. The mean velocity of the jet can be seen to gradually decrease and bend downstream as more and more fluid is entrained by the jet and the crossflow from the annular jet mixes with the jet. Comparison between figures 2.7-2.11 for the primary jets only case demonstrates the effect of the annular jet on the primary jet flow. In addition, negative velocities are clearly evident on the upstream side of the primary jet for planes up to Y=1.0 in., while the downstream side of the jet has velocities between .5 to 2 ft/sec. This is caused by a clockwise

rotating recirculation zone between the endplate and the upstream side of the primary jet. These negative velocities are seen to disappear at Y=1.0 in. due to the annular jet crossflow.

The rms velocities in figures 2.47-2.51 show increased fluctuations on the upstream side of the primary jet until the Y=1.0 in. plane is reached. Larger fluctuations are evident on the downstream side of the jet for Y=1.0 and 1.25 in. This change in turbulence is due to the deflection of the primary jet by the annular jet and the formation of a rear recirculation zone at the downstream edge of the jet.

The jet stagnation point is reached at the Y=1.5 in. plane, figure 2.52. The mean velocity is similar to figure 2.12 for the primary jets only case. The mean velocity is seen to fluctuate about zero due to the unsteady fluctuations of this stagnation point. A difference is visible between the rms velocities in figure 2.52 and figure 2.12 for the primary jets only case. For this case, the rms velocity steadily increases farther downstream, while for the primary jets only case the maximum fluctuations occur around the center of the jet. The annular jet crossflow causes a severe bending in the primary jet producing this increased turbulence downstream farther than at the center of the plot.

A comparison between the upper and lower primary jets can be seen in figure 2.53. Only approximately a 2.5 % difference is seen between the upper and lower jets maximum velocity. The rms velocity comparison again shows close

agreement between upper and lower jets. Increased turbulence is also evident on the upstream side of the primary jet due to a recirculation zone.

Figure 2.54 shows the annular jet inlet velocities taken on four edges of the annular jet at 0.08 inches from the inlet. A very flat velocity distribution similar to figure 2.33 for the annular jets only case can be seen. A mean velocity of 15.8 ft/sec is present in the center of the annular gap. The rms velocity shows larger peak values for the right and left sides of the annular jet due to the probe volume length being nearly five times larger than the grid points.

2.3.2 Mean Flowfield Results

Vector plots for the annular and primary jet case are presented in figures 2.55-2.58. The centerplane is seen in figure 2.55. The flow issuing from the annular jet can be seen entering at Y=0.85 and Y=2.15 in.. This flow penetrates up to the primary jets inlet at X=1.5 in. and then is turned parallel to the primary jets forming recirculation zones outside the annular region, $Y < 0.7$ in. and $Y > 2.3$ in., and in the center of the annular region. The primary jets can be seen bending downstream due to the annular jet interaction. Downstream of the primary jet inlet, the flow accelerates between two recirculation zones on the upper and lower walls of the rig. This flow slowly diffuses as the recirculation zones shrink in size downstream.

The recirculation zones are clearly visible with the aid of streamlines. The rear recirculation zones show symmetric placement between upper and lower portions of the rig. The two forward recirculation zones centered in the annular

region also show symmetric placement. Two additional recirculation zones outside of the annular region are also present, but since they are outside the measurement grid they do not stand out as clearly.

Comparison between planes at Z=7.4 and Z=7.6 in. (figure 2.56) show similar results. The rear recirculation zones at the Z=7.4 in. plane can be seen to be slightly forward of the recirculation zones at the Z=7.6 in. plane. In addition, the flow is seen to bend toward the lower wall at the Z=7.4 in. plane, while there is no bending in the Z=7.6 in. plane. The two forward recirculation zones are symmetric between planes at X=1.0 in., Y=1.85 in. and X=1.0 in., Y=1.1 in. for the upper and lower zones respectively.

Figure 2.57 shows plots at Z=7.3 and 7.7 in.. Symmetric flow between planes can be seen, while symmetry between upper and lower portions of the rig does not exist. Rear recirculation zones are located at approximately X=2.85 in., Y=2.1 in. for the upper zone and X=3.05 in., Y=0.9 in. for the lower zone. The placement of the upper recirculation zone forward of the lower recirculation zone indicates that the reattachment point occurs farther upstream for the lower recirculation zone. Asymmetry can also be seen for the forward recirculation zones in the Z=7.7 in. plane. Placement of the forward recirculation zones in the Z=7.3 in. plane is symmetric.

Planes at Z=7.2 in and Z=7.8 in. are seen in figure 2.58. Rear recirculation zones here are symmetric between planes and between upper and lower halves of the rig. Forward recirculation zones are clearly present at Z=7.2 in., but are

very disordered at Z=7.8 in.. These planes are outside the primary jet inlet diameter, and therefore more of the flow moves directly downstream instead of being entrained into the forward recirculation zones.

More vector plots are seen in figures C51-C62 in Appendix C. The annular jet inlet extends between 6.8 in ≤ Z ≤ 8.2 in., where a finer grid was used. Table(2.2) presents approximate forward and rear recirculation zone centers. From this table, some trends are evident about the recirculation zones. The forward recirculation zones placement is steady between 7.2 in. ≤ Z ≤ 7.8 in.. Outside these limits no center is well defined within the measured portion of the flow. Rear recirculation zones tend to move downstream and toward upper and lower walls of the rig. Rear recirculation zone locations are visible between 6.8 in. ≤ Z ≤ 8.2 in. within the measured flow.

Backflow can be seen upstream of X=1.5 in., even out to the limits of the cell. Recirculating flow could exist in this region, but due to beam restrictions points closer to the wall could not be measured. Measurements downstream of X=1.5 in. show that the flow velocity accelerates from X=1.5 in. on downstream between recirculation zones and then diffuses as the recirculation zones are passed. This is seen to happen to the cell boundaries.

Comparing vector plots to the primary jets only case some similarities can be seen. The influence of the primary jets on the flowfield is seen downstream of X=1.5 inches. Flow downstream of X=1.5 in., in the annular and primary jet case, is seen to be very similar to the flow in the primary jets only case. Recirculation zones for the annular and primary jet case are larger and extend downstream

farther, but the flow is still seen to accelerate past the recirculation region and then diffuse. This is an indication of how much influence the primary jets have on the flow.

2.3.3 Turbulent Flowfield Results

The U_{rms} and V_{rms} YZ plane contour plots are presented in figures 2.59-2.62. Figure 2.59 are plots for the station at X=0.5 in.. Both plots show a flat profile outside of the annular jet inlet and inside the annular jet region. Peak fluctuations occur in the annular gap where fluid is entering.

The U_{rms} and V_{rms} plots at X=1.0 in. can be seen in figure 2.60. The magnitude of the fluctuations increase and spread out from X=0.5 in. to X=1.0 in.. Fluctuations at the center of the annular region have increased due to the pair of counter rotating recirculation zones formed in this region. Magnitudes outside the annular jet remain small compared to the annular jet region.

Plots at X=1.5 in. show a definite change in the U_{rms} and V_{rms} velocity distribution due to primary jet interaction, figure 2.61. The U_{rms} plot shows decreased turbulence at the centerplane, Z=7.5 in., from top to bottom walls of the rig due to the primary jets. Three pairs of peak fluctuations occur on the sides of the centerplane. The peaks at the bottom and top walls are caused by the flow above and below the annular jets accelerating around the primary jets and flowing downstream. The pair of peaks at the center of the rig correspond to increased flow around the primary jets from recirculating fluid in the center of the annular jet. The turbulence diffuses as the edges of the cell are reached.

The V_{rms} plot at X=1.5 inches shows decreased magnitudes at the upper and lower walls at the rig centerplane. A peak is observed at the center of the cell due to the fluctuation of the stagnation point of the primary jets. The magnitudes dissipate as the cell boundaries are reached.

The U_{rms} component at X=2.0 in, figure 2.62, shows a decrease at both upper and lower walls in the rig center and peak magnitudes occur along the rig centerline between Z=7.0 in. and Z=8.3 in.. The drop in magnitude along the upper and lower walls is due to a recirculation zone, while the peaks at the center of the rig are caused from fluid being accelerated between the upper and lower recirculation zones. The V_{rms} component at X=2.0 in. shows peak velocities along the rig centerline between Z=7.0 in. and Z=7.9 in.. Similar results are evident at downstream locations, figures C63-C68 in Appendix C.

Figures 2.63 & 2.64 show line plots of U_{rms} and V_{rms} velocities as it develops in the rig for planes at Z=7.0, 7.5, and 8.0 inches. Peak U_{rms} fluctuations are at the annular jet exit and immediately downstream of the primary jets. Peak V_{rms} fluctuations can be seen in the region of the primary jet stagnation. On downstream, the magnitudes decrease and spread out. Uniform fluctuations from the bottom to the top walls can be seen at X=6.0 inches. Magnitudes at X=6.0 inches are slightly larger than the primary jets case and much smaller than the annular jet case.

The two-dimensional turbulent kinetic energy contour plots are presented in figures 2.65 & 2.66. The K' distribution at X=0.5 and 1.0 in., figure 2.65, show

similar distributions. Peak turbulence occurs at the edges of the annular jet where large shear stress is present. Outside the annular inlet, the turbulence is uniform to the cell boundaries and walls. The plot at X=1.0 in. shows peak magnitudes nearly doubling with increased turbulence within the annular region. Distributions towards the cell boundaries continue to be uniform.

The plot at X=1.5 inches shows peak turbulence occurring at the rig center and at the top and bottom walls. The decrease seen in the rms plots is also seen here in figure 2.66. The trends seen in this plot corresponds to the trends explained in the rms plots in figure 2.61.

At X=2.0 in., peak turbulence values can be seen at the center of the rig with a sharp drop in turbulence energy between Z=7.0 and 8.0 inches at the upper and lower walls. The formation of the downstream recirculation regions in these areas are responsible for the drop in turbulence energy. Magnitudes decrease as cell boundaries and walls are reached. Similar trends are present in plots downstream, see figures C69-C71 in Appendix C.

Figure 2.67 contains the two-dimensional turbulent kinetic energy distribution throughout the rig at the planes Z=7.0, 7.5, and 8.0 inches. The largest turbulence energy can be seen concentrated in the region of annular and primary jet intersection at X=1.5 and 2.0 inches. Magnitudes decay and spread downstream and away from the rig centerplane. Uniform turbulence energy between upper and lower walls is present at X=6.0 inches.

YZ plane contour plots of the XY plane Reynolds shear stress are in figures 2.68 & 2.69. The U'V' distribution at X=0.5 in. is seen in figure 2.68. Negative stresses are observed at the edges of the annular jet inlet due to the transfer of momentum from the edges of the annular jet to the fluid within the rig. A constant distribution is seen throughout the rest of the plane indicating very little momentum transfer. Similar results occur at X=1.0 in.. Here, the magnitudes of the stresses have nearly doubled and spread to the inner annular jet region. A uniform region is still seen throughout the rest of the plane.

At the X=1.5 in. plane, three regions of decreased, or negative, stress is seen separated by a strip of increased U'V' at Z=7.5 in.. The three regions of decreased magnitude occurs in the same area as the peak fluctuations occurred for the U_{rms} plot in figure 2.61. The negative values are therefore caused by the increased velocity gradients in these regions as the flow accelerates around the primary jets. The central peak must be caused by the cross jets entering in this location. Outside of the annular jet inlet, Z=6.8 and Z=8.2 in., a uniform shear stress extends to the cell boundaries.

At X=2.0 in., a region of peak positive U'V' occurs along the upper half of the rig while negative U'V' occurs through the lower half of the rig. The magnitudes continue to decrease and the peaks tend to spread toward the walls and boundaries of the rig on downstream. The peak through the rig at Z=7.5 in. seems to exist on downstream. Similar distributions are present downstream of X=2.0 inches. Figures C72-C74 in Appendix C contains these plots.

Figure 2.70 shows line plots of the Reynolds shear stress as it develops downstream at planes Z=7.0, 7.5, and 8.0 inches. The largest fluctuation of shear stress is present at X=1.5 inches. Here, primary and annular jet interaction produces large velocity gradients and momentum transfer. Downstream and away from the centerplane, magnitudes decay and approach a uniform distribution of shear stress at X=6.0 inches.

Table 2.1 Primary Jets Only Recirculation Zone Locations

	FORWARD ZONES				REAR ZONES			
	upper		lower		upper		lower	
Z (in)	X (in)	Y (in)	X (in)	Y (in)	X (in)	Y (in)	X (in)	Y (in)
6.5	1.2	2.4	1.3	<0.5	-	-	-	-
6.6	1.0	2.25	1.0	0.75	2.9	>2.5	2.7	<0.5
6.7	0.85	2.15	0.85	0.85	3.15	2.35	3.0	<0.5
6.8	0.8	2.05	0.8	0.95	3.5	2.4	0.2	0.5
6.9	0.65	2.0	0.65	0.95	3.4	2.35	3.3	0.7
7.0	<0.5	2.1	<0.5	0.95	3.45	2.25	3.2	0.7
7.1	<0.5	2.0	<0.5	1.0	3.5	2.3	3.4	0.7
7.2	<0.5	2.0	<0.5	1.0	3.45	2.2	3.6	0.7
7.3	-	-	-	-	3.35	2.2	3.3	0.8
7.4	-	-	-	-	3.45	2.2	3.7	0.7
7.5	-	-	-	-	3.5	2.2	3.8	0.7
7.6	-	-	-	-	3.5	2.1	3.7	0.7
7.7	-	-	-	-	3.4	2.15	3.5	0.7
7.8	<0.5	2.0	<0.5	1.0	3.5	2.2	3.4	0.8
7.9	<0.5	2.0	<0.5	1.0	3.4	2.2	3.2	0.8
8.0	0.65	1.95	0.5	1.0	3.35	2.2	-	-
8.1	0.7	2.0	0.7	1.0	3.25	2.25	3.4	0.7
8.2	0.8	2.05	0.8	0.95	3.35	2.3	3.2	0.7
8.3	0.85	2.05	0.85	0.9	3.0	2.3	3.1	0.7
8.4	1.1	2.15	1.0	0.85	3.0	2.3	3.0	<0.5
8.5	1.3	2.35	1.3	0.7	2.7	>2.5	2.7	<0.5
8.6	1.5	2.5	1.5	0.6	-	-	-	-

Table 2.2 Annular and Primary Jets Recirculation Zone Locations

	FORWARD ZONES				REAR ZONES			
	upper		lower		upper		lower	
Z (in)	X (in)	Y (in)	X (in)	Y (in)	X (in)	Y (in)	X (in)	Y (in)
6.8	-	>2.5	-	<0.5	-	>2.5	-	<0.5
6.9	-	>2.5	-	<0.5	3.4	2.4	-	<0.5
7.0	-	>2.5	-	<0.5	3.4	2.3	3.3	<0.5
7.1	-	>2.5	-	-	3.5	2.2	3.2	0.8
7.2	1.1	1.7	1.1	1.3	3.1	2.1	3.0	0.9
7.3	1.0	1.8	1.0	1.1	2.9	2.1	3.0	0.9
7.4	1.0	1.8	1.0	1.1	2.7	2.1	2.8	0.9
7.5	1.0	1.8	1.0	1.1	2.8	2.1	2.8	0.9
7.6	1.0	1.8	1.0	1.2	2.9	2.1	2.9	0.9
7.7	0.7	1.8	1.0	1.2	2.8	2.1	3.1	0.8
7.8	-	-	0.7	1.2	3.0	2.15	3.0	0.8
7.9	-	-	-	-	3.3	2.2	3.3	0.8
8.0	-	-	-	-	3.1	2.2	3.5	0.7
8.1	-	-	-	-	3.1	2.3	3.5	0.7
8.2	-	-	-	-	3.3	>2.5	3.5	0.7

6.0 in. ≤ Z ≤ 9.0 in.

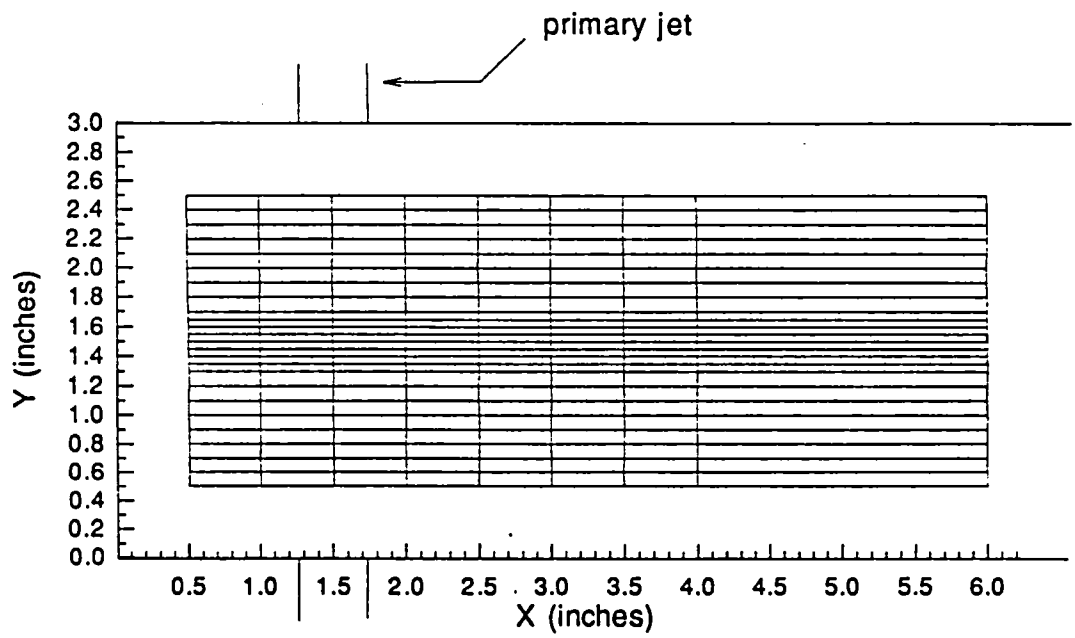

Figure 2.1 Primary Jets Only XY Plane Sampling Grid

6.0 in. ≤ Z ≤ 6.7 in. AND 8.3 in. ≤ Z ≤ 9.0 in.

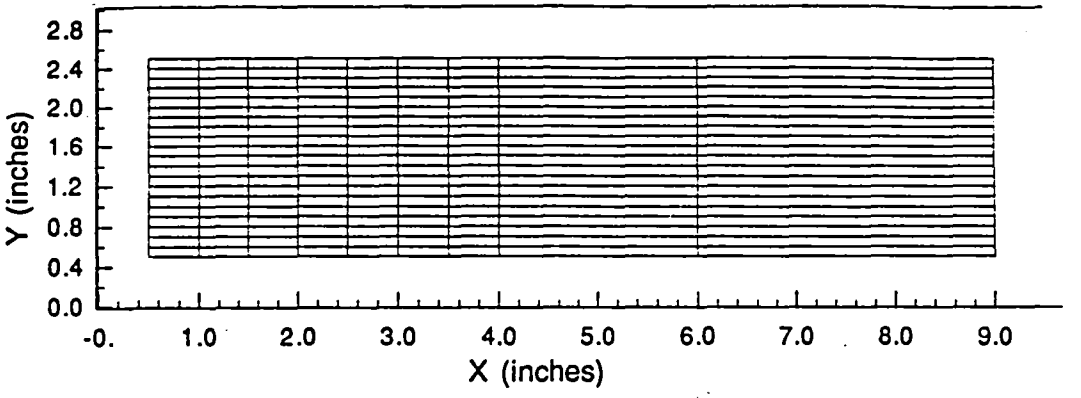

6.8 in. ≤ Z ≤ 8.2 in.

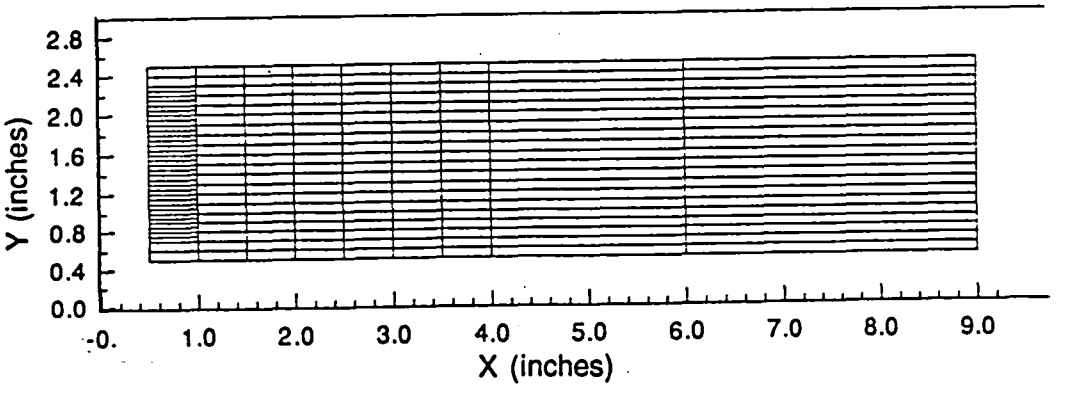

Figure 2.2 Annular Jets Only XY Plane Sampling Grids

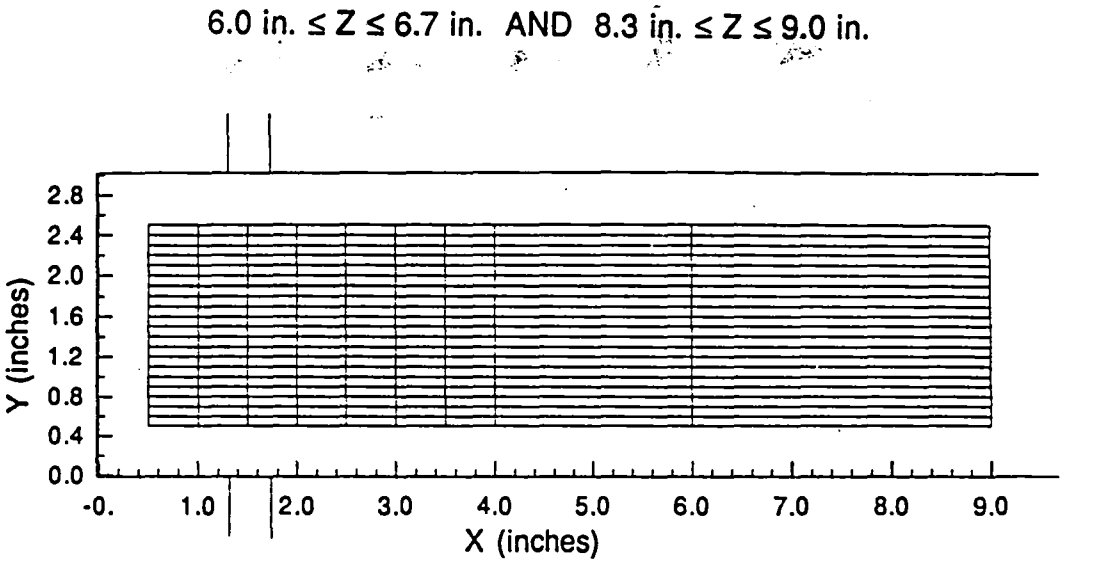

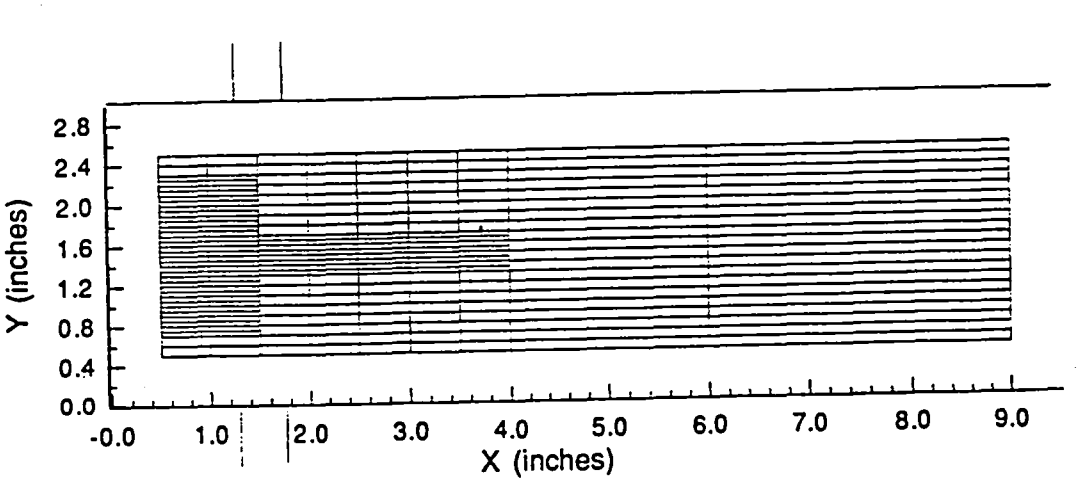

Figure 2.3 Annular and Primary Jets XY Plane Sampling Grids

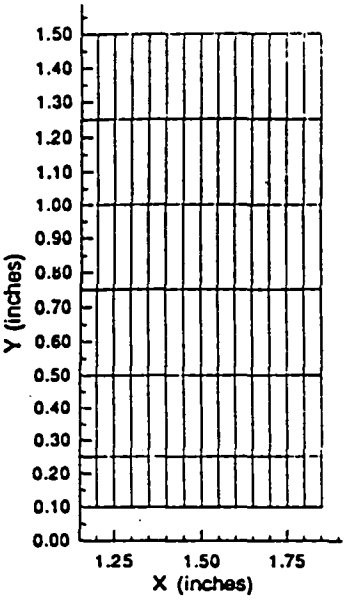

Figure 2.4 XY Plane Primary Jets Sampling Grid

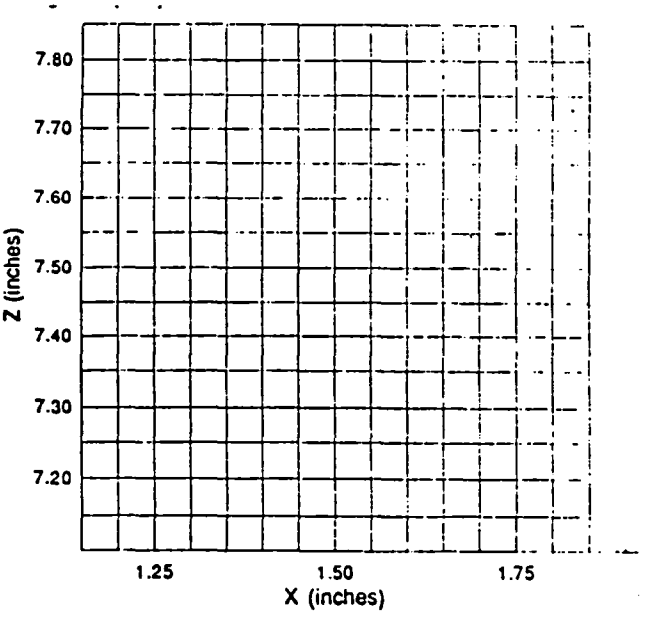

Figure 2.5 XZ Plane Primary Jets Sampling Grid

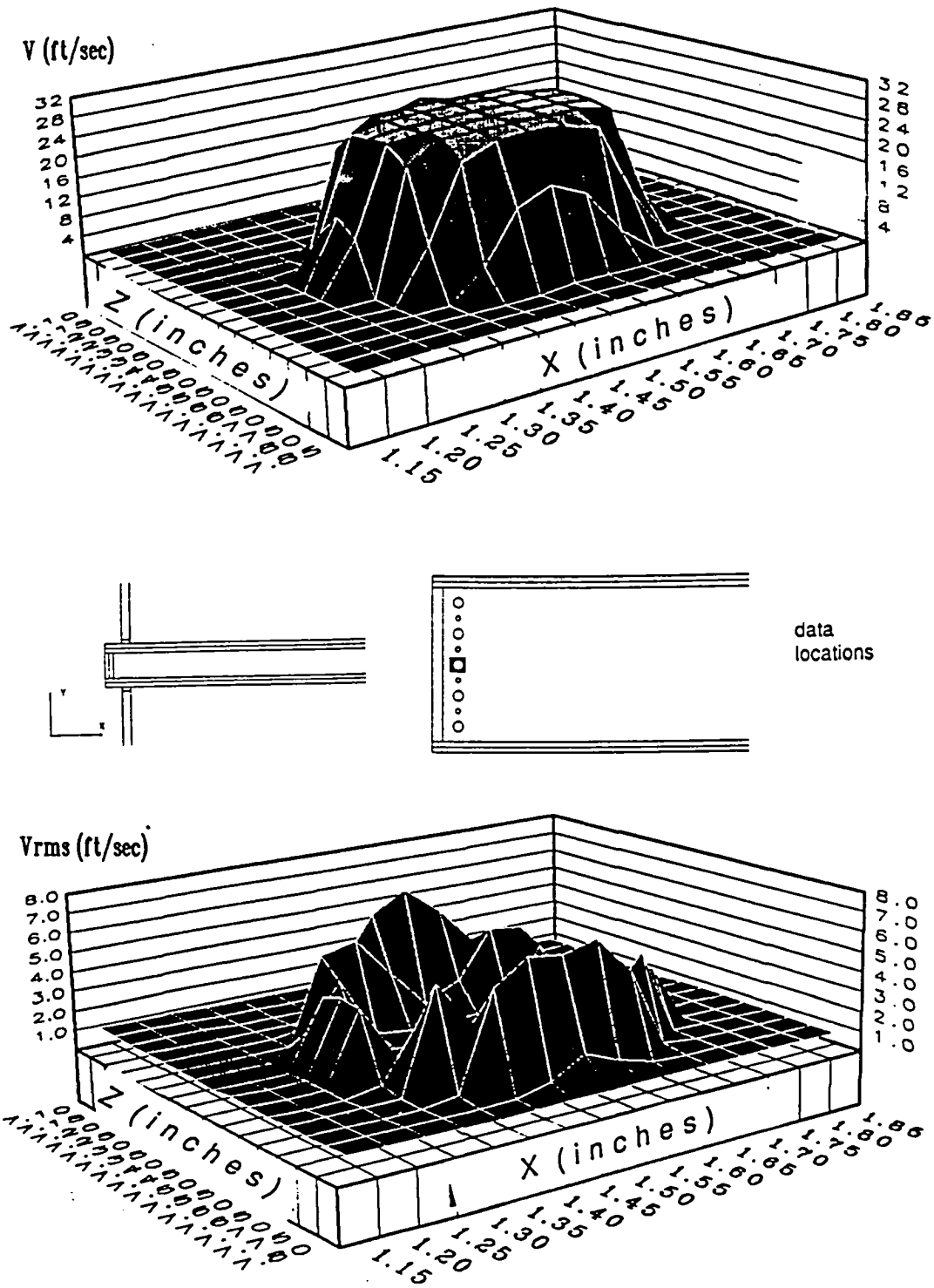

Figure 2.6 Primary Jets Only $\bar{V}$ and V_{rms} Distribution of the Primary Jets at Y=0.1 inches

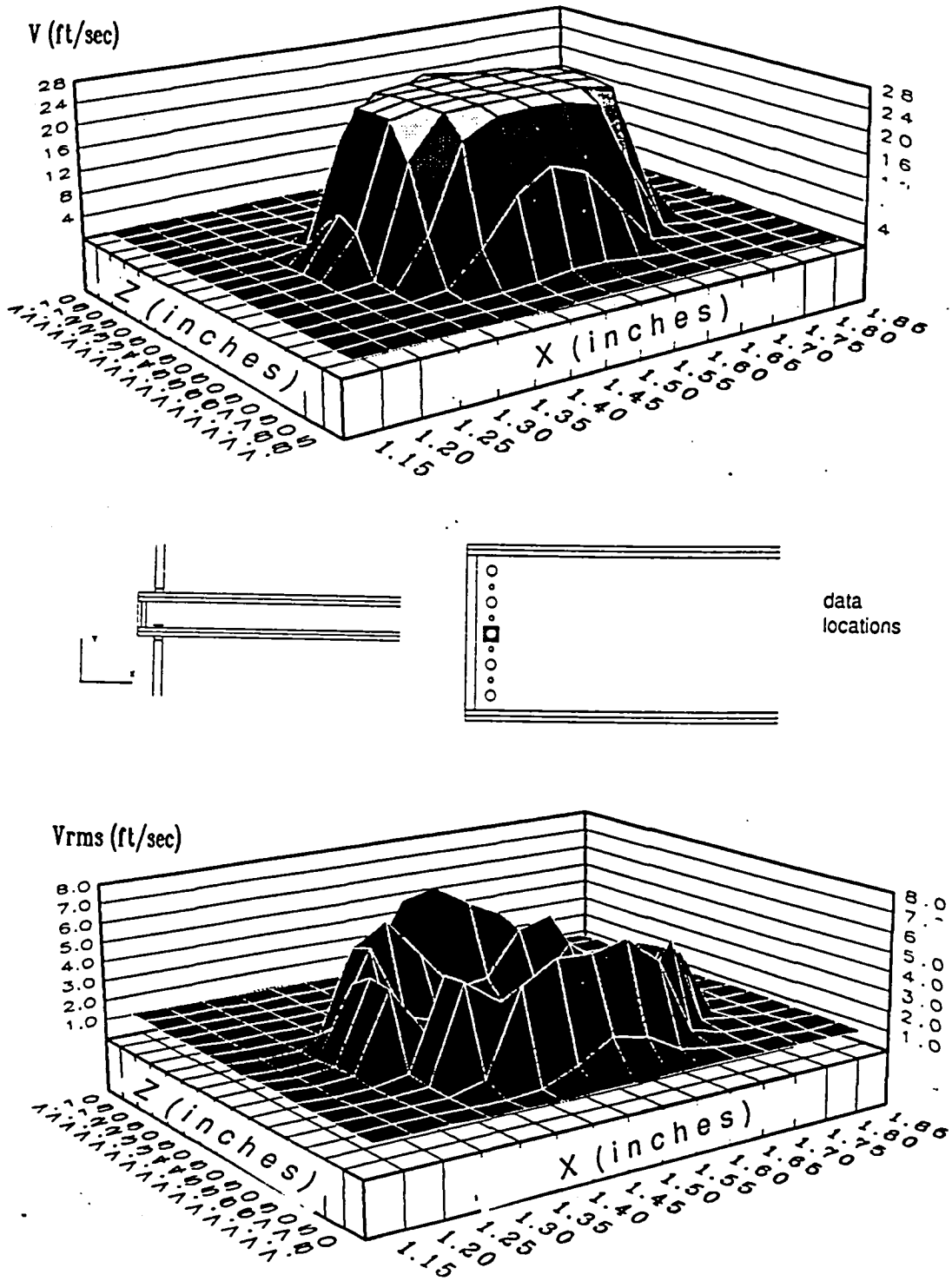

Figure 2.7 Primary Jets Only $\bar{V}$ and V_{rms} Distribution of the Primary Jets at Y=0.25 inches

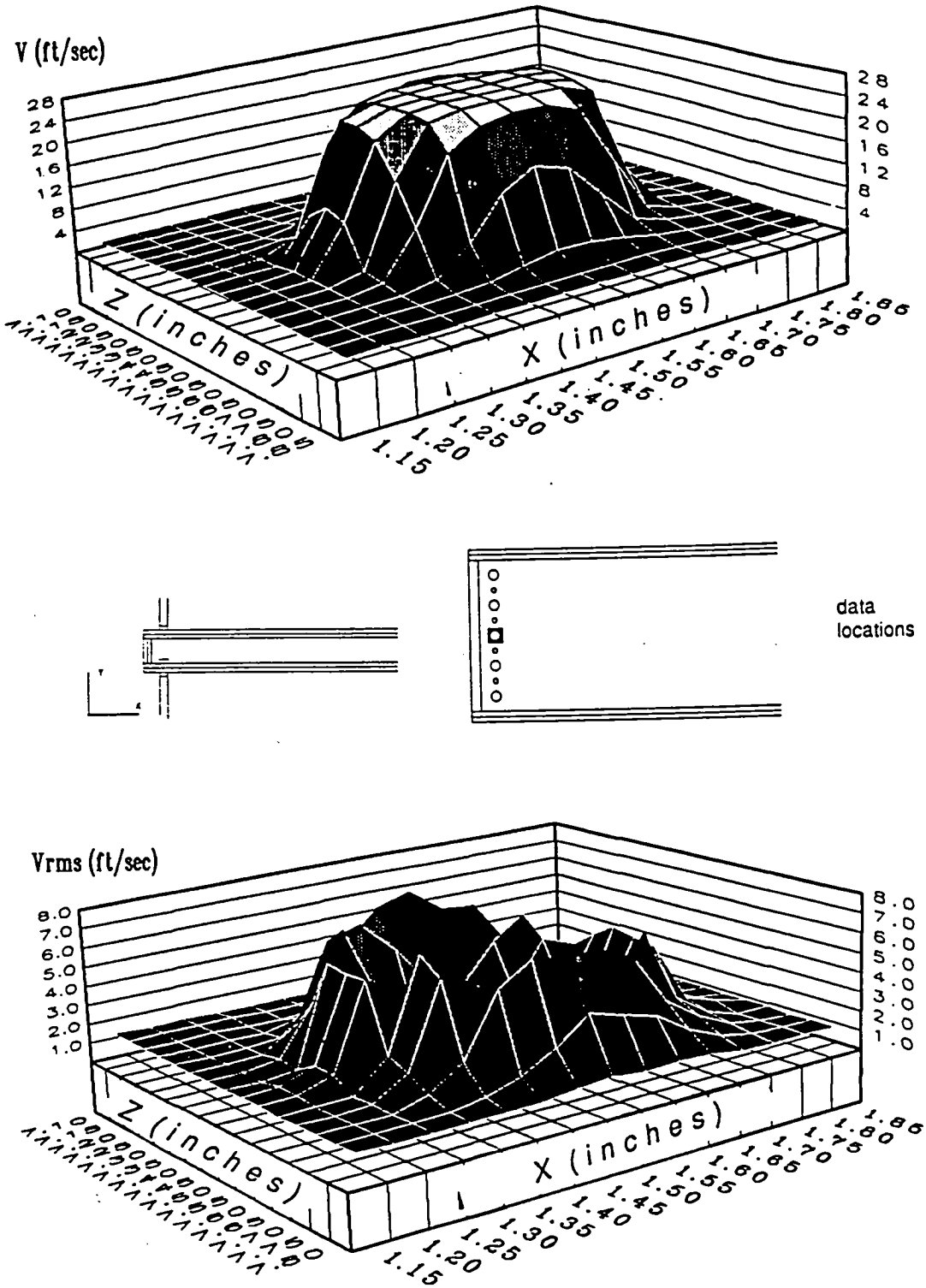

Figure 2.8 Primary Jets Only $\bar{V}$ and V_{rms} Distribution of the Primary jets at Y=0.5 inches

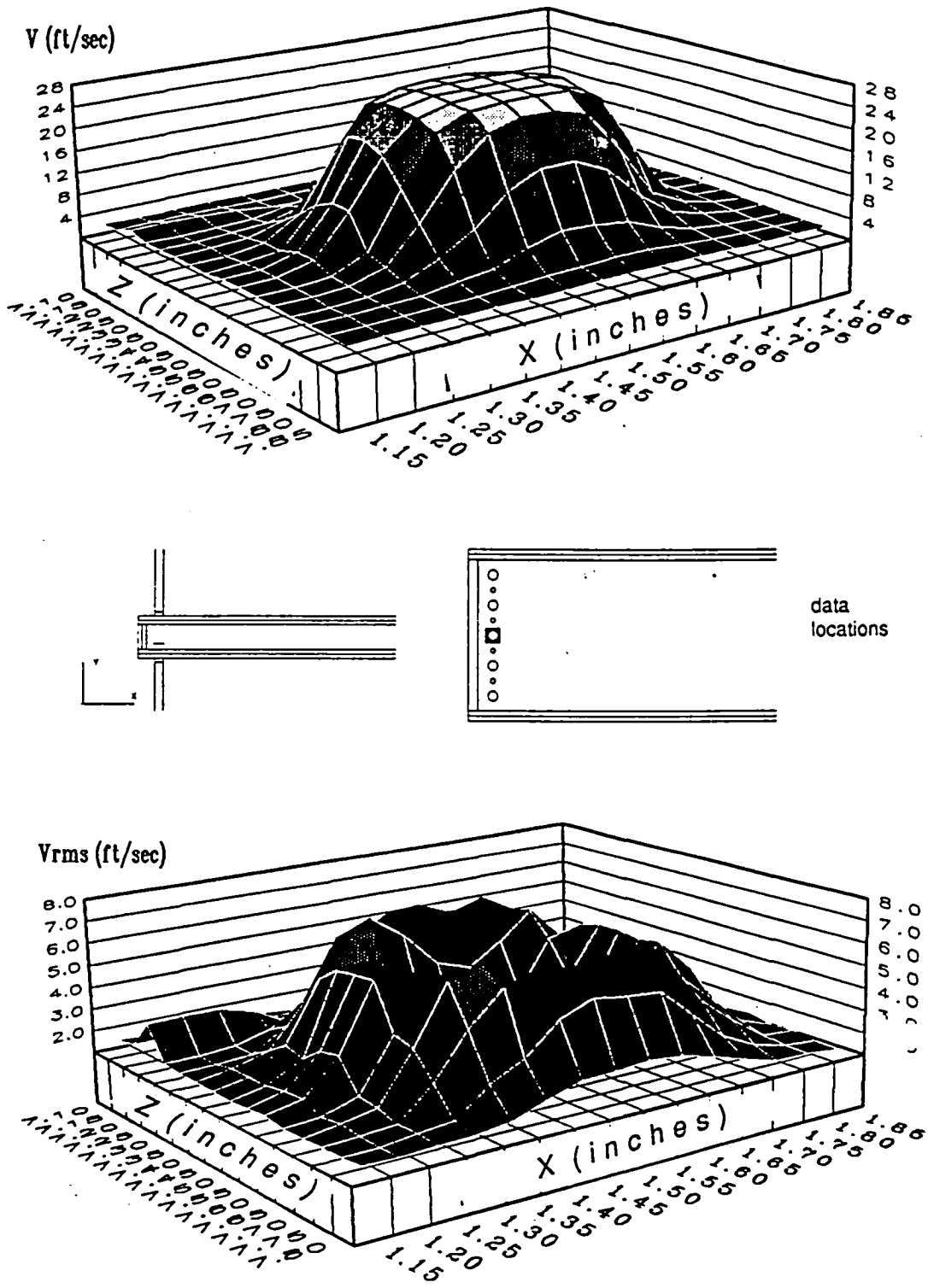

Figure 2.9 Primary Jets Only $\bar{V}$ and V_{rms} Distribution of the Primary Jets at Y=0.75 inches

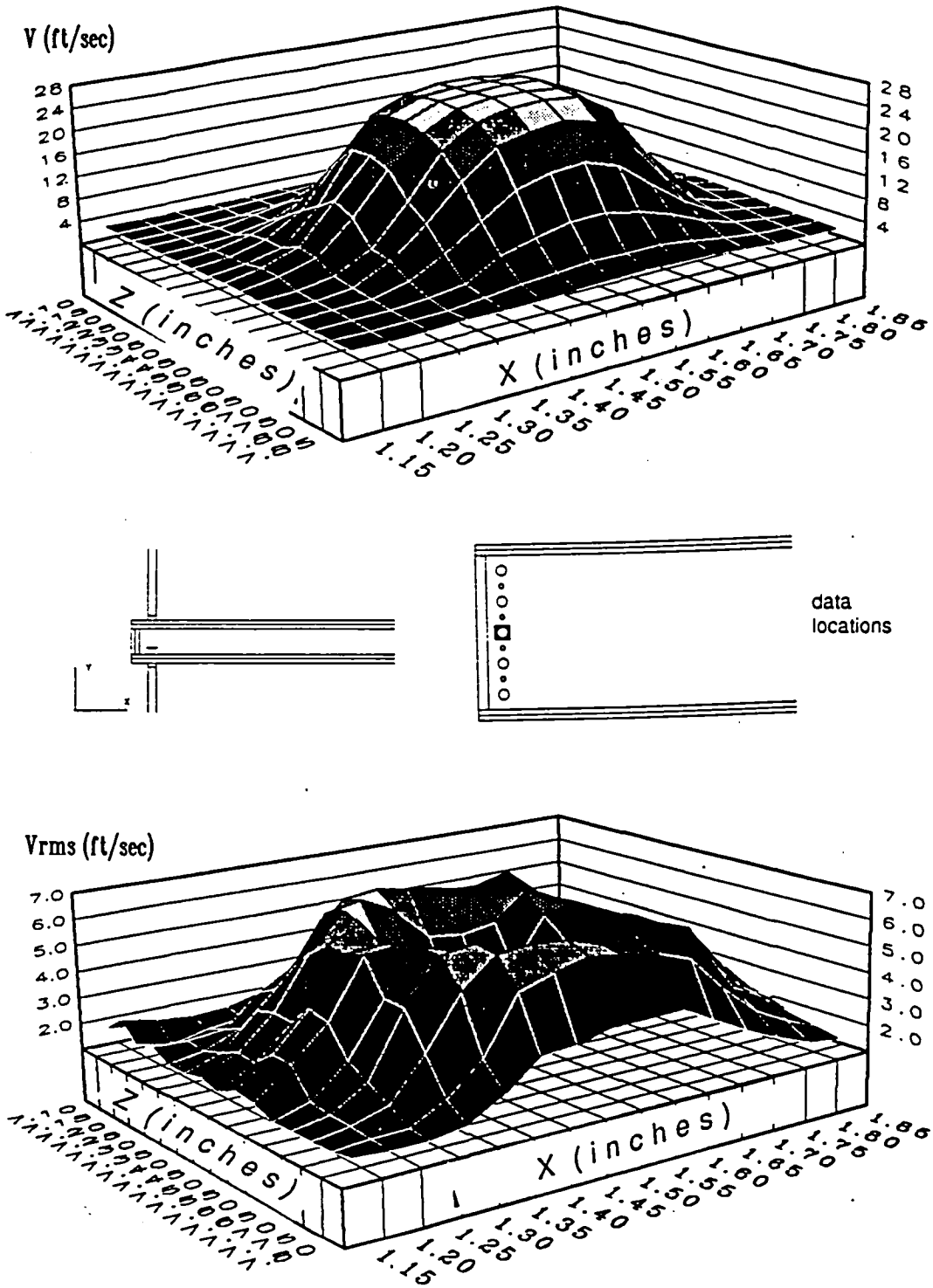

Figure 2.10 Primary Jets Only $\bar{V}$ and V_{rms} Distribution of the Primary Jets at Y=1.0 inches

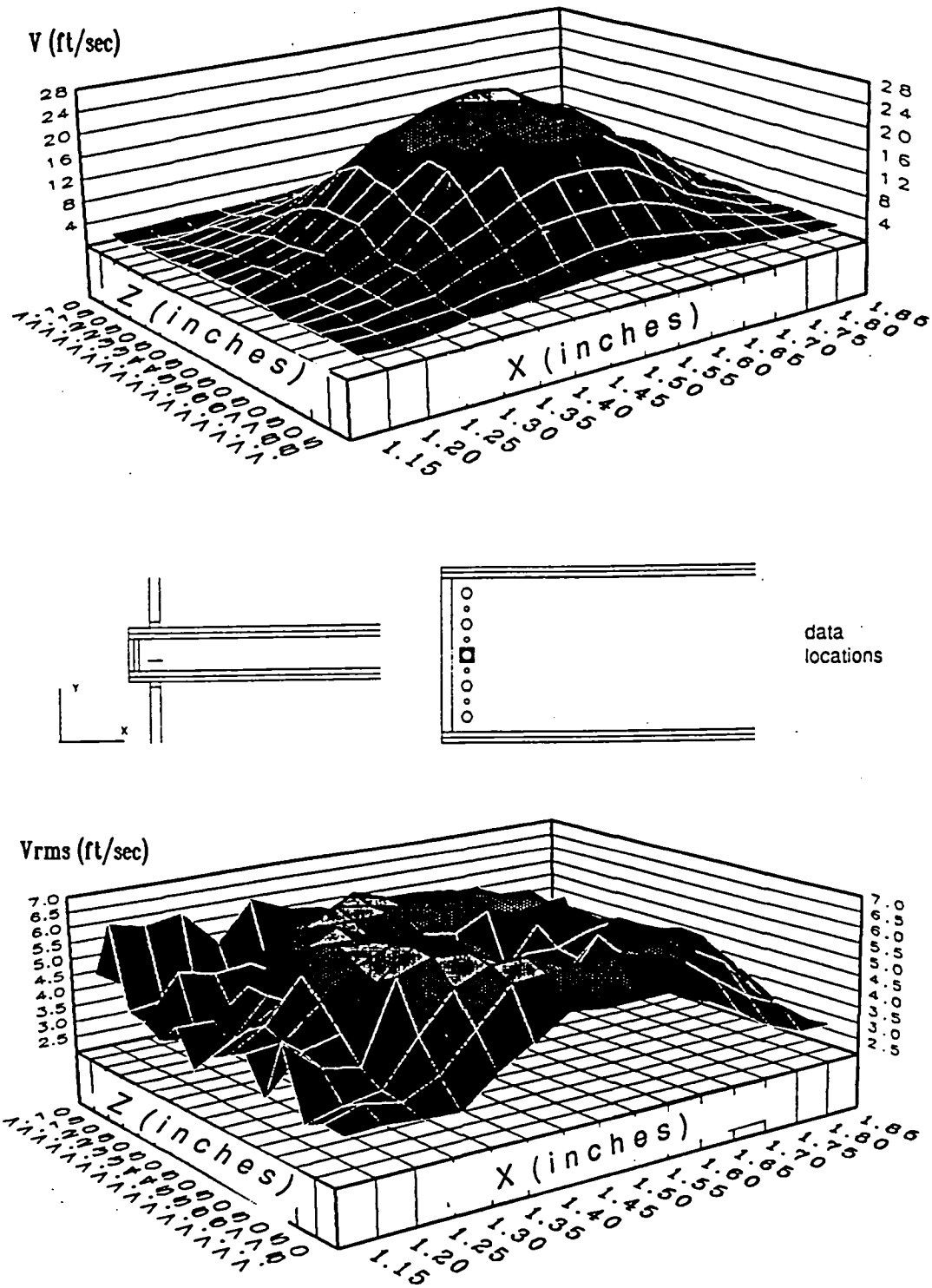

Figure 2.11 Primary Jets Only $\bar{V}$ and V_{rms} Distribution of the Primary Jets at Y=1.25 inches

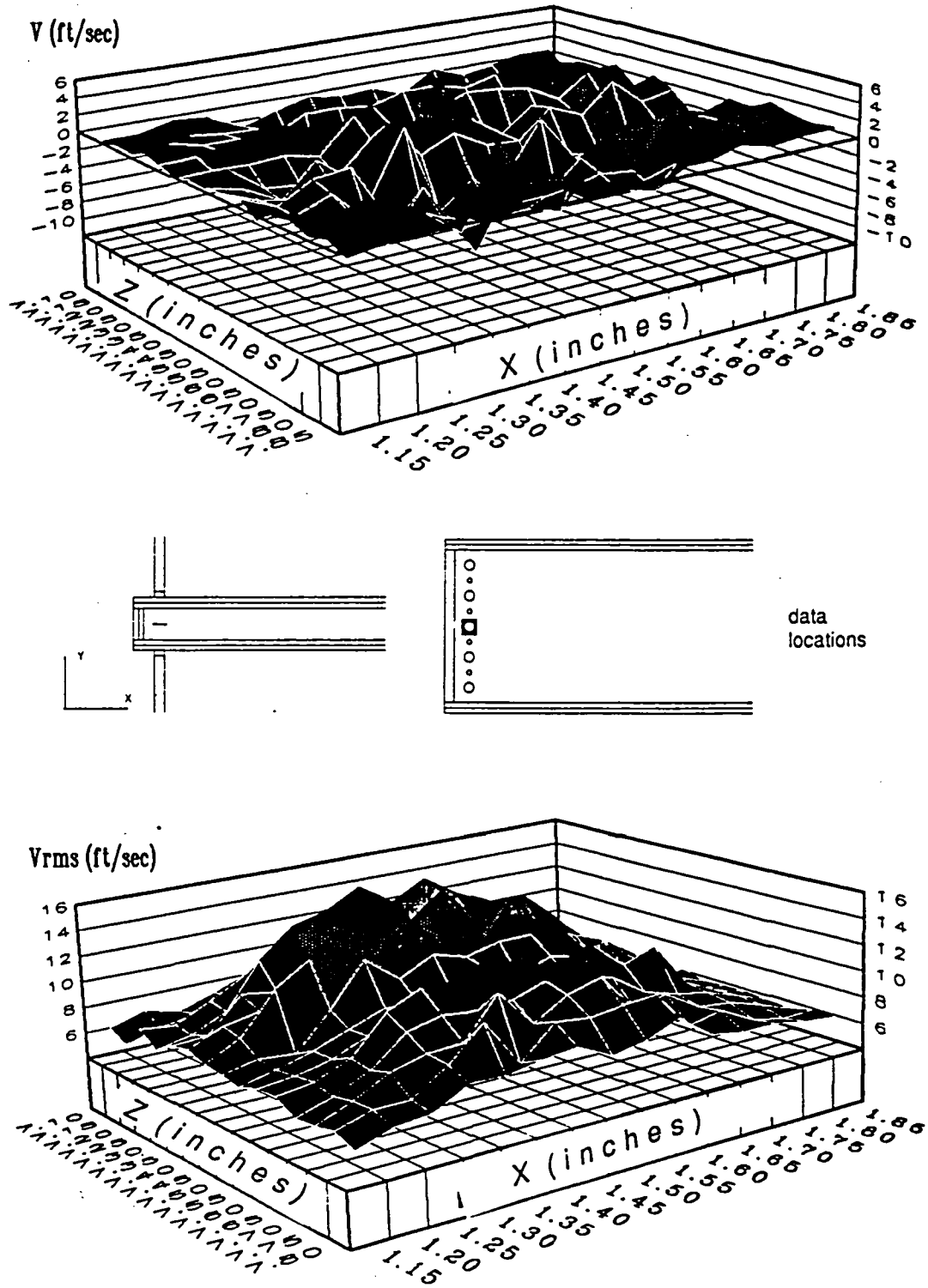

Figure 2.12 Primary Jets Only $\tilde{V}$ and V_{rms} Distribution of the Primary Jets at Y=1.5 inches

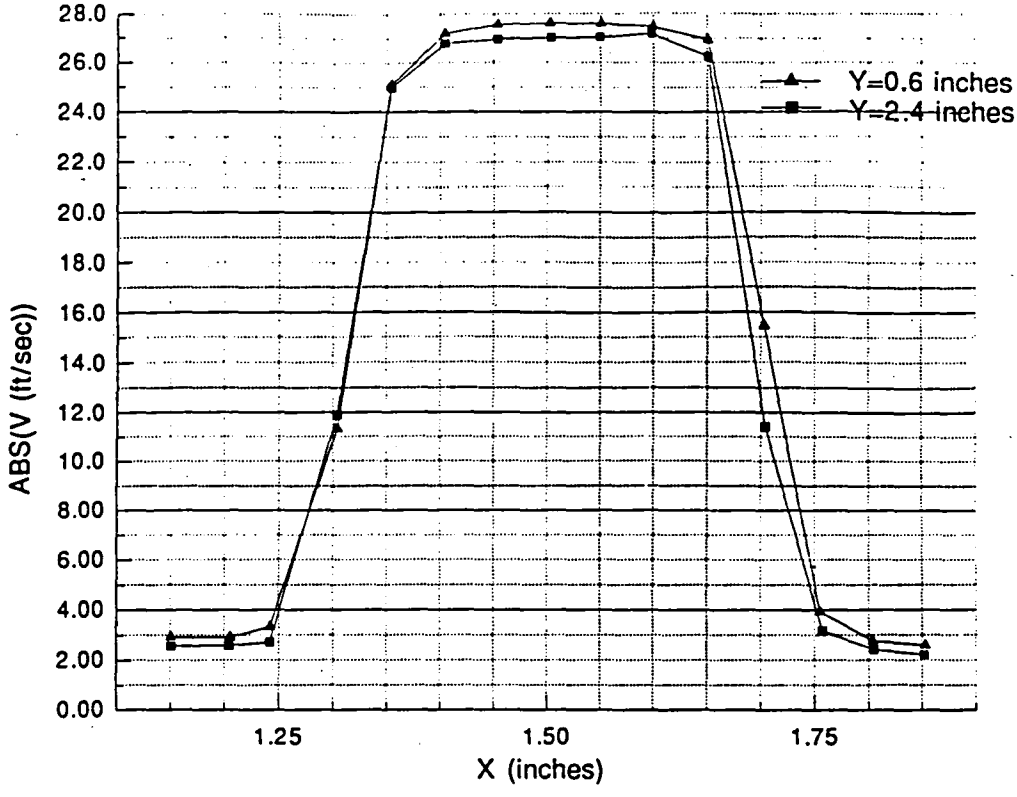

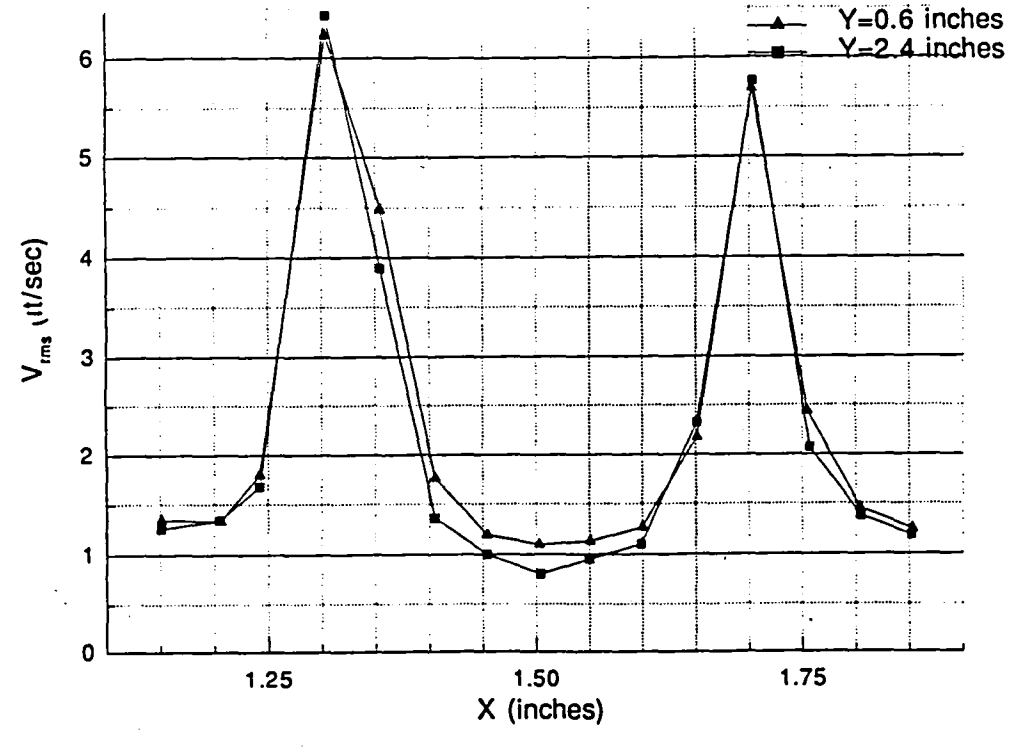

Figure 2.13 Primary Jets Only $\bar{V}$ and V_{rms} Distribution Comparison of the Primary Jets at Y=0.6 in. and Y=2.4 in.

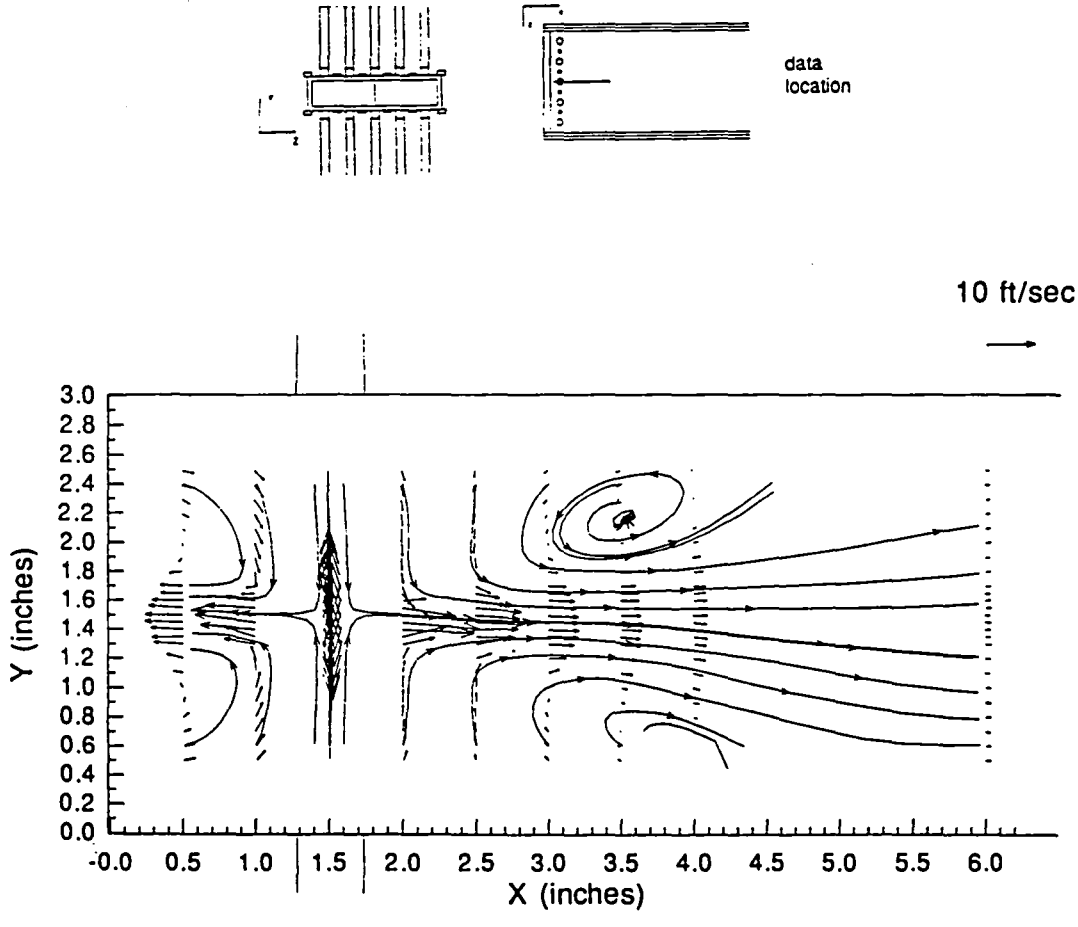

Figure 2.14 Primary Jets Only Mean Velocity Vector Plot at Z=7.5 in.

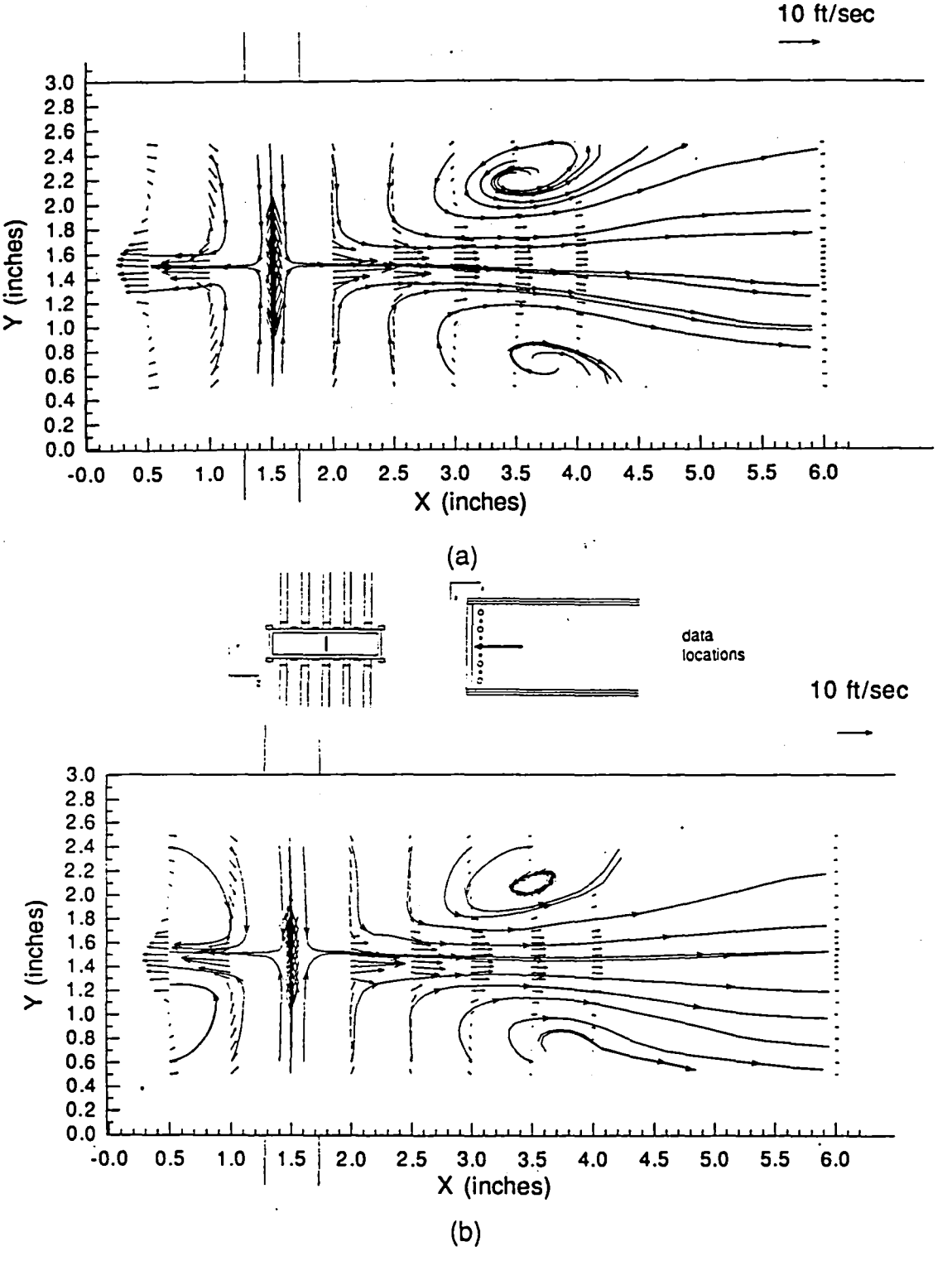

Figure 2.15 Primary Jets Only Mean Velocity Vector Plots
a) Z=7.4 in.; b) Z=7.6 in.

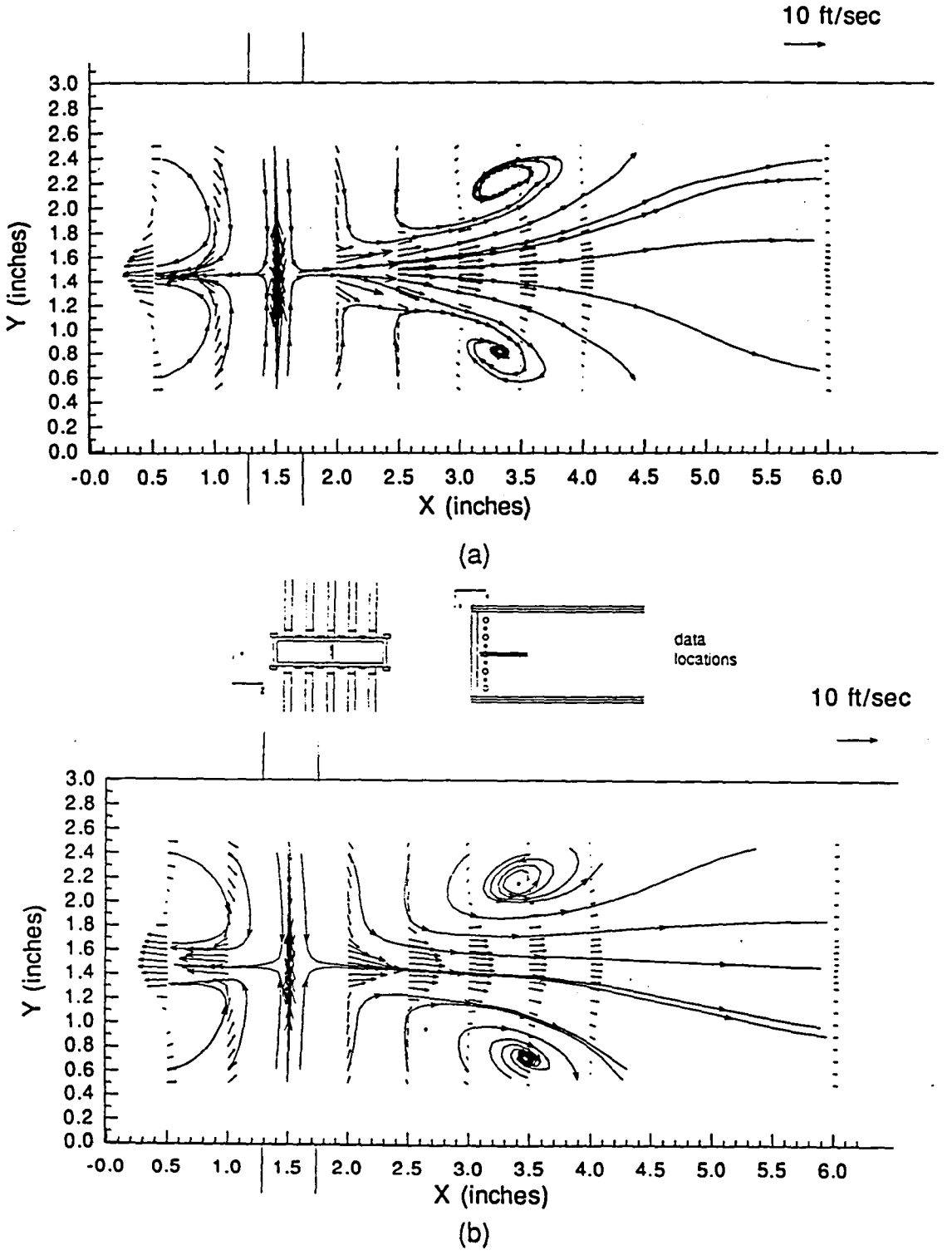

Figure 2.16 Primary Jets Only Mean Velocity Vector Plots
a) Z=7.3 in.; b) Z=7.7 in.

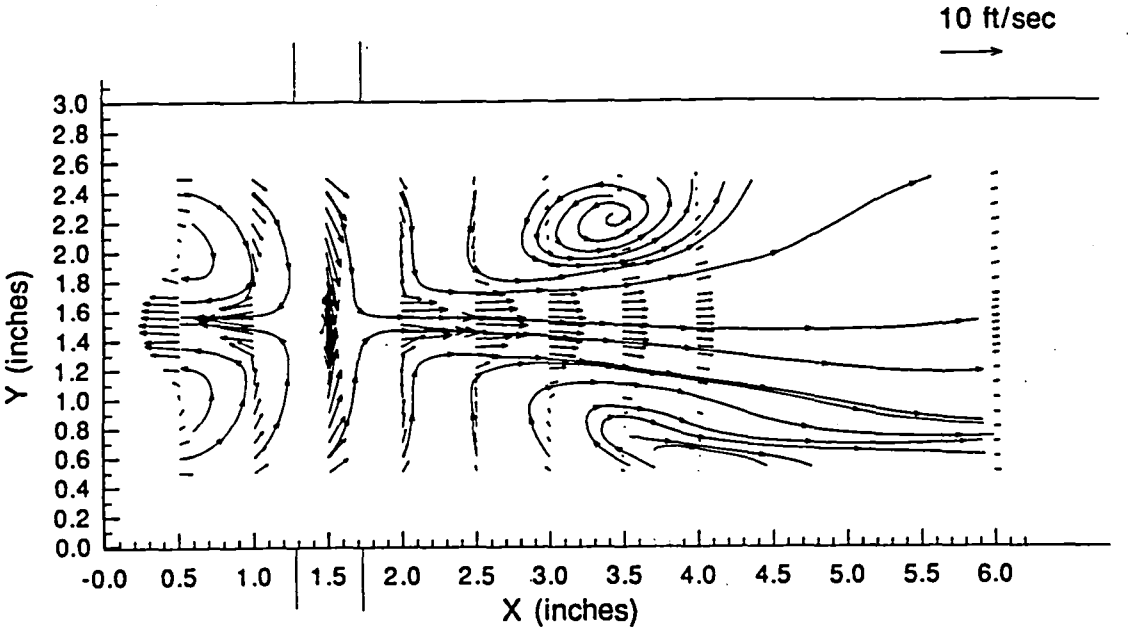

(a)

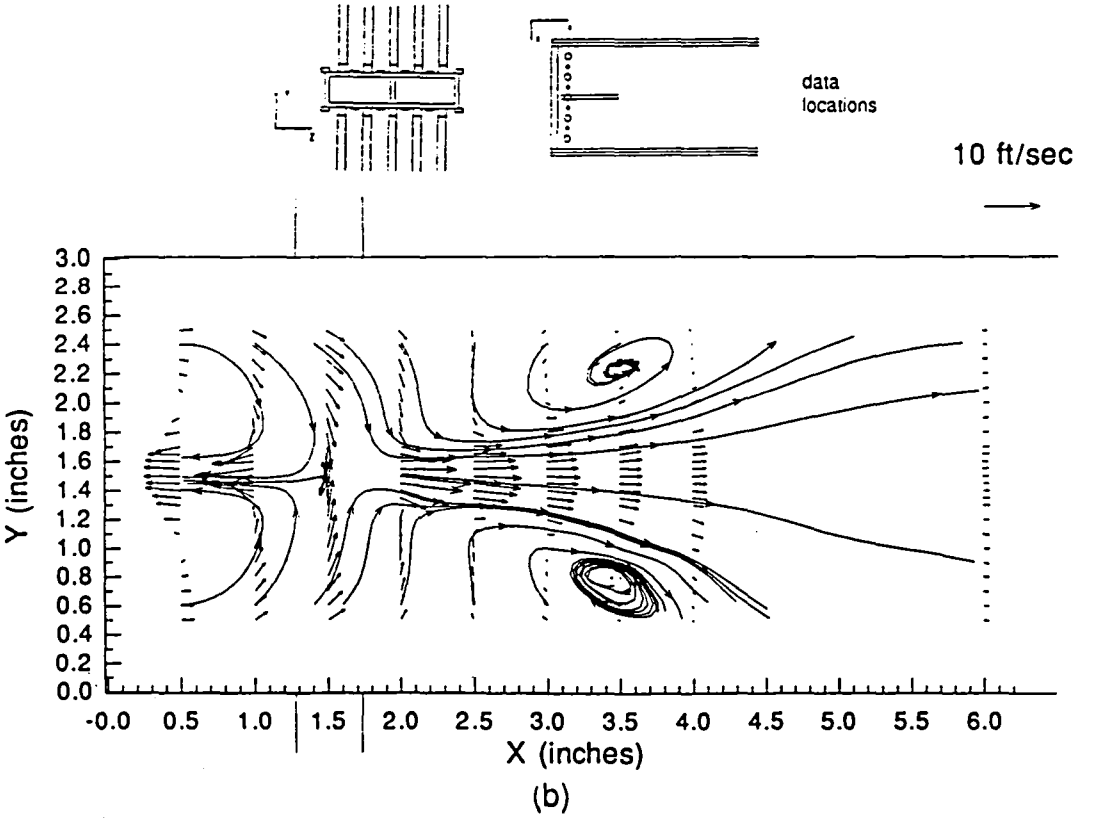

(b)

Figure 2.17 Primary Jets Only Mean Velocity Vector Plots
a) Z=7.2 in.; b) Z=7.8 in.

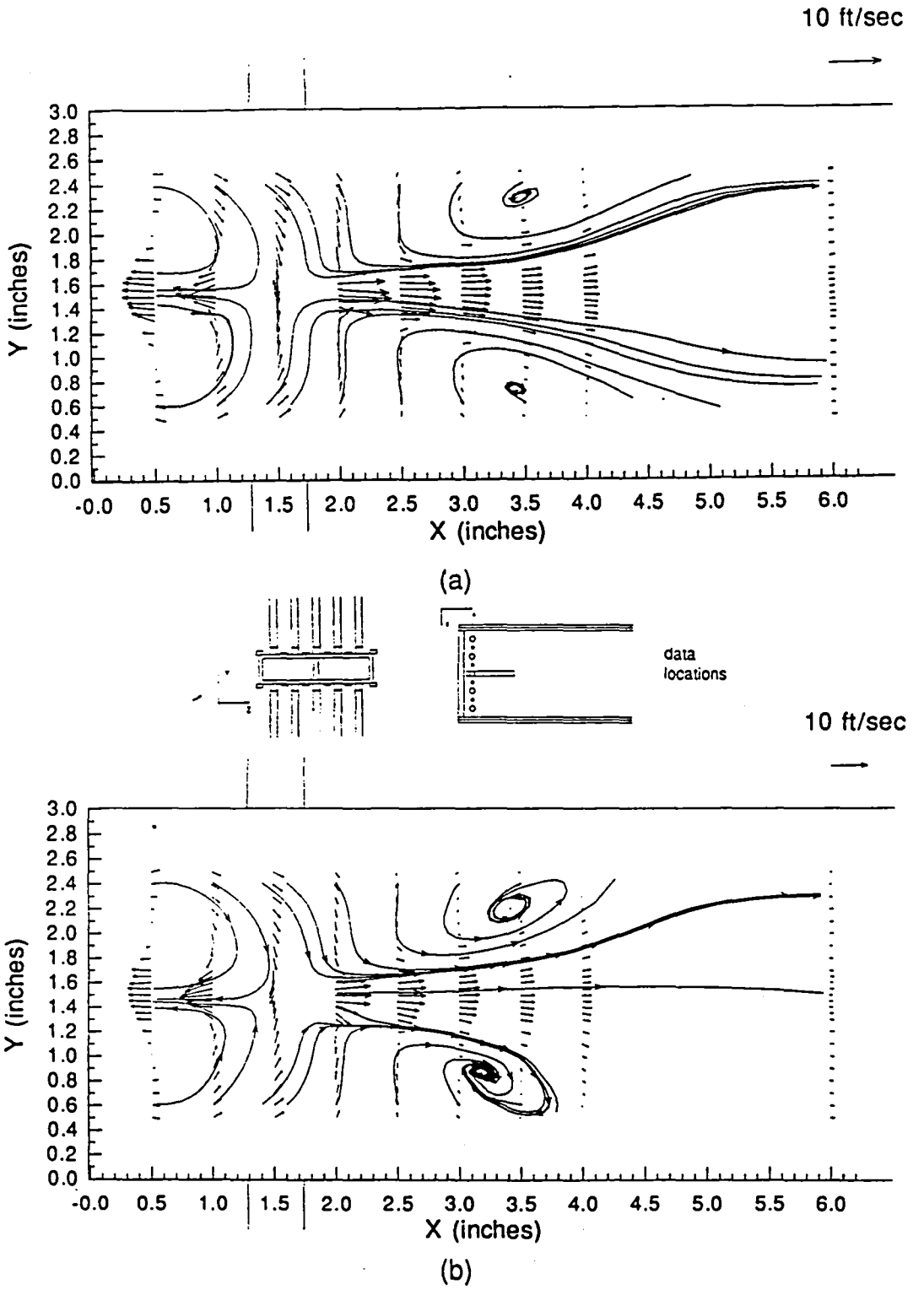

Figure 2.18 Primary Jets Only Mean Velocity Vector Plots
a) Z=7.1 in.; b) Z=7.9 in.

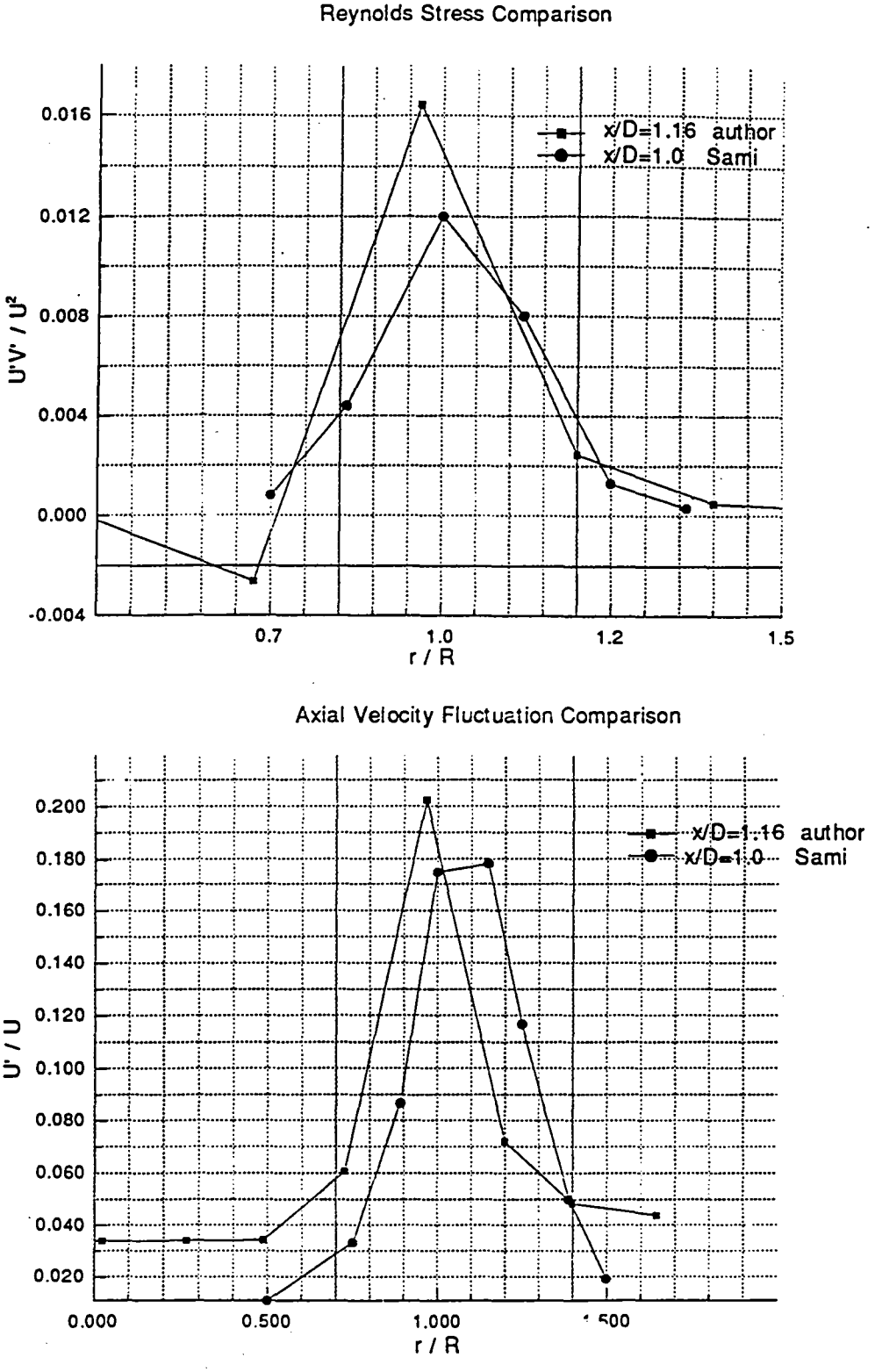

Figure 2.19 Reynolds Shear Stress and Turbulence Intensity Comparison

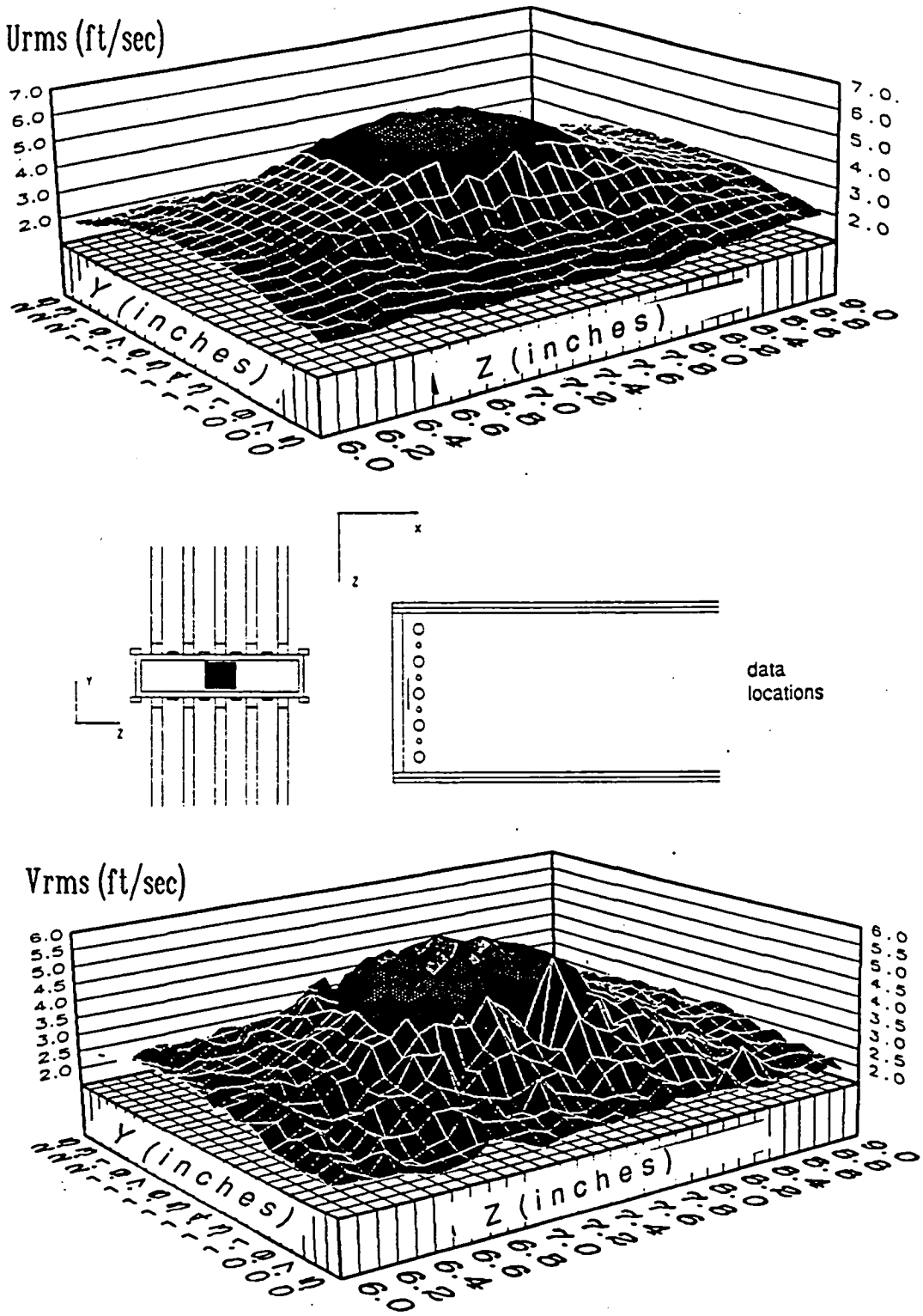

Figure 2.20 Primary Jets Only Contour Plot of U_{rms} and V_{rms} at X=0.5 in.

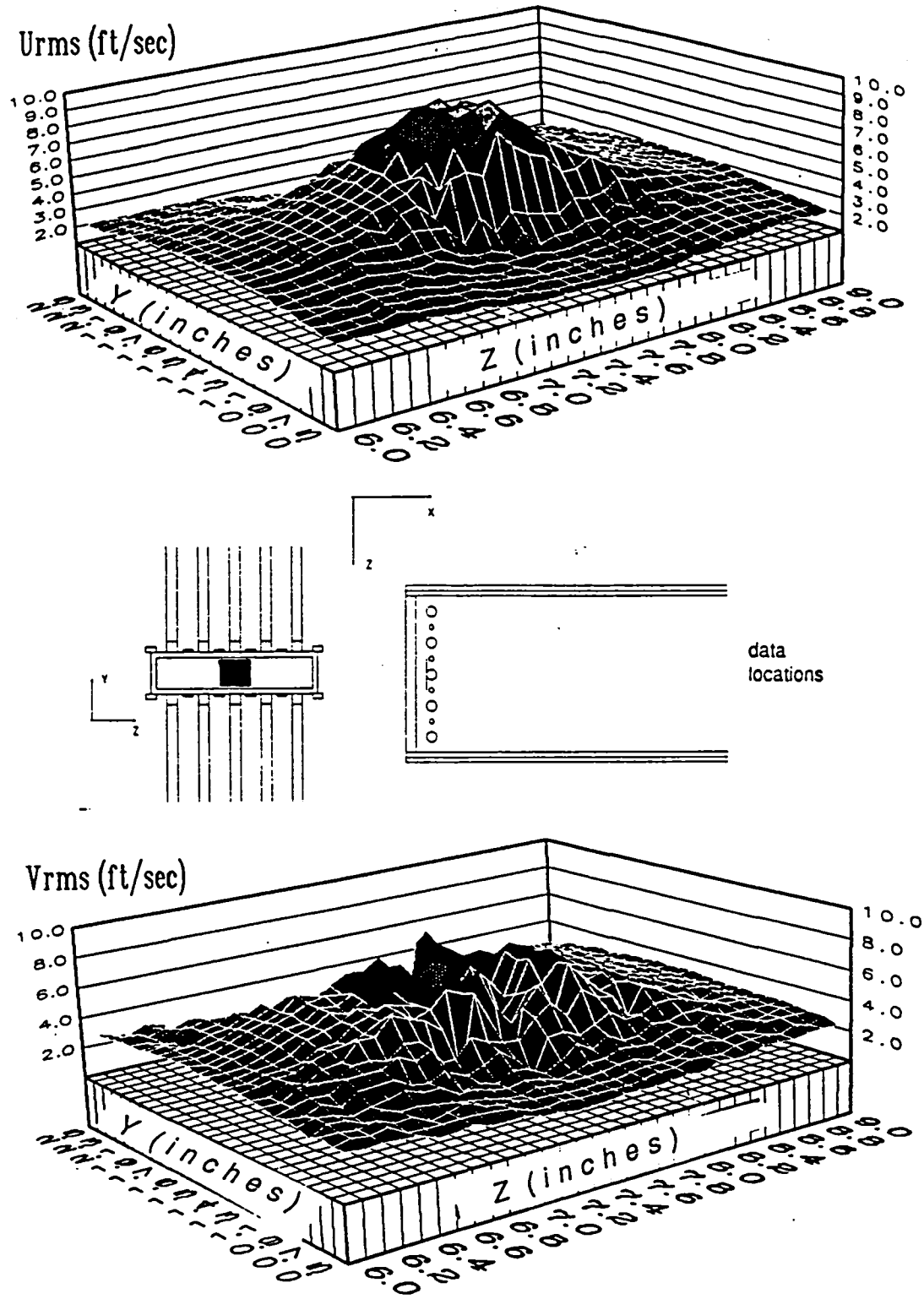

Figure 2.21 Primary Jets Only Contour Plot of U_{rms} and V_{rms} at X=1.0 in.

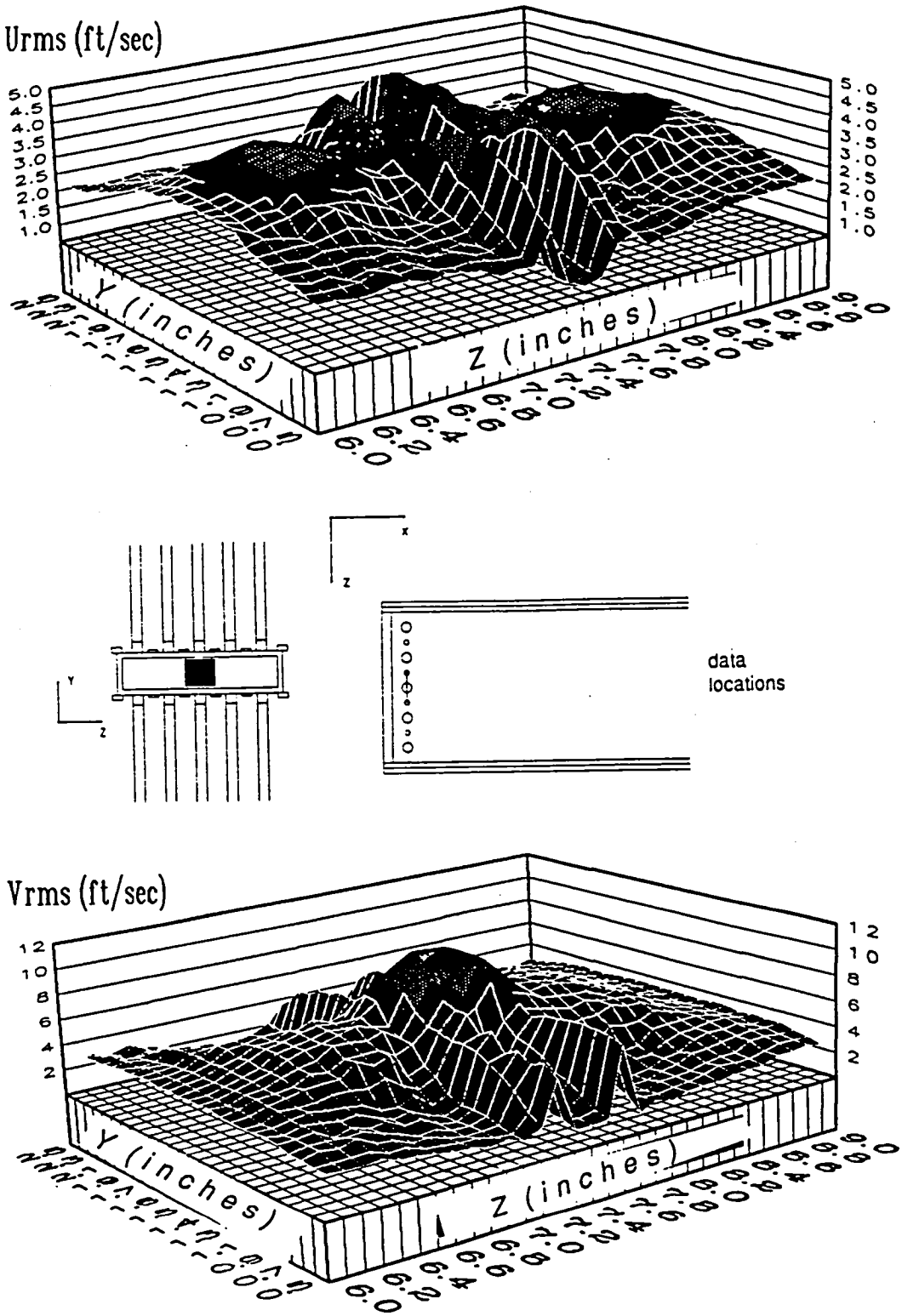

Figure 2.22 Primary Jets Only Contour Plot of U_{rms} and V_{rms} at X=1.5 in.

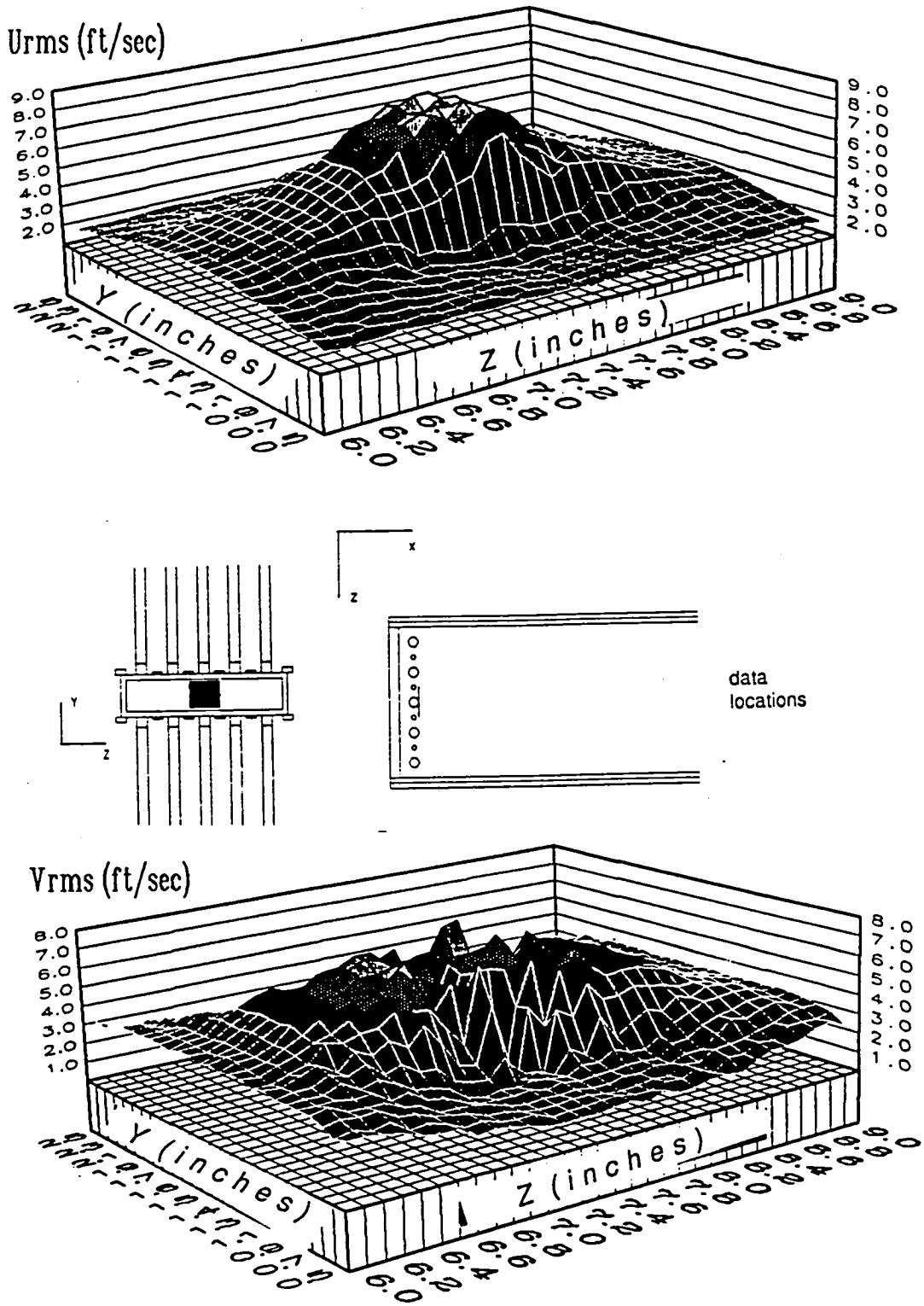

Figure 2.23 Primary Jets Only Contour Plot of U_{rms} and V_{rms} at X=2.0 in.

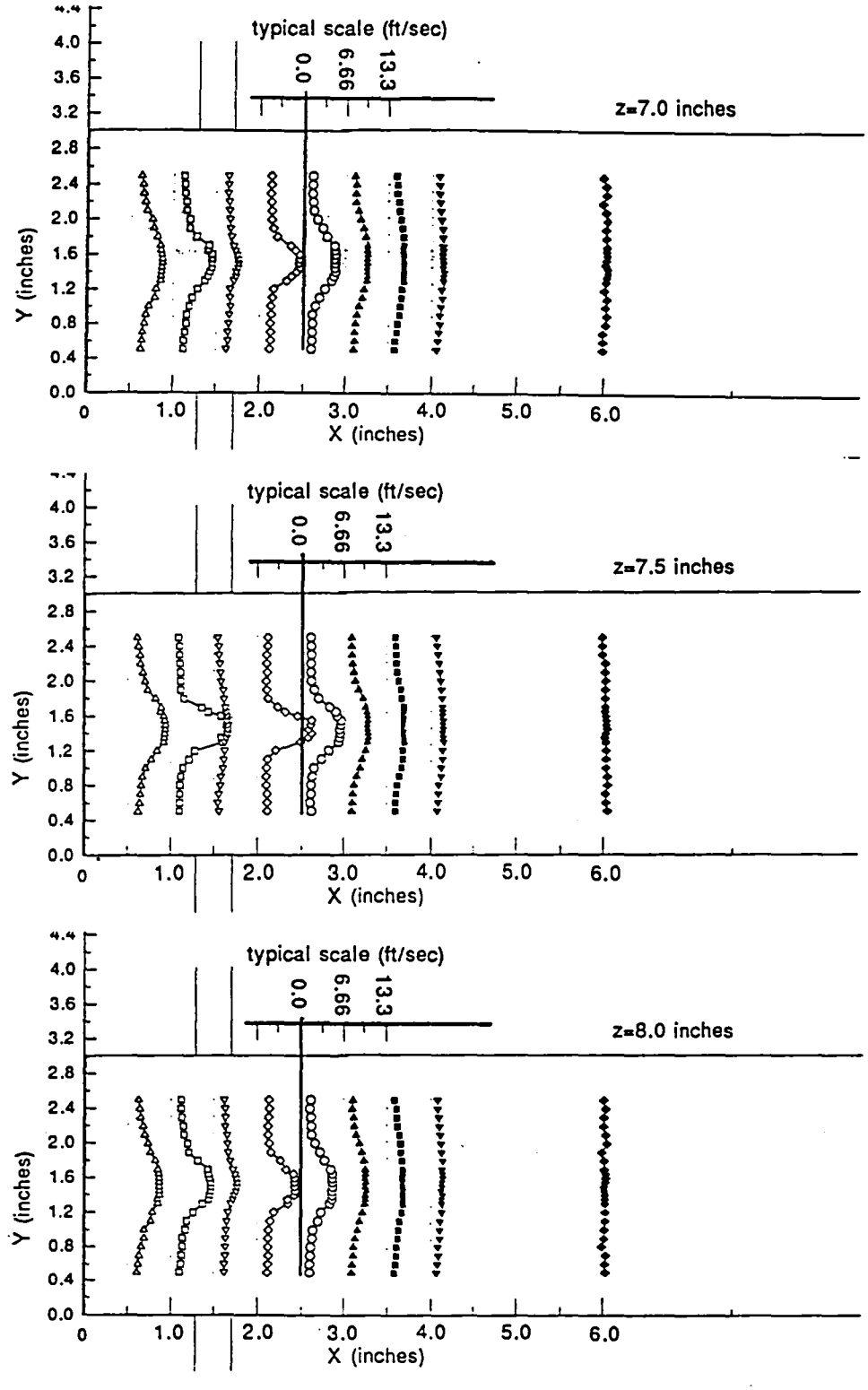

Figure 2.24 Primary Jets Only U_{rms} Distribution

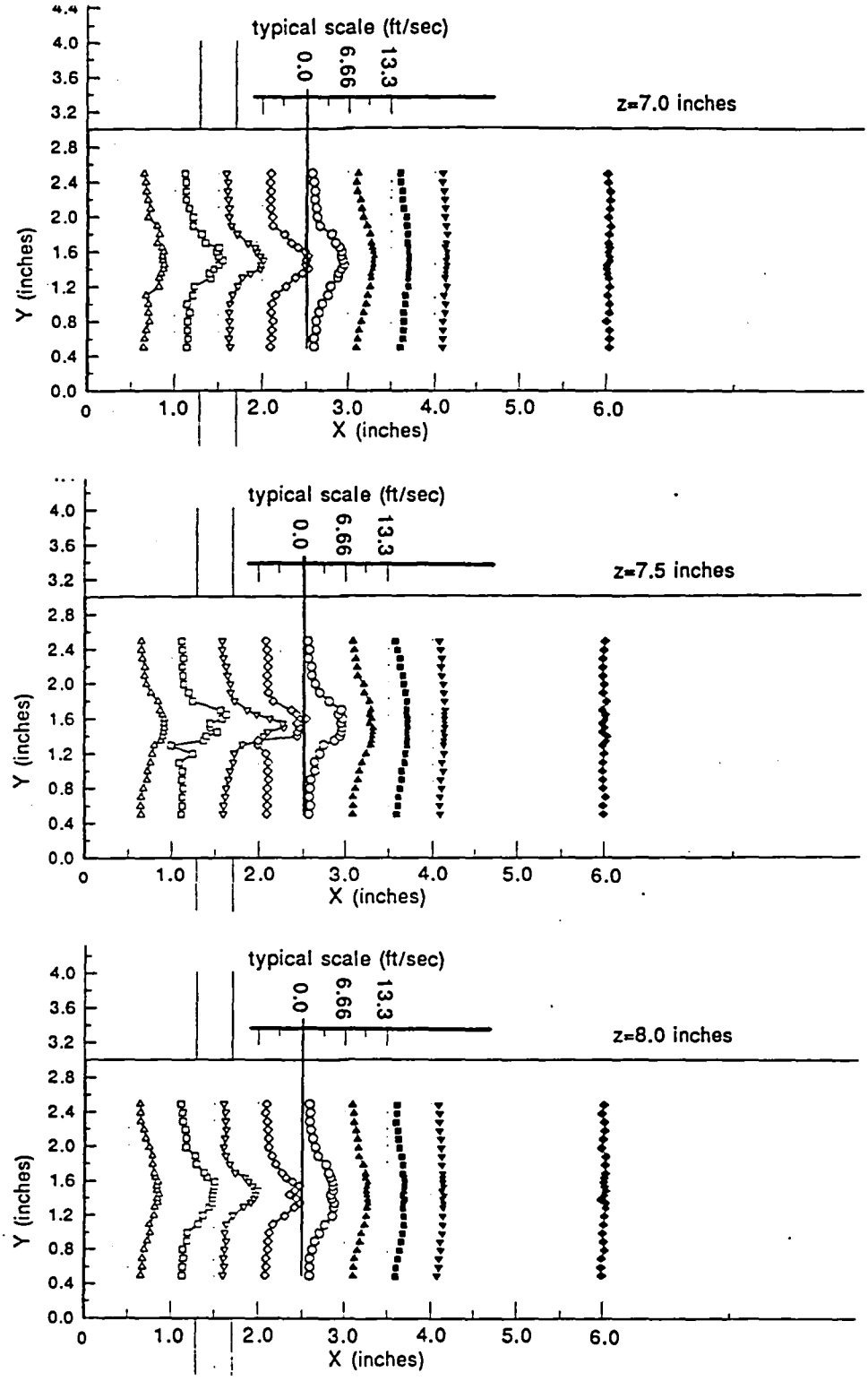

Figure 2.25 Primary Jets Only V_{rms} Distribution

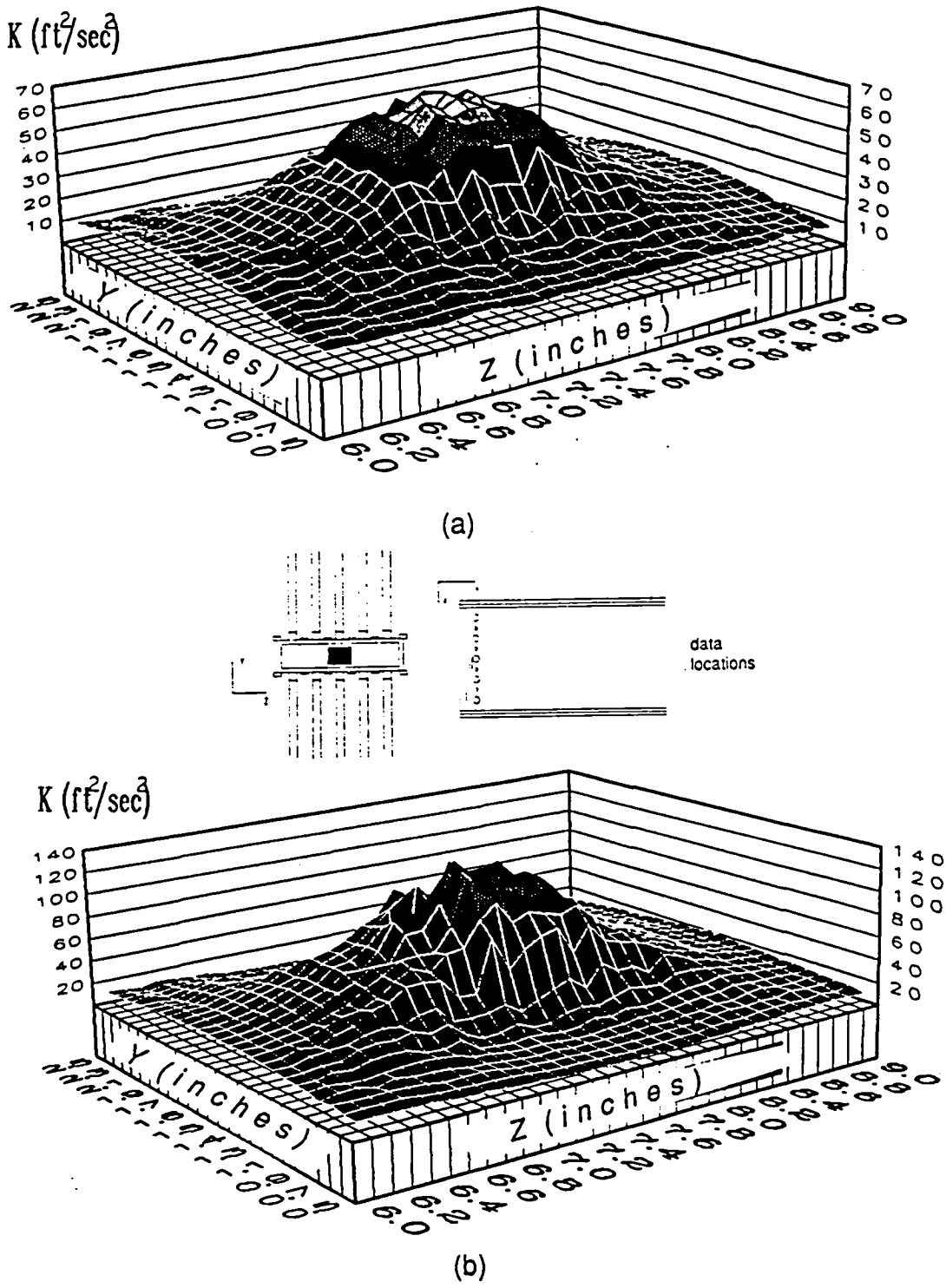

Figure 2.26 Primary Jets Only Contour Plot of K' at
a) X=0.5 in.; b) X=1.0 in.

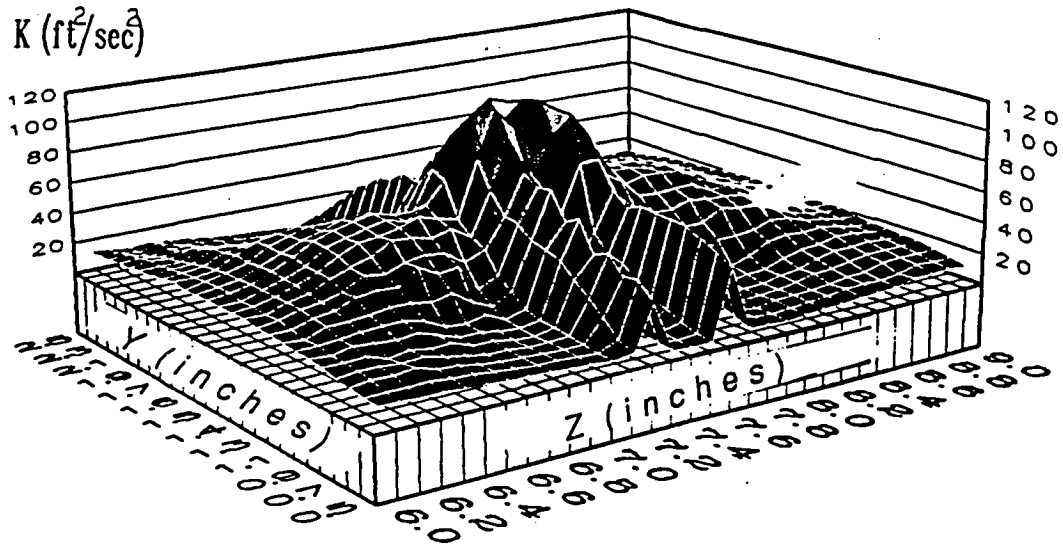

(a)

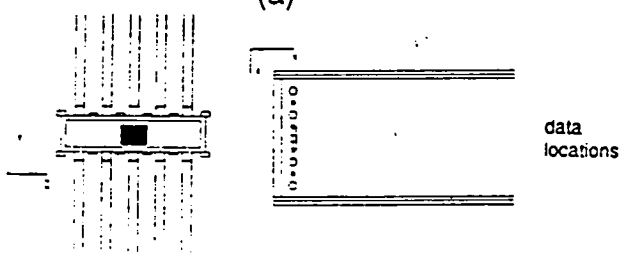

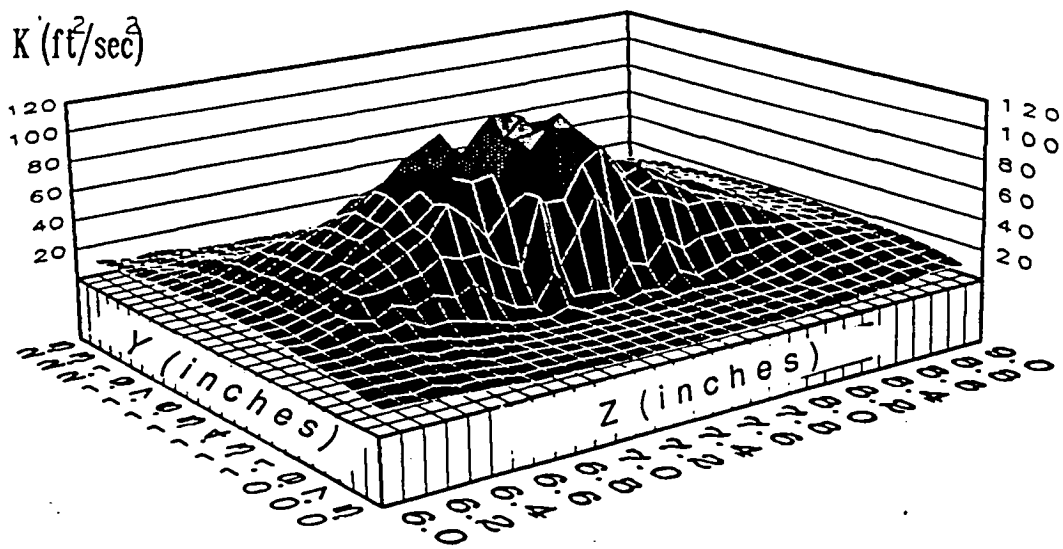

(b)

Figure 2.27 Primary Jets Only Contour Plot of K' at
a) X=1.5 in.; b) X=2.0 in.

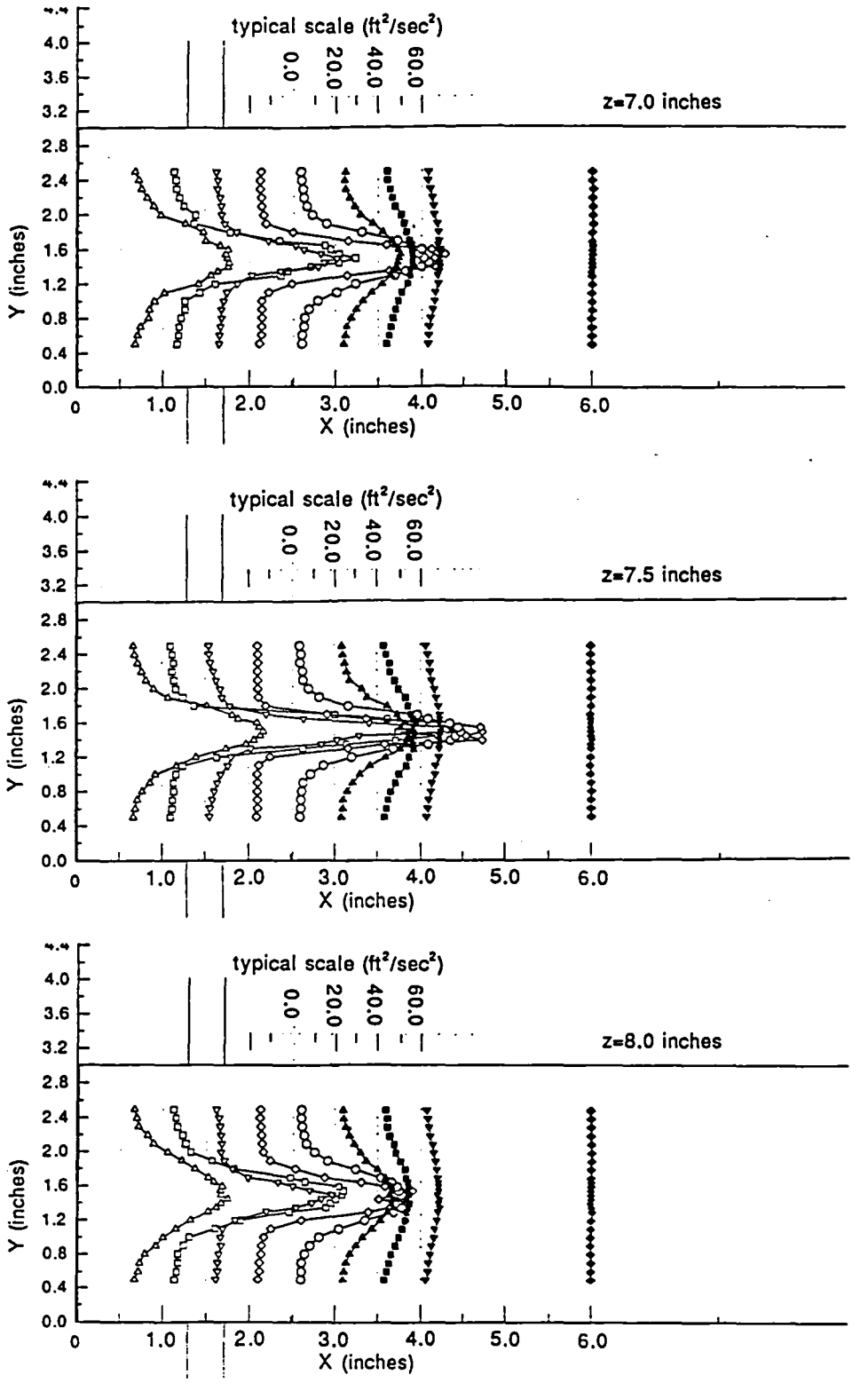

Figure 2.28 Primary Jets Only K' Distribution

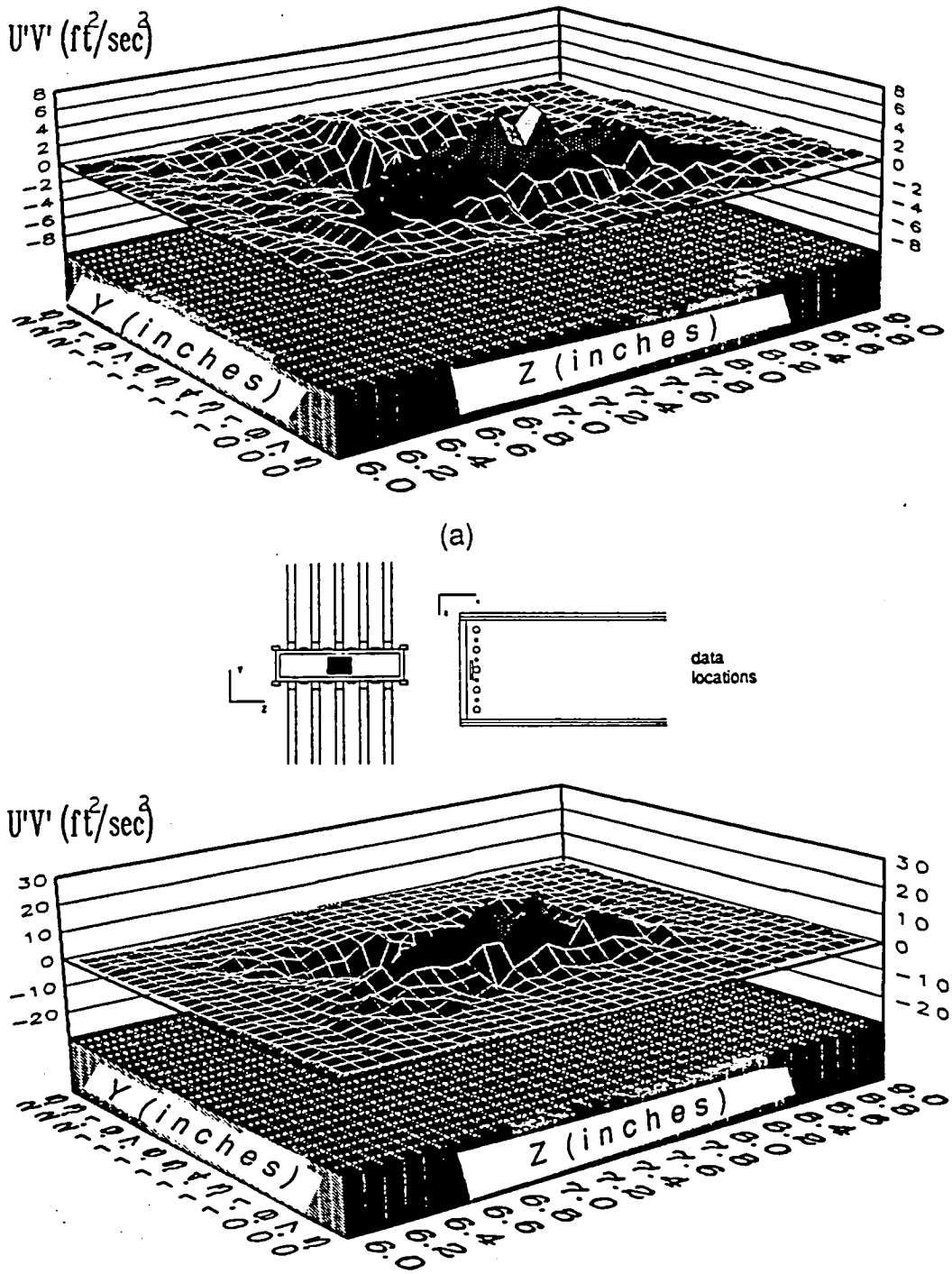

Figure 2.29 Primary Jets Only Contour Plot of U'V' at
a) X=0.5 in.; b) X=1.0 in.

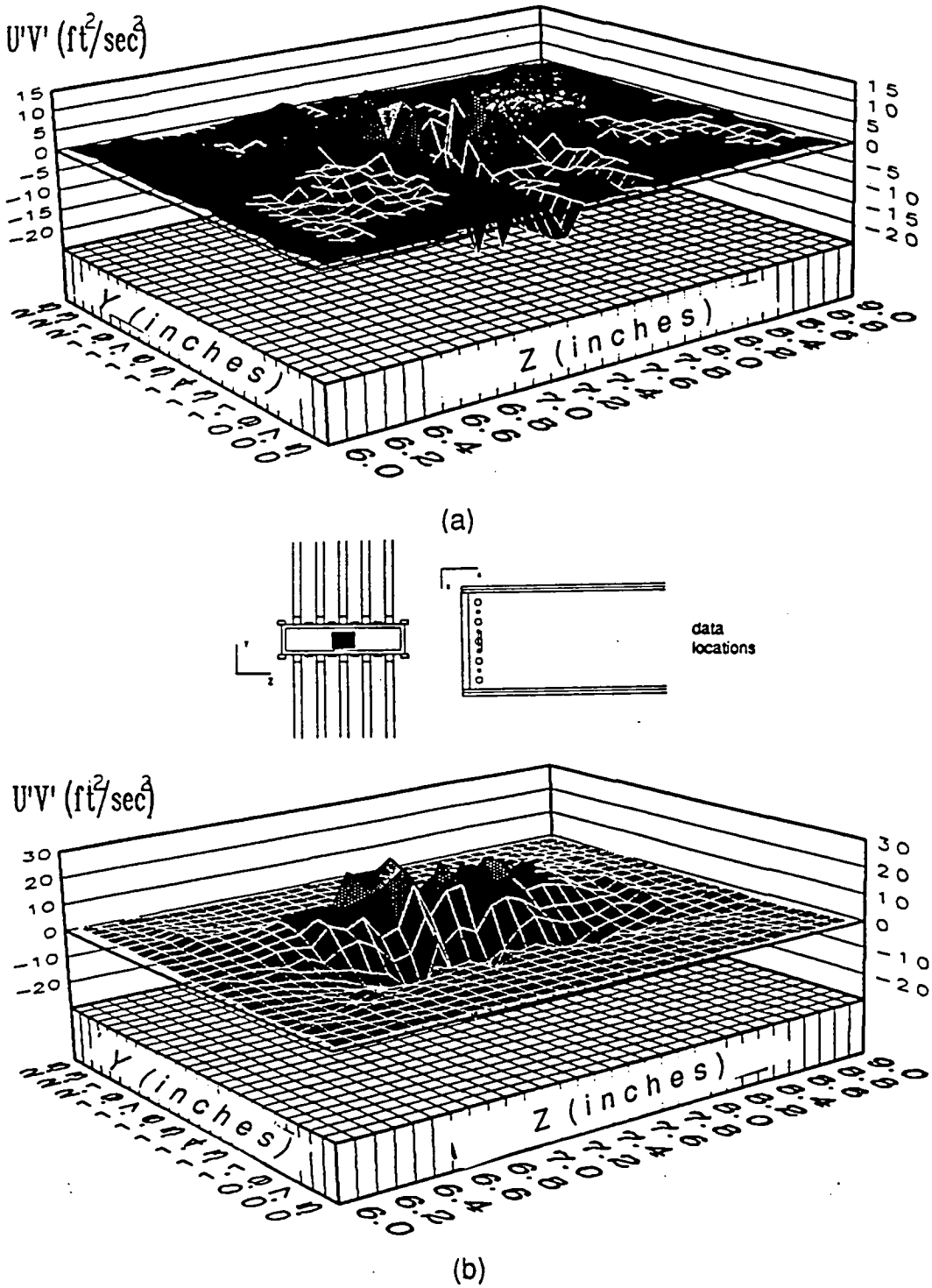

Figure 2.30 Primary Jets Only Contour Plot of U'V' at
a) X=1.5 in.; b) X=2.0 in.

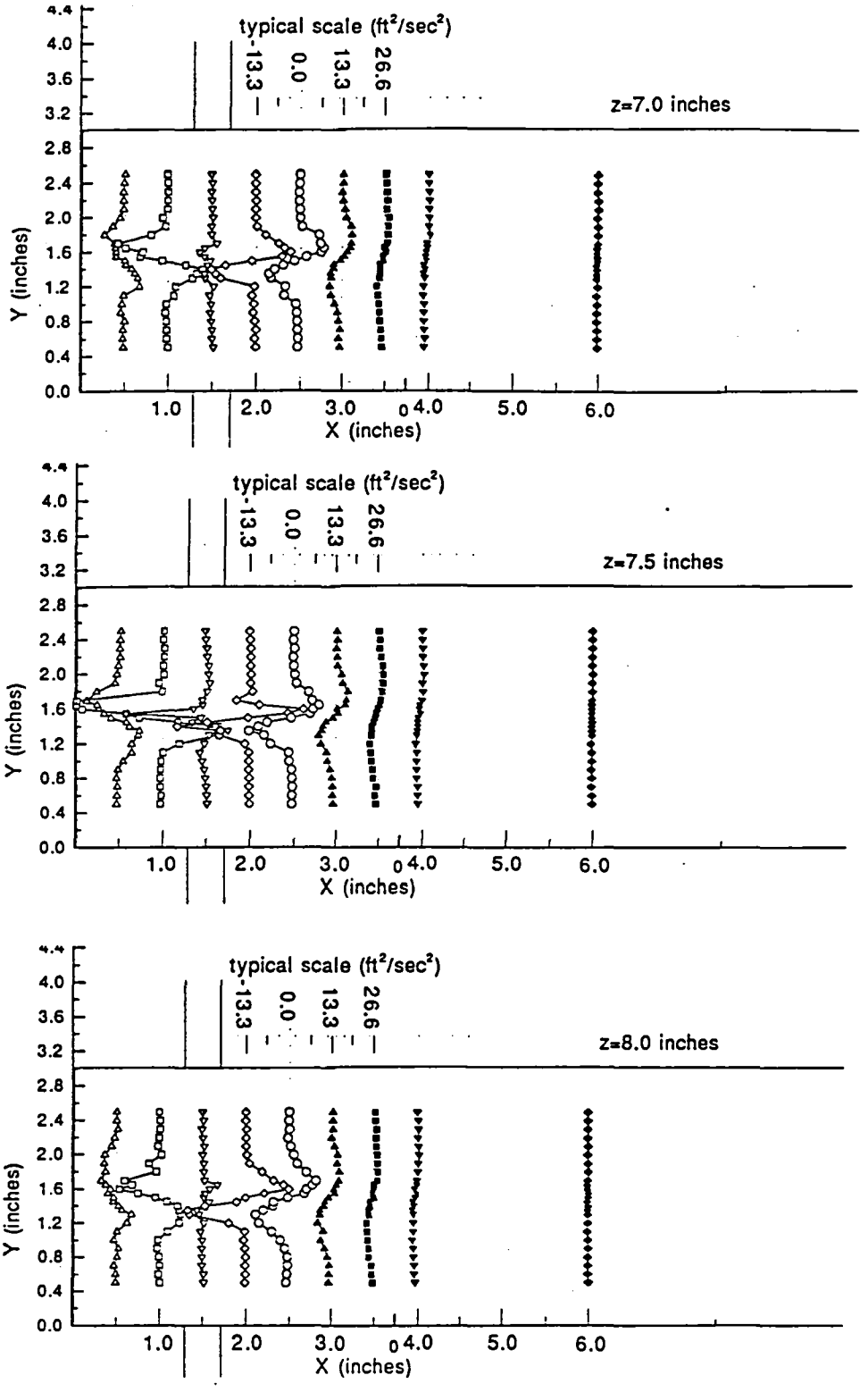

Figure 2.31 Primary Jets Only U'V' Distribution

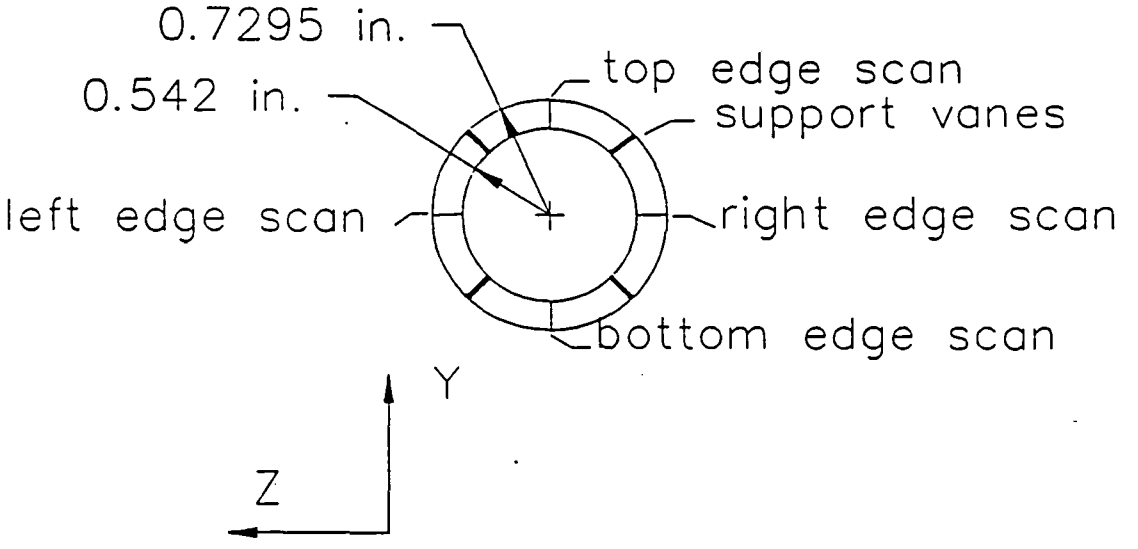

Figure 2.32 Annular Jet Scans For Inlet Conditions

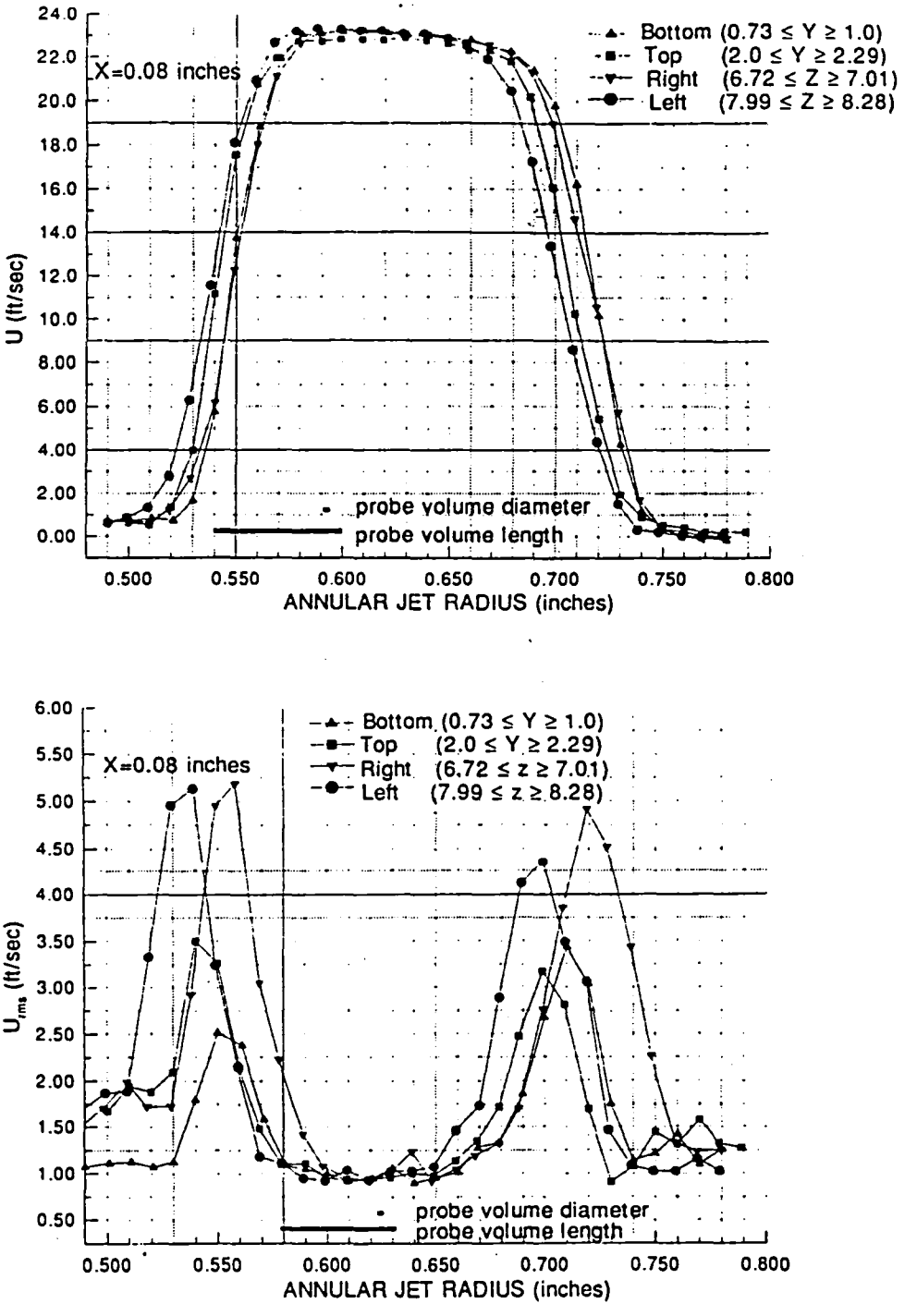

Figure 2.33 Annular Jets Only $\bar{U}$ and U_{rms} Distribution of the Annular Jets at X=0.08 in.

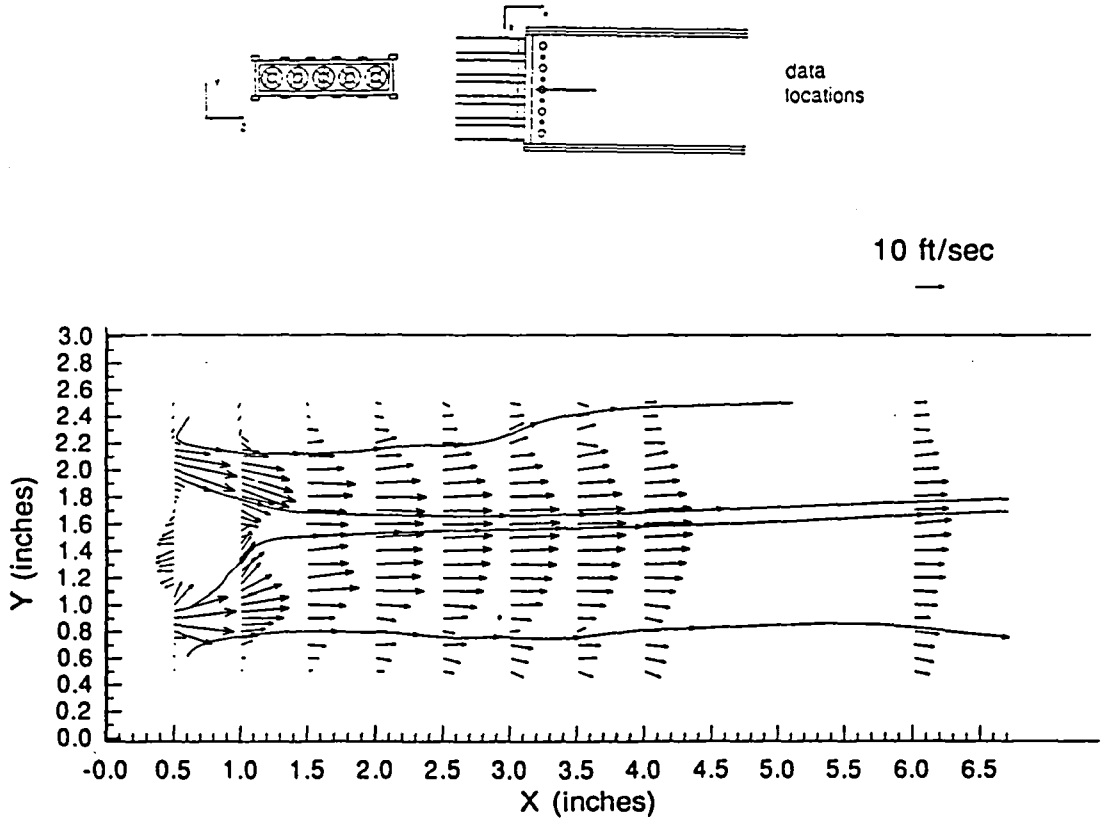

Figure 2.34 Annular Jets Only Mean Velocity Vector Plot at Z=7.5 in.

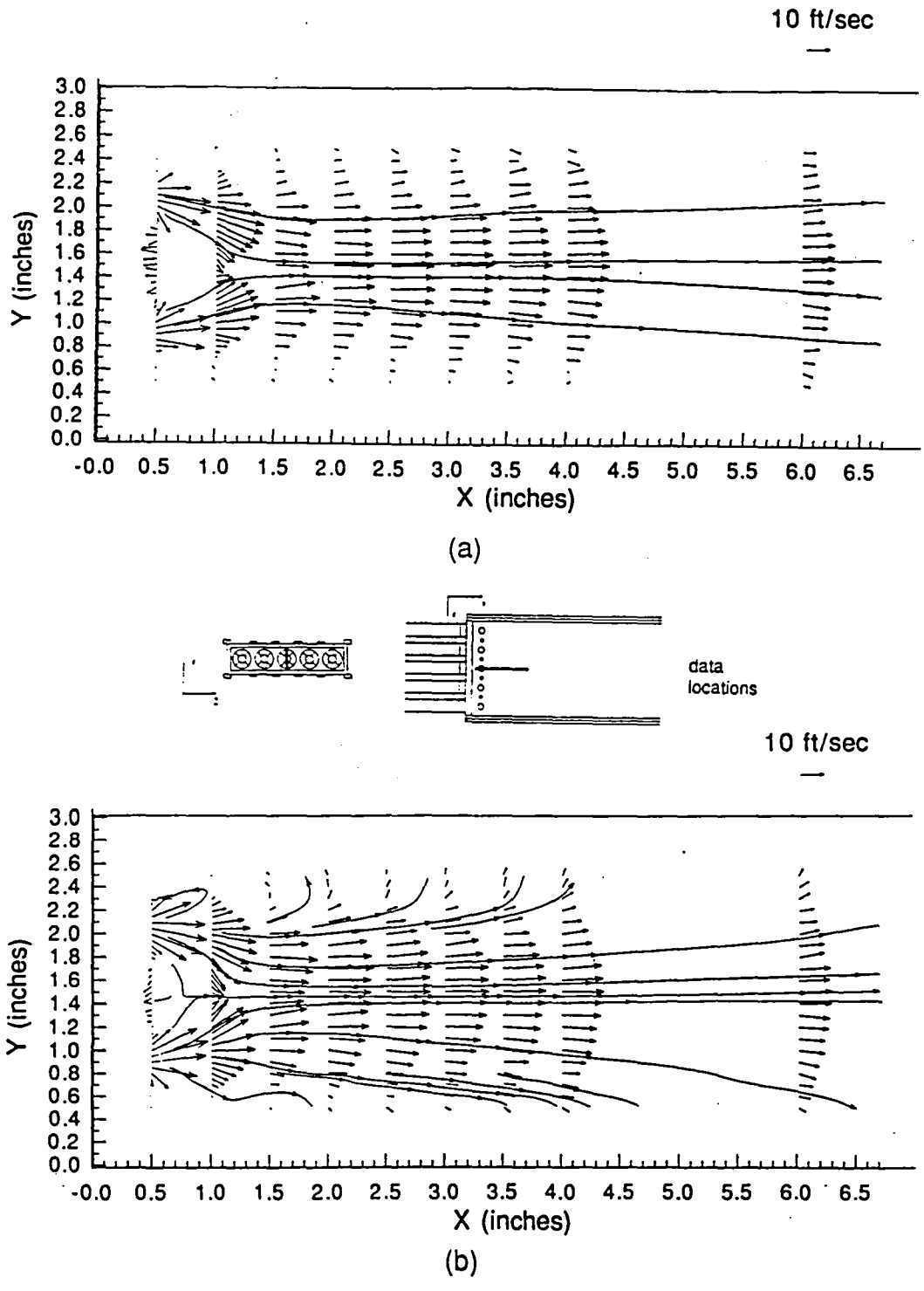

Figure 2.35 Annular Jets Only Mean Velocity Vector Plots
a) Z=7.4 in.; b) Z=7.6 in.

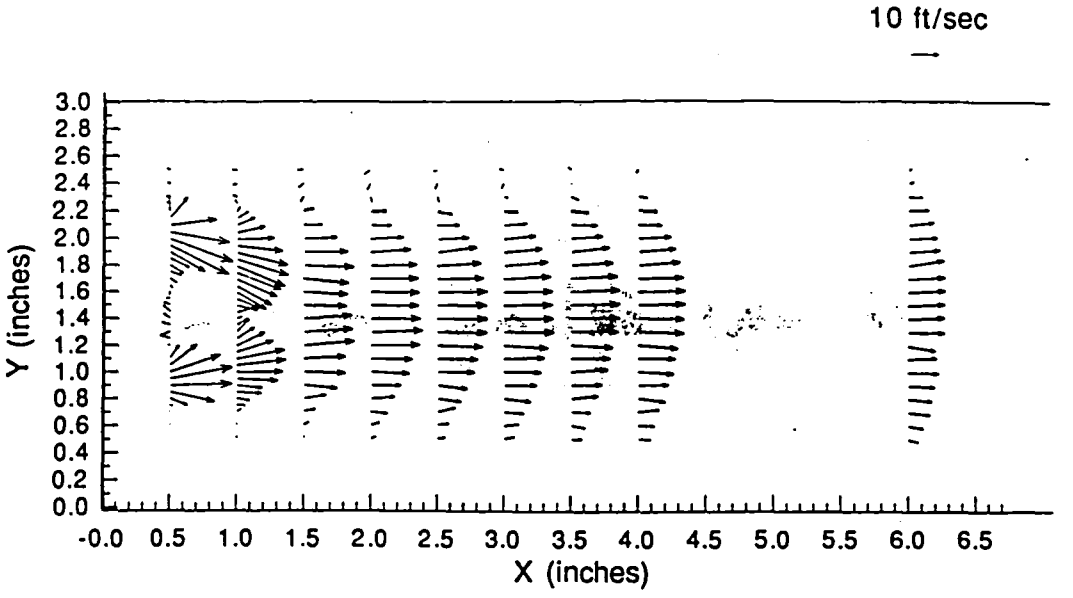

(a)

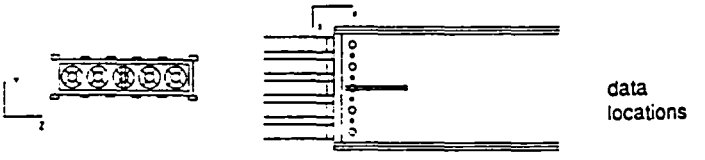

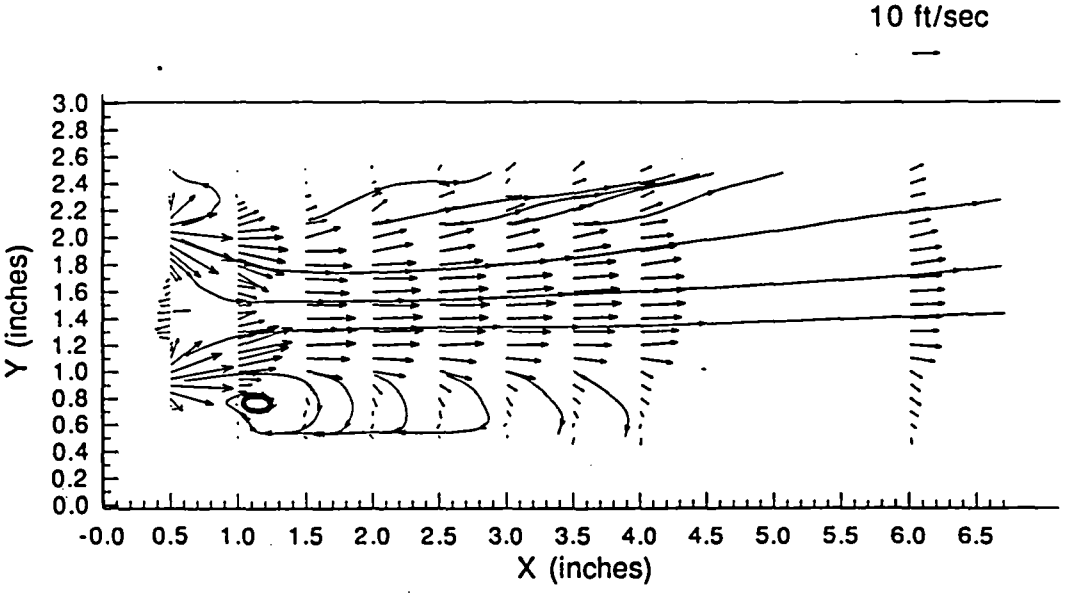

(b)

Figure 2.36 Annular Jets Only Mean Velocity Vector Plots
a) Z=7.3 in.; b) Z=7.7 in.

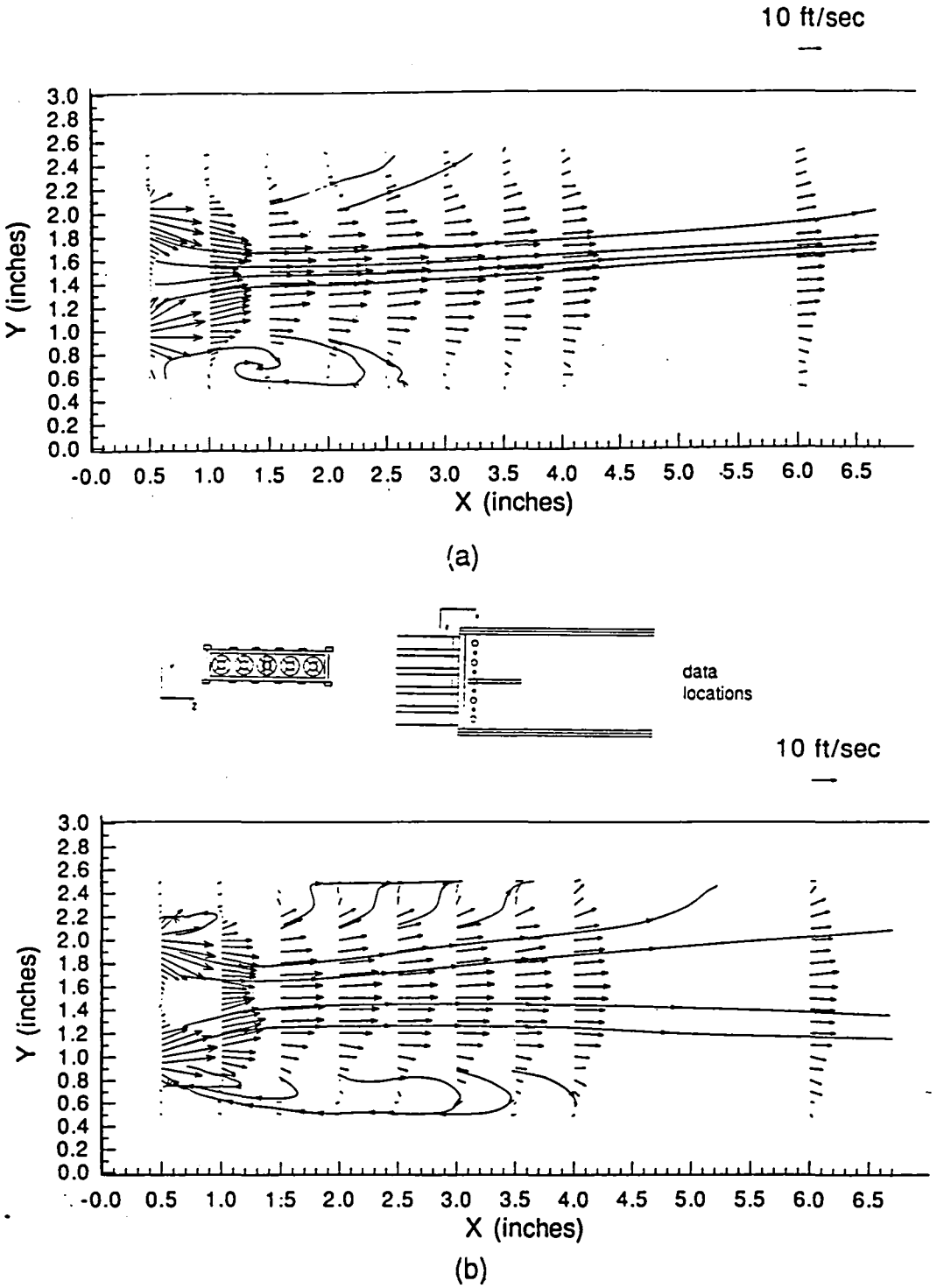

Figure 2.37 Annular Jets Only Mean Velocity Vector Plots
a) Z=7.2 in.; b) Z=7.8 in.

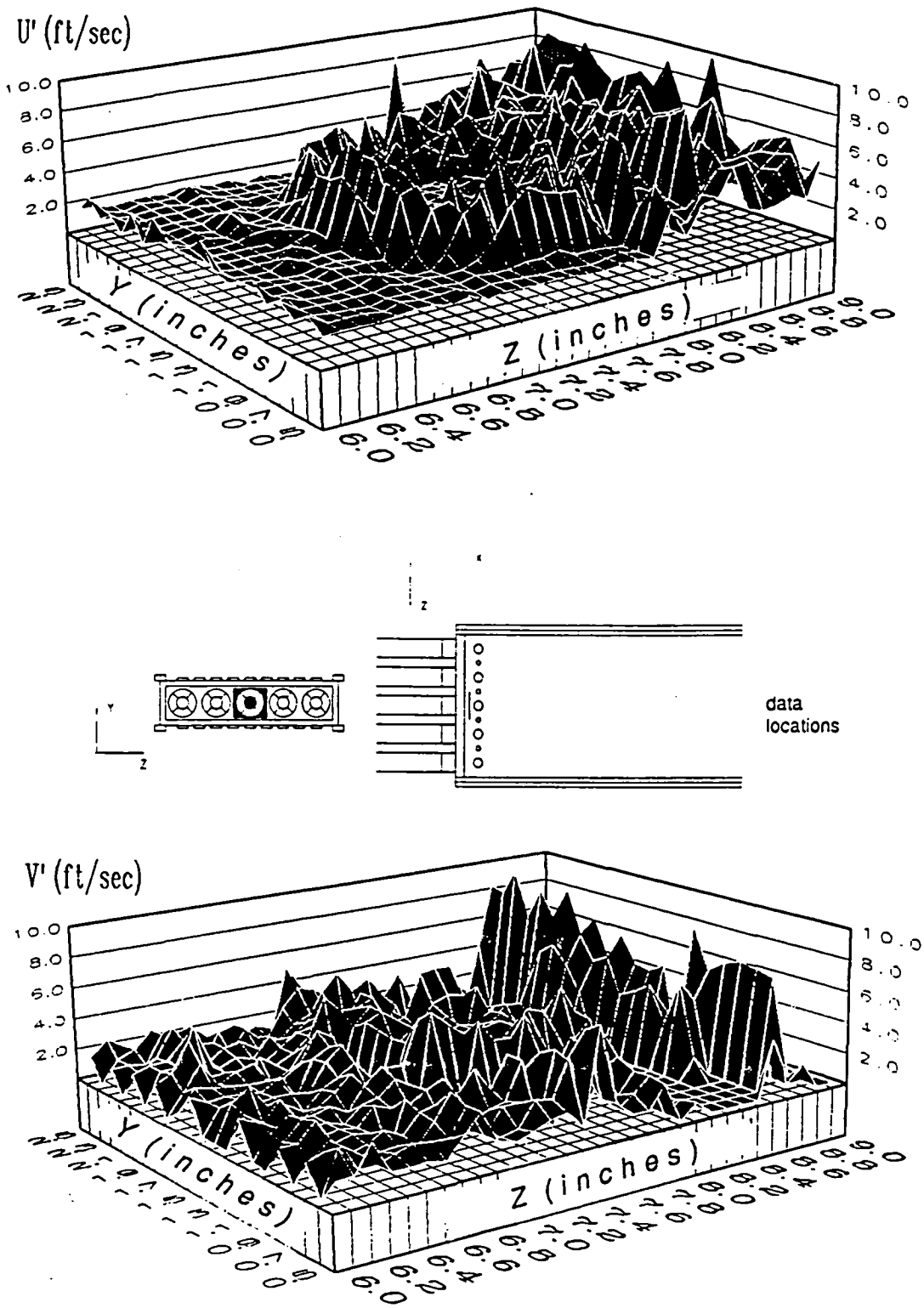

Figure 2.38 Annular Jets Only Contour Plot of U_{rms} and V_{rms} at X=0.5 in.

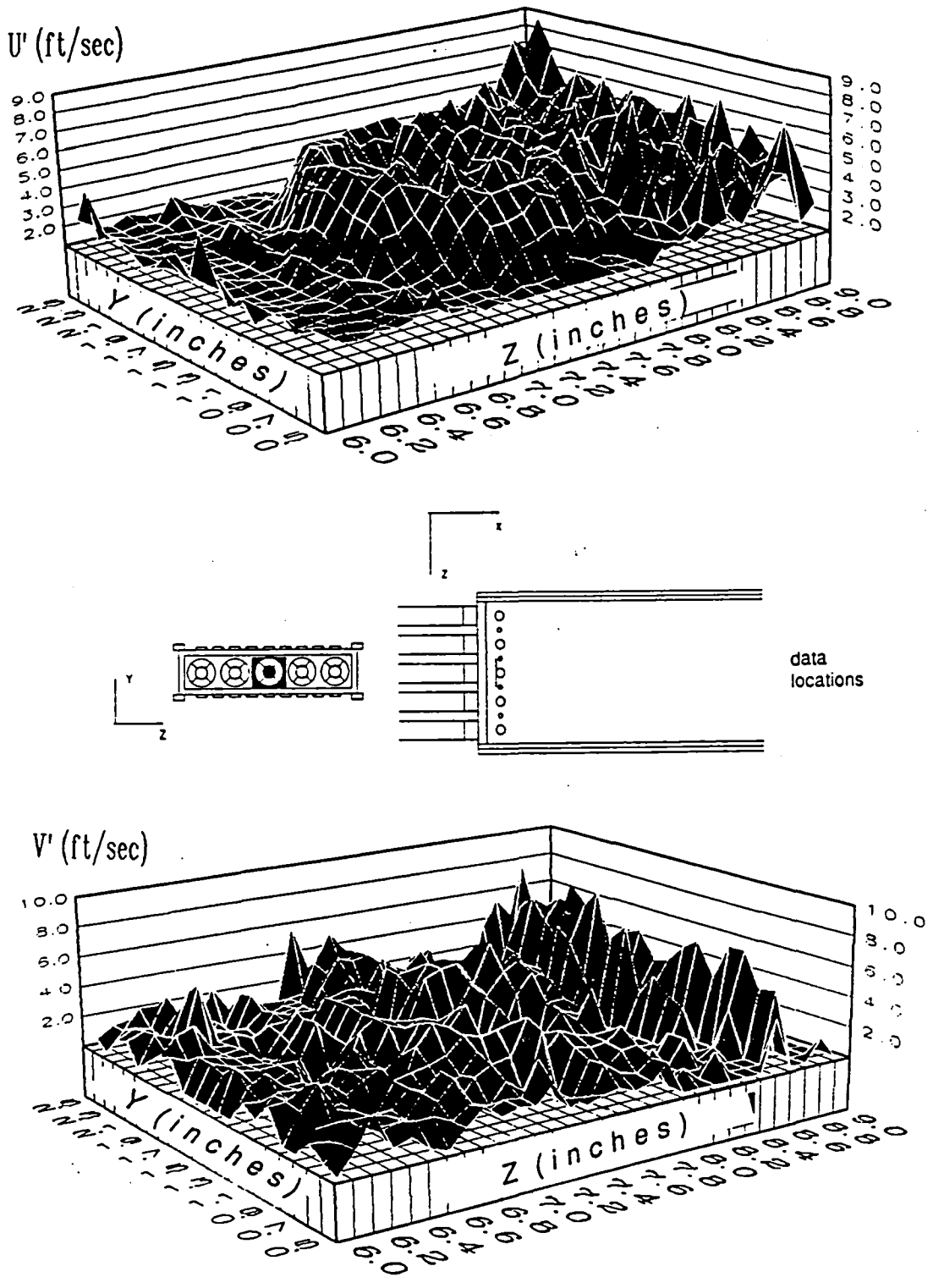

Figure 2.39 Annular Jets Only Contour Plot of U_{rms} and V_{rms} at X=1.0 in.

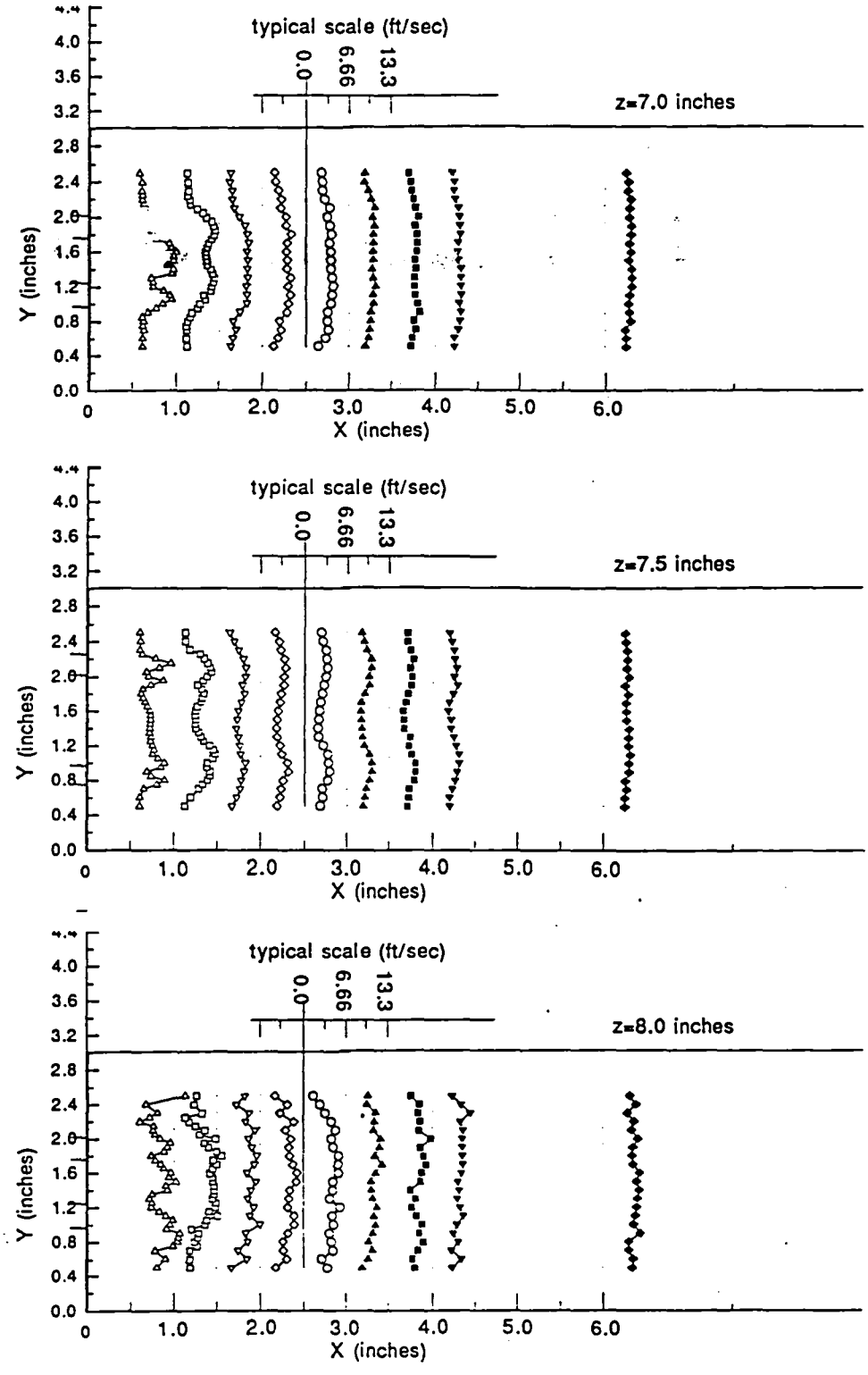

Figure 2.40 Annular Jets Only U_{rms} Distribution

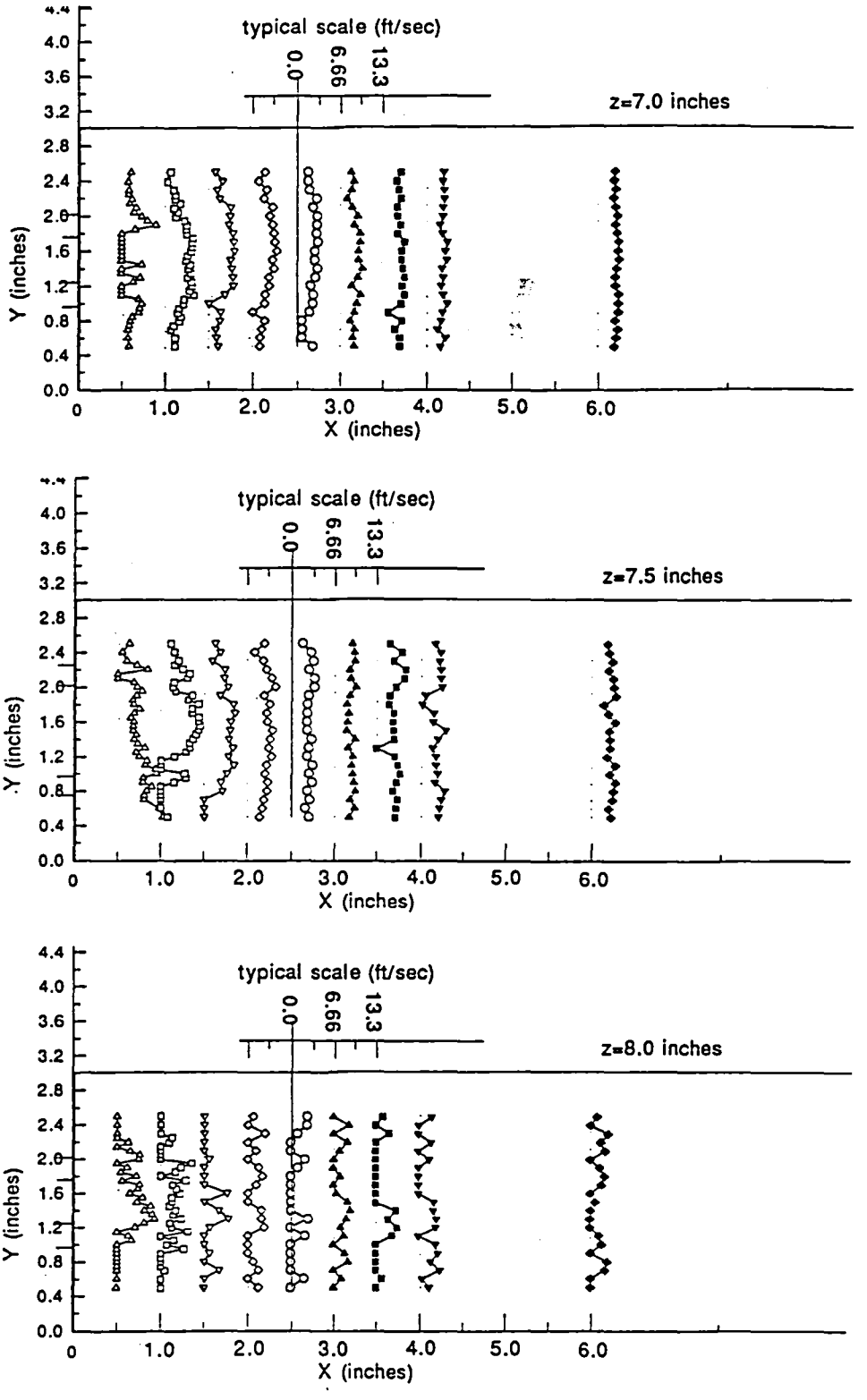

Figure 2.41 Annular Jets Only V_{rms} Distribution

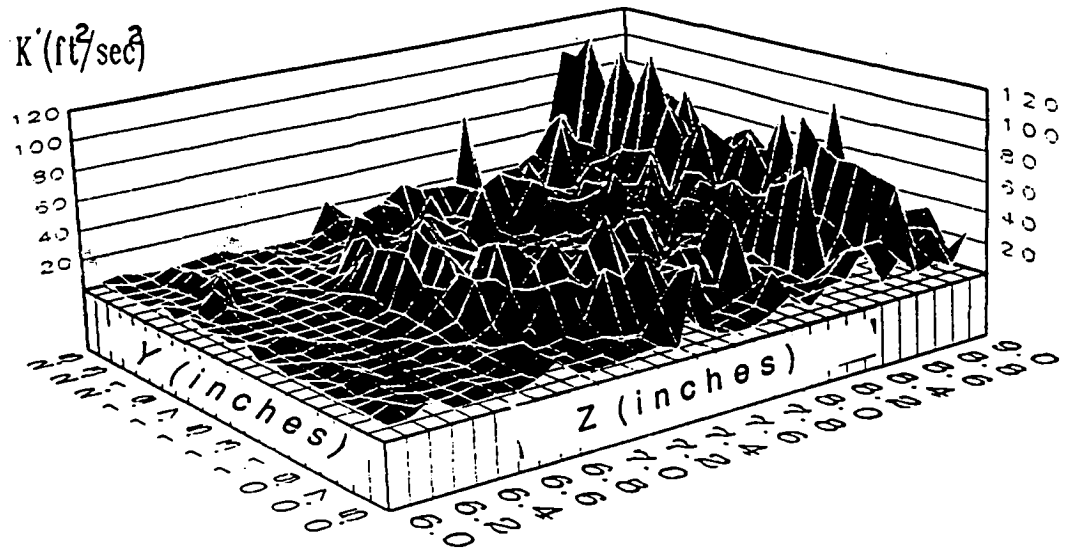

(a)

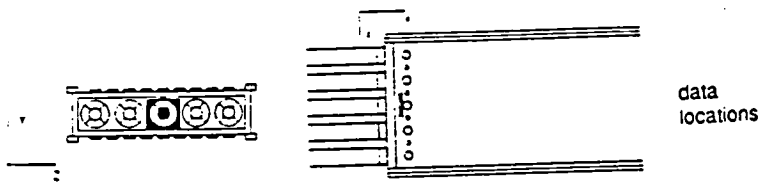

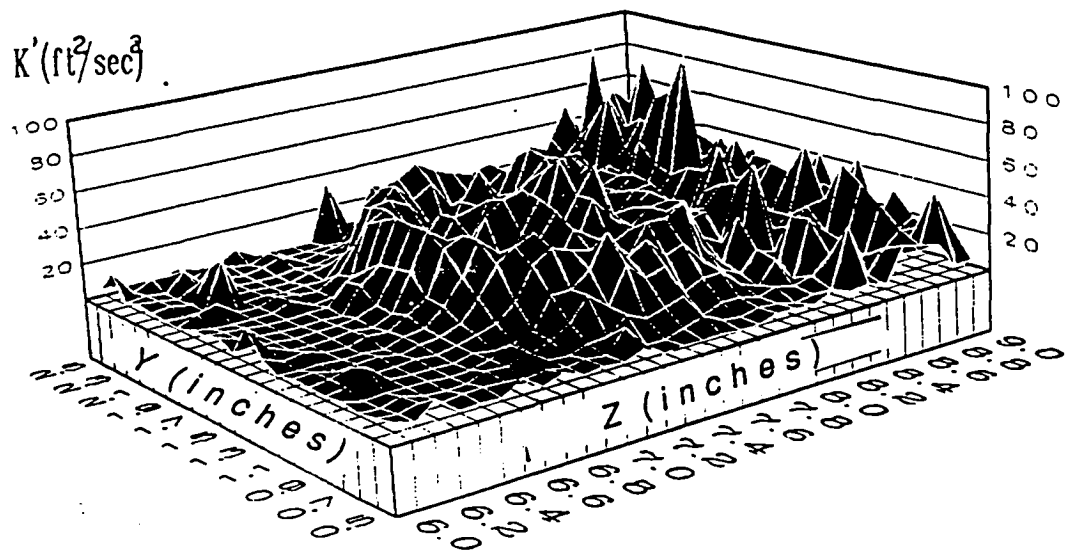

(b)

Figure 2.42 Annular Jets Only Contour Plot of K' at
a) X=0.5 in.; b) X=1.0 in.

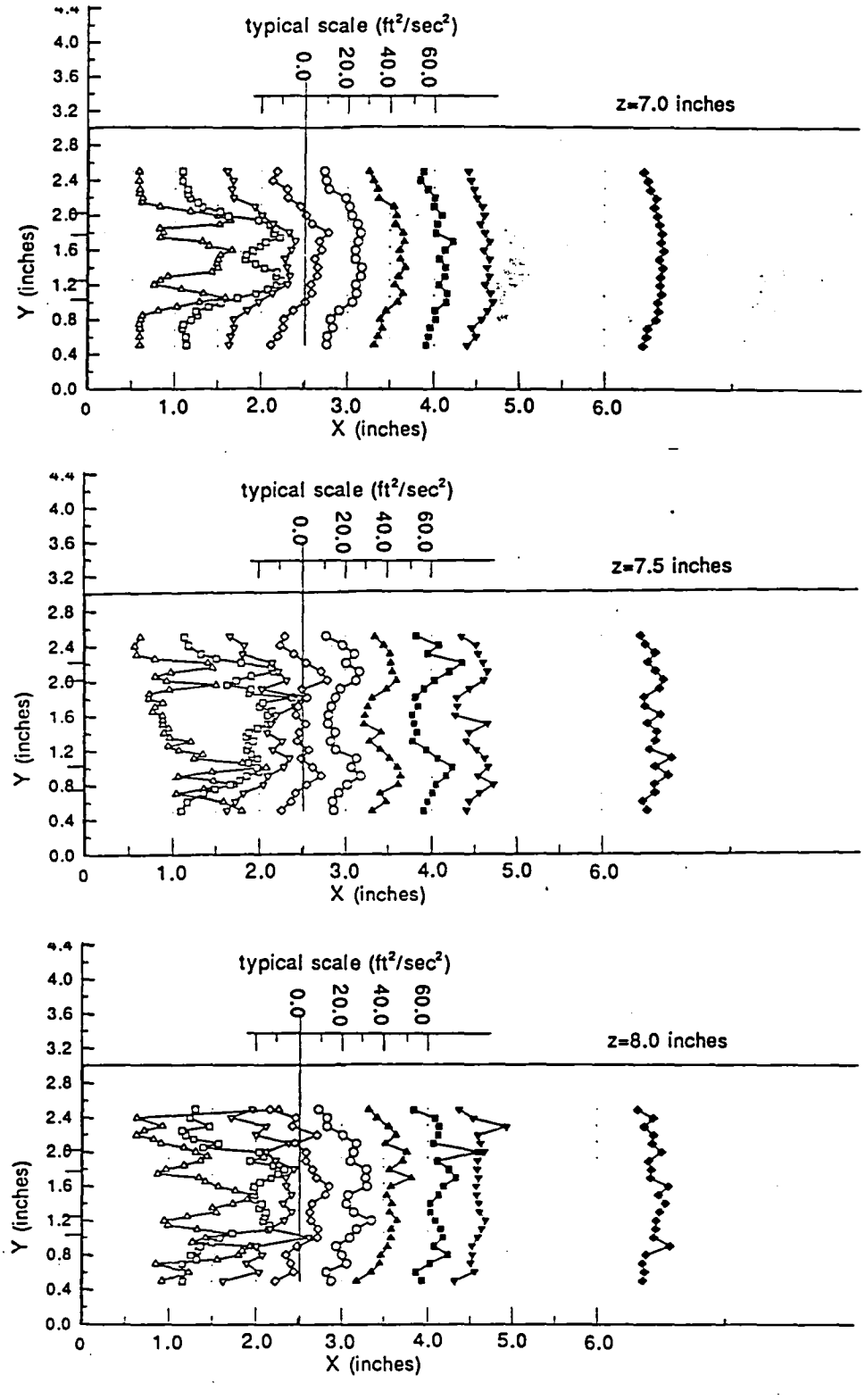

Figure 2.43 Annular Jets Only K' Distribution

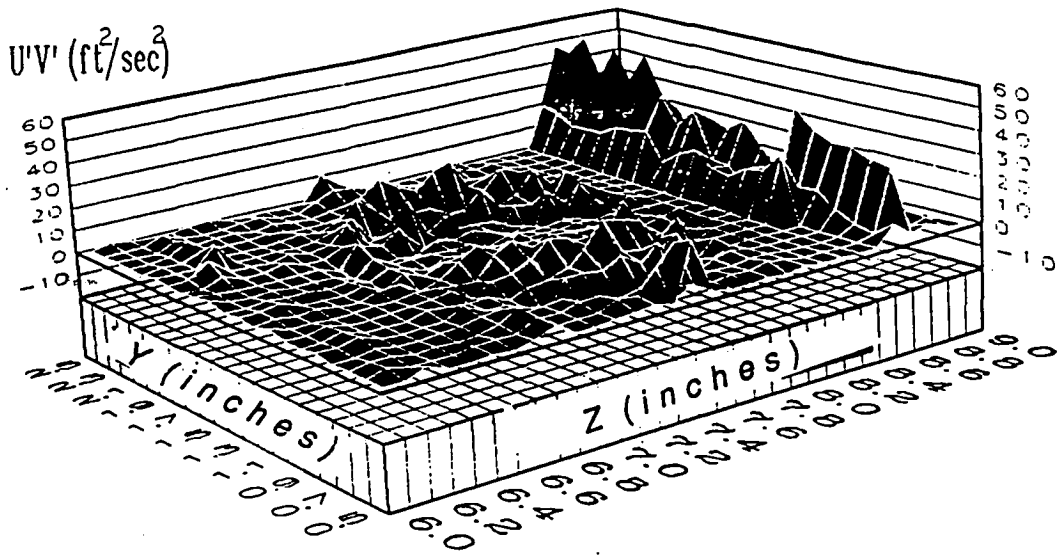

(a)

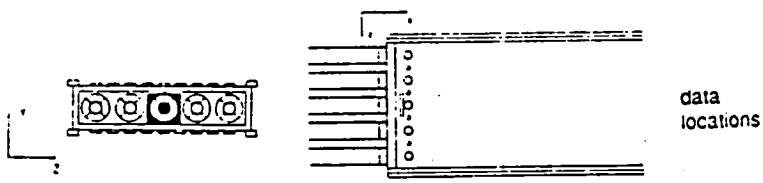

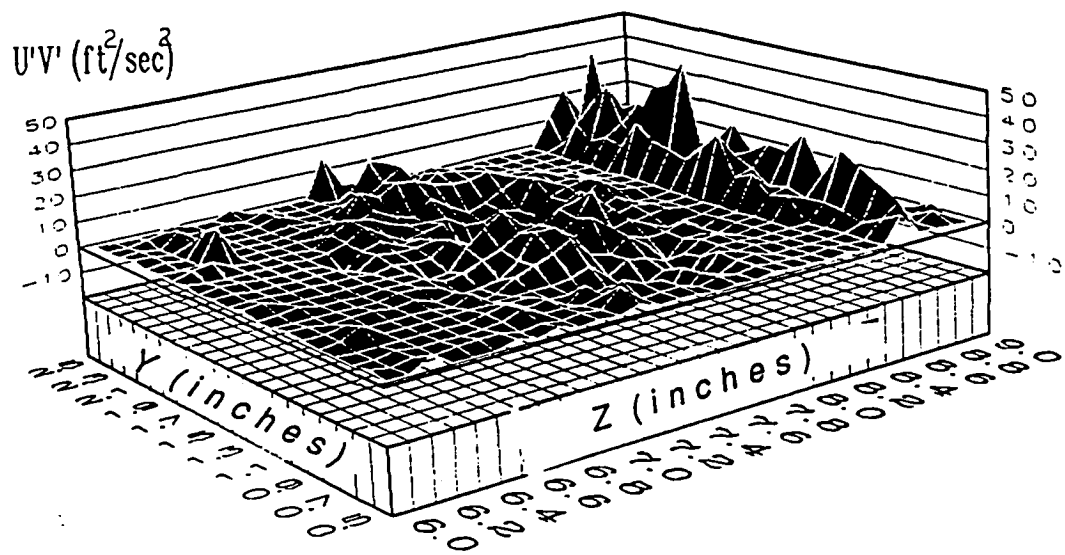

(b)

Figure 2.44 Annular Jets Only Contour Plot of U'V' at
a) X=0.5 in.; b) X=1.0 in.

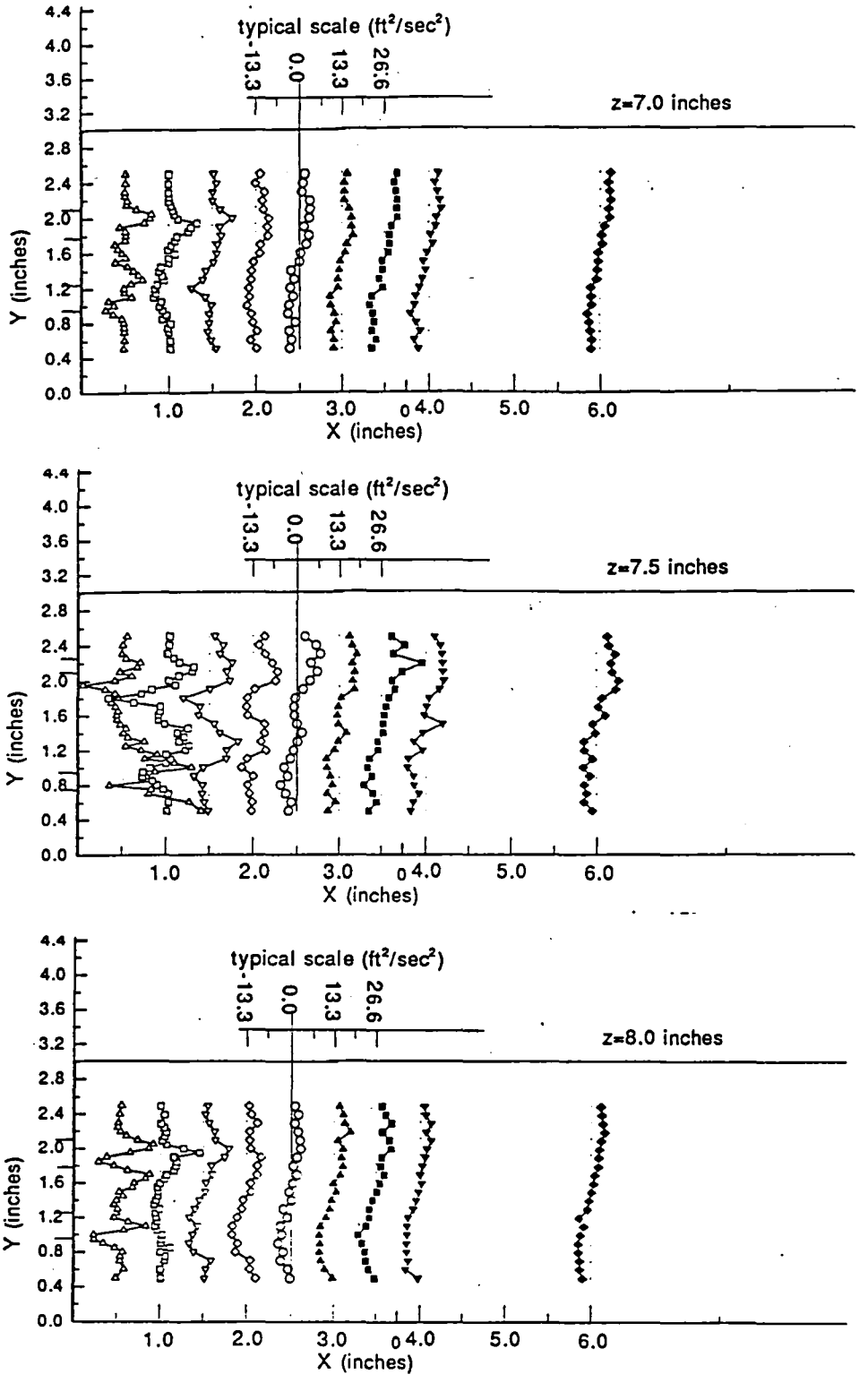

Figure 2.45 Annular Jets Only U'V' Distribution

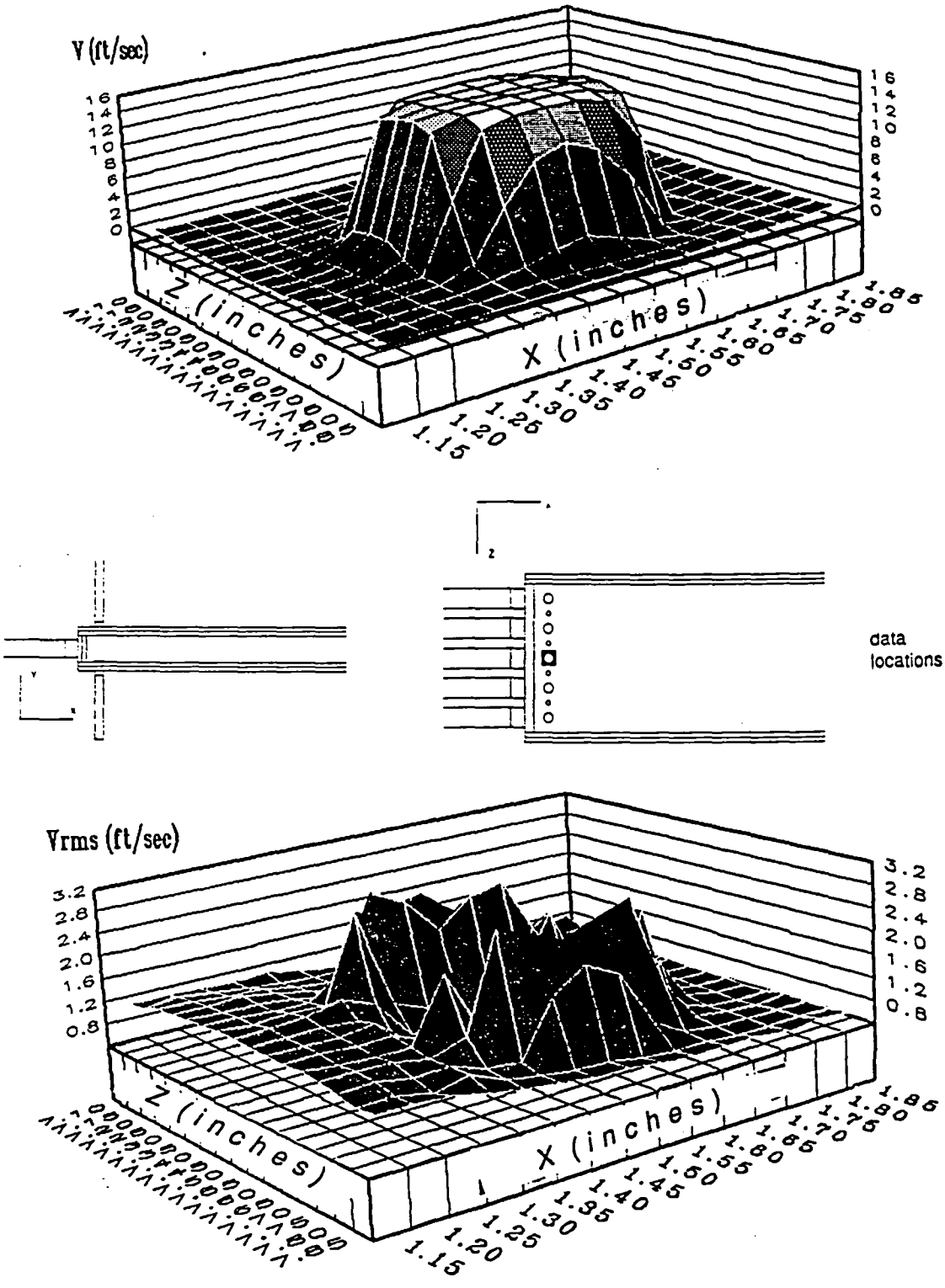

Figure 2.46 Annular and Primary Jets $\bar{V}$ and V_{rms} Distribution of the Primary Jets at Y=0.1 inches

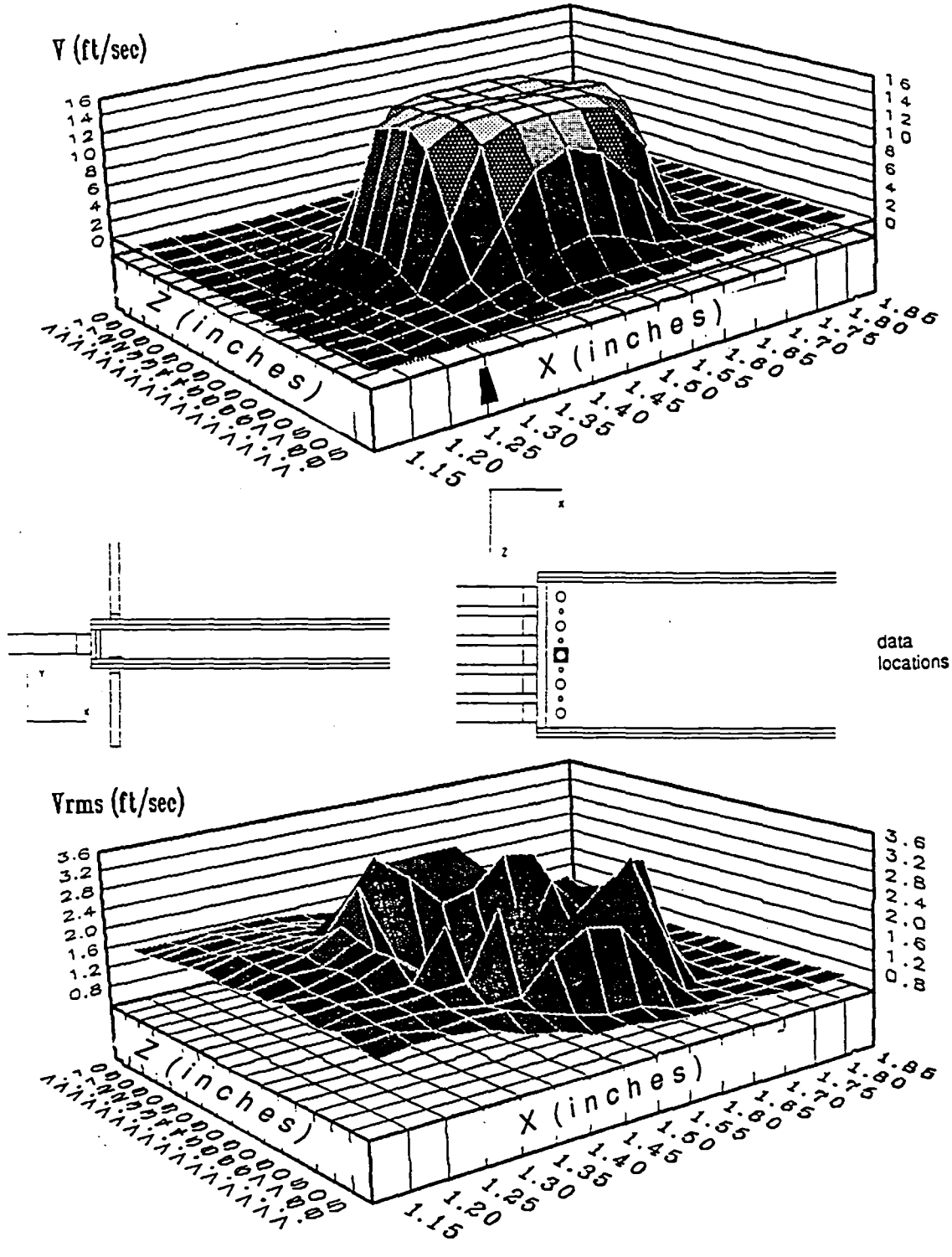

Figure 2.47 Annular and Primary Jets $\bar{V}$ and V_{rms} Distribution of the Primary Jets at Y=0.25 inches

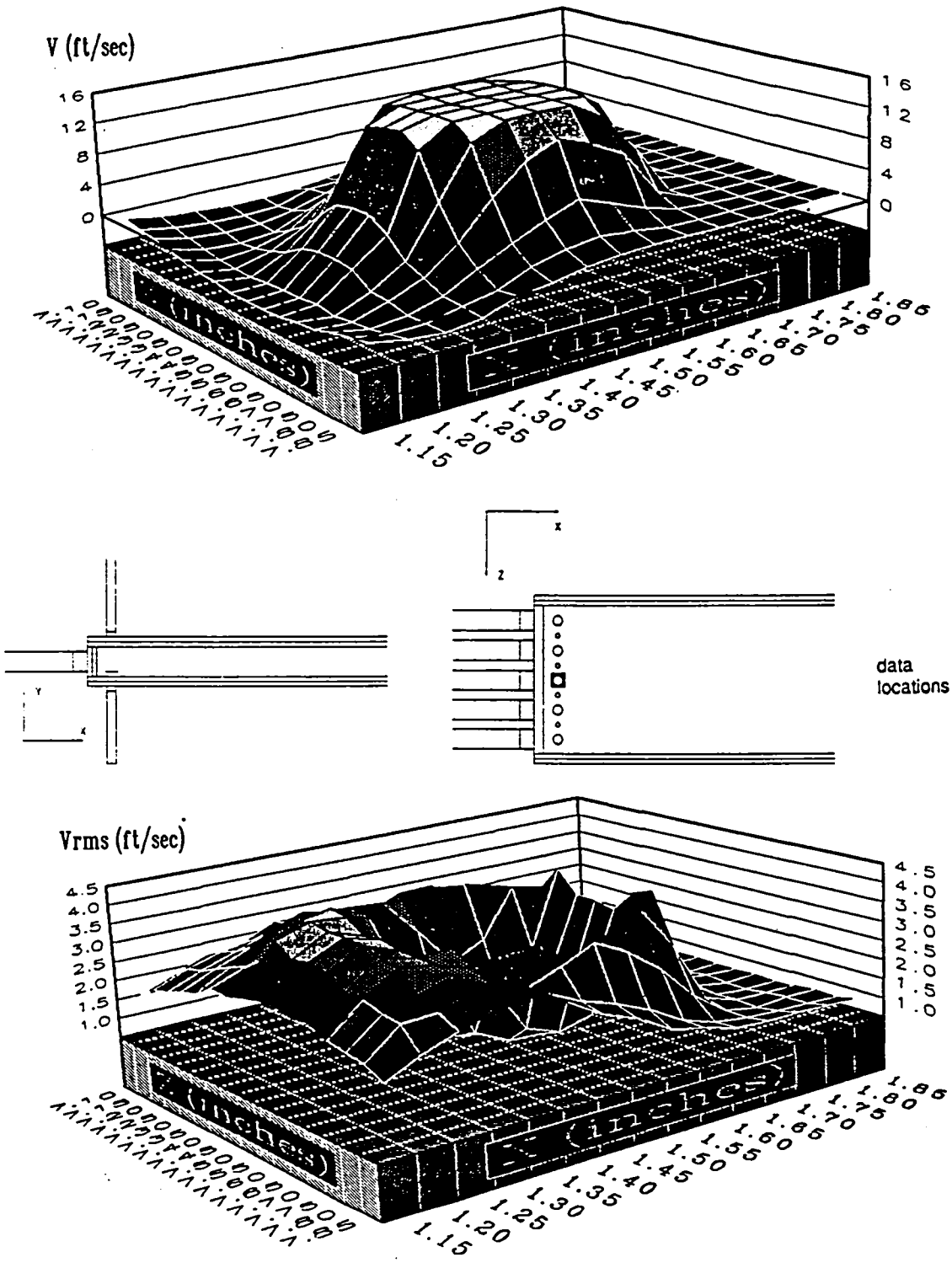

Figure 2.48 Annular and Primary Jets $\bar{V}$ and V_{rms} Distribution of the Primary Jets at Y=0.5 inches

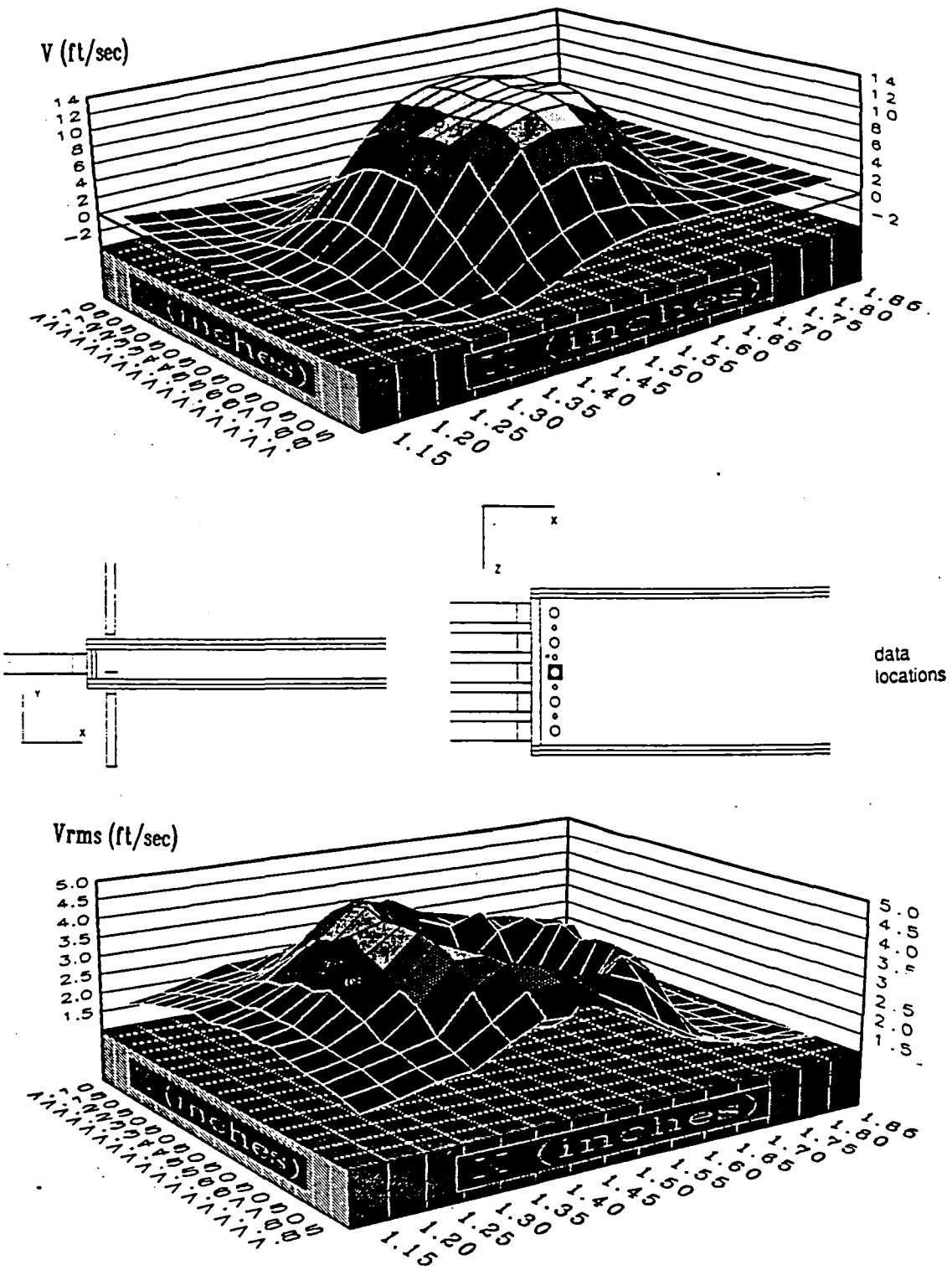

Figure 2.49 Annular and Primary Jets $\tilde{V}$ and V_{rms} Distribution of the Primary Jets at Y=0.75 inches

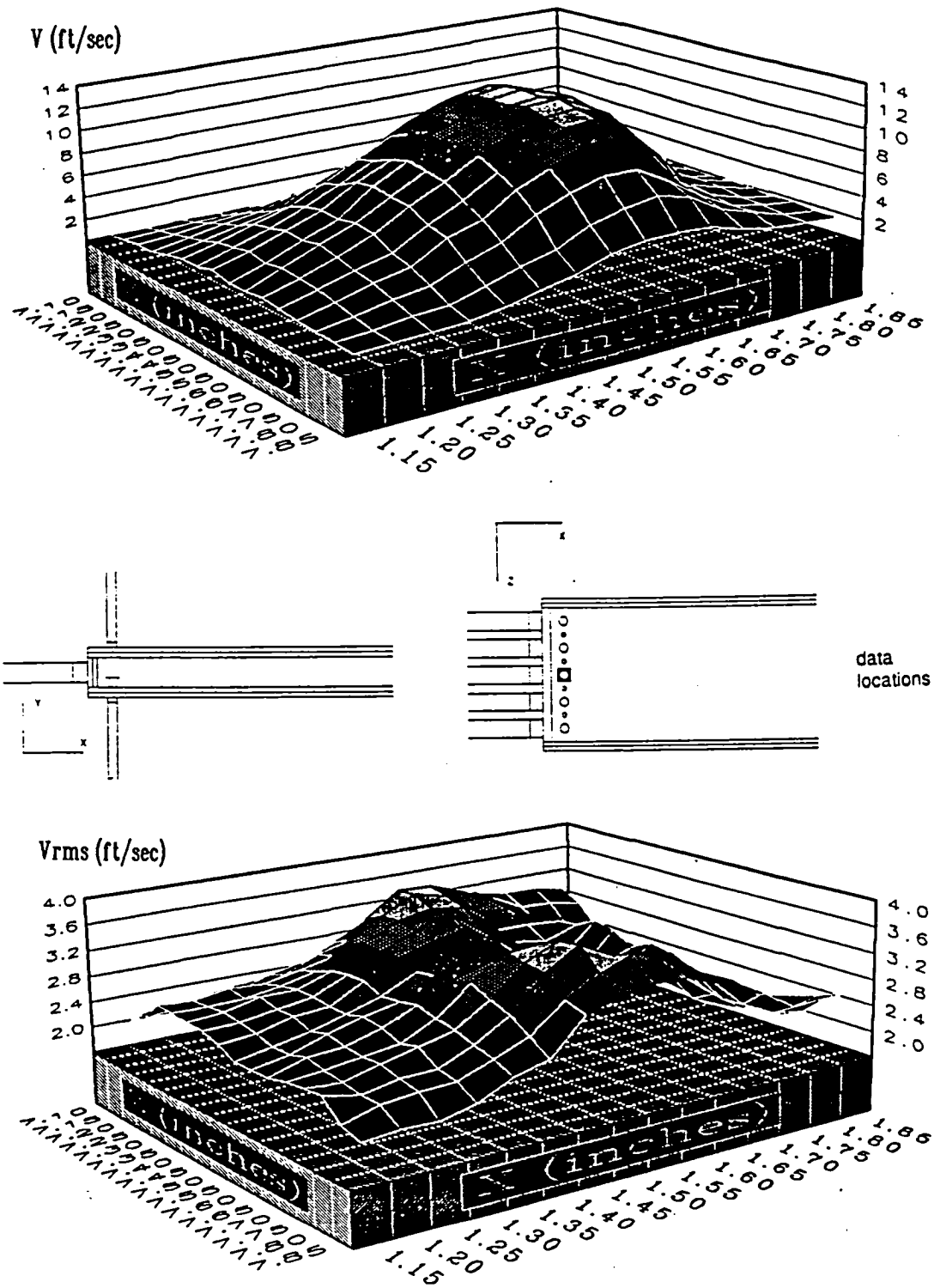

Figure 2.50 Annular and Primary Jets $\bar{V}$ and V_{rms} Distribution of the Primary Jets at Y=1.0 inches

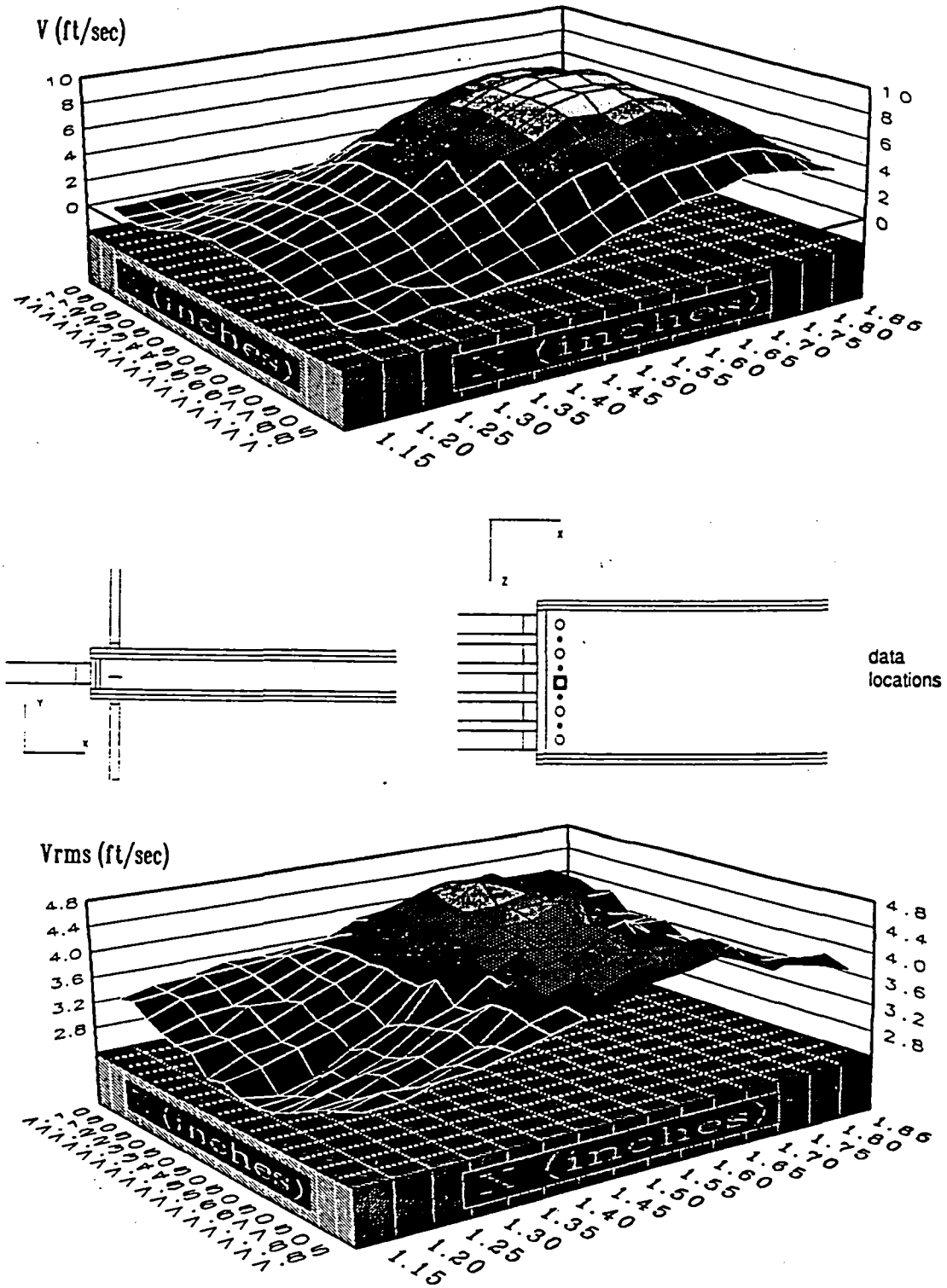

Figure 2.51 Annular and Primary Jets $\bar{V}$ and V_{rms} Distribution of the Primary Jets at Y=1.25 inches

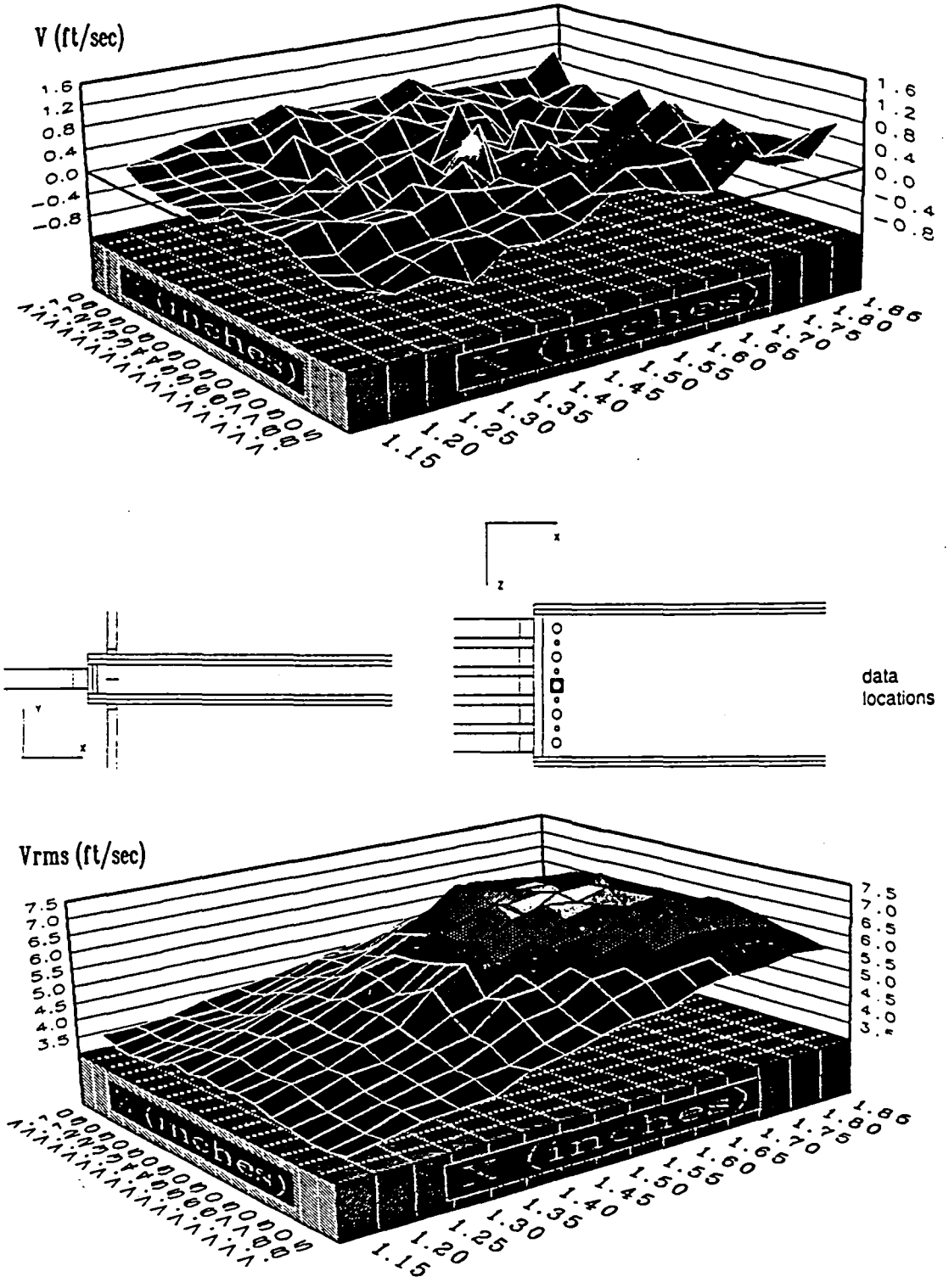

Figure 2.52 Annular and Primary Jets $\tilde{V}$ and V_{rms} Distribution of the Primary Jets at Y=1.5 inches

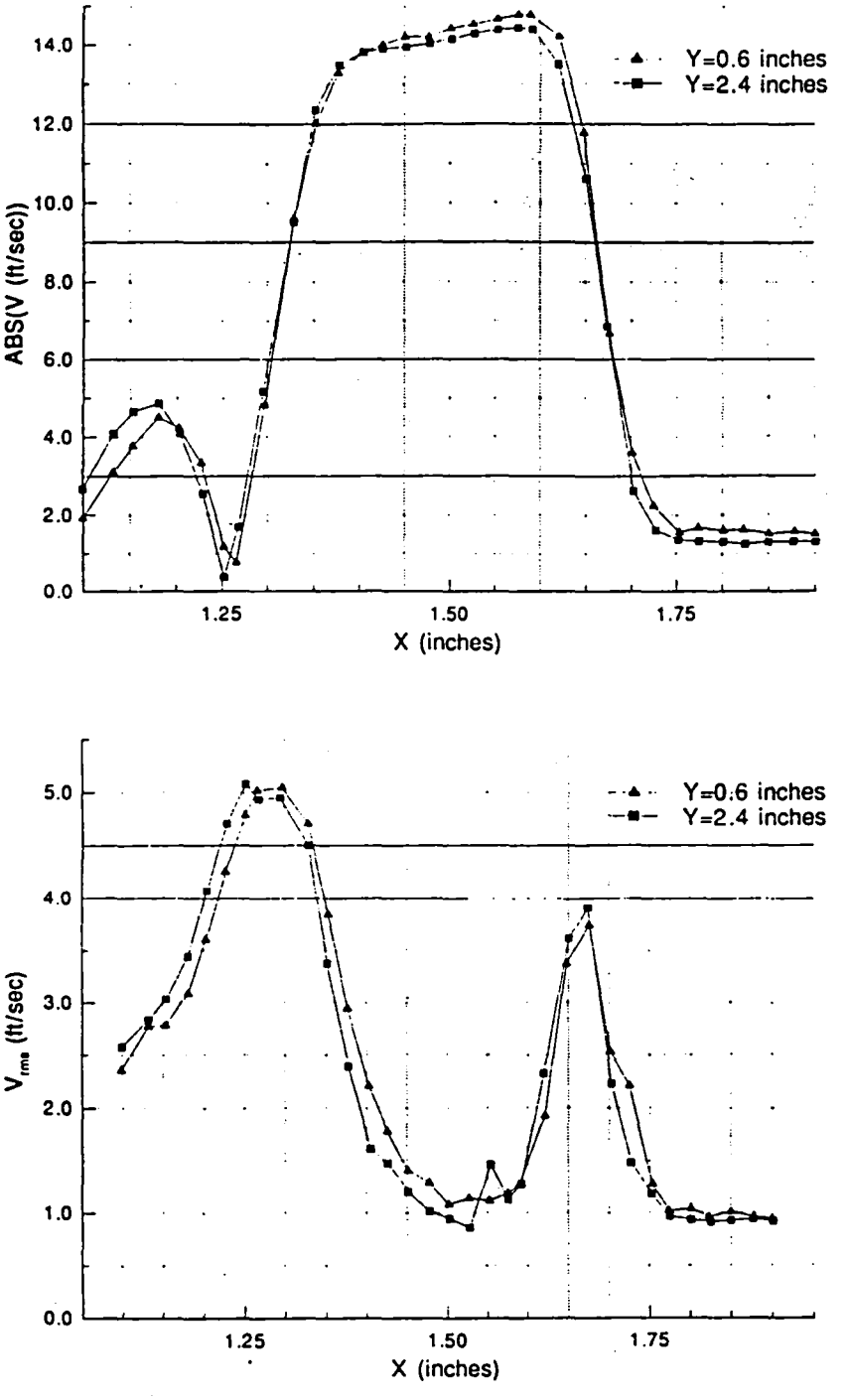

Figure 2.53 Annular and Primary Jets $\bar{V}$ and V_{rms} Distribution Comparison of the Primary Jets at Y=0.6 in. and Y=2.4 in.

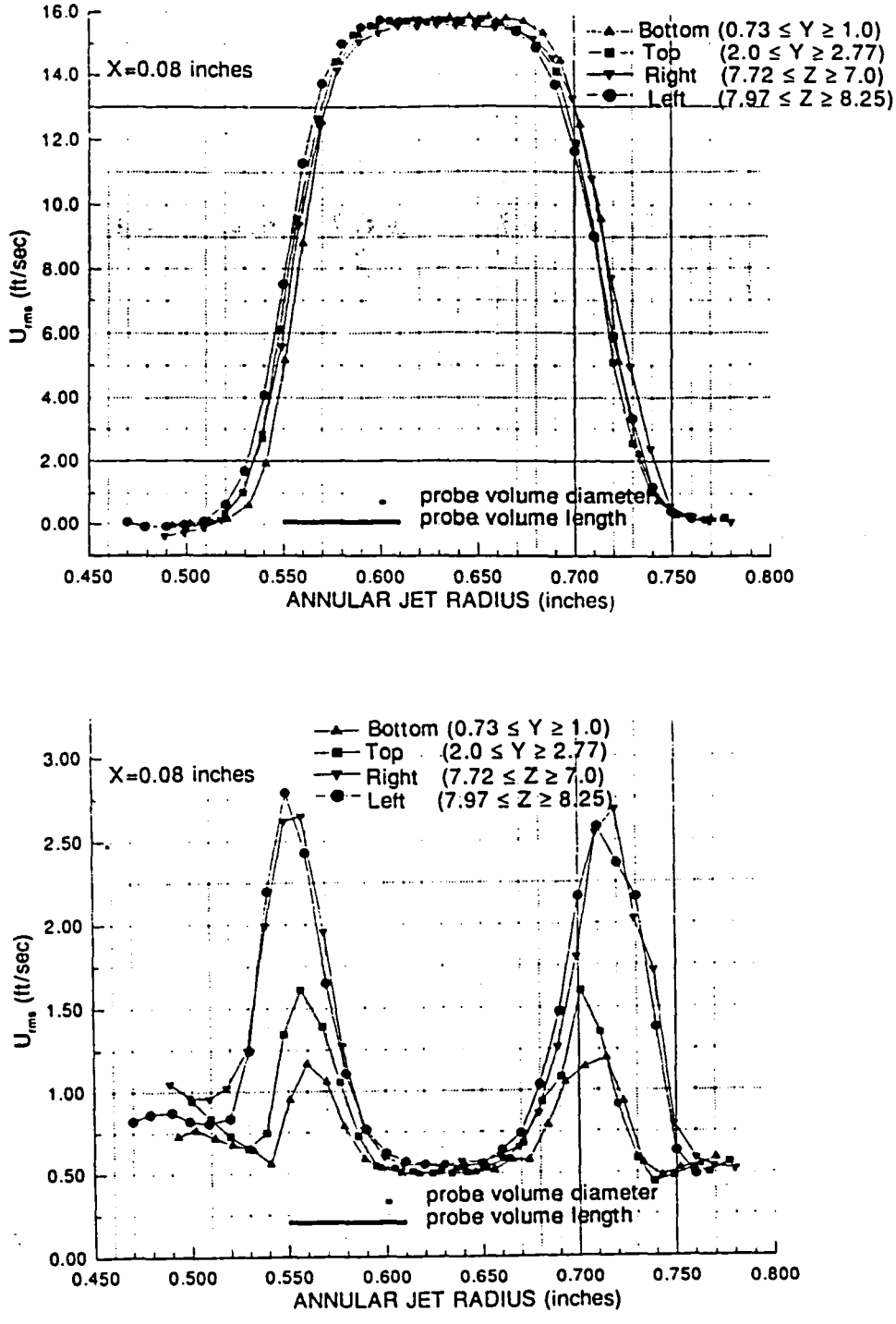

Figure 2.54 Annular and Primary Jets $\tilde{U}$ and U_{rms} Distribution of the Annular Jets at X=0.08 in.

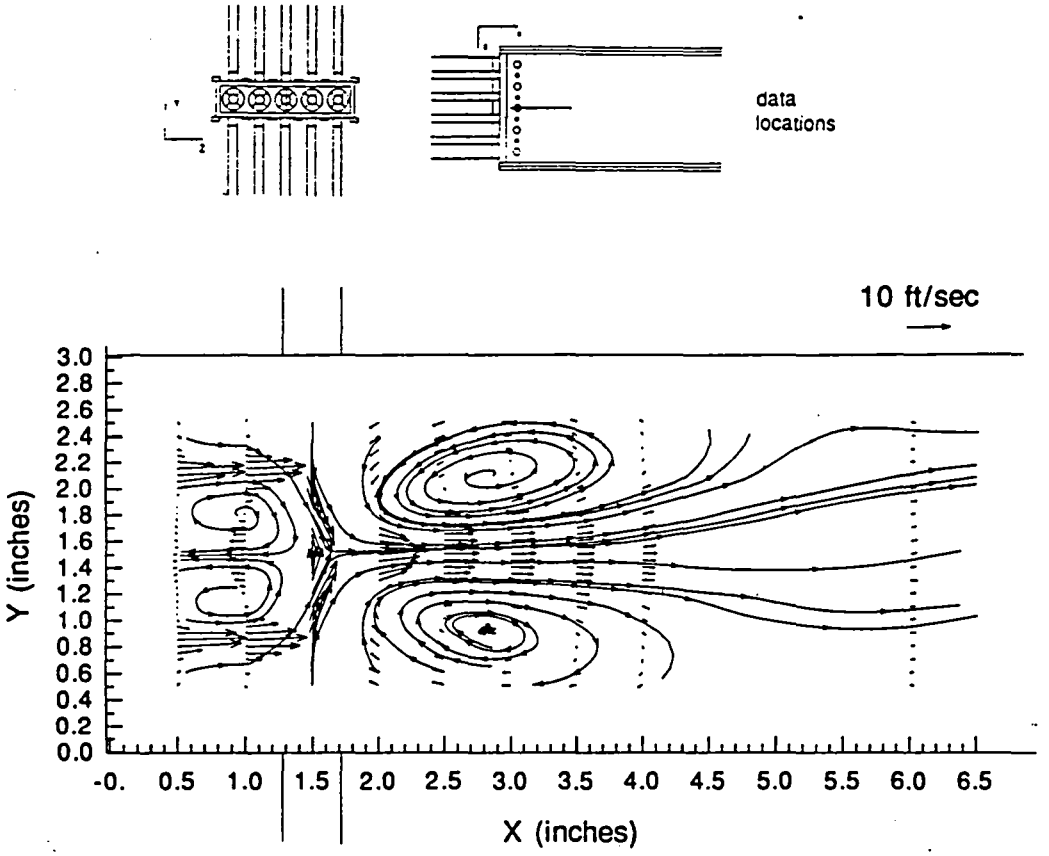

Figure 2.55 Annular and Primary Jets Mean Velocity Vector Plot at Z=7.5 in.

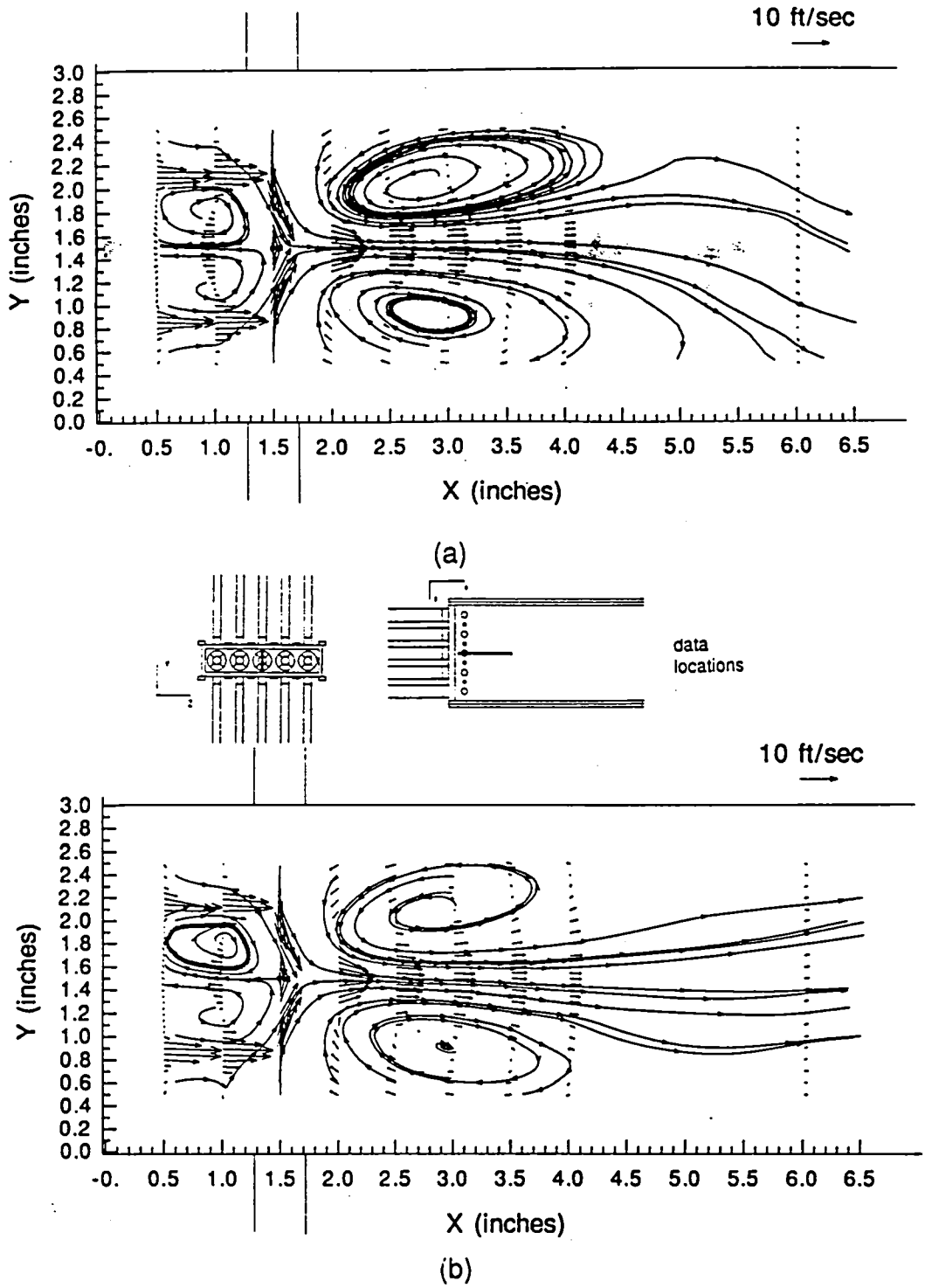

Figure 2.56 Annular and Primary Jets Mean Velocity Vector plots at a) Z=7.4 in.; b) Z=7.6 in.

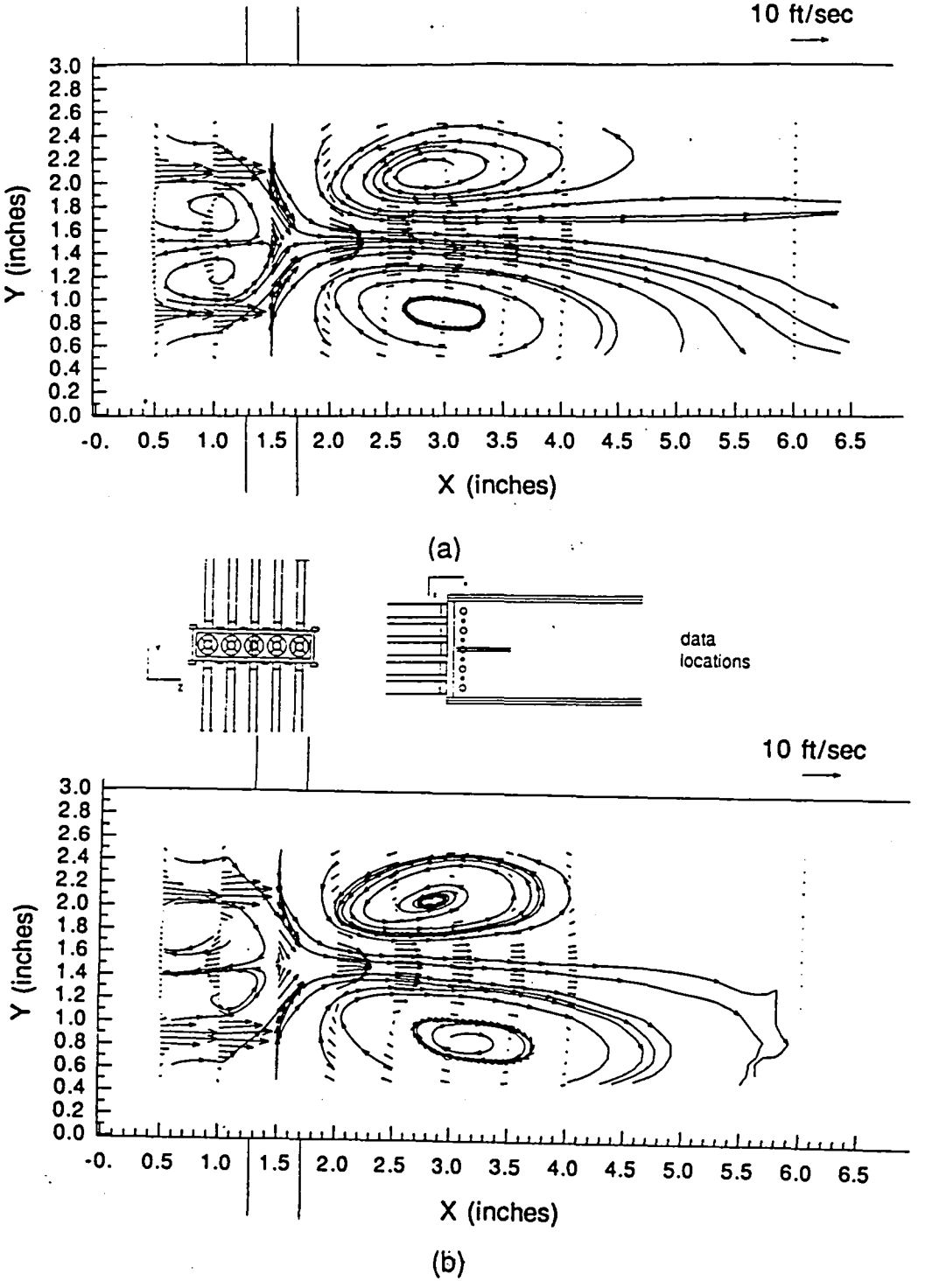

Figure 2.57 Annular and Primary Jets Mean Velocity Vector plots at a) Z=7.3 in.; b) Z=7.7 in.

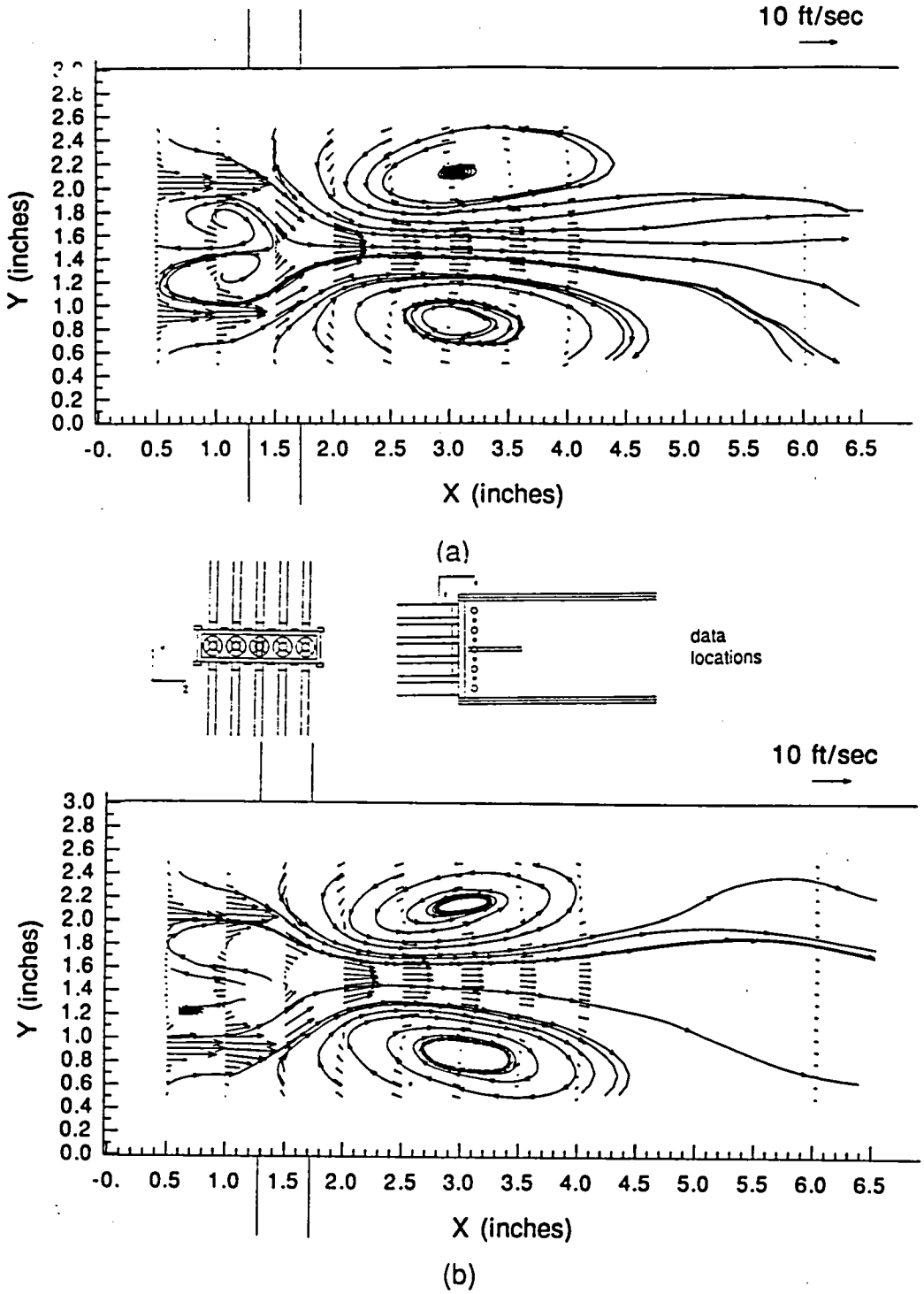

Figure 2.58 Annular and Primary Jets Mean Velocity Vector plots at a) Z=7.2 in.; b) Z=7.8 in.

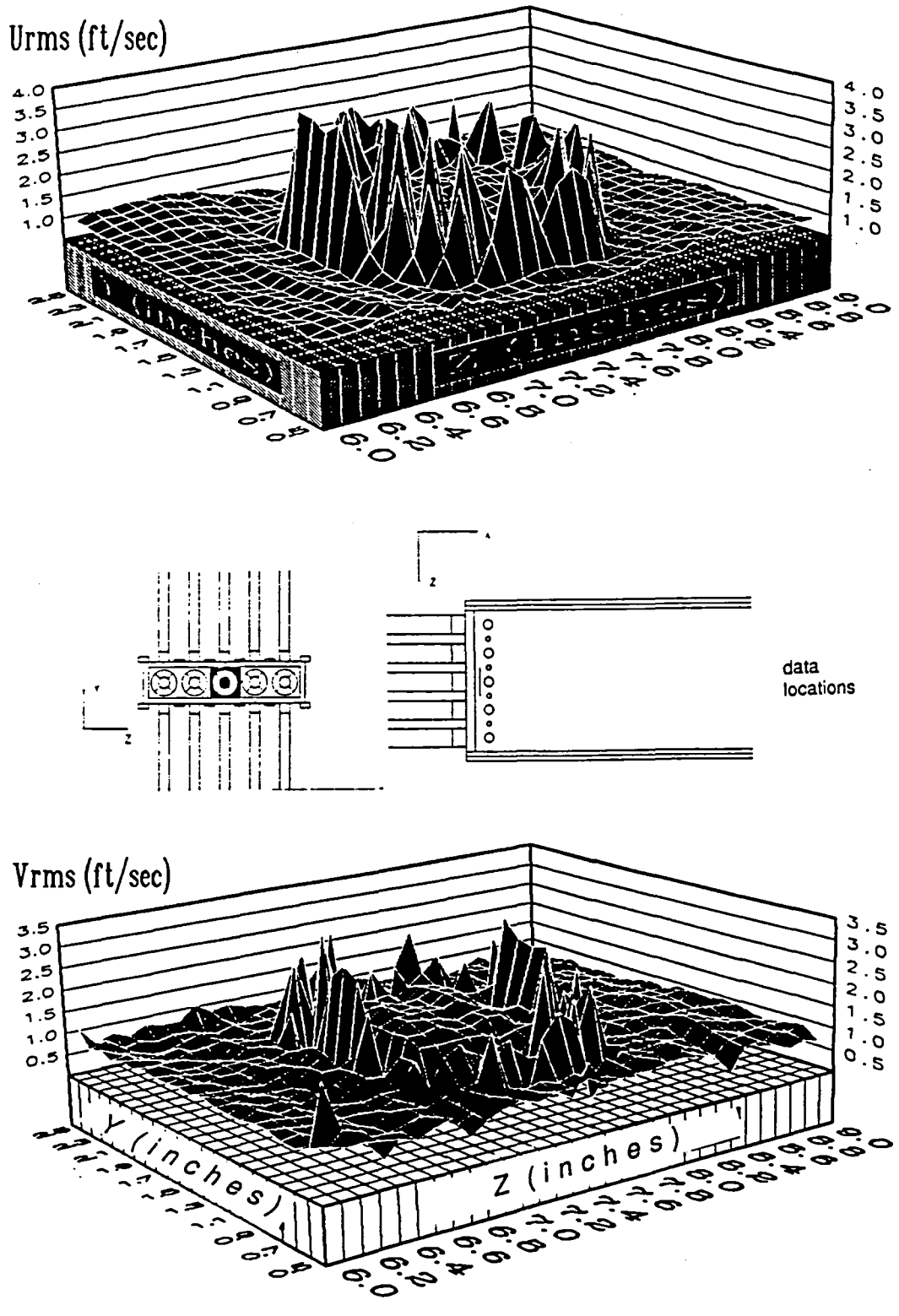

Figure 2.59 Annular and Primary Jets Contour Plot of U_{rms} and V_{rms} at X=0.5 in.

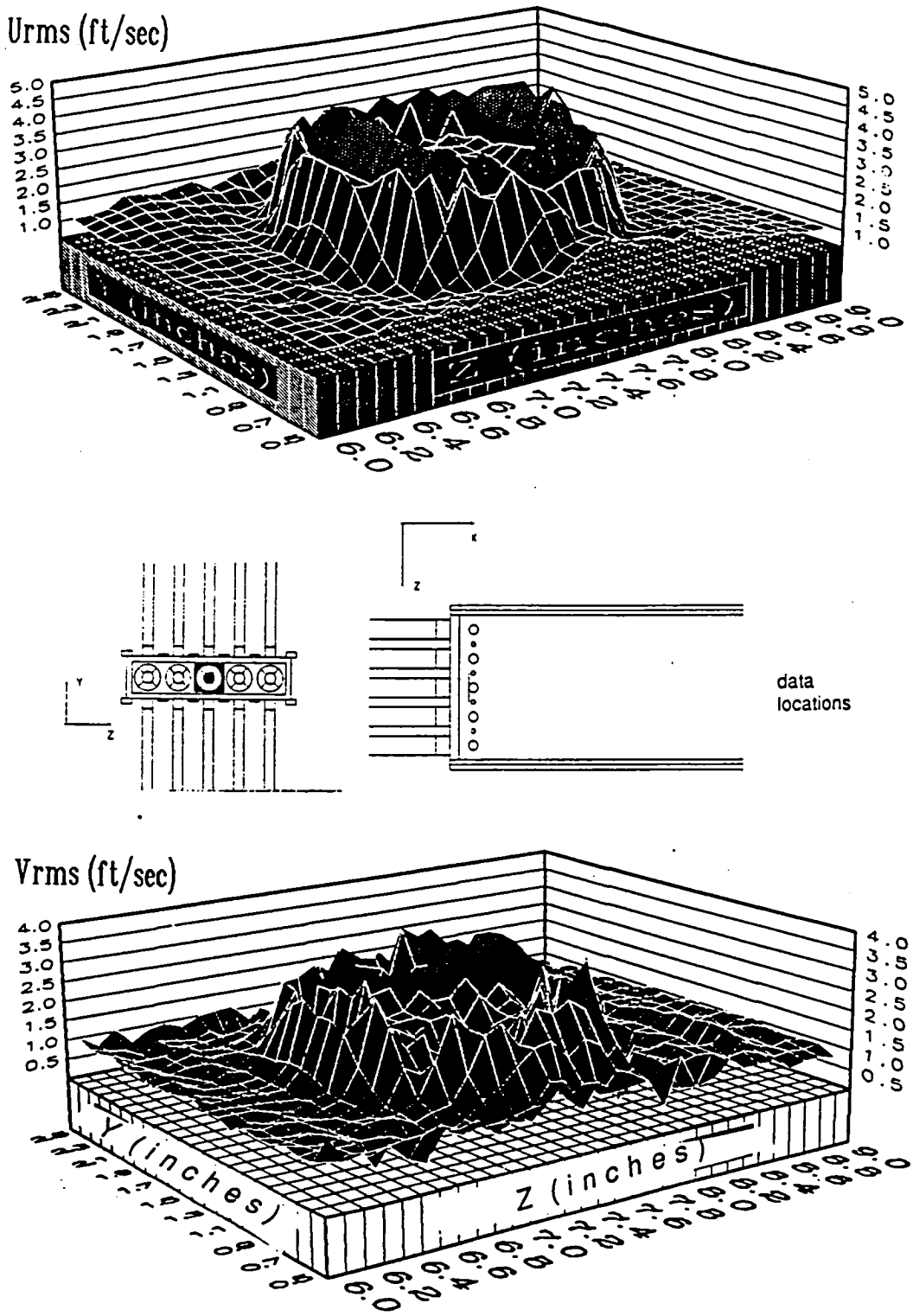

Figure 2.60 Annular and Primary Jets Contour Plot of U_{rms} and V_{rms} at X=1.0 in.

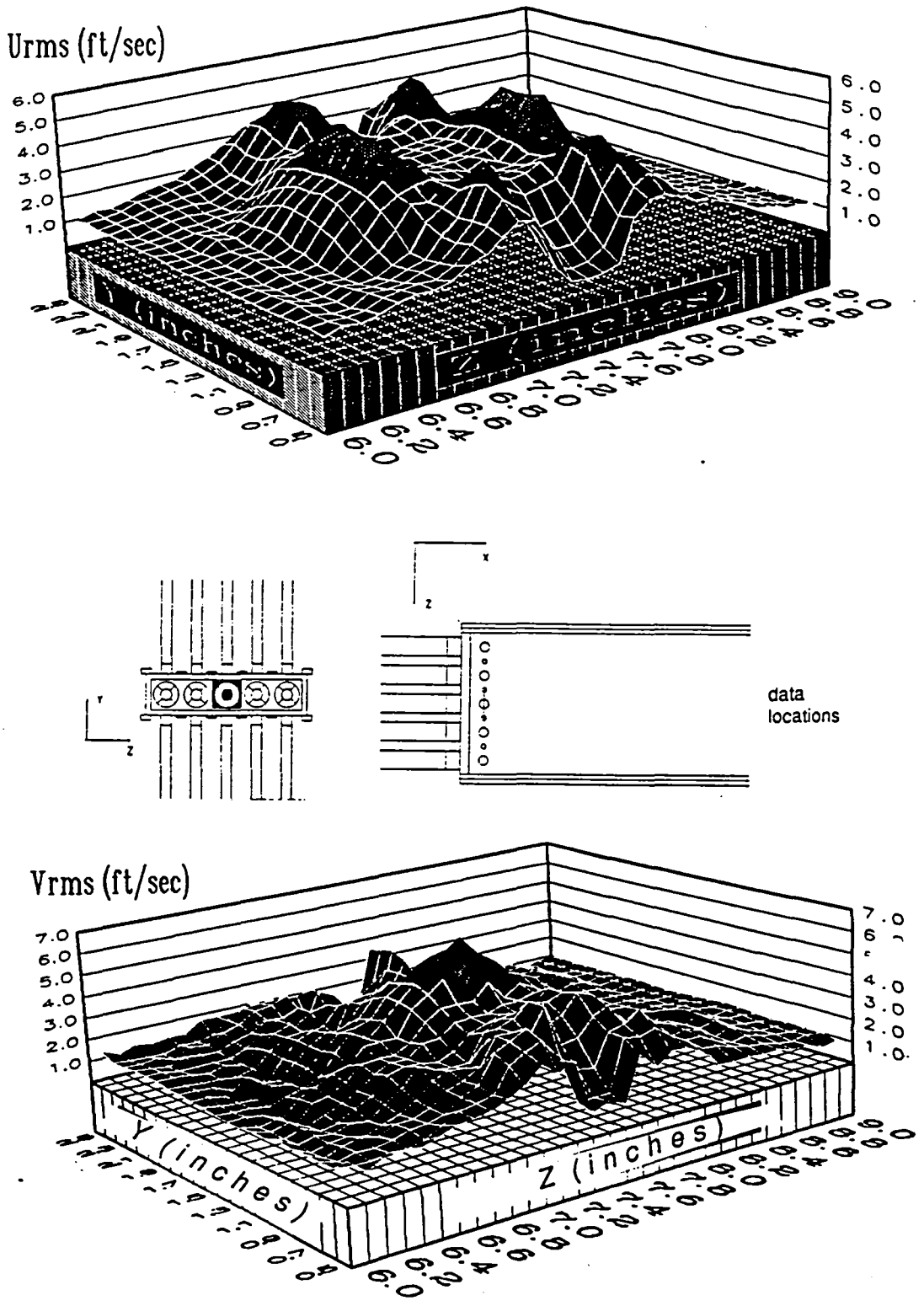

Figure 2.61 Annular and Primary Jets Contour Plot of U_{rms} and V_{rms} at X=1.5 in.

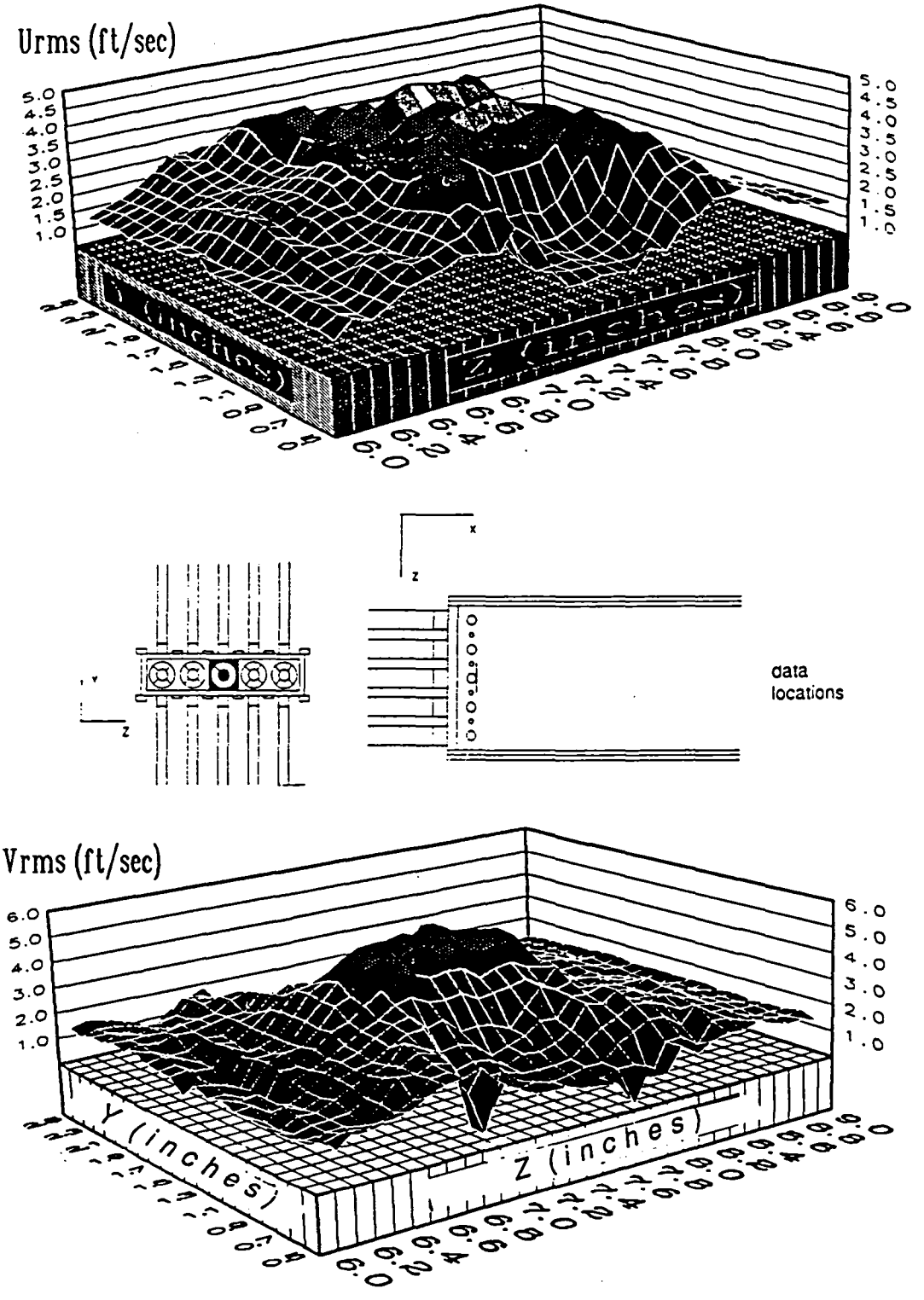

Figure 2.62 Annular and Primary Jets Contour Plot of U_{rms} and V_{rms} at X=2.0 in.

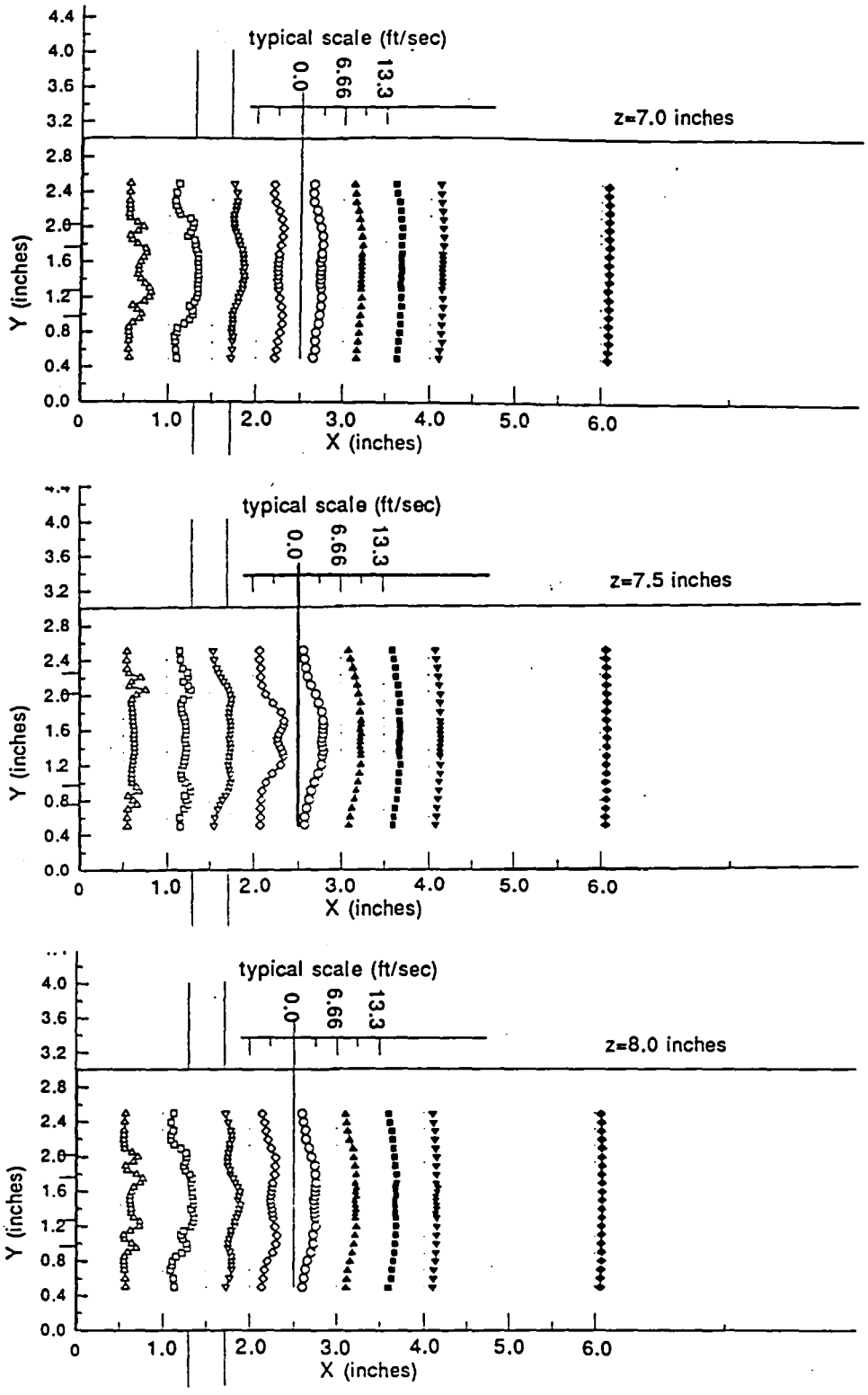

Figure 2.63 Annular and Primary Jets U_{rms} Distribution

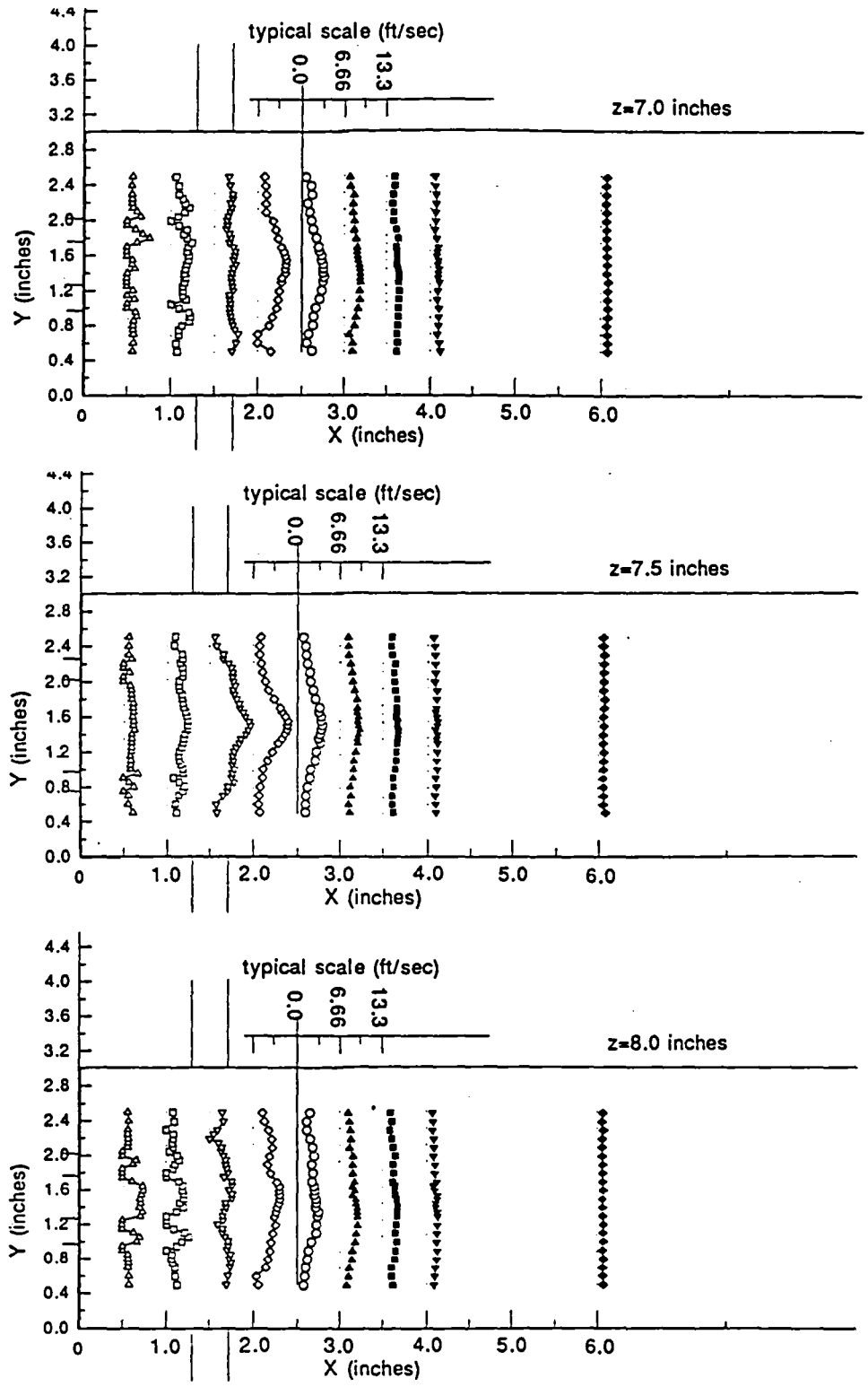

Figure 2.64 Annular and Primary Jets V_{rms} Distribution

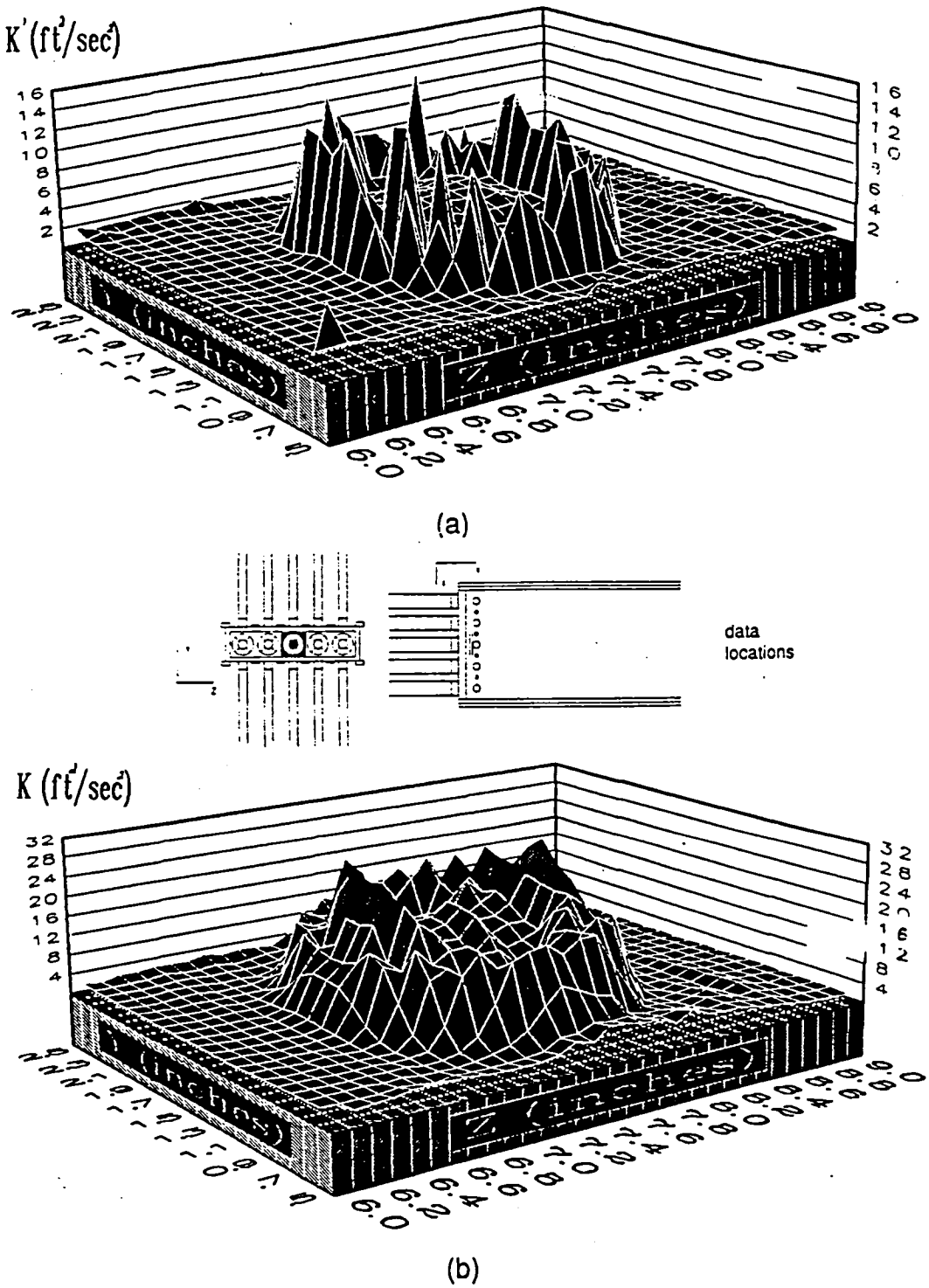

Figure 2.65 Annular and Primary Jets Contour Plot of K' at a) X=0.5 in.; b) X=1.0 in.

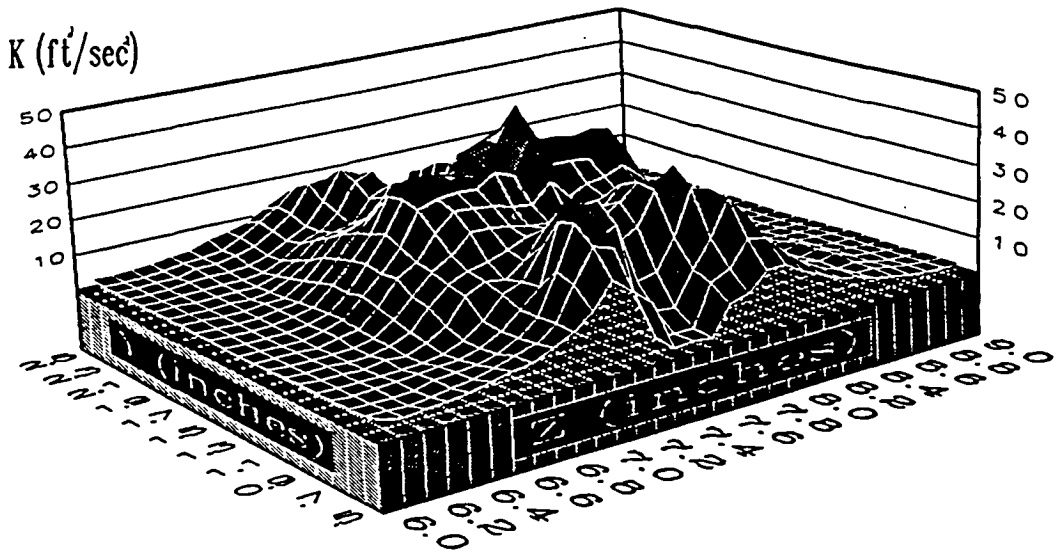

(a)

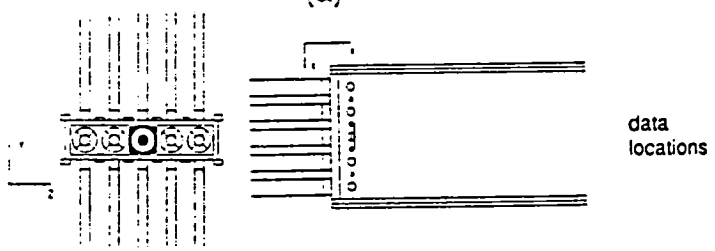

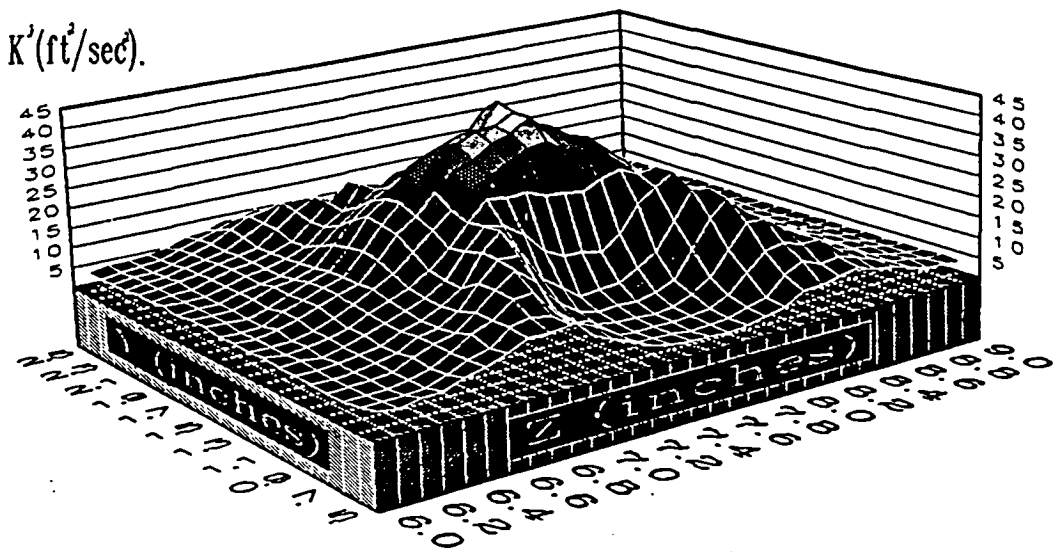

(b)

Figure 2.66 Annular and Primary Jets Contour Plot of K' at a) X=1.5 in.; b) X=2.0 in.

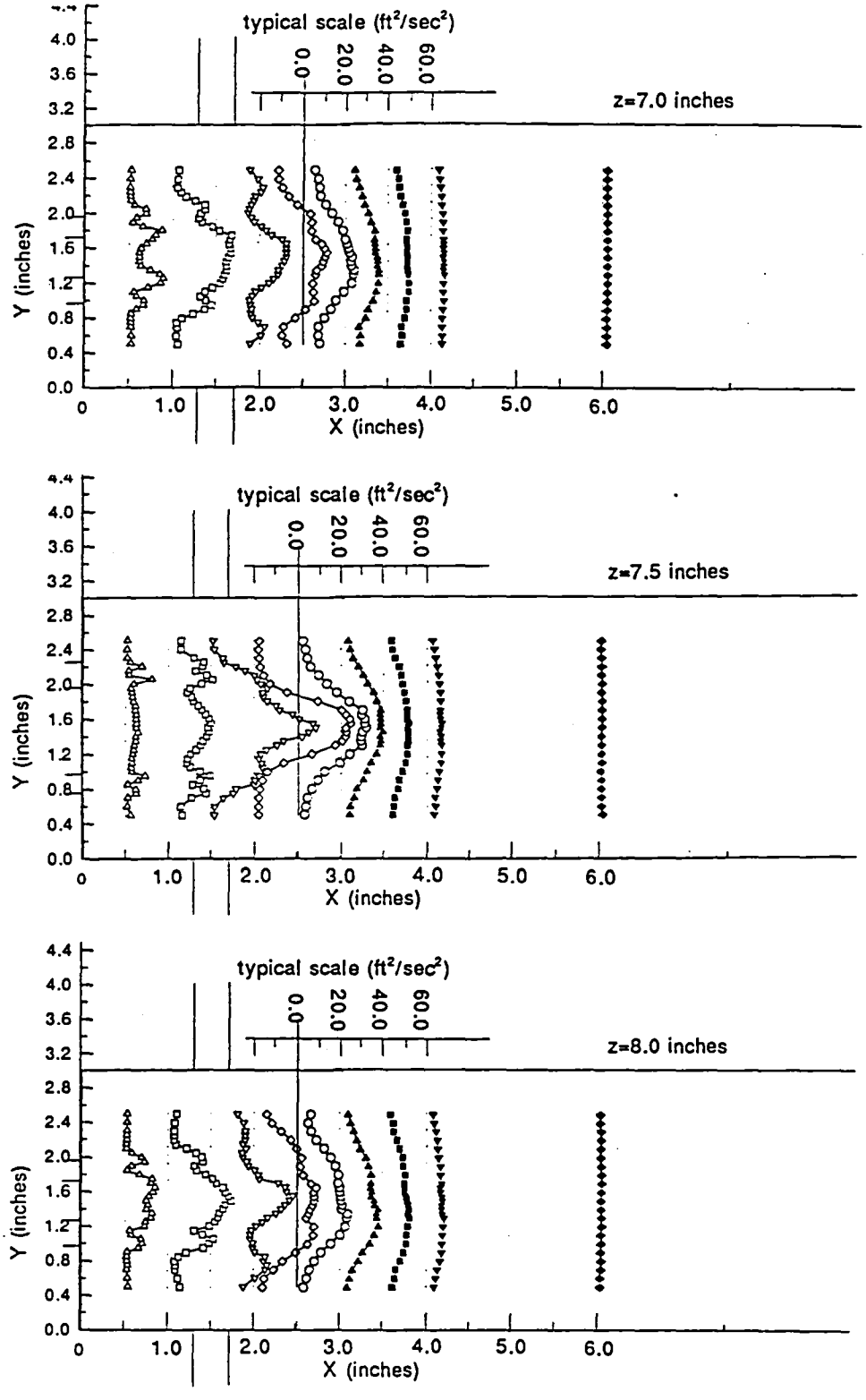

Figure 2.67 Annular and Primary Jets K' Distribution

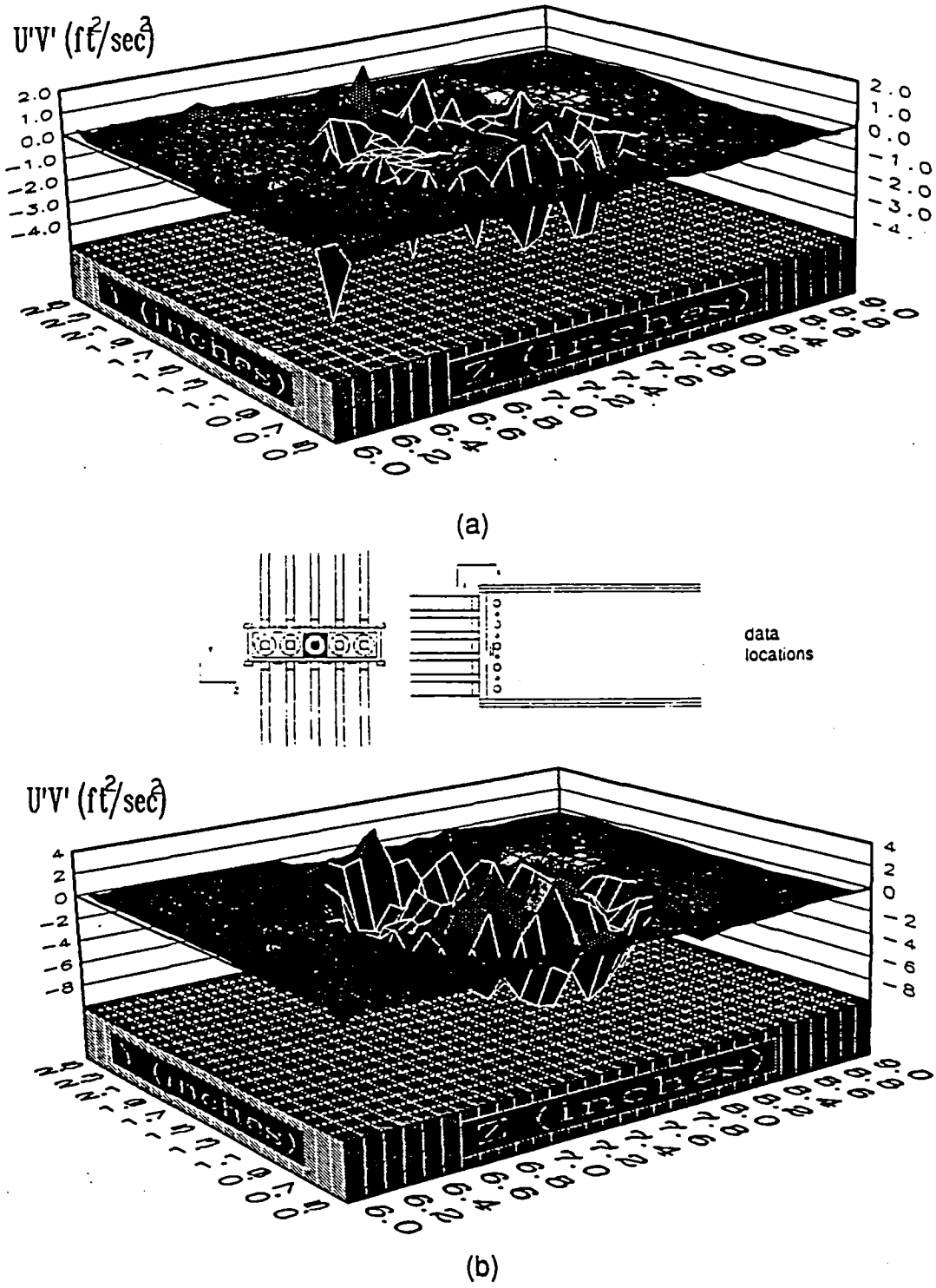

Figure 2.68 Annular and Primary Jets Contour Plot of U'V' at a) X=0.5 in.; b) X=1.0 in.

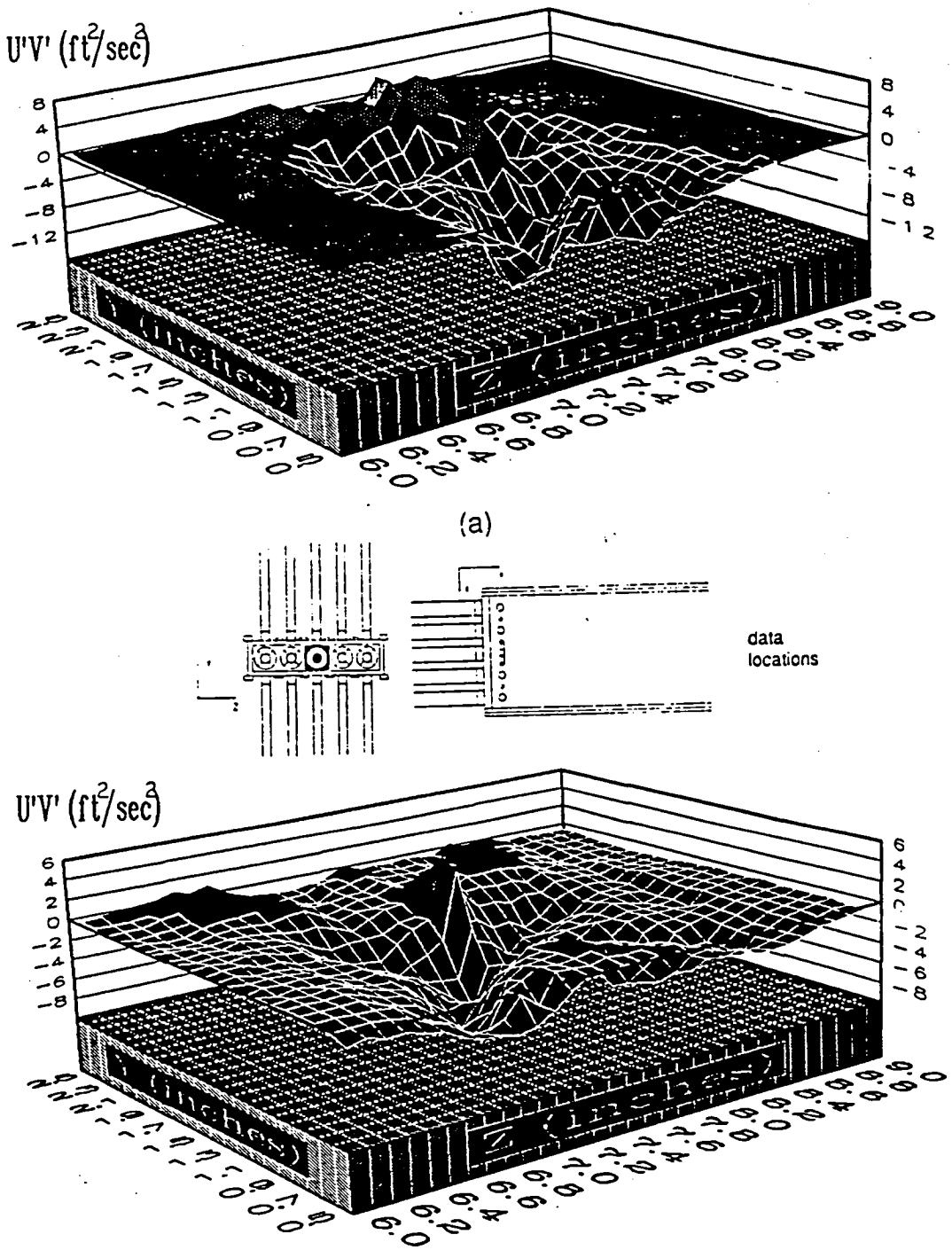

Figure 2.69 Annular and Primary Jets Contour Plot of U'V' at a) X=1.5 in.; b) X=2.0 in.

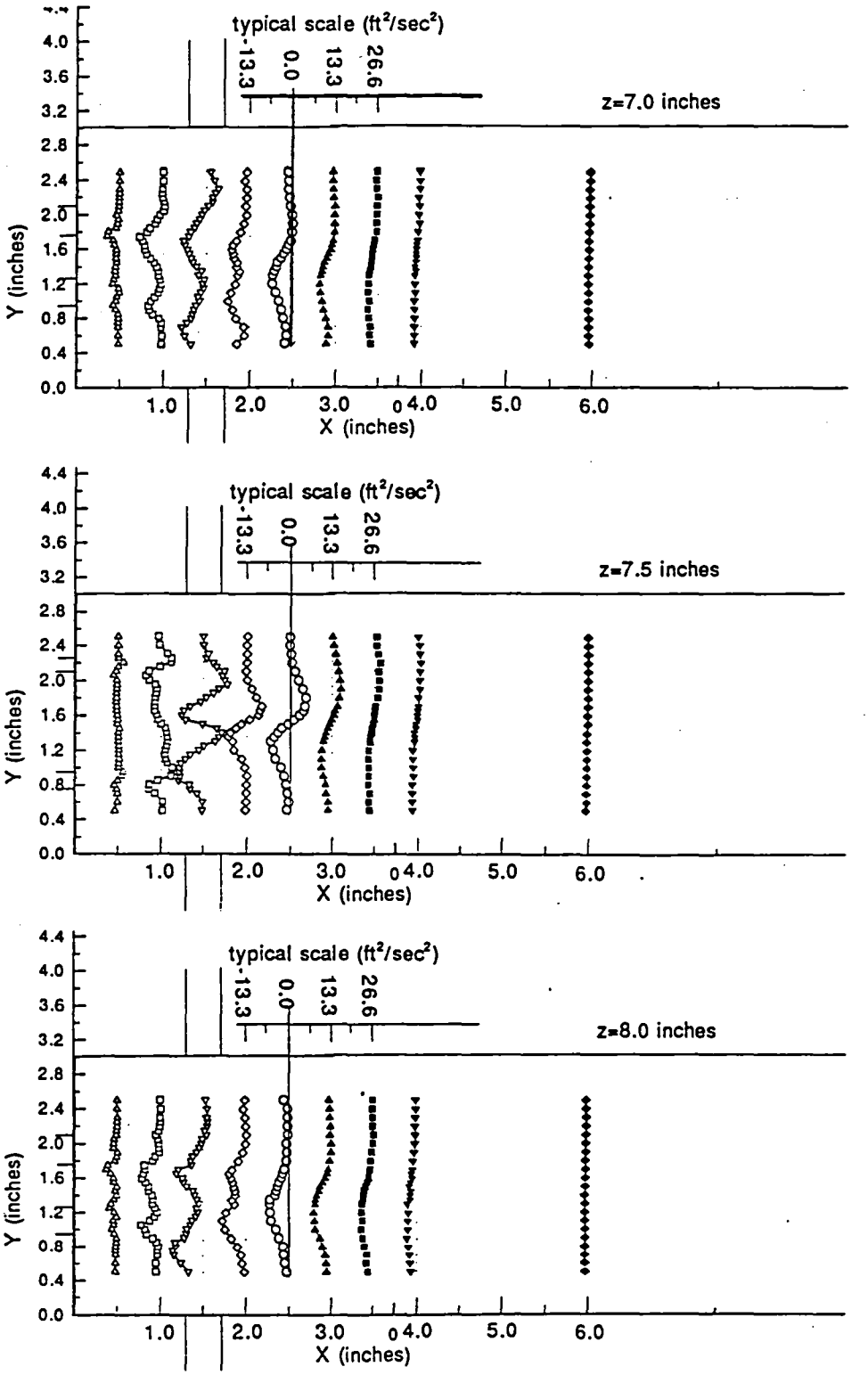

Figure 2.70 Annular and Primary Jets U'V' Distribution

CHAPTER 3

SCALAR CONCENTRATION MEASUREMENTS

The technique called marker nephelometry was used to obtain scalar concentration values for the three different geometries of the combustor model investigated earlier. For a more extensive review of the technique see reference [16] or references [7&8], which used similar data processing equipment that was used for this study.

3.1 Primary Jets Only

Marker particles were introduced into the combustor model through the lower primary jet for this case. Data collected for this case will provide qualitative information about the mixing of the two primary jets.

Results for the primary jets only case are presented in figures 3.1-3.12. Mean concentration values were obtained by averaging 127 frames of images of the XY plane. Figures 3.1 & 3.2 are single and 127 frame averages of images taken at Z=7.5 inches. The spread at the impingement region is less visible in the average picture due to oscillations of this region above and below the centerline. By averaging, the observable oscillations are reduced. Pictures in figures 3.3-3.6 are .5 inches from the rig centerplane. The spreading of the jet impingement point

can clearly be seen in all of the pictures due to spreading of smoke in the XZ plane. The turbulent nature of the flow is evident by the difference between single and averaged frame pictures. Symmetry should exist between averaged frames since each is the same distance from the rig centerplane.

Figures 3.7-3.12 present three dimensional and line plots of the concentration inside the rig. The line plots are taken at stations of constant X from the lower to upper wall of the rig. At Z=7.5 in., the smoke entering the lower primary jet enters the rig up to the stagnation point with the opposing jet. Smoke is moved upstream and downstream by the jet stagnation point spreading radially in the XZ plane. The line plots indicate that concentrations between upper and lower walls increase farther downstream and show a peak concentration near the rig centerline. Moving .5 inches away from the Z=7.5 in. plane, Z=7.0 and 8.0 in., line plots show an increased minimum concentration level at stations upstream and downstream of the primary jets. Peak concentrations still exist near the rig centerline at Y=1.5 inches. A peak can also be seen in the 3D plots near X and Y =1.5 inches due to the spreading of the smoke from the stagnation regions of the primary jets in the XZ plane. Even farther away from the centerplane, Z=6.5 and 8.5 in., the concentration levels spread out even more with peak values slightly above the rig centerline. As the smoke becomes completely mixed with air entering the upper primary jet, concentration levels are nearly equal from bottom to top walls of the rig downstream of X=1.0 in..

Figure 3.12 shows a line plot comparing concentrations along the primary jet axis of the different Z planes measured. Planes equal distance from the center plane, Z=7.5 in., should be symmetric due to rig symmetry. Planes at Z=6.5 and 7.0 in. have peak concentrations placed closer to the upper wall of the rig than planes at Z=8.0 and 8.5 inches. A flapping motion of the stagnation region was observed in the XY plane. This behavior was also observed by Miau, Sun, and Yao in reference [5]. This flapping motion should also be present in the YZ plane if symmetry is valid, and if more pronounced may cause a tilt of the stagnation region. Sivasgaram and Whitelaw, reference [3], investigated the effect of geometric asymmetries in opposing jets and found that this stagnation region was very sensitive to geometry. Therefore, any slight misalignment in the jet could cause these asymmetries to arise.

3.2 Annular Jets Only

For the annular jets only case, no qualitative information can be collected from the data since all air entering the model was mixed with seed particles. The pictures here do aid in flow visualization.

Pictures for the annular jets only case are presented in figures 3.13-3.18. Single and 127 frame averages of the XY plane at Z=7.5 in. are seen in figures 3.13 & 3.14. Smoke entering the annular jet is seen to close behind the center portion of the annular jet and travel downstream. Recirculation zones behind the center portion of the annular jet and along the upper and lower walls are present.

The pictures at Z=7.0 and 8.0 inches have larger recirculation zones along the upper and lower walls.

3.3 Annular and Primary Jets

For the annular and primary jets case marker particles were introduced into the combustor model through the annular jets only and through the lower primary jet. This will allow the observation of the mixing between the annular and primary jets.

3.3.1 Smoke in Primary Jets

Results for smoke in the lower primary jet with annular jet flow are in figures 3.19-3.30. Figures 3.19 & 3.20 show single and 127 frame average at Z=7.5 inches. The effect of the annular jet can be seen by the bending of the flow from the primary jets downstream. The single frame picture has higher concentrations of smoke from the lower primary jet downstream than the averaged picture, thus demonstrating the unsteadiness of the flow. Planes at Z=7.0 and 8.0 inches, figures 3.21-3.24, higher concentrations of smoke are seen in the corners and along the upper and lower walls in the averaged pictures. Similarity between planes is also seen demonstrating symmetry.

Three dimensional and line plots of the mean concentration are in figures 3.25-3.30. At Z=7.5 inches, the influence of the annular jet on the primary jets is clearly apparent. Most of the smoke entering from the primary jet is pushed downstream with very little smoke being mixed upstream of the upper primary jet.

Comparisons with figure 3.7, with no annular flow, concentration levels of five to six times larger exist in the same area. Downstream of the primary jets, concentration profiles between the upper and lower walls smooth out with peak values on the lower side of the centerline. As the planes move farther away from the centerplane, the maximum concentration levels occur just above the rig centerline. Concentration levels along the upper half of the rig for X < 1.5 inches remain relatively small compared to the levels when no annular jet flow is used in figures 3.7-3.11.

Figure 3.30 presents a comparison of concentration profiles along the primary jet axis for Z=6.5 to 8.5 inches. Symmetry between planes at Z=7.0 and 8.0 inches and Z=6.5 to 8.5 inches is seen to exist with the largest deviation between the plots along the upper wall of the rig. Comparison with figure 3.12, with no annular jet flow, shows reduced concentration levels in the middle and upper half of the rig when the annular jet is on.

3.3.2 Smoke in Annular Jet

Results for smoke entering the annular jet with primary jets on is in figures 3.31-3.41. Single frame and 127 frame averages for the Z=7.5 in plane are in figures 3.31 & 3.32. Single and average frames are similar in appearance. Higher concentrations downstream of the primary jets is present for the single frame picture, while the average picture has a more uniform distribution between walls. At Z=7.0 and 8.0 inches, figures 3.33-3.36, the average frames show higher

concentrations in the corners and along the upper and lower walls of the rig, similar to when smoke was in the primary jets.

Mean concentrations are plotted in figures 3.37-3.41 with smoke in the annular jet. From the Z=7.5 in. plane, the annular jet flow has a flat concentration distribution between upper and lower walls, up to the primary jet entrance. The smoke is then squeezed between the primary jets and gradually spreads out between upper and lower walls downstream. Farther from the centerplane, the concentration distribution flattens out. Distributions in the Z=7.0 and 8.0 in. planes have constant values near the walls and flat top profiles across the annular jet inlet upstream of the primary jets. At Z=6.5 and 8.5 in. this is not seen, and higher concentrations are downstream of X=1.5 inches. Higher concentrations exist on the upper than lower walls in all these plots, possibly indicating nonuniform smoke in the annular jet or gaussian beam effects in the laser sheet.

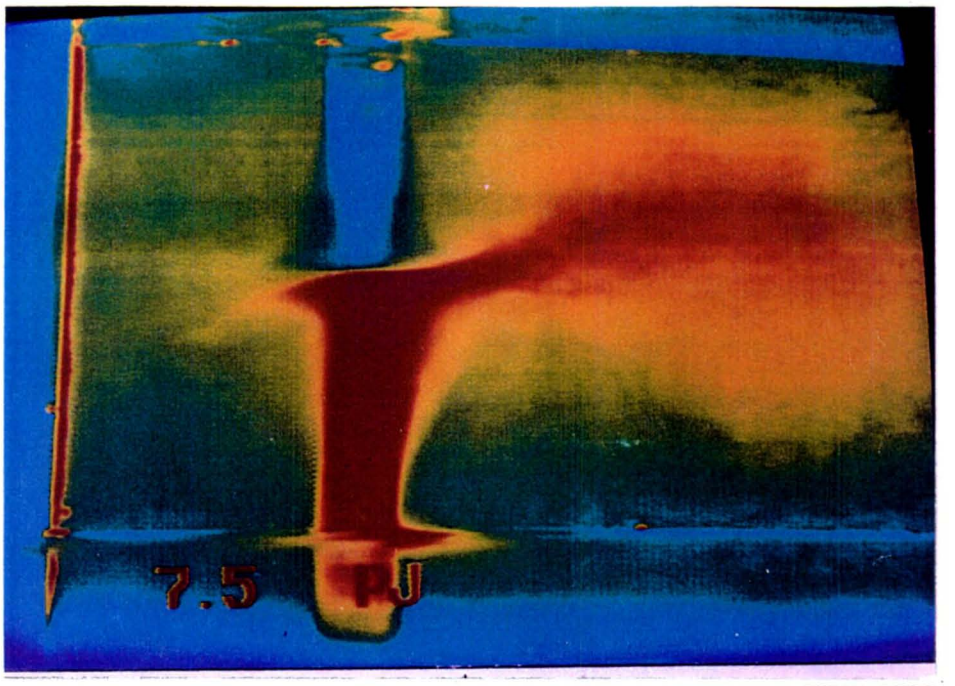

TE92-2590

Figure 3.1 Primary Jets Only Single Frame Picture, Z=7.5 inches

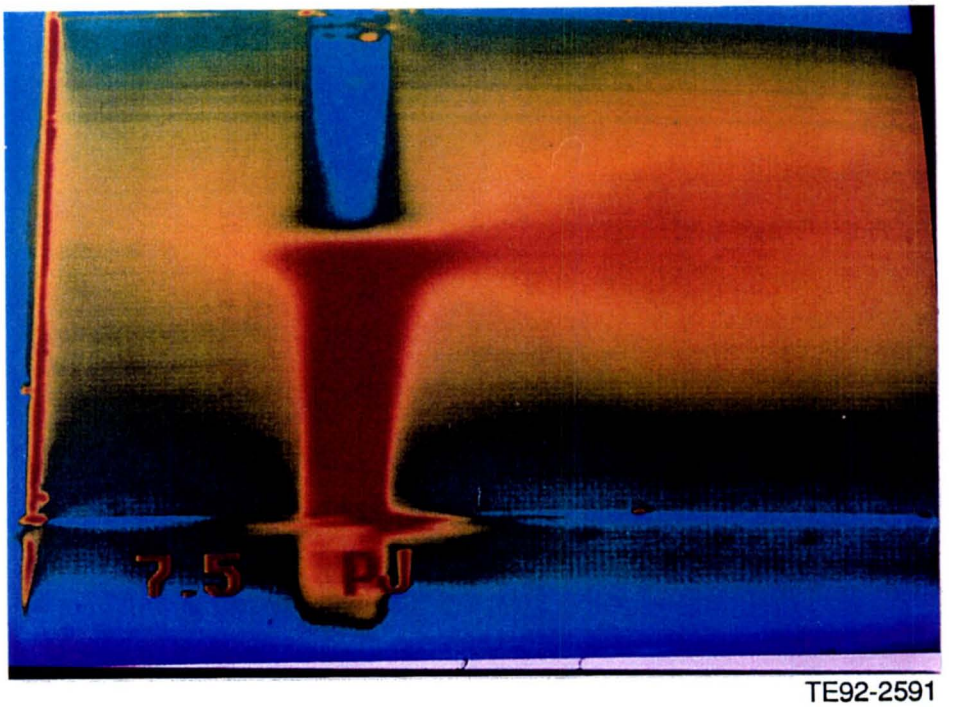

TE92-2591

Figure 3.2 Primary Jets Only 127 Frame Average, Z=7.5 inches

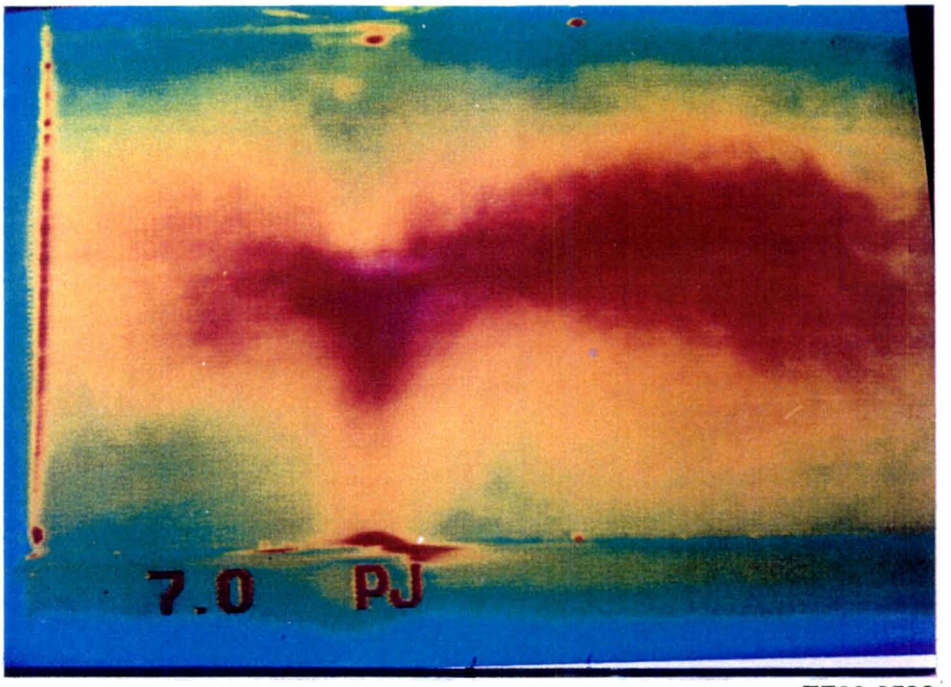

TE92-2592

Figure 3.3 Primary Jets Only Single Frame Picture, Z=7.0 inches

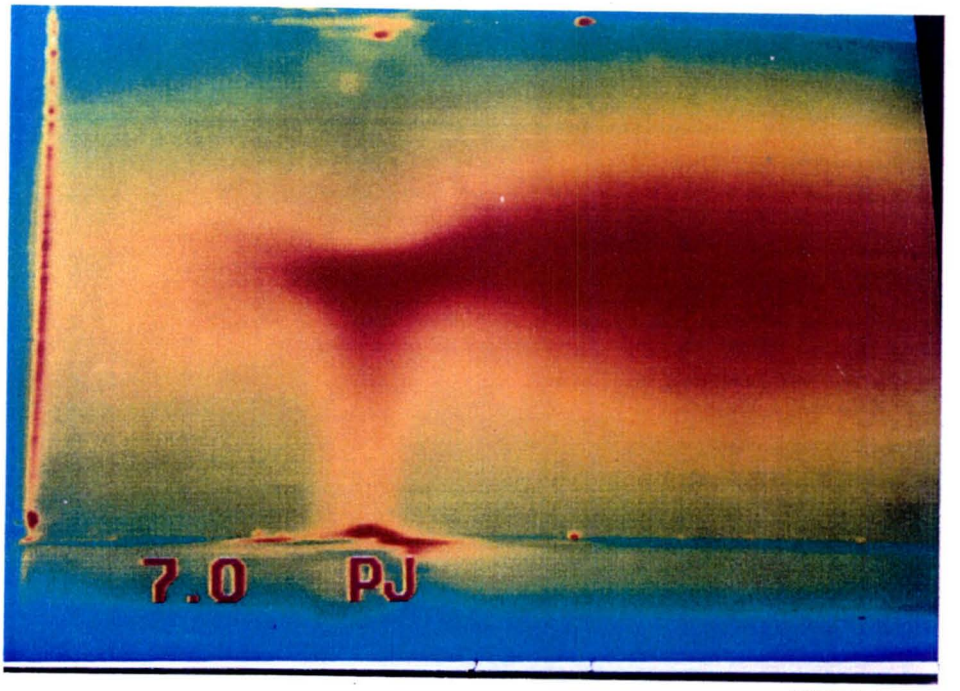

TE92-2593

Figure 3.4 Primary Jets Only 127 Frame Average, Z=7.0 inches

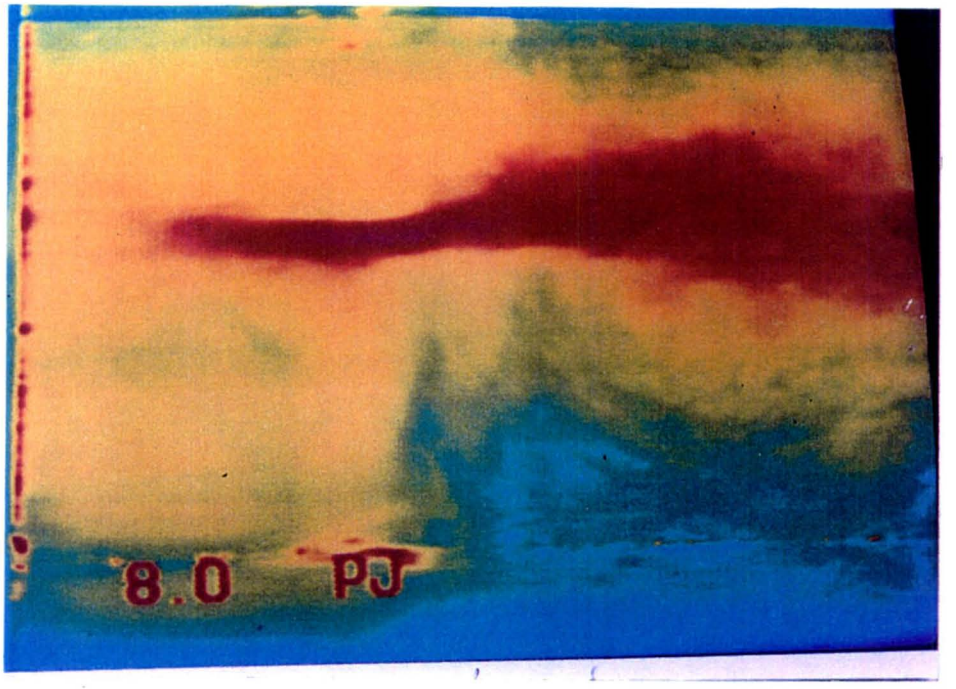

TE92-2594

Figure 3.5 Primary Jets Only Single Frame Picture, Z=8.0 inches

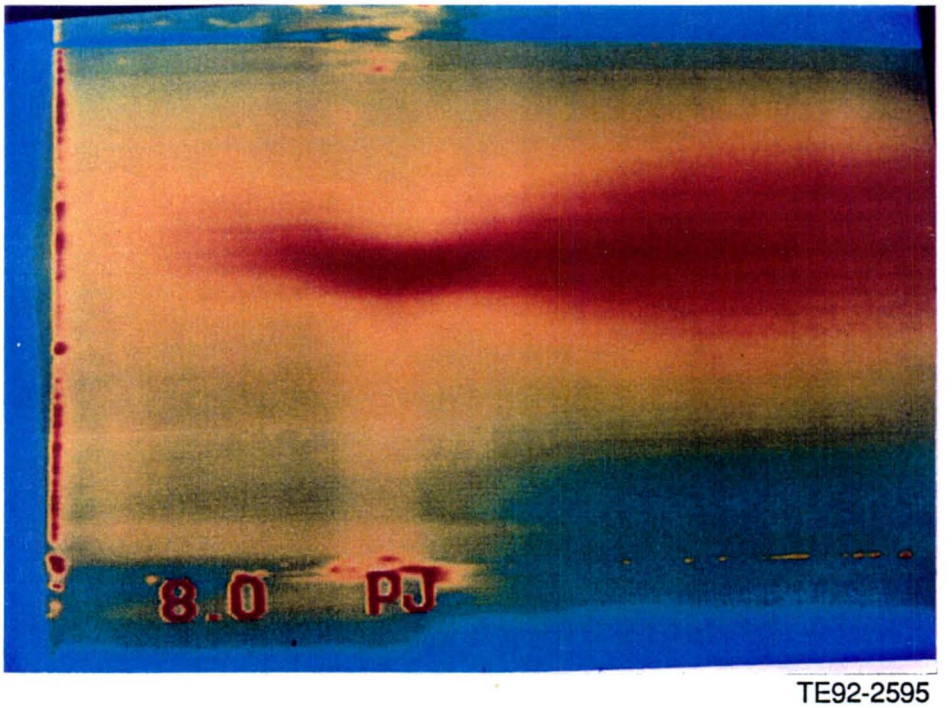

TE92-2595

Figure 3.6 Primary Jets Only 127 Frame Average, Z=8.0 inches

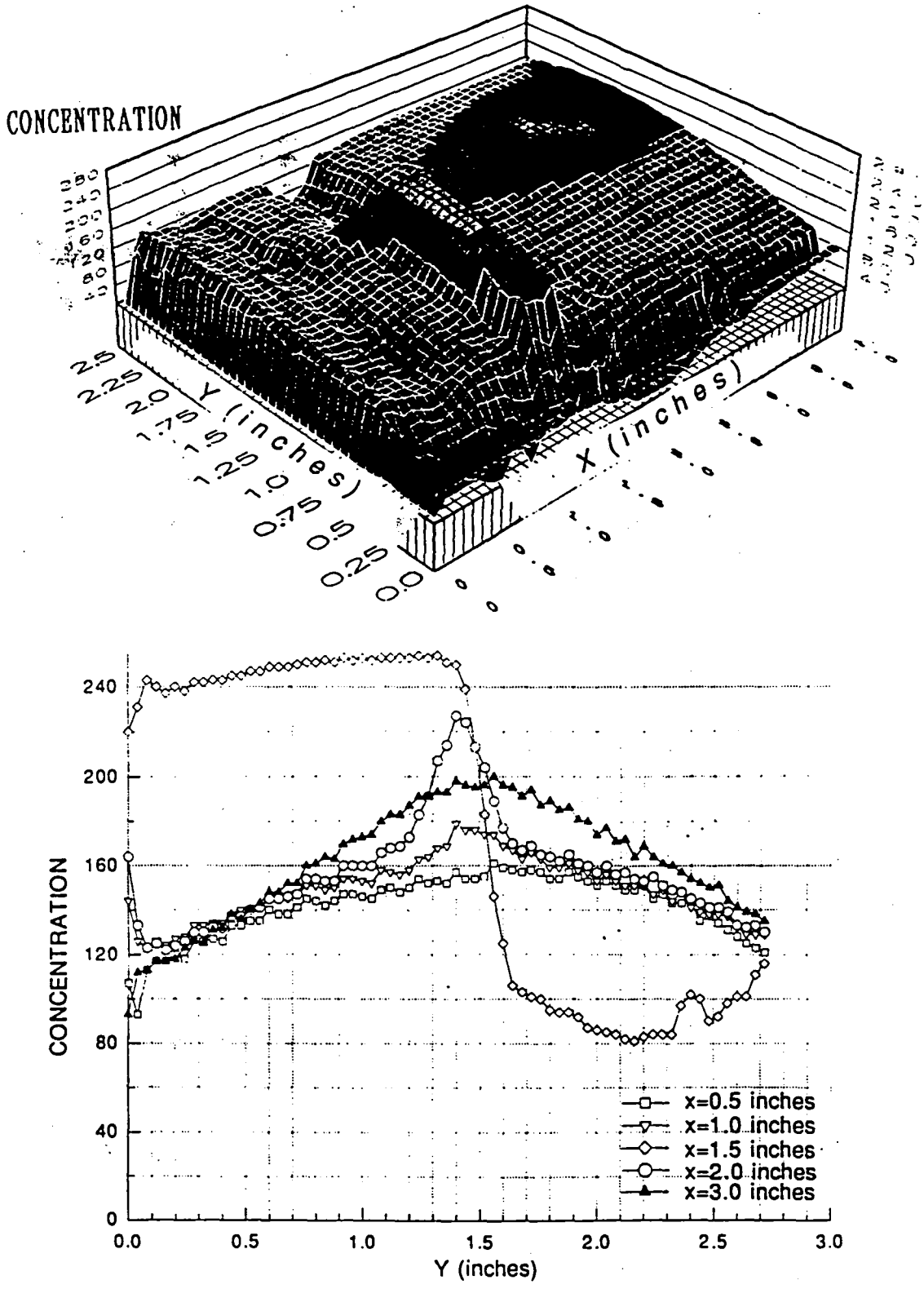

Figure 3.7 Primary Jets Only Mean Concentration Distribution, Z=7.5 inches

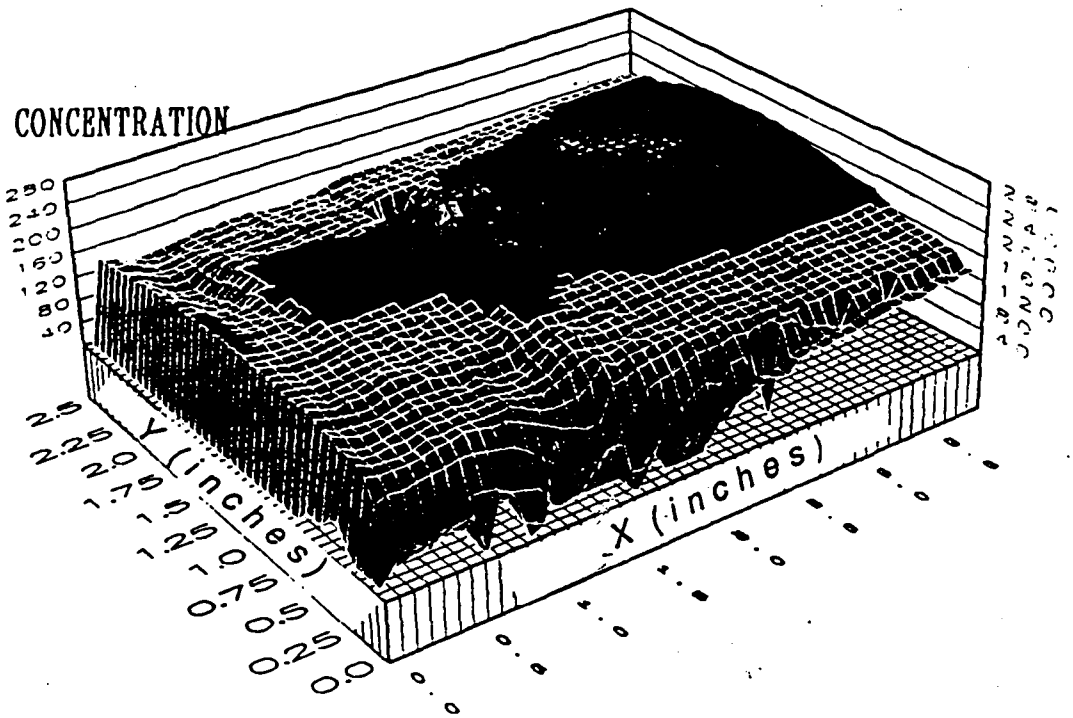

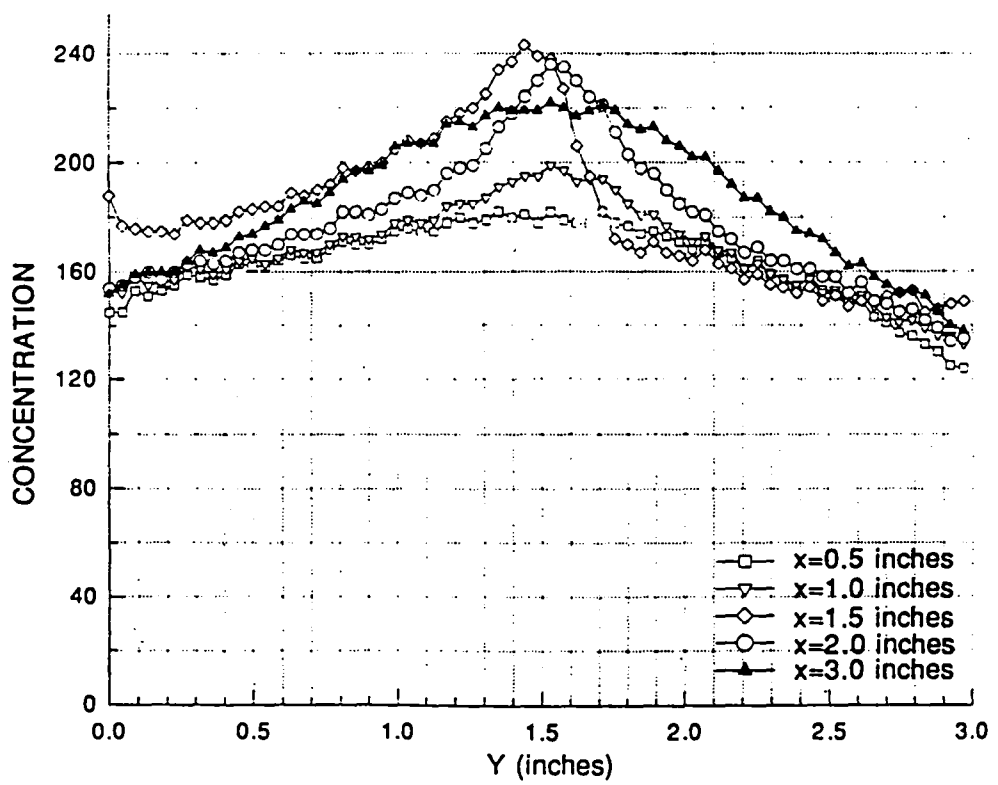

Figure 3.8 Primary Jets Only Mean Concentration Distribution, Z=7.0 inches

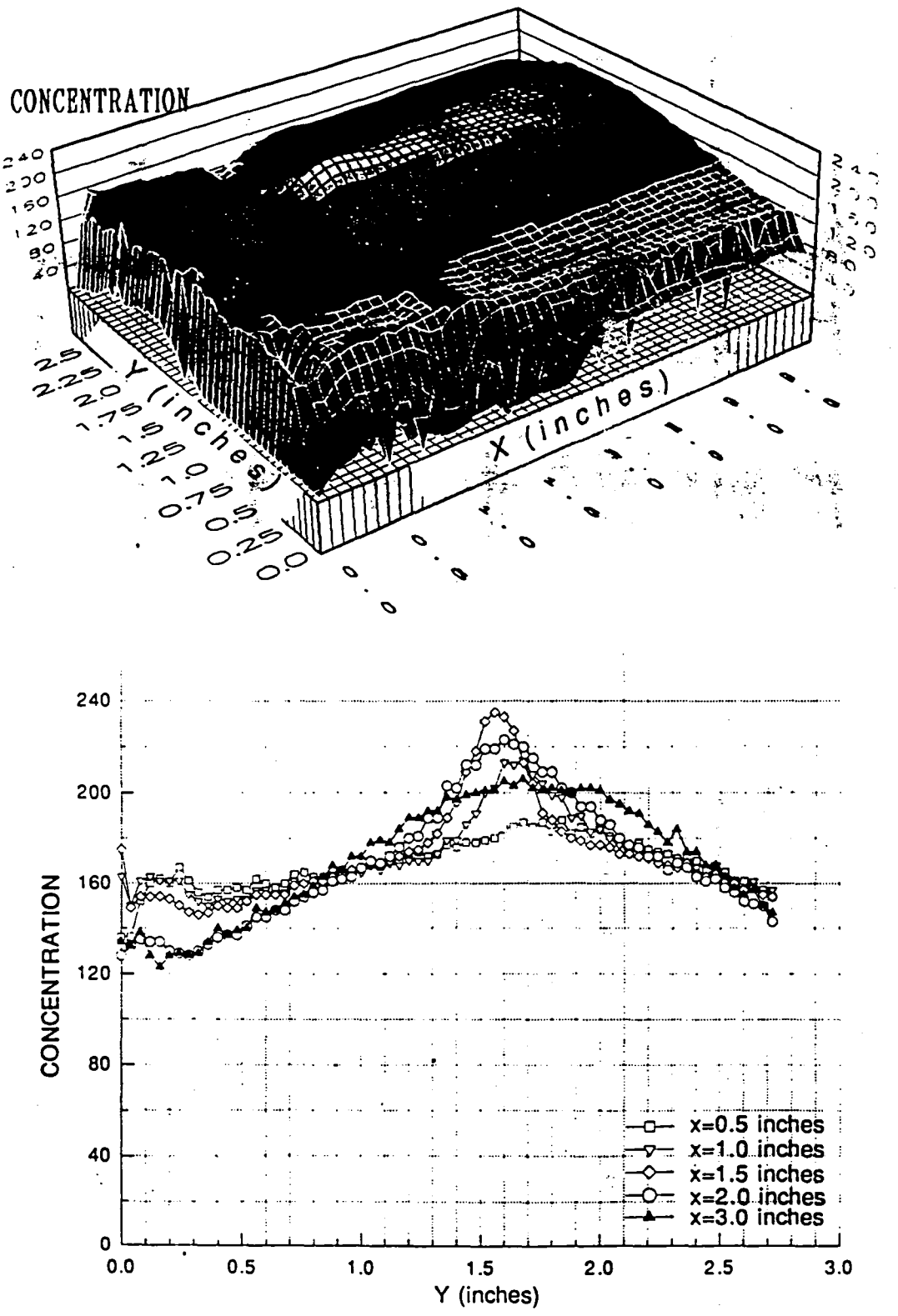

Figure 3.9 Primary Jets Only Mean Concentration Distribution, Z=8.0 inches

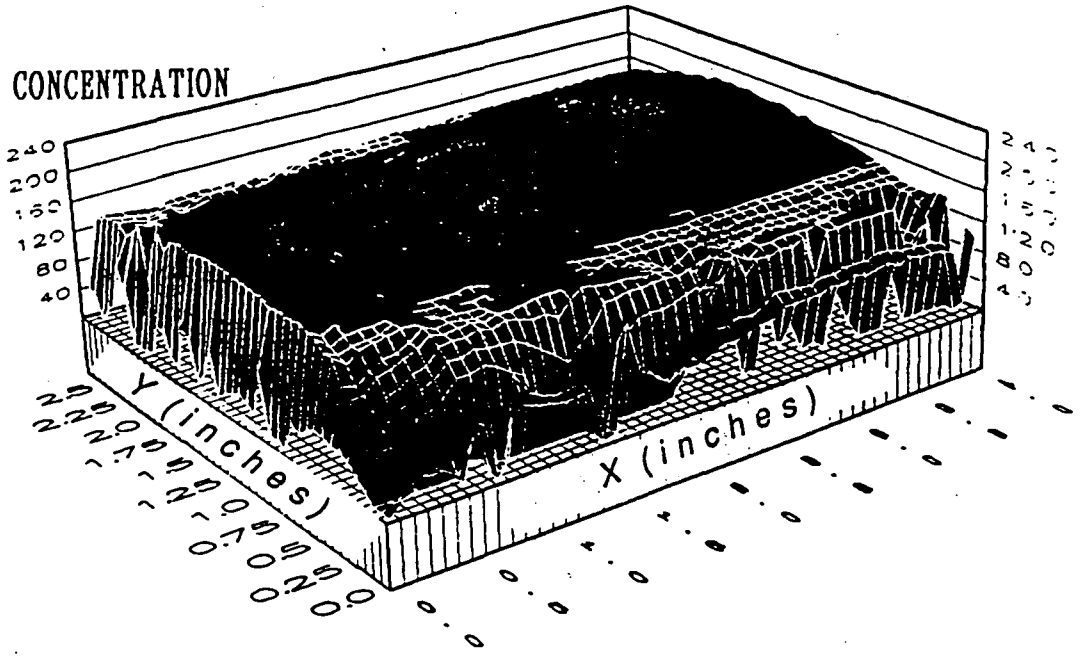

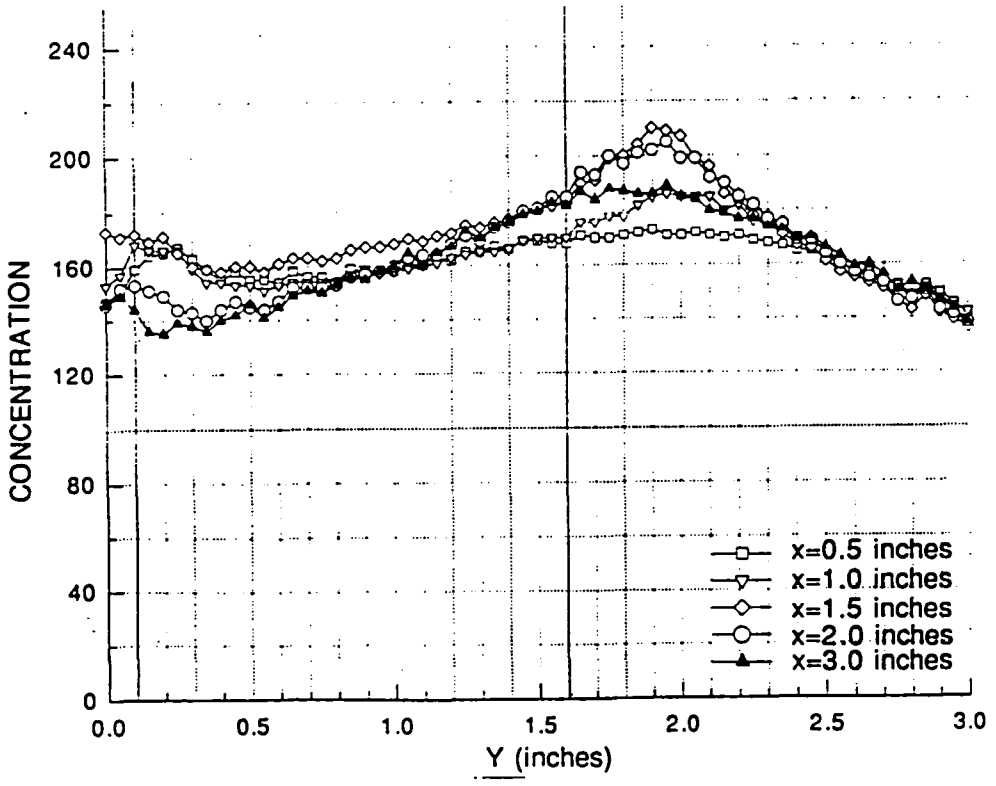

Figure 3.10 Primary Jets Only Mean Concentration Distribution, Z=6.5 inches

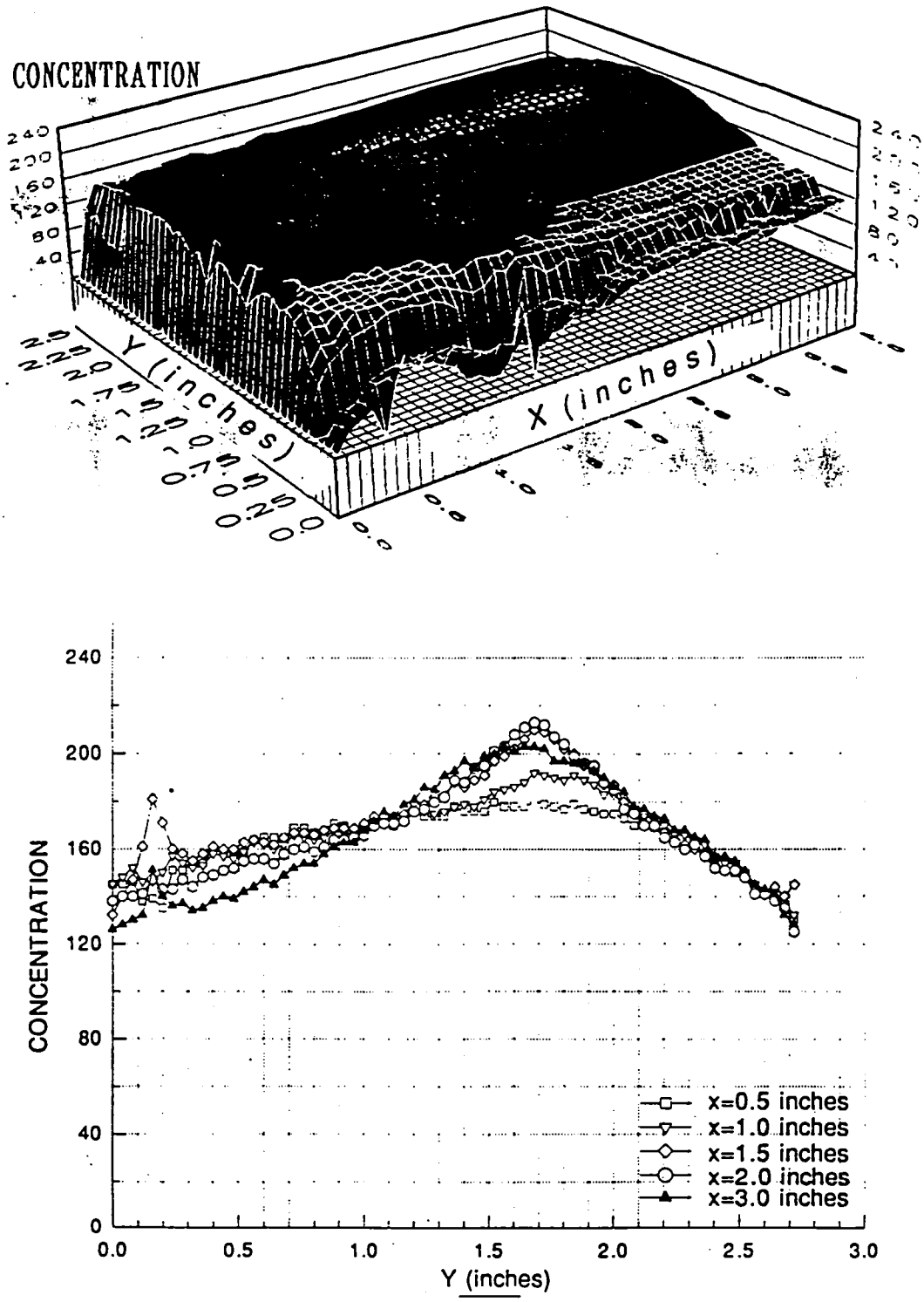

Figure 3.11 Primary Jets Only Mean Concentration Distribution, Z=8.5 inches

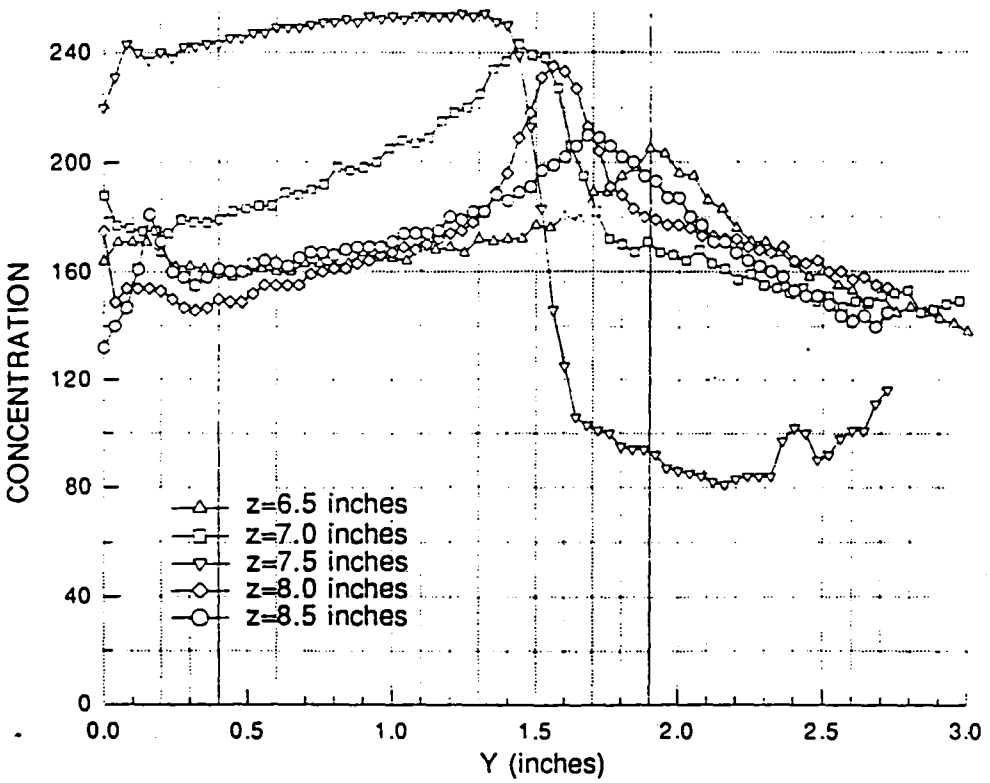

Figure 3.12 Primary Jets Only Mean Concentration Along Primary Jet Axis, X=1.5 inches

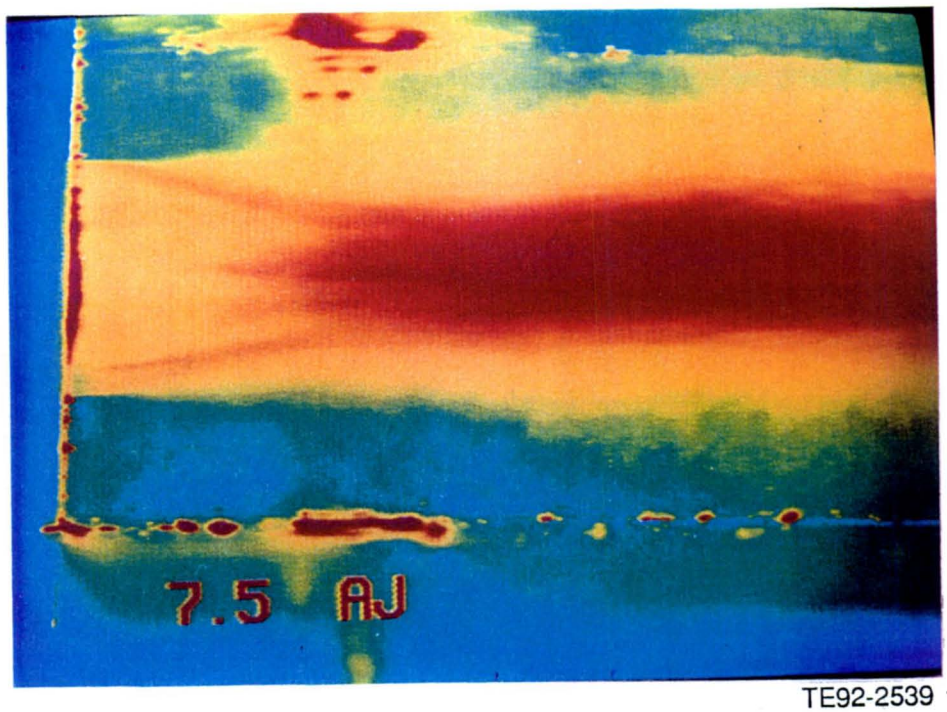

TE92-2539

Figure 3.13 Annular Jets Only Single Frame Picture, Z=7.5 inches

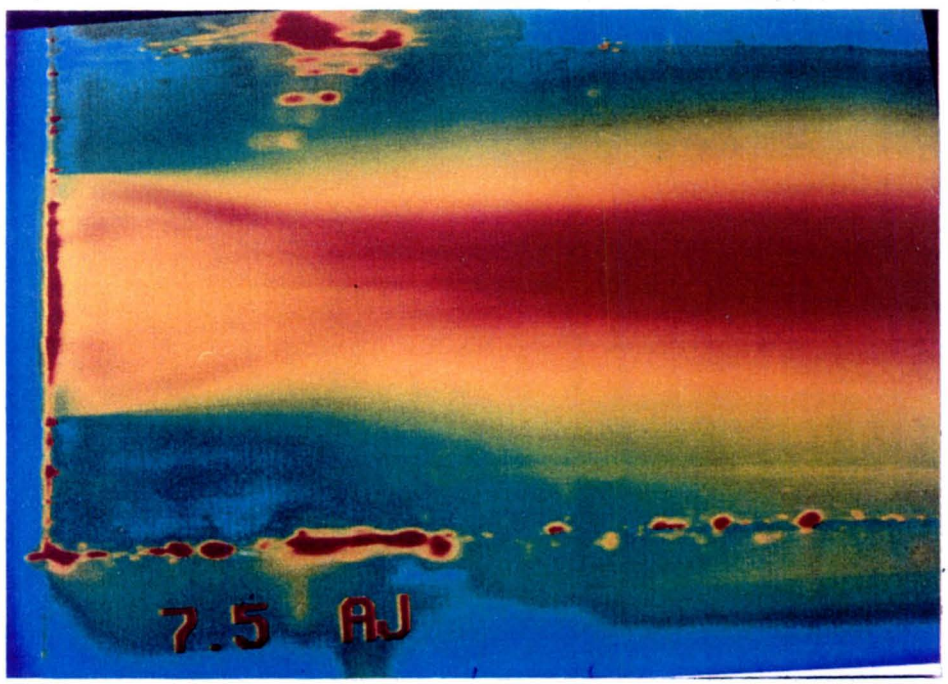

TE92-2540

Figure 3.14 Annular Jets Only 127 Frame Average Picture, Z=7.5 inches

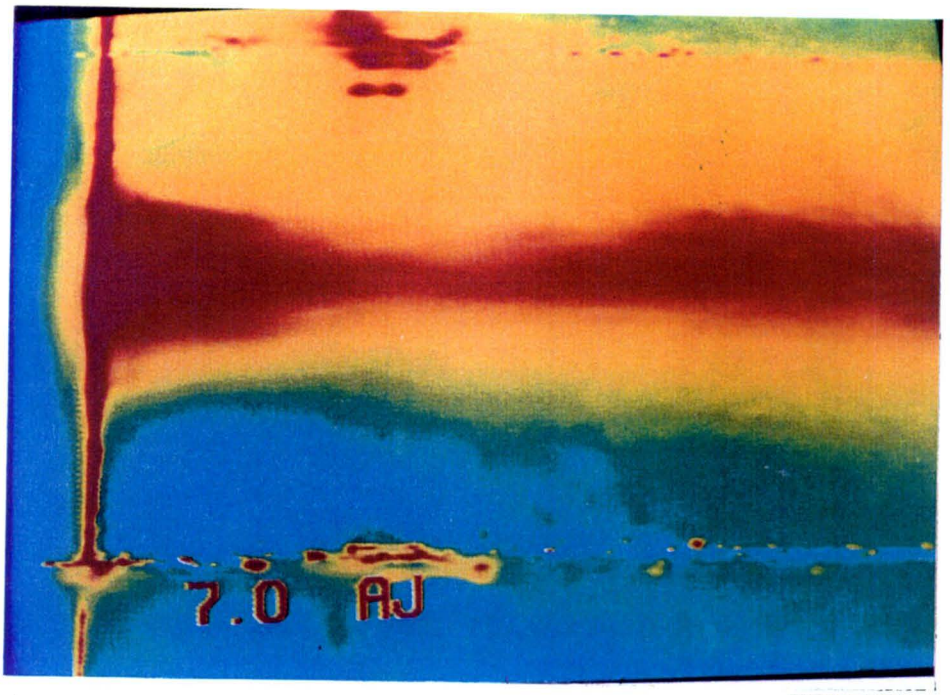

TE92-2541

Figure 3.15 Annular Jets Only Single Frame Picture, Z=7.0 inches

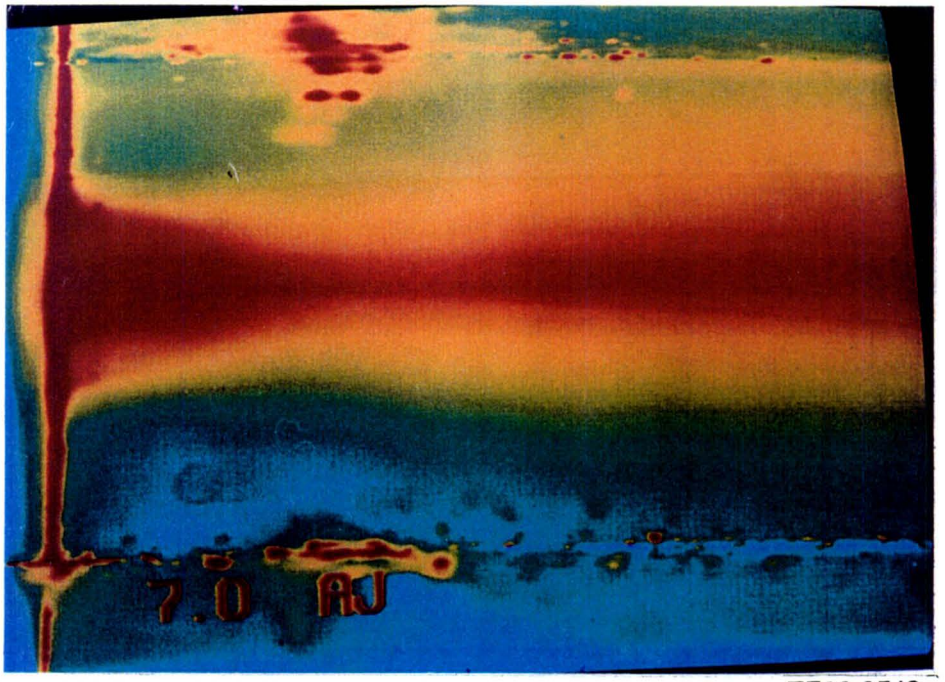

TE92-2542

Figure 3.16 Annular Jets Only 127 Frame Average Picture, Z=7.0 inches

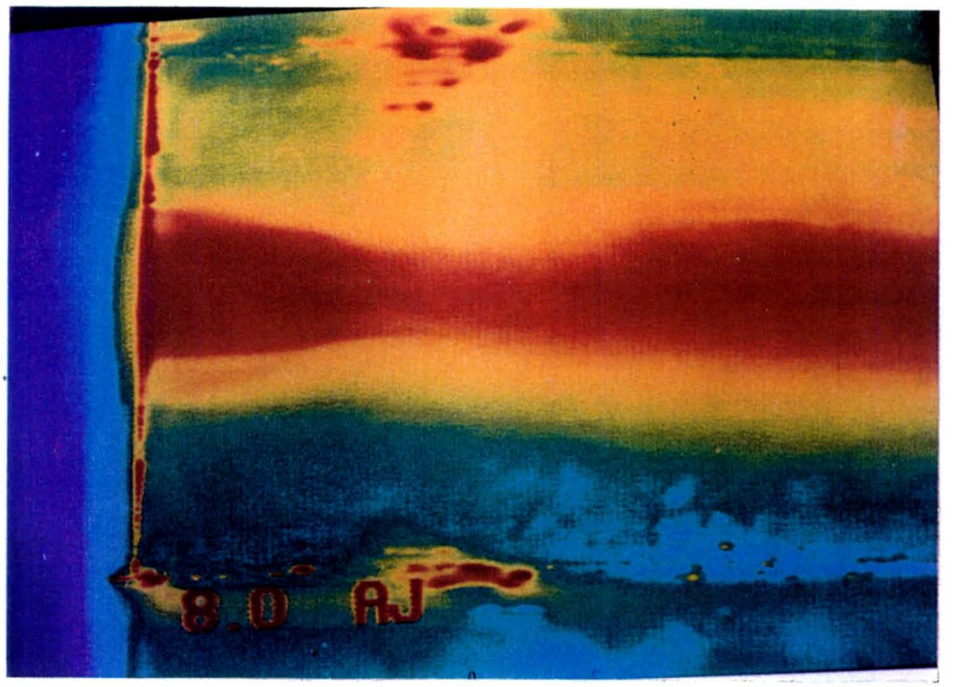

TE92-2543

Figure 3.17 Annular Jets Only Single Frame Picture, Z=8.0 inches

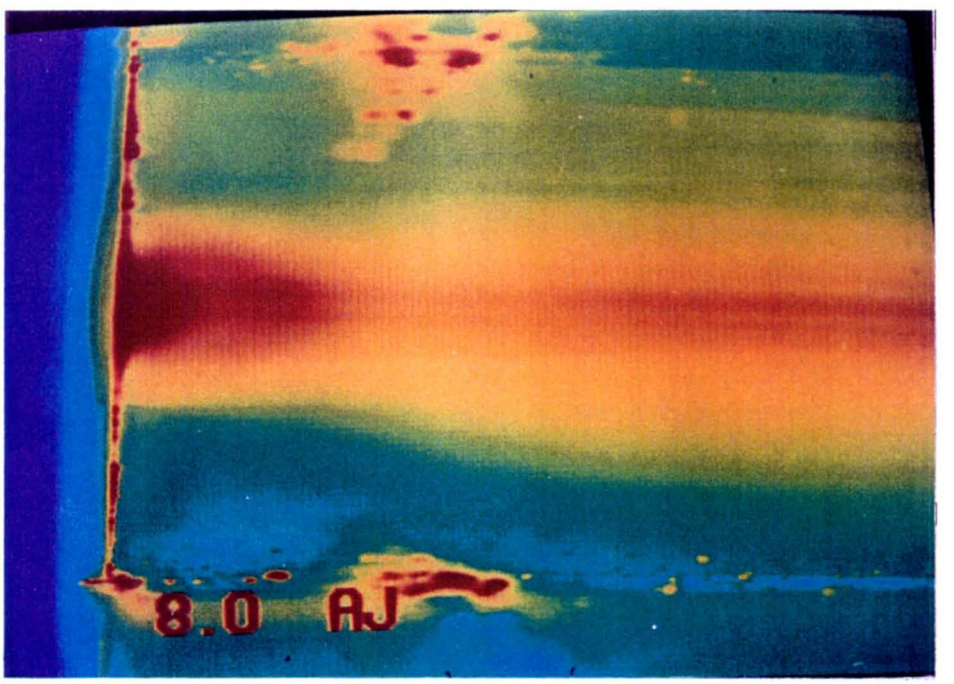

TE92-2544

Figure 3.18 Annular Jets Only 127 Frame Average Picture, Z=8.0 inches

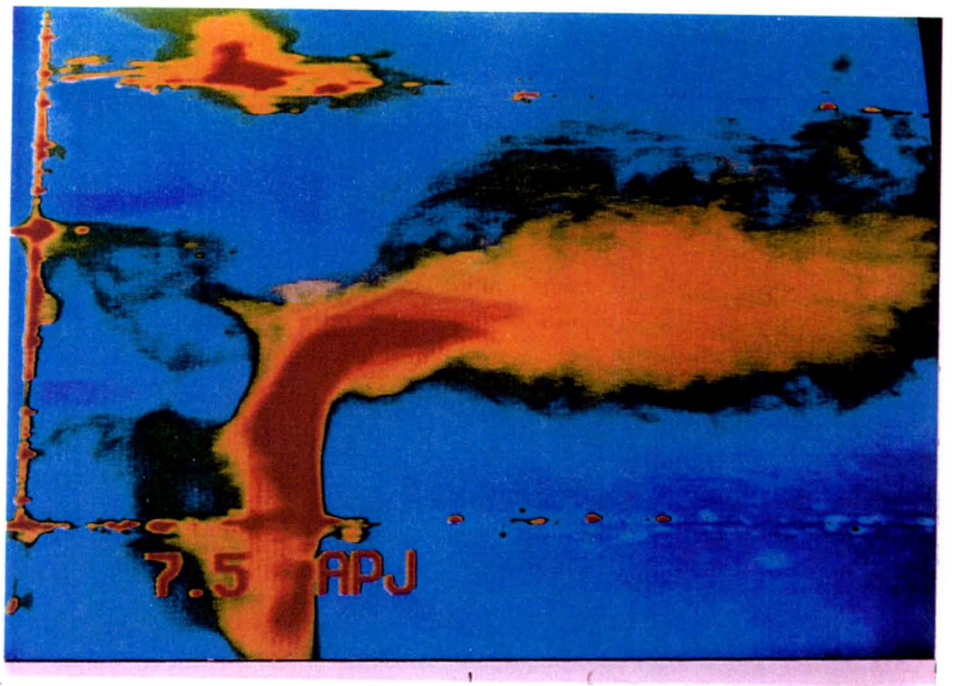

TE92-2652

Figure 3.19 Annular and Primary Jets With Smoke in Primary Jet
Single Frame Picture, Z=7.5 inches

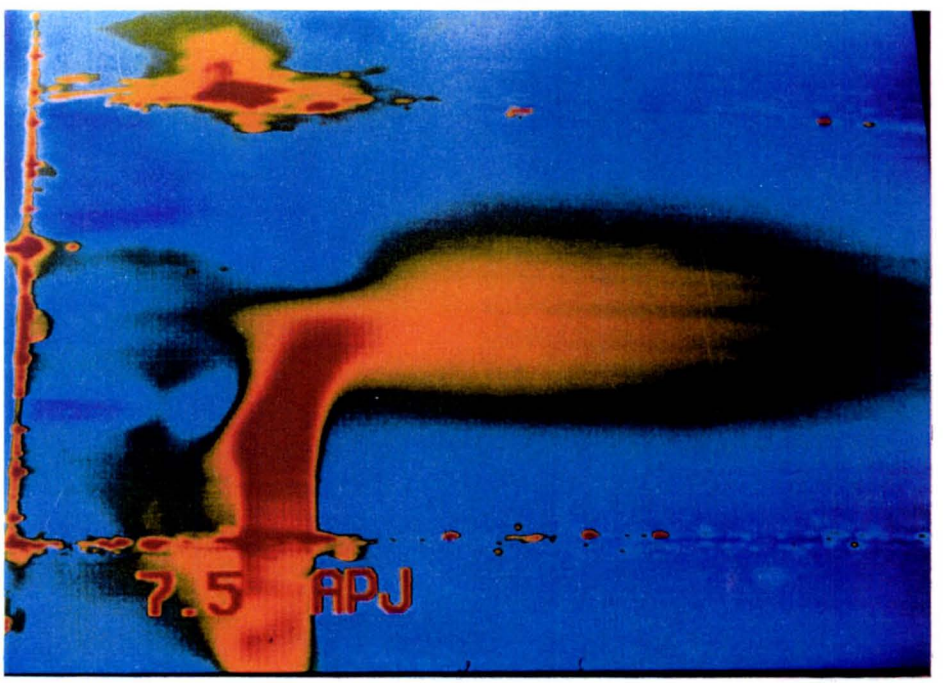

TE92-2653

Figure 3.20 Annular and Primary Jets With Smoke in Primary Jet
127 Frame Average Picture, Z=7.5 inches

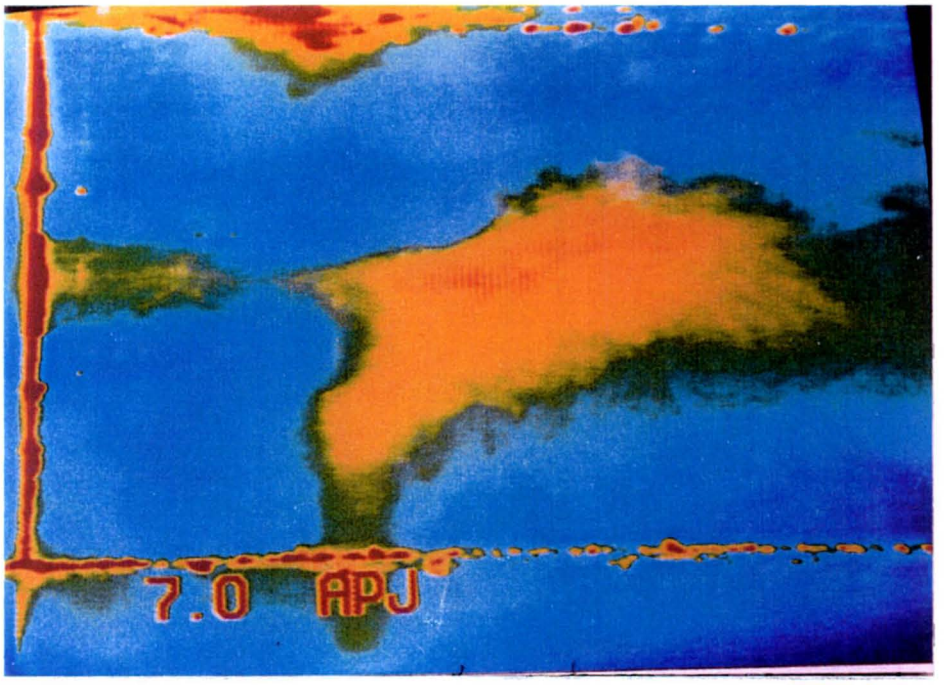

TE92-2654

Figure 3.21 Annular and Primary Jets With Smoke in Primary Jet Single Frame Picture, Z=7.0 inches

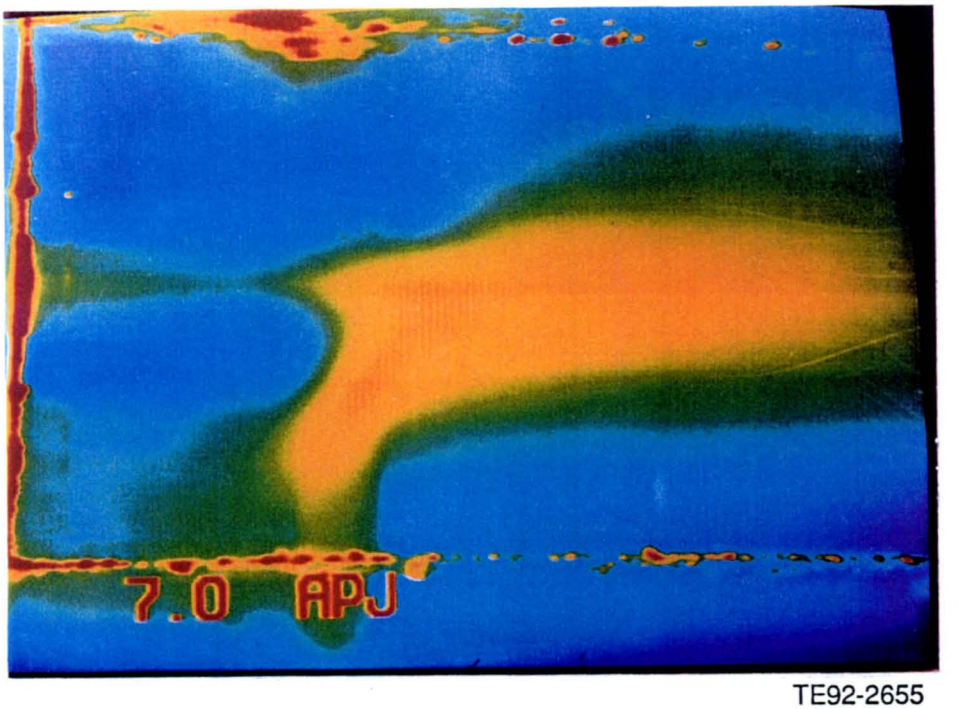

TE92-2655

Figure 3.22 Annular and Primary Jets With Smoke in Primary Jet 127 Frame Average Picture, Z=7.0 inches

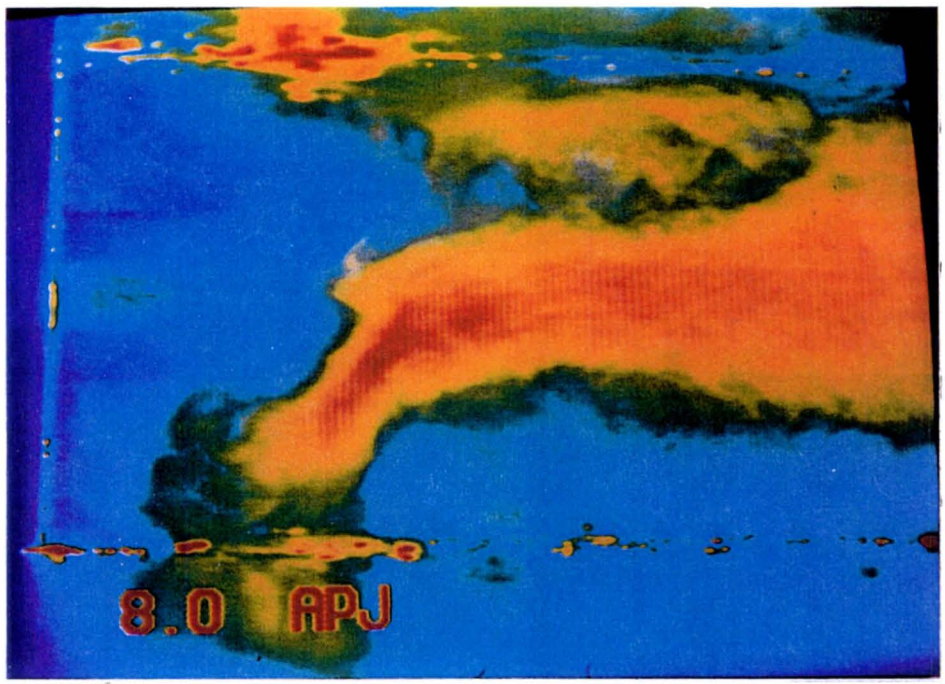

TE92-2656

Figure 3.23 Annular and Primary Jets With Smoke in Primary Jet
Single Frame Picture, Z=8.0 inches

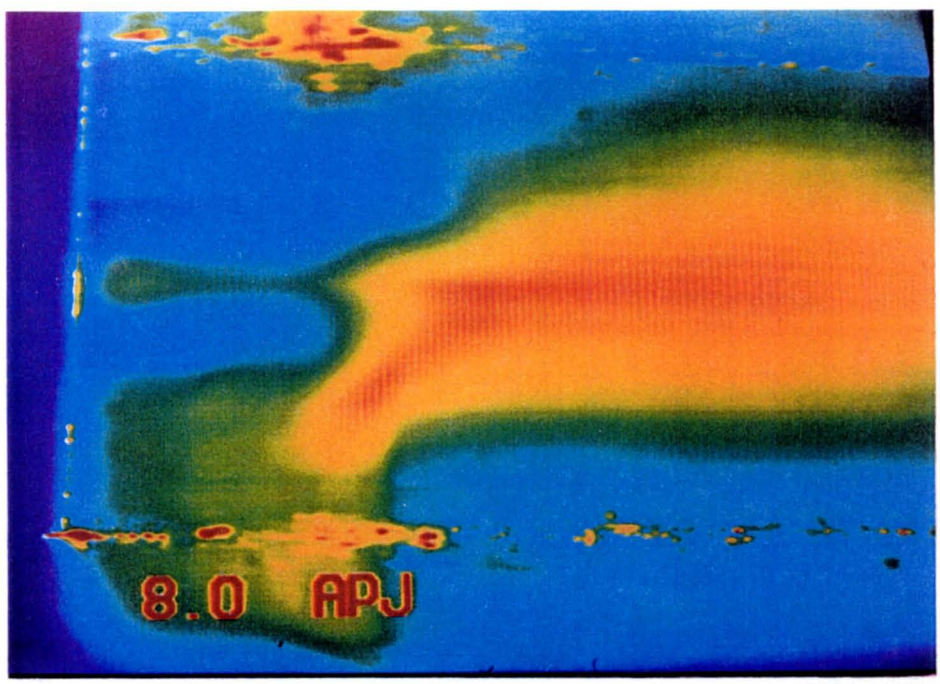

TE92-2657

Figure 3.24 Annular and Primary Jets With Smoke in Primary Jet
127 Frame Average Picture, Z=8.0 inches

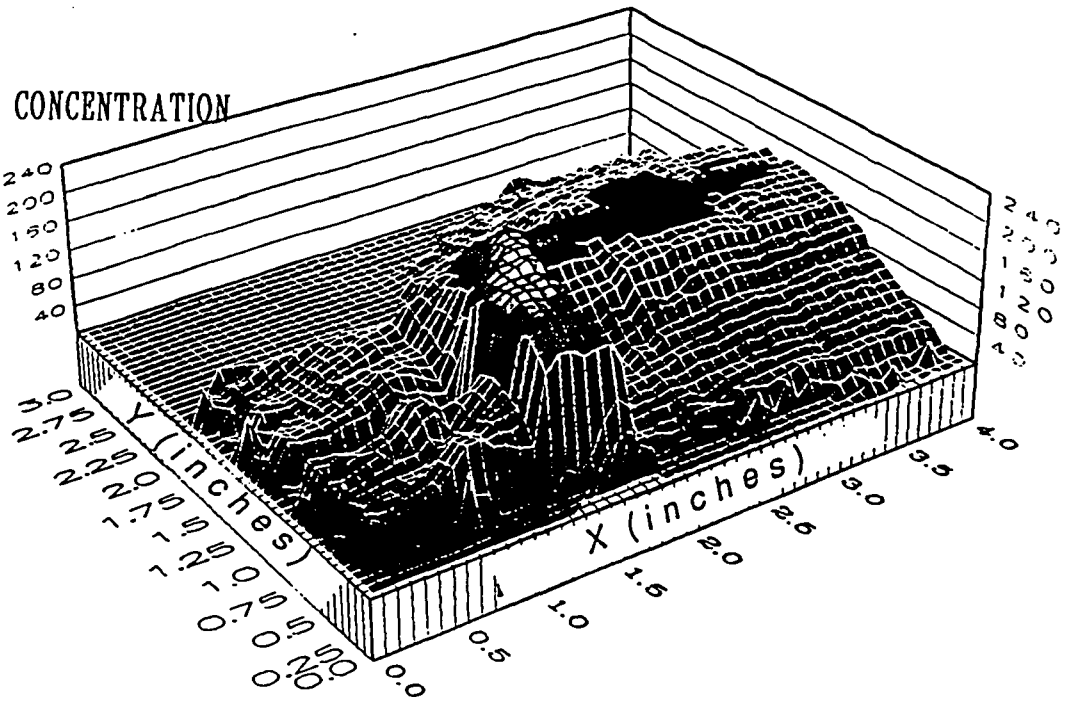

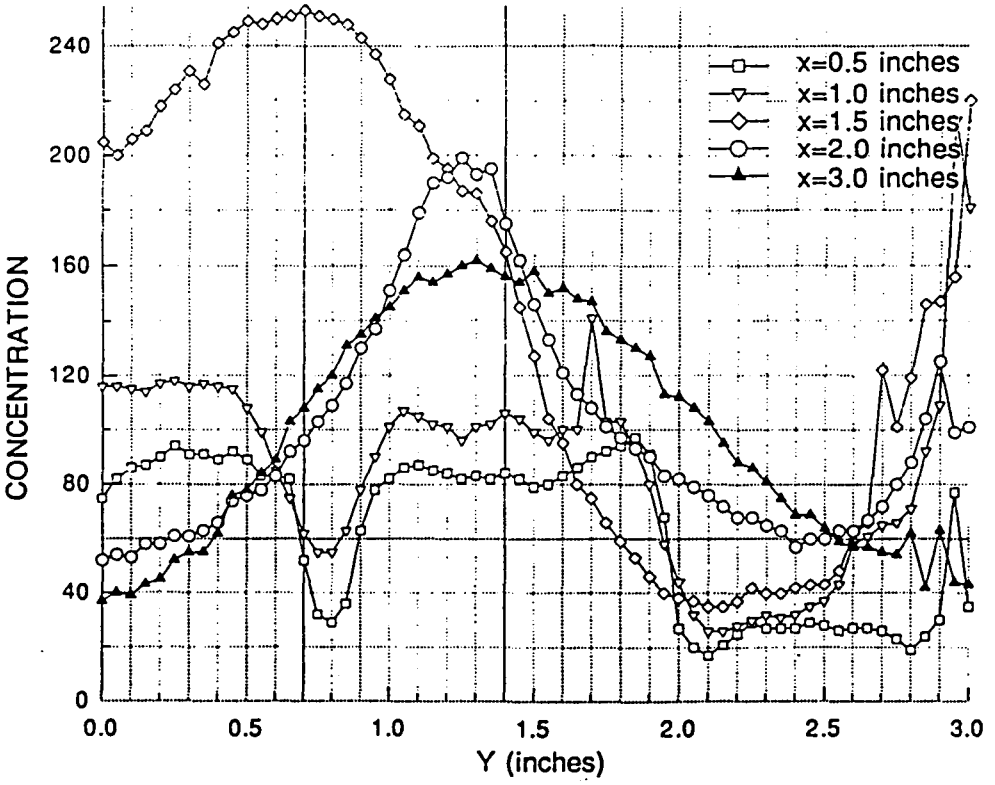

Figure 3.25 Annular and Primary Jets Mean Concentration Distribution With Smoke in Lower Primary Jet, Z=7.5 inches

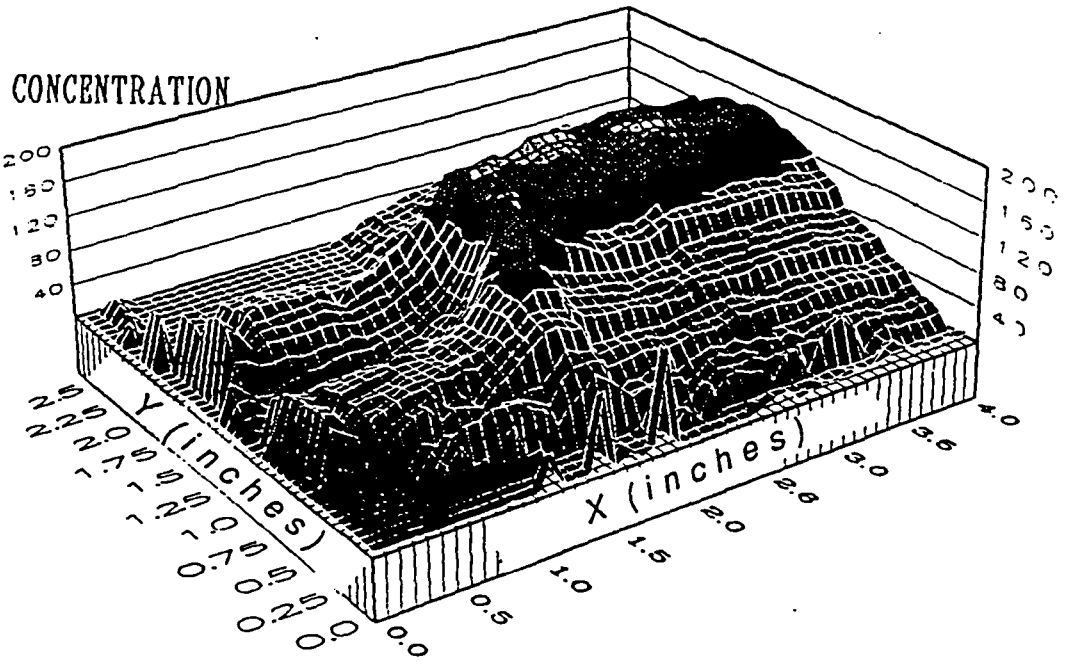

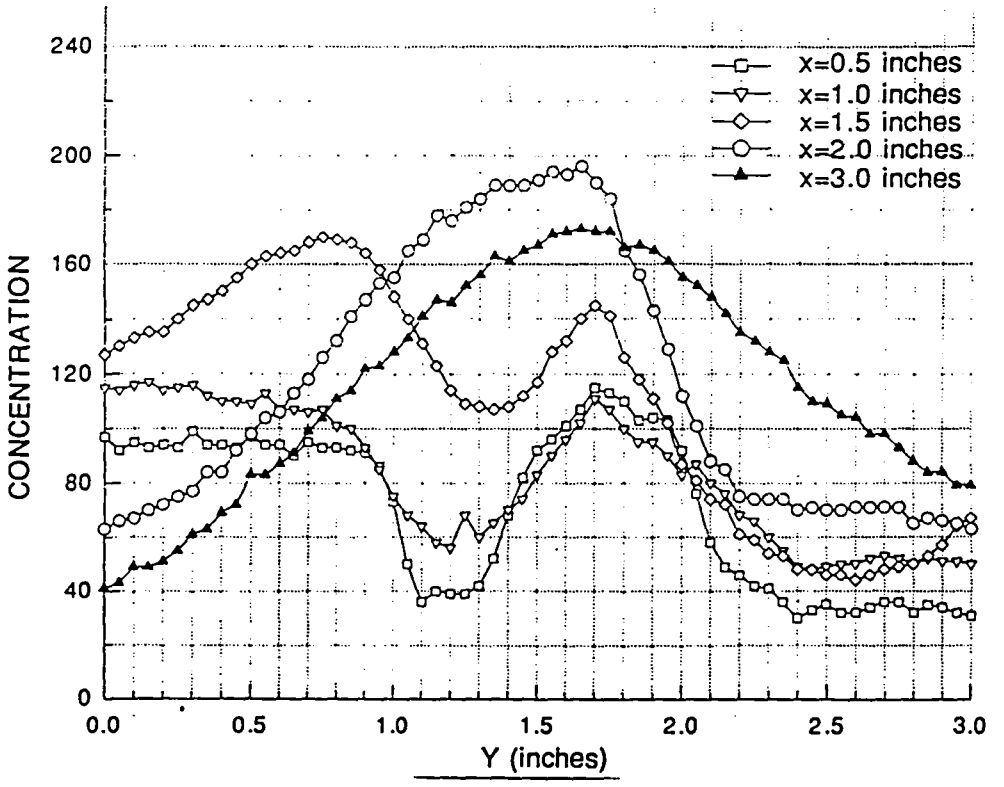

Figure 3.26 Annular and Primary Jets Mean Concentration Distribution With Smoke in Lower Primary Jet, Z=7.0 inches

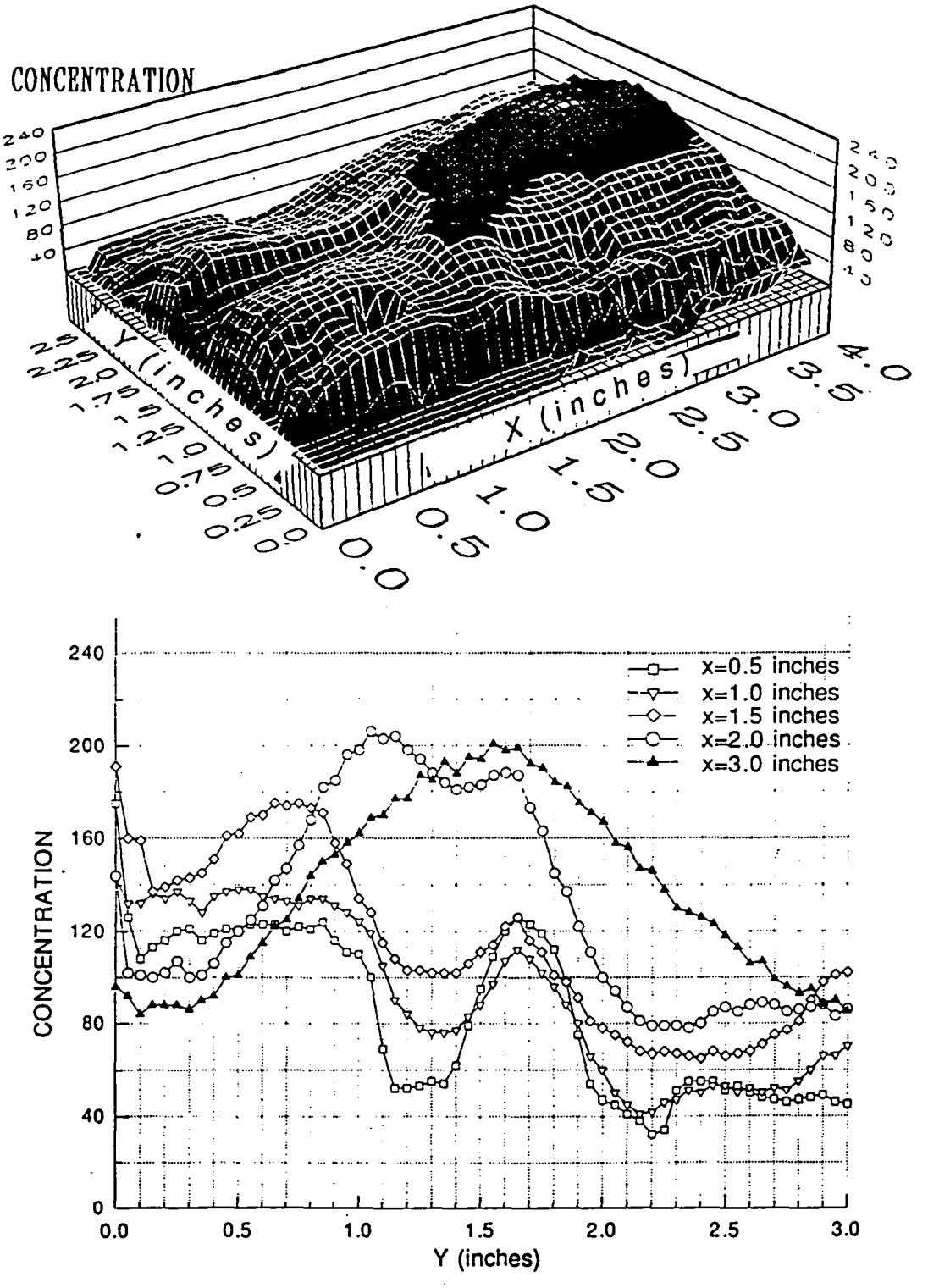

Figure 3.27 Annular and Primary Jets Mean Concentration Distribution With Smoke in Lower Primary Jet, Z=8.0 inches

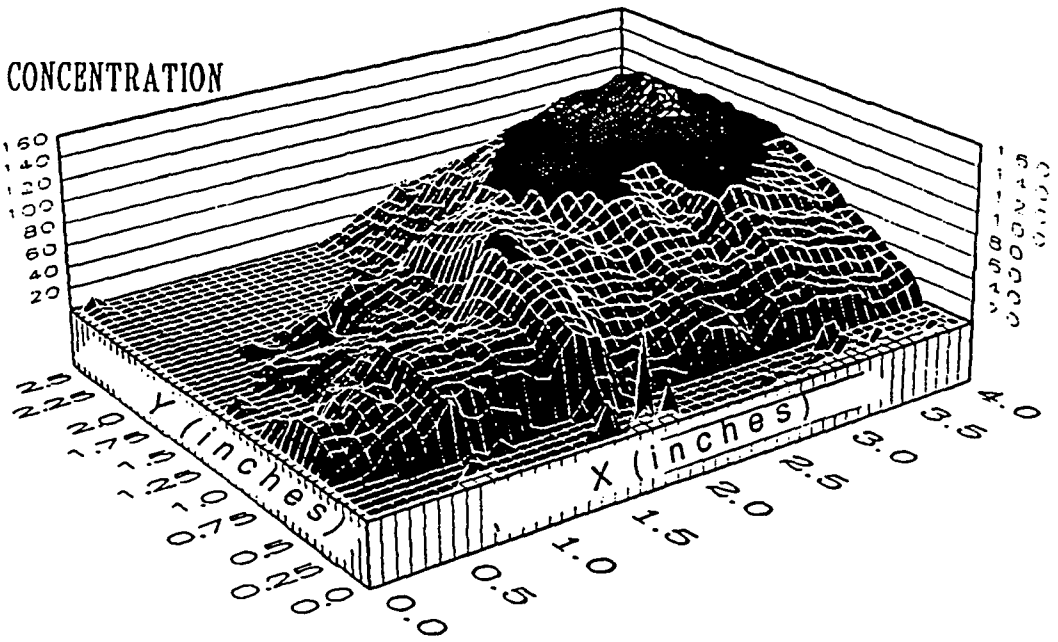

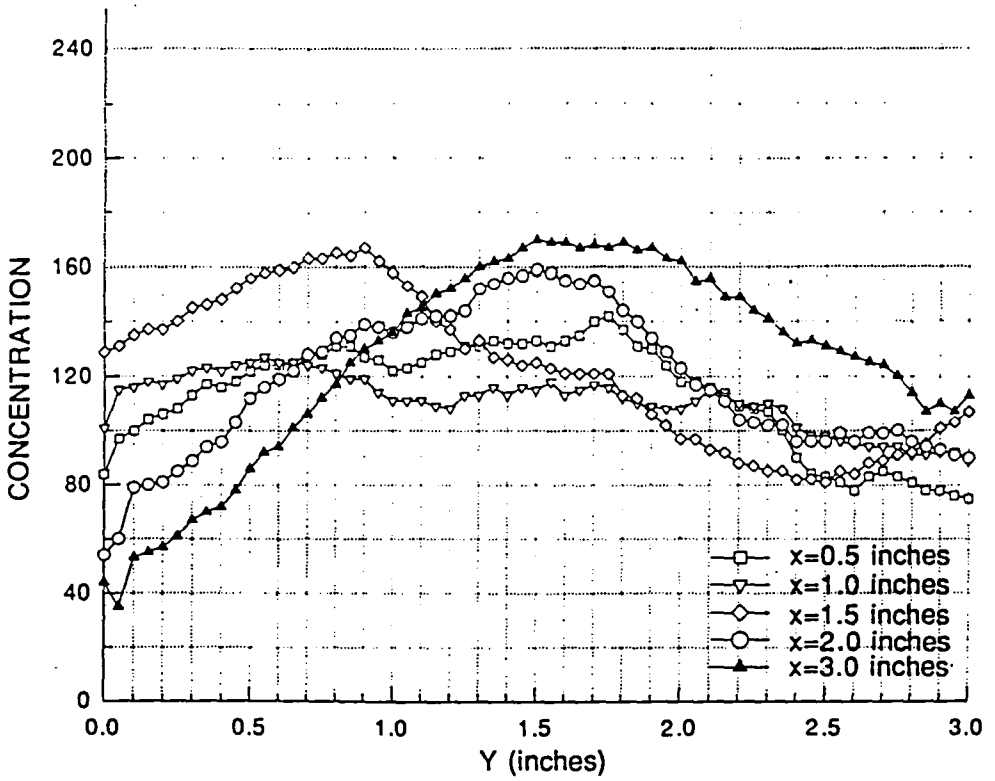

Figure 3.28 Annular and Primary Jets Mean Concentration Distribution With Smoke in Lower Primary Jet, Z=6.5 inches

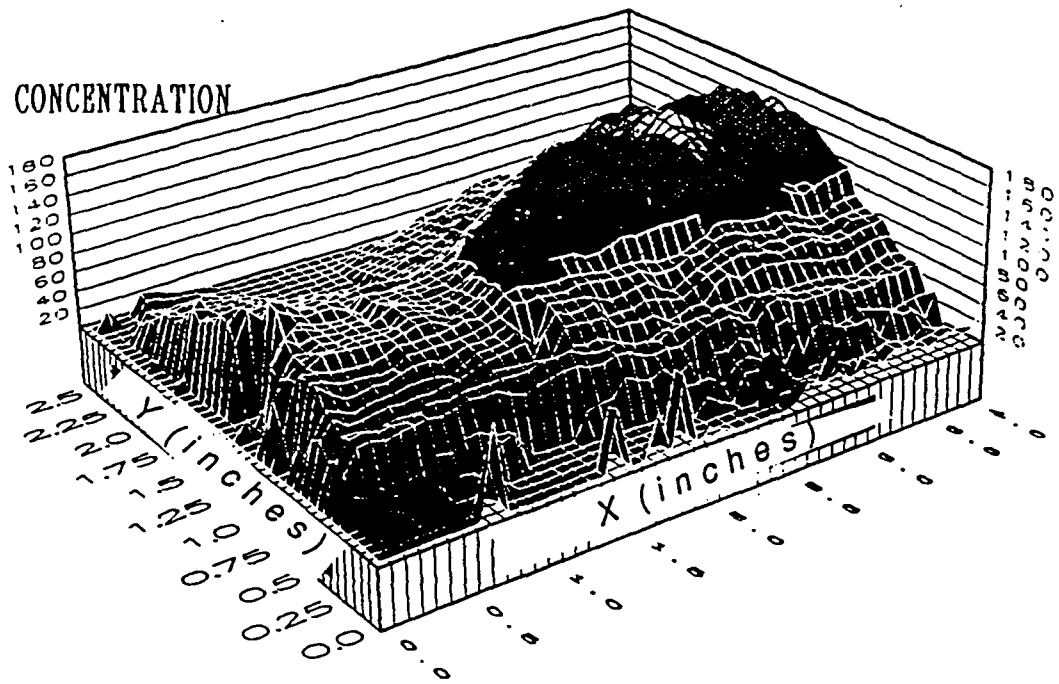

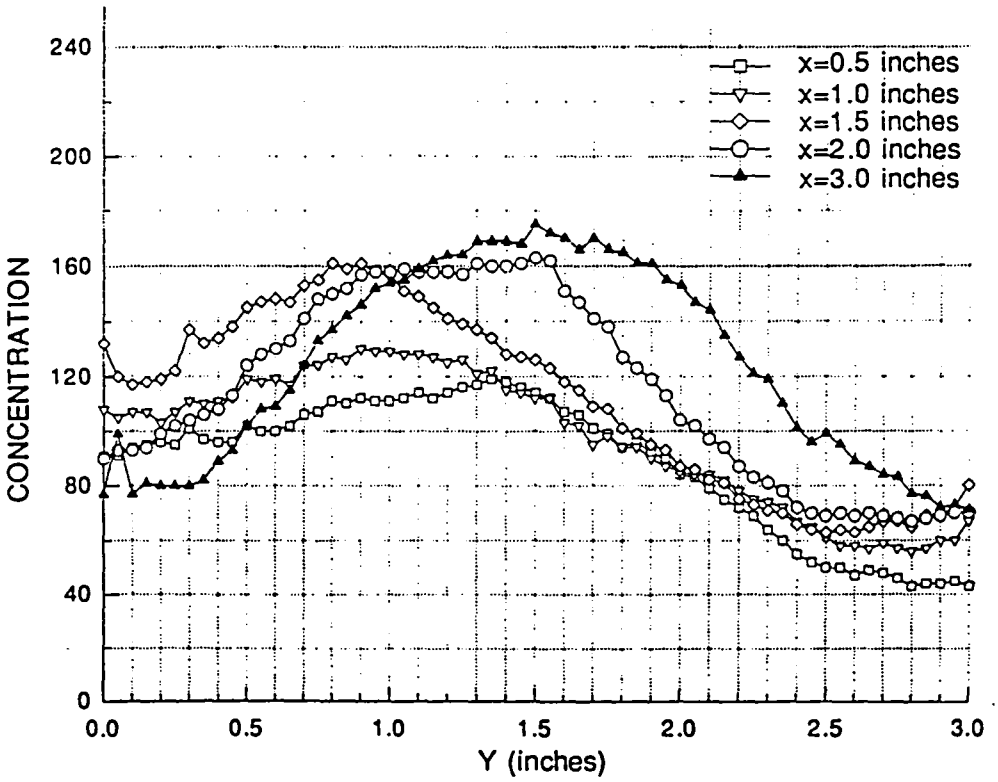

Figure 3.29 Annular and Primary Jets Mean Concentration Distribution With Smoke in Lower Primary Jet, Z=8.5 inches

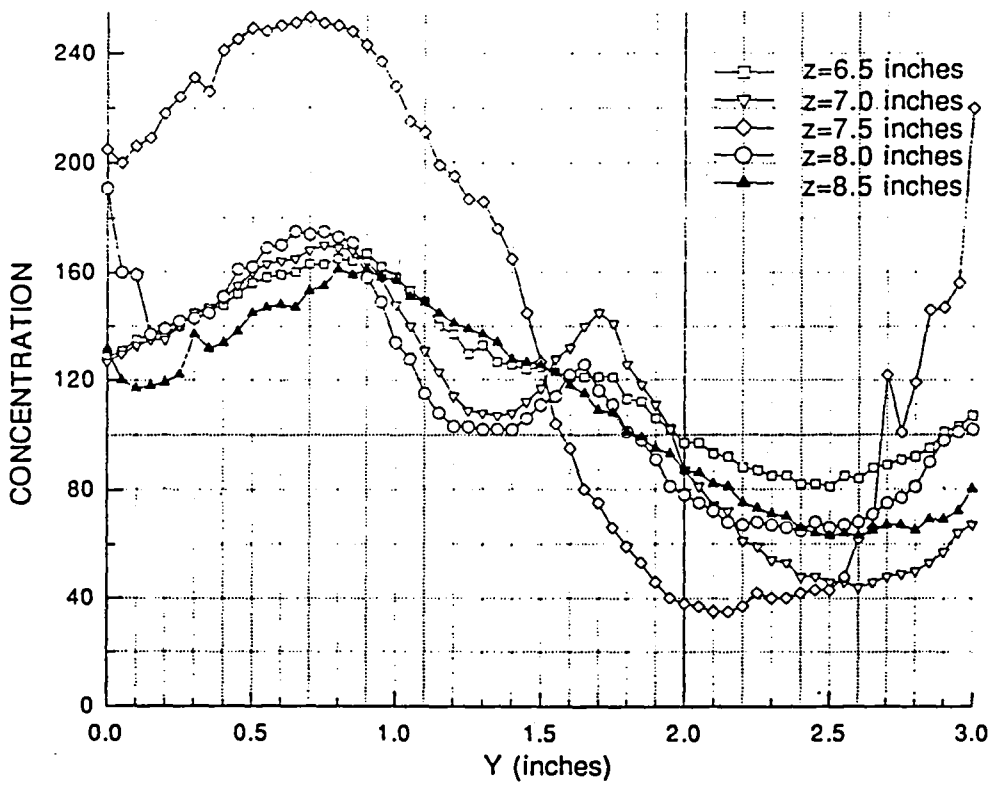

Figure 3.30 Annular and Primary Jets Mean Concentration Along Primary Jet Axis With Smoke in Lower Primary Jet, X=1.5 inches

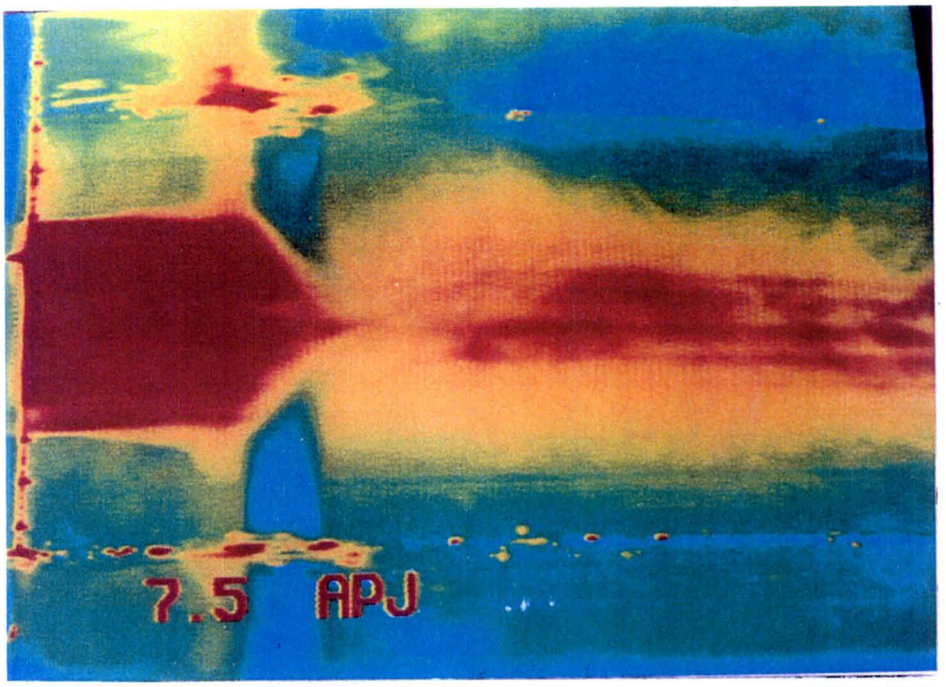

TE92-2664

Figure 3.31 Annular and Primary Jets With Smoke in Annular Jet
Single Frame Picture, Z=7.5 inches

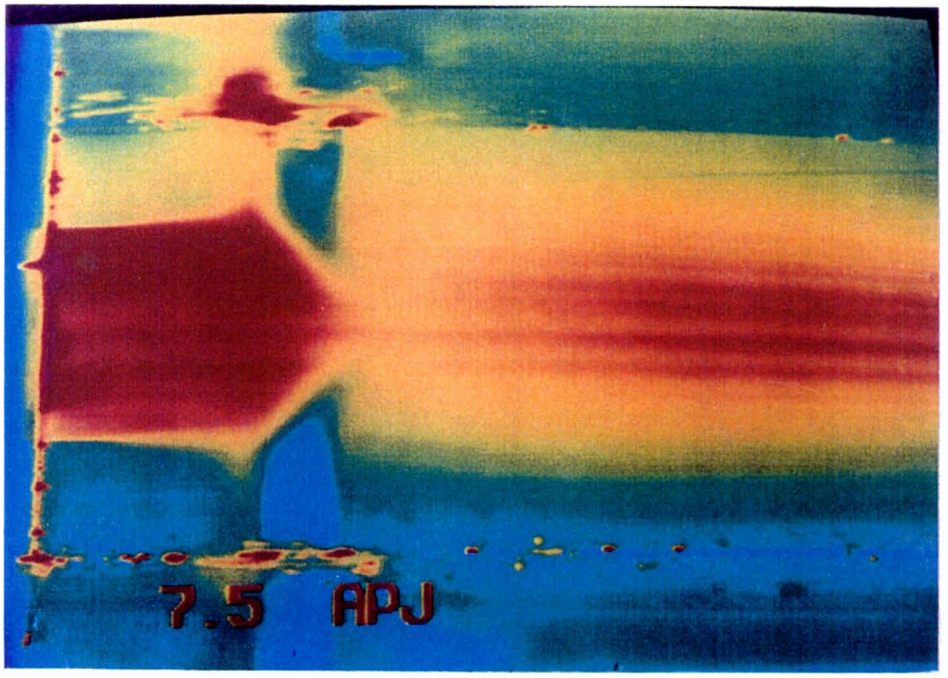

TE92-2665

Figure 3.32 Annular and Primary Jets With Smoke in Annular Jet
127 Frame Average Picture, Z=7.5 inches

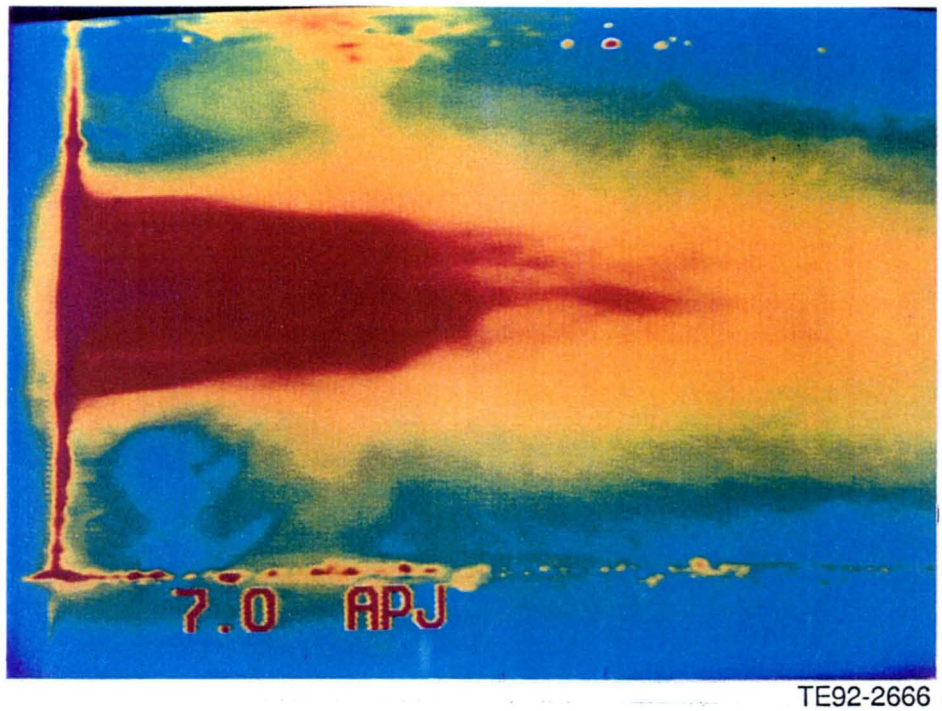

TE92-2666

Figure 3.33 Annular and Primary Jets With Smoke in Annular Jet Single Frame Picture, Z=7.0 inches

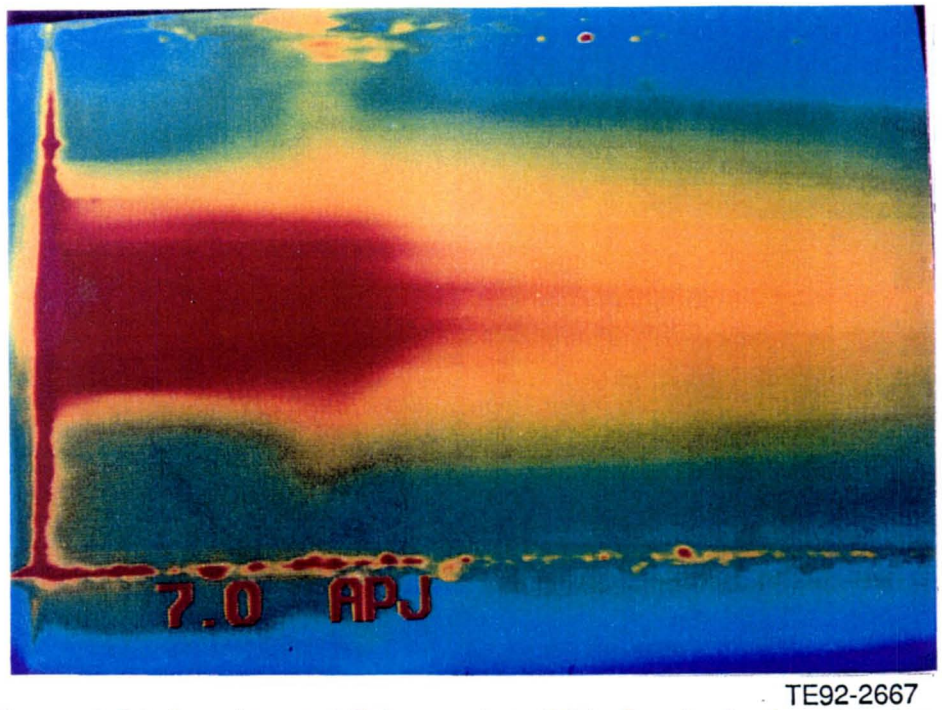

TE92-2667

Figure 3.34 Annular and Primary Jets With Smoke in Annular Jet 127 Frame Average Picture, Z=7.0 inches

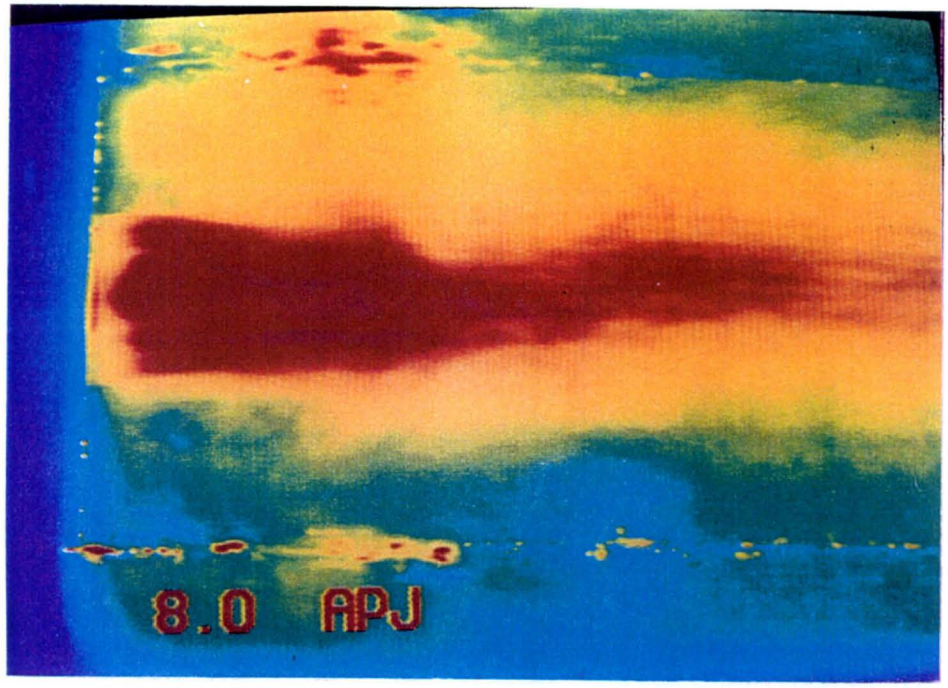

TE92-2668

Figure 3.35 Annular and Primary Jets With Smoke in Annular Jet
Single Frame Picture, Z=8.0 inches

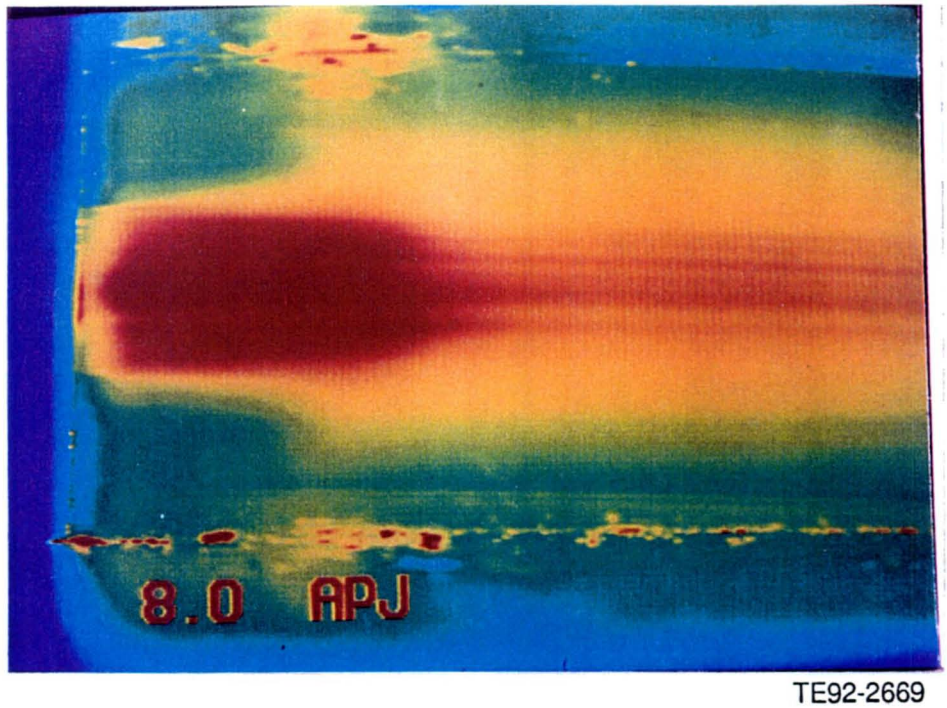

TE92-2669

Figure 3.36 Annular and Primary Jets With Smoke in Annular Jet
127 Frame Average Picture, Z=8.0 inches

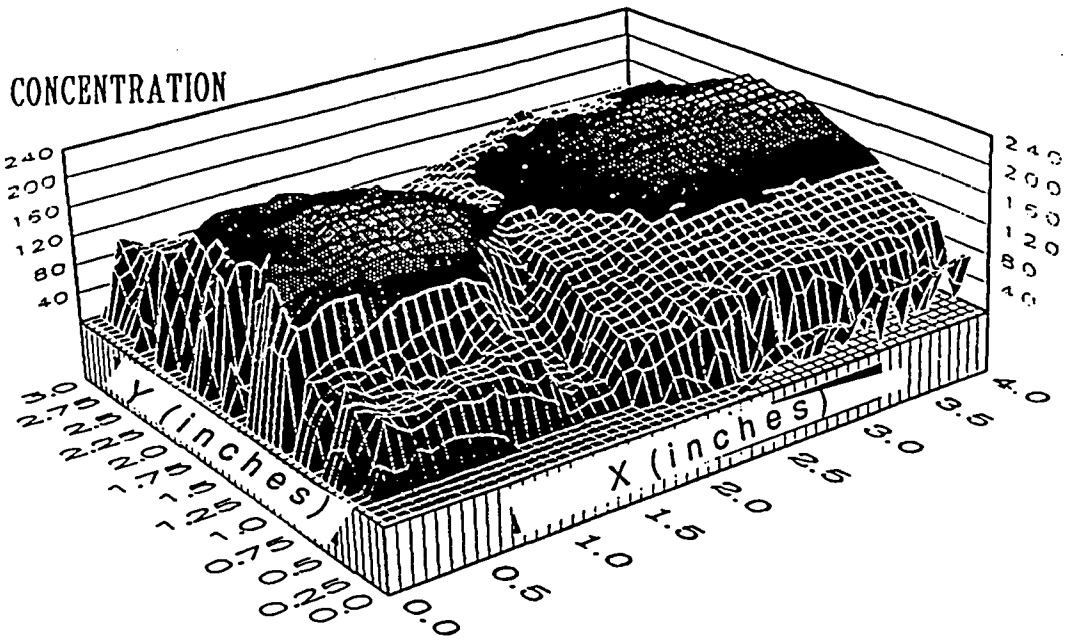

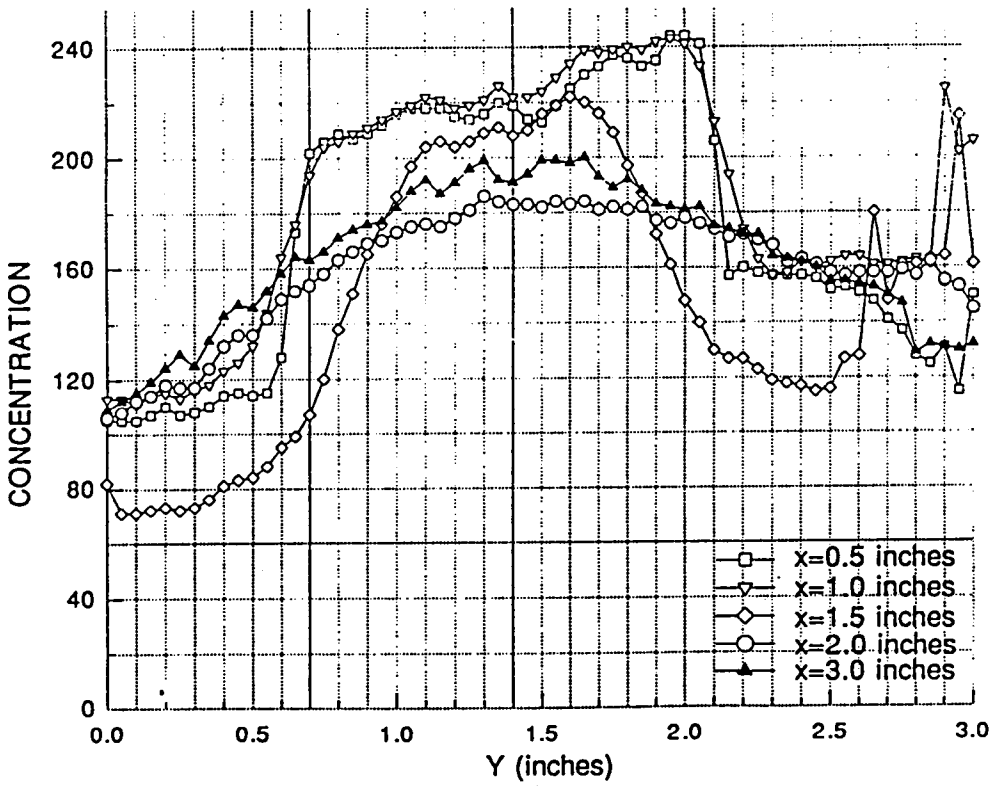

Figure 3.37 Annular and Primary Jets Mean Concentration Distribution With Smoke in Annular Jet, Z=7.5 inches

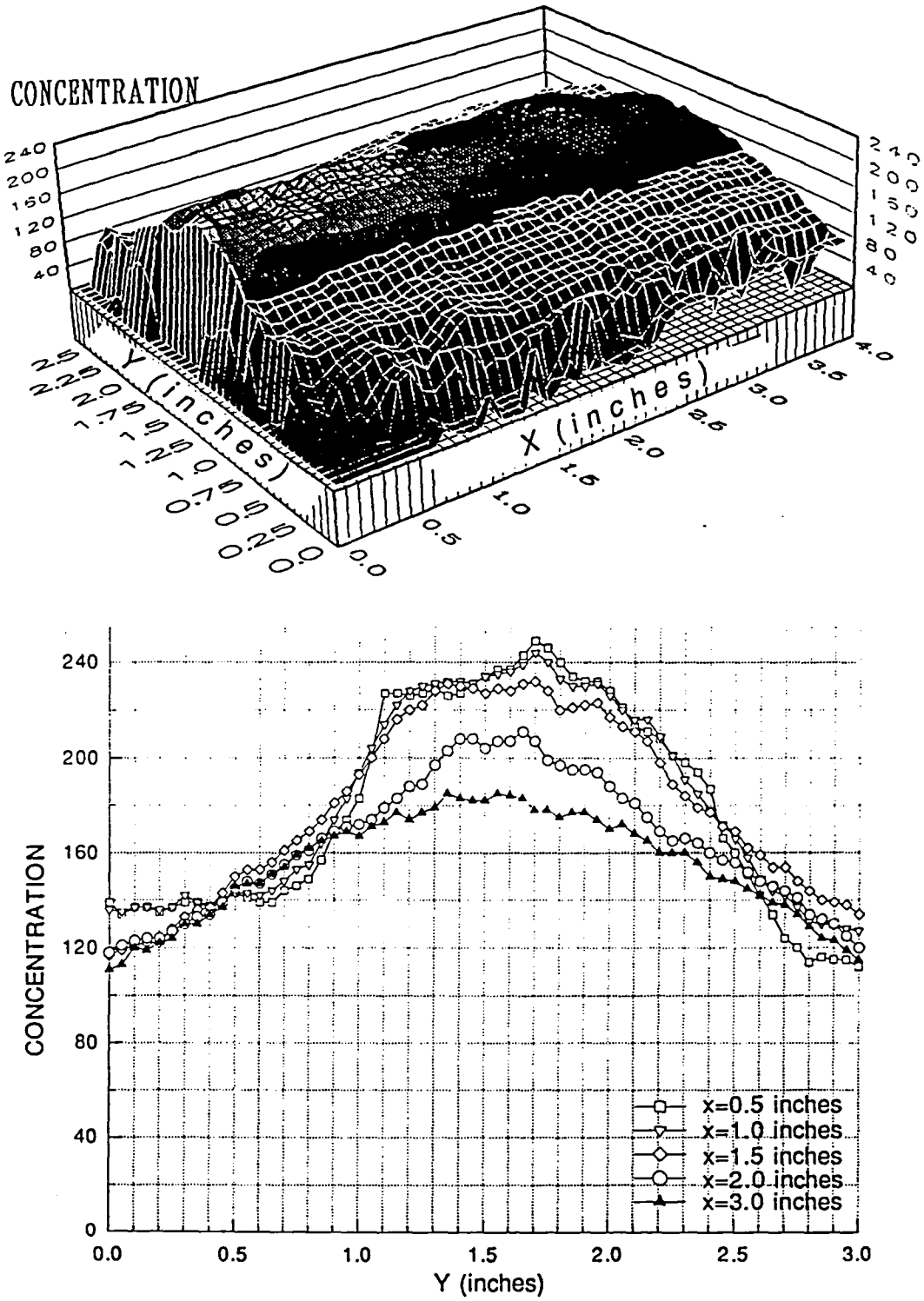

Figure 3.38 Annular and Primary Jets Mean Concentration Distribution With Smoke in Annular Jet, Z=7.0 inches

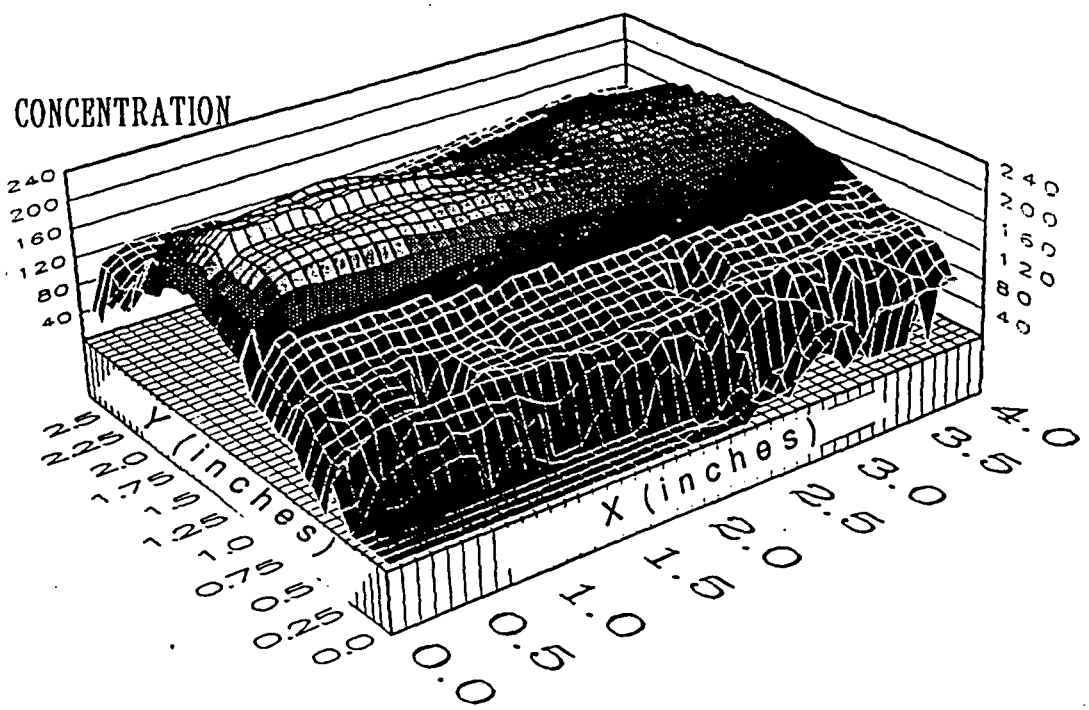

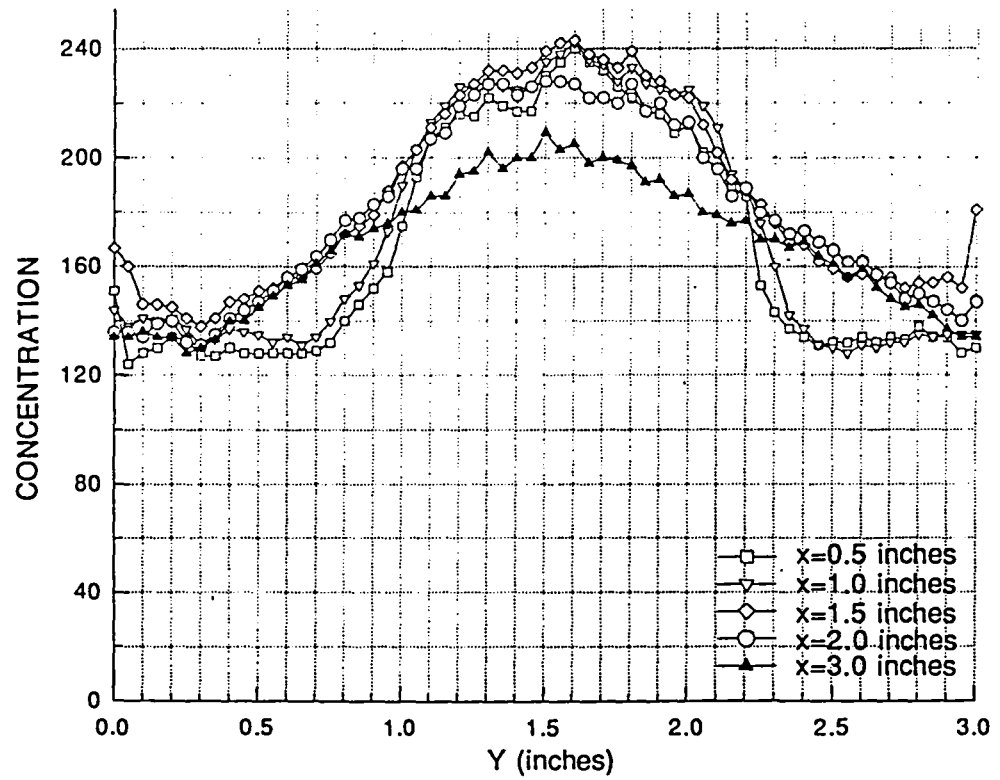

Figure 3.39 Annular and Primary Jets Mean Concentration Distribution With Smoke in Annular Jet, Z=8.0 inches

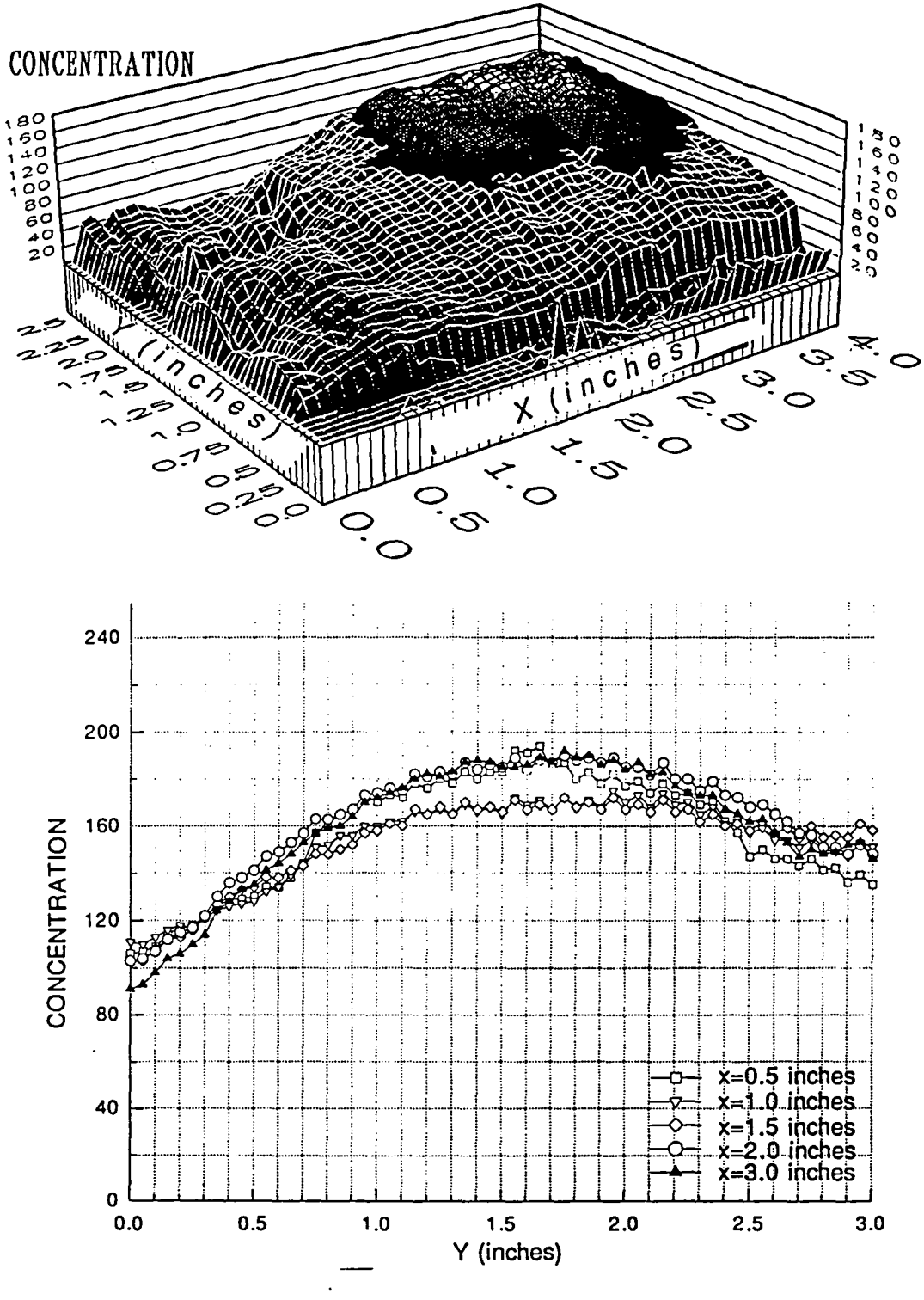

Figure 3.40 Annular and Primary Jets Mean Concentration Distribution With Smoke in Annular Jet, Z=6.5 inches

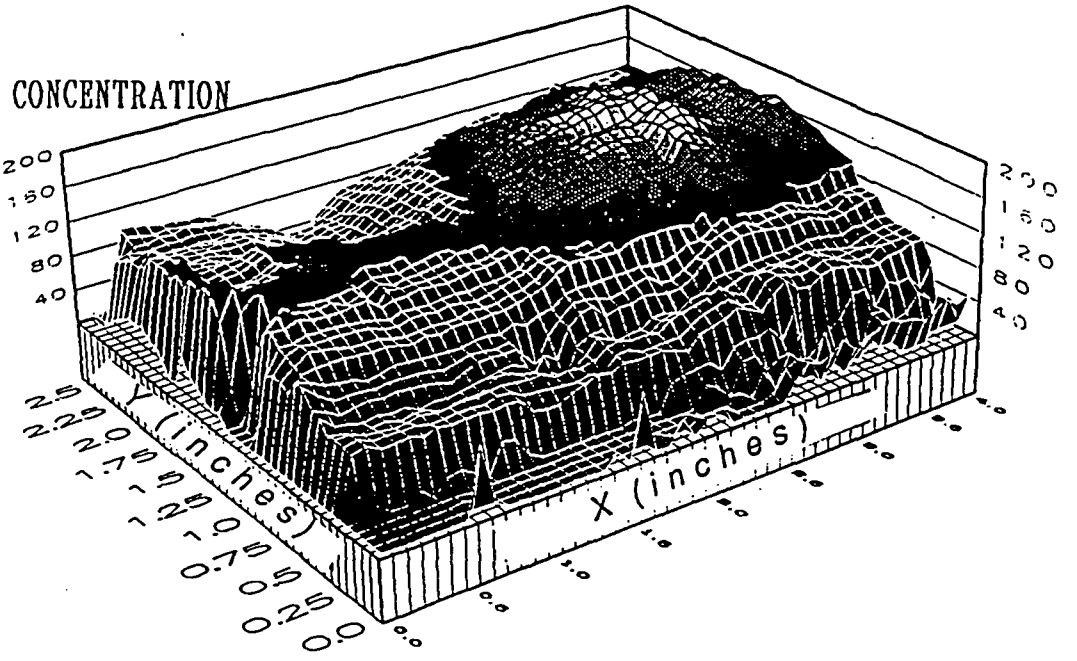

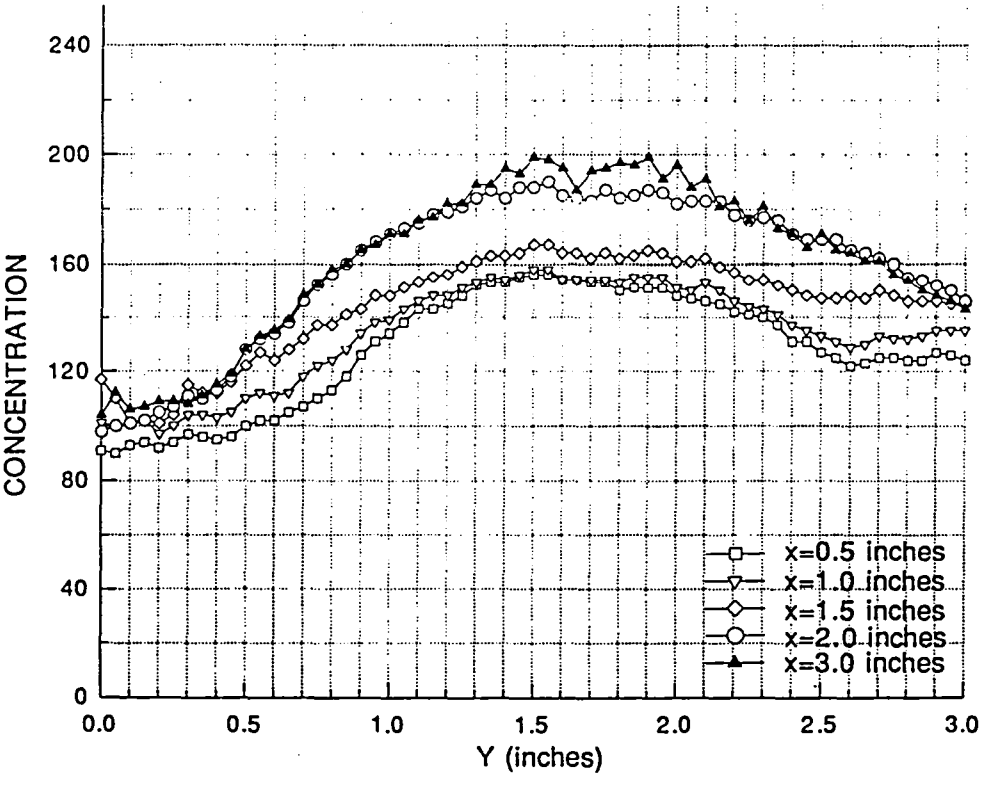

Figure 3.41 Annular and Primary Jets Mean Concentration Distribution With Smoke in Annular Jet, Z=8.5 inches

CHAPTER 4

SUMMARY AND CONCLUSIONS

A Laser Doppler Velocimeter and laser sheet imaging techniques were used in this investigation to provide non intrusive measurements of the flowfield in an annular combustor model. Three different geometrical configurations of the annular combustor model were investigated. These configurations consisted of primary jets only, annular jets only, and annular and primary jets together.

4.1 LDV Measurements

A one component LDV system was used to provide two dimensional mean velocity measurements in the combustor model. From the LDV data, the root-mean-square velocity, two-dimensional turbulent kinetic energy, and one Reynolds shear stress component was calculated. Major features of the flowfield include recirculating flow, primary and annular jet interaction, high turbulence, and unsteady flow.

In the primary jets only configuration, four recirculation zones were observed in the model. Two counter rotating recirculation zones were set up between the endplate and the primary jets on upper and lower halves of the rig. These zones were observed to move toward the primary jets and upper and lower walls the

further measurements moved from the rig centerplane. Another two counter rotating recirculation zones also formed downstream of the primary jets on the upper and lower halves of the rig. These recirculation zones moved upstream and toward upper and lower walls of the rig the further measurements moved from the rig centerplane. The turbulent energy was mainly concentrated at the center of the test cell between the endplate and the primary jet entrance. The turbulence slowly decayed further downstream.

For the annular jets only case, two recirculation zones were formed along the upper and lower walls of the combustor. These recirculation zones extend downstream from the annular jet entrance and showed no definite center as the recirculation zones did in the primary jets only case. Two smaller counter rotating recirculation zones also formed behind the center of the annular jet. The greatest turbulent energy and shear stress existed at the inlet of the annular jet. As in the primary jets only case, the turbulence decayed farther downstream.

For the primary and annular jets case, four recirculation zones occurred in the combustor. Two large recirculation zones downstream of the primary jets along the upper and lower walls and two zones upstream of the primary jets between the edges of the annular jet and the upper and lower walls were present. Two additional recirculation zones were formed behind the center of the annular jet. The highest turbulent energy and shear stress was at X=1.5 inches where the annular and primary jets interact. Turbulence levels decayed and dispersed, as in the primary jets only case, downstream.

The most pronounced result from the data is the effect the primary jets had on the flowfield. The annular jets only case had more scattered data than any of the other geometries. When the primary jets and annular jets were used together the resulting data was much more symmetric than in the annular jets only case. In addition, recirculation zones were much more defined with the primary jets on.

The combustor model was designed to model the primary zone of a typical gas turbine engine combustor and help understand the flow within the combustor. The objective of this thesis was to provide data that can be used to check the advantages and shortcomings of computational models. The quality of this data should be sufficient so that computational models can be checked.

4.2 Concentration Measurements

A non-intrusive technique called marker nephelometry was used to obtain concentration measurements in the combustor. The flow was seeded using atomized propylene glycol and a laser sheet as a light source for the measurements. A video camera and video cassette recorder was used to record the mixing within the combustor.

Large amounts of data was collected to help observe mixing of primary jets and annular jets. The concentration information provided by the image processing software and hardware provides qualitative information about the flow.

This flow visualization showed the flow to be very turbulent and unsteady. All geometries investigated were highly sensitive to alignment of geometry and inlet conditions. Care had to be taken to assure primary jets were aligned and the

annular jet endplate was placed perpendicular to all combustor walls in order to avoid flow asymmetries. Even after alignment of all geometries, asymmetries still were seen in concentration and velocity data.

Recirculation zones within the primary zone of the combustor are important and desired to provide adequate time for chemical reactions and uniformity throughout the entire combustor. Results from velocity and concentration measurements provide information that can be used to determine the desirability of the configurations. Recirculation zones for the primary jets only case provided good mixing upstream and downstream of the primary jet entrance. This configuration should provide enough mixing to provide flame stability within the recirculating regions. The annular and primary jets case produced much more well defined and shorter recirculation zones than either of the other configurations. This configuration would most likely provide the best results. Large concentrations were seen to exist at the annular jet exit to provide unfailing ignition and more uniformly mixed concentrations along upper and lower walls of the model providing flame stability. The worst configuration of the combustor model would be the annular jets only case. The recirculation zones along upper and lower walls had no well defined center and extended very far downstream. The recirculation zones would not provide adequate mixing within a reasonable combustor length.

This Page Intentionally Left Blank

BIBLIOGRAPHY

BIBLIOGRAPHY

[1] Khan, Z. A., Whitelaw, J. H., "Vector and Scalar Characteristics of Opposing Jets Discharging Normally into a Cross-Stream," Int. J. Heat and Mass Transfer, Vol. 23, 1980, PP. 1673-1680.

[2] Atkinson, K. N., Khan, Z. A., Whitelaw, J. H., "Experimental Investigation of Opposed Jets Discharging Normally into a Cross-Stream," J. Fluid Mech., Vol. 115, 1982, pp. 493-504.

[3] Sivasgaram, S., Whitelaw, J. H., "Flow Characteristics of Opposing Rows of Jets in a Confined Space," Proc. Inst. Mech. Engrs., Vol 200, 1986, pp. 71-75.

[4] Miau, J. J., Sun, D. J., "Visualization of Impinging Flow in a Side-Inlet Square Duct," AIAA-88-0502, 1988.

[5] Miau, J. J., Sun, D. J., Yao, L. S., "Streamwise Vorticies Generated by Impinging Flows in a Confined Duct," Experiments in Fluids, Vol. 7, 1989, pp. 497-500.

[6] Barron, D. A., "LDV Measurements in an Annular Combustor Model," MS Thesis, Purdue University, August, 1986.

[7] Seal, Michael II, D., "An Experimental Study of Swirling Flows As Applied to Annular Combustors," MS Thesis, Purdue University, May, 1988.

[8] Morgan, D., "Concentration Measurements in a Cold Flow Model Annular Combustor Using Laser Induced Fluorescence," MS Thesis, Purdue University, August, 1988.

[9] Roesler, T. C., "Investigation of Bias Errors in Laser Doppler Velocimeter Measurements, MS Thesis, Purdue University, August, 1980.

[10] Durst, F., Melling, A., Whitelaw, J. H., "Principles and Practice of Laser Doppler Anemometry," Academic Press, 1976.

[11] TSI Model 1980 Counter Type Signal Processor Manual, TSI Incorporated.

[12] TSI Model 9306 Six-Jet Atomizer Instruction Manual, TSI Incorporated, 1980.

[13] Rosensweig, H.C., Hottel, H.C., Williams, G.C., "Smoke-Scattered Light Measurements of Turbulent Concentration Fluctuations," Chemical Eng. Sci., Vol. 15, 1961, pp. 111-129.

[14] Becker, H.A., Hottel, H.C., Williams, G.C., "On Light-Scatter Technique for the Study of Turbulence and Mixing," Journal of Fluid Mechanics, Vol. 30, 1967, pp. 259-284.

[15] Becker, H.A., Hottel, H.C., Williams, G.C., "The Nozzle-Fluid Concentration Field of the Round, Turbulent, Free Jet," Journal of Fluid Mechanics, Vol. 30, 1967, pp. 285-303.

[16] Becker, H.A., "Mixing, Concentration Fluctuations, and Marker Nephelometry, "Studies in Convection, Vol. 2, edited by B.E. Launder, Academic Press, New York, 1977, pp. 45-139.

[17] Shaughnessy, E.J., Morton, J.B., "Laser Light-Scattering Measurements of Particle Concentration in a Turbulent Jet," Journal of Fluid Mechanics, Vol. 80, part 1, 1977, pp. 129-148.

[18] Long, M.B., Chu, B.T., Chang, R.K., "Instantaneous Two-Dimensional Gas Concentration Measurements by Light Scattering," AIAA Journal, Vol. 19,1981, pp. 1151-1157.

[19] Edwards, Robert V., "Report of the Special Panel on Statistical Partical Bias Problems in Laser Anemometry," Journal of Fluids Engineering, Vol. 109, pp. 89-93, June 1987.

[20] Sami, S., Carmody, T. and Rouse, H., "Jet Diffusion in the Region of Flow Establishment," Journal of Fluid Mechanics, Vol. 27. pp. 231-252.

[21] Rajaratnam, N., "Turbulent Jets," Elsevier Scientific Publishing Company, Amsterdam, 1976, pp. 115-129.

[22] Ko, N.W.M., Chan, W.T., "The Inner Regions of Annular Jets," Journal of Fluid Mechanics, Vol. 93, part 3, pp. 549-584, Nov. 1978.

[23] Kuhlman, John M., "Variation of Entrainment in Annular Jets," AIAA Journal, Vol. 25, No. 3, March 1987.

APPENDICES

Appendix A

Velocity Measurements and Statistics Calculation

Since only a one component LDV system was used to determine U, V, U', V', U'V', and K', measurements in the coordinate directions only to determine these quantities would be in error. Measurements must be taken at +/- 45° to the coordinate axes in the plane of each component. By taking measurements at +/- 45° both the U' and V' velocity fluctuations contribute to the instantaneous Doppler frequency.

Referring to figure A1 velocity measurements at +/- 45° are

$$\overline{U_{+45}} = \frac{1}{\sqrt{2}}(\overline{U} + \overline{V}) \tag{A1}$$

$$\overline{U_{-45}} = \frac{1}{\sqrt{2}}(\overline{U} - \overline{V}) \tag{A2}$$

adding equatiions A1 and A2 we have

$$\overline{U_{+45}} + \overline{U_{-45}} = \frac{2}{\sqrt{2}} \overline{U}$$

$$\overline{U} = \frac{1}{\sqrt{2}}(\overline{U_{+45}} + \overline{U_{-45}}) \tag{A3}$$

Subtracting equation A2 from A1

$$\overline{U_{+45}} - \overline{U_{-45}} = \frac{2}{\sqrt{2}}\overline{V}$$

$$\overline{V} = \frac{1}{\sqrt{2}}(\overline{U_{+45}} - \overline{U_{-45}}) \qquad \text{(A4)}$$

The instantaneous velocity, U, is made up of a mean term, $\bar{U}$, and a fluctuation term, U'. The time average of the square of equation A1 is

$$\overline{(\overline{U_{+45}} + U'_{+45})^2} = \frac{1}{2}\overline{((\overline{U} + U') + (\overline{V} + V'))^2} \qquad \text{(A5)}$$

expanding A5 results in

$$\overline{U_{+45}}^2 + \overline{U'_{+45}}^2 + 2\overline{\overline{U_{+45}}U'_{+45}} = \frac{1}{2}[\overline{(\overline{U} + U')(\overline{U} + U')}$$

$$+ \overline{(\overline{V} + V')(\overline{V} + V')} + 2\overline{(\overline{U} + U')(\overline{V} + V')}]$$

$$=\frac{1}{2}\{ \overline{U}^2 + \overline{U'^2} + 2\overline{\overline{U}\,U'} + \overline{V}^2 + \overline{V'^2} + 2\overline{\overline{V}\,V'}$$

$$+ 2(\overline{U}\,\overline{V} + \overline{U'\,V'} + \overline{\overline{U}\,V'} + \overline{\overline{V}\,U'}) \} \qquad \text{(A6)}$$

since

$$\overline{U_{+45}} = \frac{1}{\sqrt{2}}(\overline{U} + \overline{V}) \qquad\qquad U'_{+45} = \frac{1}{\sqrt{2}}(U' + V')$$

the average of the product of these terms is

$$2\overline{U_{+45}\,U'_{+45}} = \overline{U\,U'} + \overline{U\,V'} + \overline{V\,U'} + \overline{V\,V'}$$

Therefore, terms on the right side of equation A6 cancel resulting in

$$\overline{U_{+45}}^2 + \overline{U'_{+45}}^2 = \frac{1}{2}\left(\overline{U}^2 + \overline{U'^2} + \overline{V}^2 + \overline{V'^2} + 2\overline{U}\,\overline{V} + 2\overline{U'\,V'} \right) \quad \text{(A7)}$$

Squaring the mean of equation A1 results in

$$\overline{U_{+45}}^2 = \frac{1}{2}\left(\overline{U}^2 + 2\overline{U}\,\overline{V} + \overline{V}^2 \right) \quad \text{(A8)}$$

Subtracting equation A8 from equation A7 results in

$$\overline{U'^2_{+45}} = \frac{1}{2}\left(\overline{U'^2} + 2\overline{U'V'} + \overline{V'^2} \right) \quad \text{(A9)}$$

A similar result can be achieved by using the -45° component.

$$\overline{U'^2_{-45}} = \frac{1}{2}\left(\overline{U'^2} - 2\overline{U'V'} + \overline{V'^2} \right) \quad \text{(A10)}$$

By subtracting equation A10 from equation A9 a relation for the Reynolds shear stress term in the XY plane results.

$$\overline{U'V'} = \frac{1}{2}\left(\overline{U'^2_{+45}} - \overline{U'^2_{-45}} \right) \quad \text{(A11)}$$

By adding equation A10 to equation A11 a relation for the rms velocities in the two coordinate directions and the +/- 45° directions results.

$$\overline{U'^2} + \overline{V'^2} = \overline{U'^2_{+45}} + \overline{U'^2_{-45}}$$

Since measurements have been made along +/- 45° directions and the horizontal

direction can be found.

$$\overline{V'^2} = \overline{U'_{+45}{}^2} + \overline{U'_{-45}{}^2} - \overline{U'^2} \qquad \text{(A13)}$$

The two-dimensional turbulent kinetic energy term can now be calculated by

$$K' = \overline{U'^2} + \overline{V'^2} \qquad \text{(A14)}$$

The results of equation A4, A11, A13, and A14 are used to calculate the quantities of interest.

In order to allow measurements at +/- 45° the transmitting optics had to be rotated about the optical axis. This rotation limited the portion of the rig that could be measured due to beam interference with the edges of the rig resulting in no probe volume formation. Vertical travel of the probe volume was limited between .5 in. $\leq Y \leq$ 2.5 in..

Orientation of the beams with in the rig are seen in figure A2. The beam located on the optical axis was aligned parallel to the lower wall of the test rig for each measurement. This orientation will make the measurements taken not exactly along the axis intended. Figure A3 shows a sketch of measurements taken. Since the beam angle was approximately five degrees, the cosine of the half angle, 2.5 degrees, is 0.999 indicating that negligible amount of error occurs in the measurements.

From the Doppler frequency received from the signal processor computations were done to calculate a mean and rms velocity. For each data point reported an average of 10,000 samples taken at 1,000 Hz sampling frequency was used to determine the statistics. The mean velocity was calculated

by using the equation

$$\overline{U} = \frac{\sum_{i=1}^{N} U_i}{N} \tag{A15}$$

where N is the number of samples taken and U_i is the instantaneous velocity. The rms velocity was calculated using

$$U_{rms} = \left[\frac{\sum_{i=1}^{N} U_i^2 - \sum_{i=1}^{N} U_i \sum_{i=1}^{N} U_i}{N} \right]^{\frac{1}{2}} \tag{A16}$$

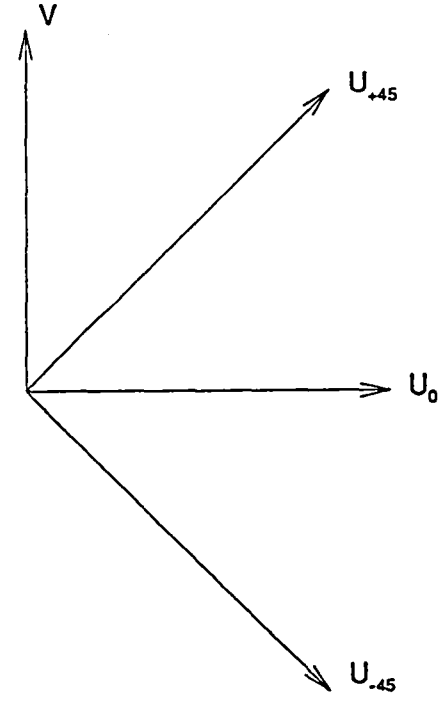

Figure A1 Velocity Measurement Coordinate Relations

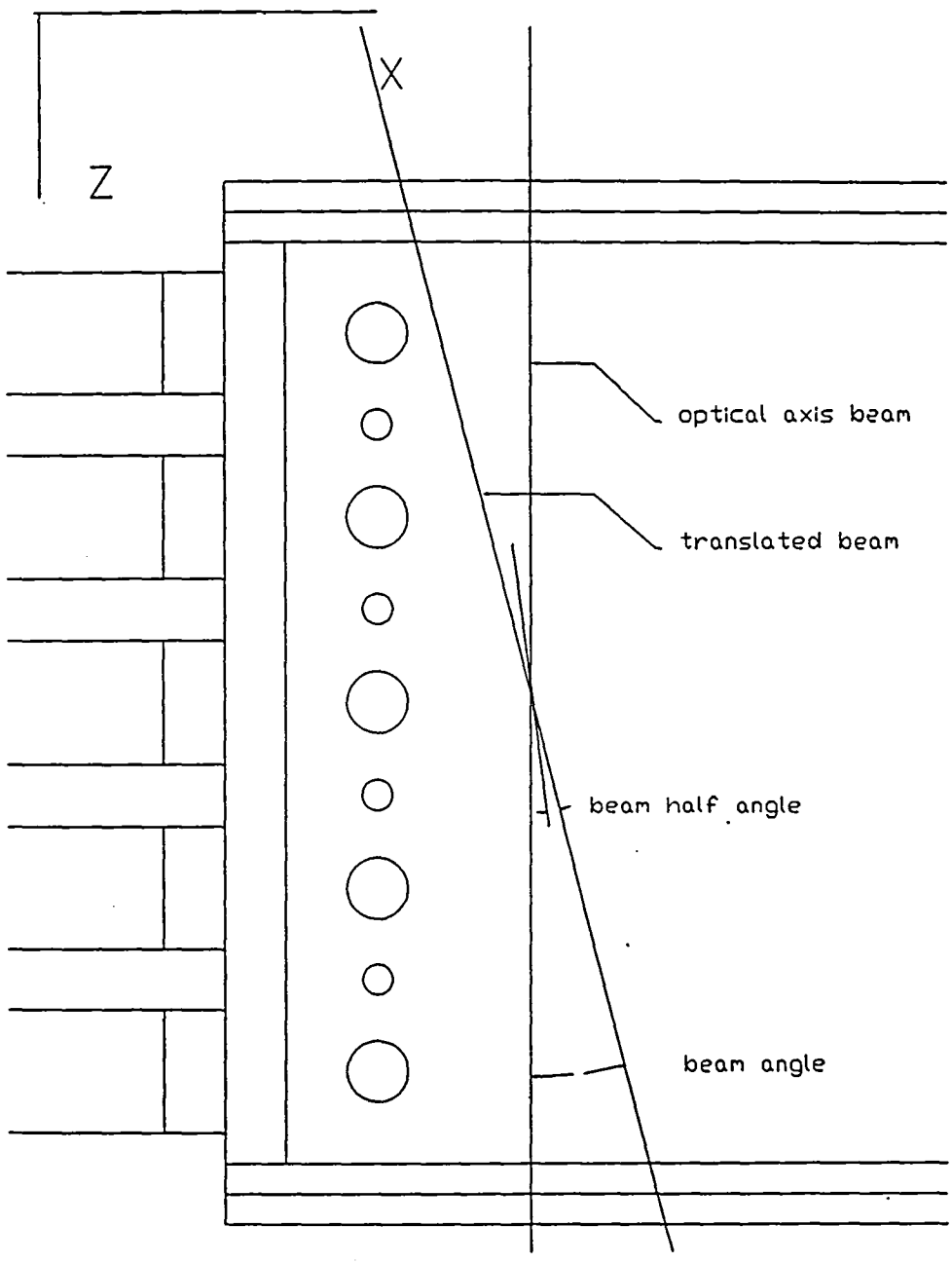

Figure A2 Orientation of Beams for Velocity Measurements

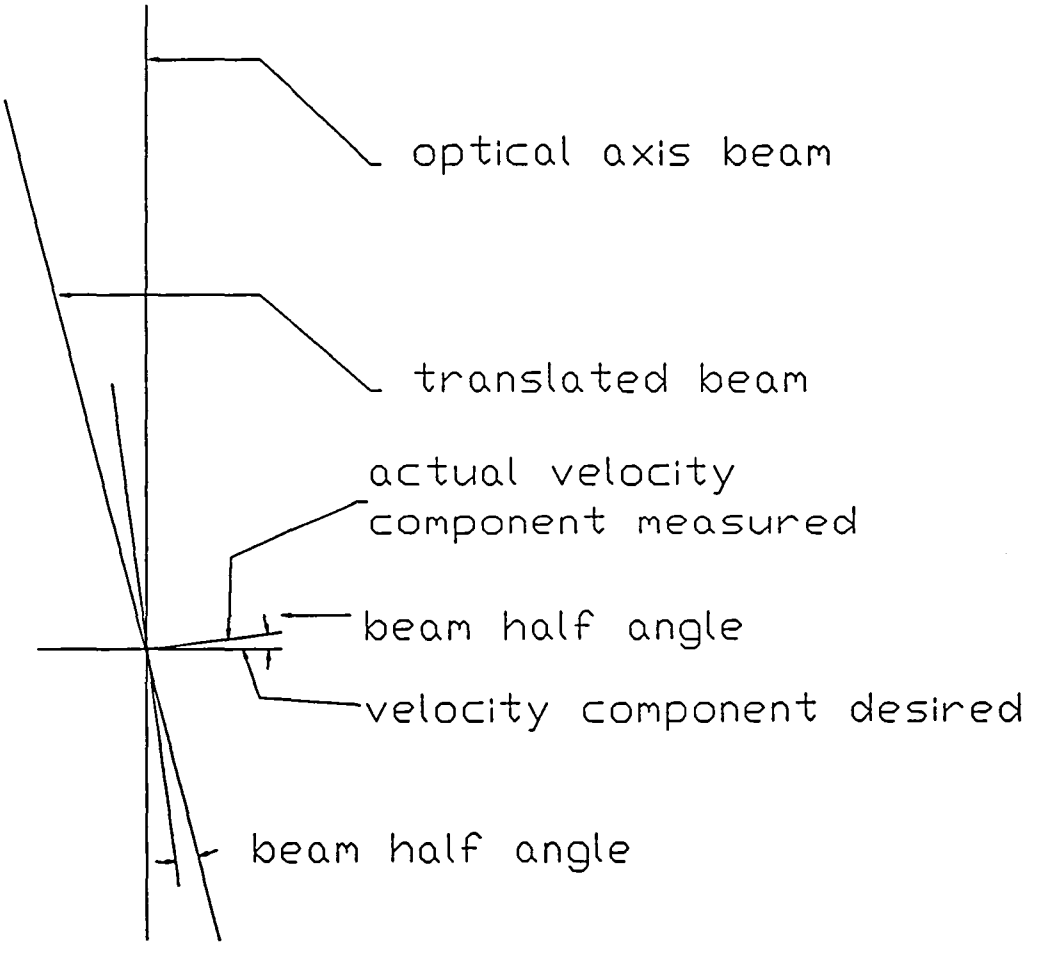

Figure A3 Actual and Desired Velocity Component Relations

Appendix B

Error Analysis

The use of a Laser Doppler Velocimeter for velocity measurements has an advantage of being non-intrusive to the flowfield. One disadvantage is that care must be taken processing data in order to avoid statistical bias problems that exist with the use of an LDV system. This section will attempt to identify some possible causes of errors that accompany the use of an LDV system and estimate the uncertainty of measurements reported in this thesis.

B1.1 Sources of Statistical Bias

Velocity bias occurs due to the arrival rate of particles in the probe volume being dependent on the flow velocity. A burst mode signal processor was used in this research, which operates on the signals generated by single particles passing through the probe volume. Therefore, particles will pass through the probe volume more often when the flow velocity is high and less when the flow velocity is low. The result of simply averaging these signals would cause the mean velocity to be biased towards high values and the rms velocity to be biased toward low values.

Many different methods are available to correct for velocity bias. This research used equal time sampling to eliminate the velocity bias. Reference [9] presents a study done on velocity bias and shows that this velocity bias may be

eliminated by using equal time sampling. Data rates for the present study varied from 10,000 to 90,000 samples per second and a sampling rate of 1,000 Hz was used. Data rates remained 10 to 90 times the sampling rate. With these data rates, equal time should exist between samples.

Filter bias occurs because the tendency of real systems to have measurement efficiency dependent on the flow velocity. If flow velocities produce a frequency outside of the processors frequency range this particle will not be processed. A biased average will exist if Doppler frequencies are outside the filter settings since these frequencies will not be processed.

For this research, velocity ranges were between +/- 35 feet per second. The frequencies produced by these particles were well within the frequency response of the processor and filter settings were set to have a flat response in these frequencies.

Angle or fringe bias is caused since processors can not measure all velocities at all angles. Counter processors use a preset number of fringes that must be crossed by a particle before a signal is accepted as valid. Therefore, some particle trajectories may not cross the required number of fringes. The flow angle range over which particles will be measured is called the acceptance angle. To correct for this bias it is desired to have the measurement system capable of measuring all flow angles encountered. According to reference [19], by using a Bragg cell with fringe velocity twice the maximum Doppler frequency this error can be corrected. A maximum Doppler frequency of 2 MHz was encountered in the

research and a Bragg cell shift of 40 MHz was used. No angle bias should exist.

Gradient bias occurs due to having a finite probe volume size and the possible existence of several different velocities in the probe volume at one time. This error is ignored in this analysis, but with an average probe volume length of 0.06 inches this error is very small compared to others.

B1.2 Uncertainty Errors

Uncertainty of measured values occur due to finite resolution of measuring devices used to determine constants and settings on equipment used in the data reduction process. Equation B1 shows the relationship between the Doppler frequency, beam angle, and wavelength of laser light used to determine the flow velocity.

$$U = \frac{\lambda}{2 \sin\left(\frac{\theta_B}{2}\right)} f_d \qquad \text{(B1)}$$

Uncertainties exist in the calculated mean velocity due to beam angle calculation and resolution of the processor to provide the Doppler frequency. In addition, a sampling error exists due to a finite number of samples being taken and an error due to rotation of the optics at +/- 45 degrees. All contribute to the total uncertainty of the velocities reported. These individual uncertainties were added together to provide a total uncertainty in reported values by the sum of squares technique, equation B2.

$$\Delta U_{tot} = \sqrt{(\Delta U_{\theta})^2 + (\Delta U_{f_D})^2 + (\Delta U_{samp})^2 + (\Delta U_{rot})^2} \qquad \text{(B2)}$$

B1.1.1 Beam Angle Uncertainty

The uncertainty due to the measurement of the beam angle is calculated by using equation B3.

$$\frac{\partial U}{\partial \Theta} = \frac{-\lambda f_D}{4} \frac{\cos\left(\frac{\Theta_B}{2}\right)}{\sin^2\left(\frac{\Theta_B}{2}\right)} \Delta\Theta \qquad \text{(B3)}$$

For a beam half angle of 2.5° and $\Delta\Theta$=.1° (0.001745 radians), an uncertainty was calculated for a representative case at X=2 in., Z=7.5 in. for the annular and primary jets case. Figure B1 shows the results of this calculation on the mean velocity.

B1.1.2 Frequency Uncertainty

The uncertainty due to the processor frequency resolution was determined by equation B4.

$$\frac{\partial U}{\partial f_D} = \frac{\lambda}{2 \sin\left(\frac{\Theta_B}{2}\right)} \Delta f_D \qquad \text{(B4)}$$

The uncertainty in Doppler frequency comes from taking the partial derivative of equation B5 with respect to the digital mantissa, D_m.

$$f_D = \frac{N \times 10^9}{D_m \times 2^{(n-2)}} \tag{B5}$$

where N =number of cycles per burst

D_m= digital mantissa

n = exponent

resulting in

$$\frac{\partial f_D}{\partial D_m} = \frac{N \times 10^9}{D_m^2 \cdot 2^{(n-2)}} \Delta D_m \tag{B6}$$

The resolution of the digital mantissa is 1 bit in 4096, ΔD_m=1. Substituting the result of equation B6 into equation B4 and rearranging results in

$$\Delta U_{f_D} = \frac{\lambda}{2 \sin\left(\frac{\Theta_B}{2}\right)} \frac{f_D^2 \, 2^{(n-2)}}{N \times 10^9} \Delta D_m \tag{B7}$$

For a beam angle of 2.5°, the uncertanties due only to the frequency resolution of the mean velocity is seen in figure B2.

B1.1.3 Sampling Uncertainty

Since only a finite number of samples were taken to determine the mean velocity, a sampling error will exist. If an infinite number of samples were taken the true mean would have been reported and therefore this error would no longer exist. The 95% confidence interval for the mean velocity is

$$\bar{U} - 1.96 \frac{U_{rms}}{\sqrt{N}} \leq \bar{U}_T \leq \bar{U} + 1.96 \frac{U_{rms}}{\sqrt{N}} \qquad \text{(B8)}$$

where U_{rms} = root mean square velocity

$\bar{U}$ = sampled mean velocity

N = number of samples

$\bar{U}_T$ = true mean velocity

For the root-mean-square velocity the 95% interval is

$$\frac{\overline{U_{rms}}}{1 + \frac{1.96}{\sqrt{2(N-1)}}} < \overline{U_{rms_T}} < \frac{\overline{U_{rms}}}{1 + \frac{1.96}{\sqrt{2(N-1)}}}$$

where U_{rmsT} is the true root-mean-square velocity.

$$U_i = U_1\cos(a_1) + U_2\cos(a_2) \tag{B10}$$

$$\overline{U_i'^2} = \overline{U_1'^2}\cos^2(a_1) + \overline{U_2'^2}\cos^2(a_2) + 2\overline{U_1'U_2'}\cos(a_1)\cos(a_2) \tag{B11}$$

Equation B10 is used to relate the mean velocities measured along lines at angles of +/- 45° and 0° to the axial coordinate (X-axis). Equation B11 is the relation between the fluctuating velocity components of the velocities measured at angles to the coordinate axis.

Equations B10 & B11 can be put into matrix form and solved for the calculated quantities $\overline{V}$, $\overline{V'}$, and U'V'.

$$\begin{bmatrix} \overline{U_0} \\ \overline{U_{+45}} \\ \overline{U_{-45}} \end{bmatrix} = \begin{bmatrix} \cos(a_{1X}) & \sin(a_{1X}) \\ \cos(a_{2X}) & \sin(a_{2X}) \\ \cos(a_{3X}) & \sin(a_{3X}) \end{bmatrix} \begin{bmatrix} \overline{U} \\ \overline{V} \end{bmatrix} \tag{B12}$$

$$\begin{bmatrix} \overline{U_0'^2} \\ \overline{U_{+45}'^2} \\ \overline{U_{-45}'^2} \end{bmatrix} = \begin{bmatrix} \cos^2(a_{1x}) & \sin^2(a_{1x}) & \cos(a_{1x})\sin(a_{1x}) \\ \cos^2(a_{2x}) & \sin^2(a_{2x}) & \cos(a_{2x})\sin(a_{2x}) \\ \cos^2(a_{3x}) & \sin^2(a_{3x}) & \cos(a_{3x})\sin(a_{3x}) \end{bmatrix} \begin{bmatrix} \overline{U'^2} \\ \overline{V'^2} \\ 2\overline{U'V'} \end{bmatrix} \tag{B13}$$

Where a_{ix} is the angle of measurement i with the X-axis. By making the assumption that the measurements along the X-axis is correct and no correction is needed, then equation B12 becomes

To determine uncertainties in V, V', and U'V', 0° is substituted into angle a_{1x} and +/- 45° +/-0.5° is substituted into angles a_{2x} and a_{3x}. These matrices can then

$$\begin{bmatrix} \overline{U_{+45}} \\ \overline{U_{-45}} \end{bmatrix} = \begin{bmatrix} \cos(a_{2x}) & \sin(a_{2x}) \\ \cos(a_{3x}) & \sin(a_{3x}) \end{bmatrix} \begin{bmatrix} \overline{U} \\ \overline{V} \end{bmatrix} \quad \text{(B14)}$$

be manipulated into equations relating calculated quantities to measured quantities. Relations in the following form result.

$$\overline{V} = C_1\overline{U_{+45}} + C_2\overline{U_{-45}}$$

$$\overline{V'} = C_3\overline{U_0} + C_4\overline{U_{+45}} + C_5\overline{U_{-45}}$$

$$\overline{U'V'} = C_6\overline{U_0} + C_7\overline{U_{+45}} + C_8\overline{U_{-45}}$$

These relations were then subtracted from the equations derived in Appendix A to result in the uncertainty due to rotating the optics. Figures B4-B6 show the uncertainty due to rotating the optics for V, V', and U'V' respectively.

B1.1.5 Total Uncertainty

Total uncertainty due to all previous sources are then calculated by using equation B2. Figures B7-B12 represents the total uncertainty for U, U', V, V', U'V', and K'.

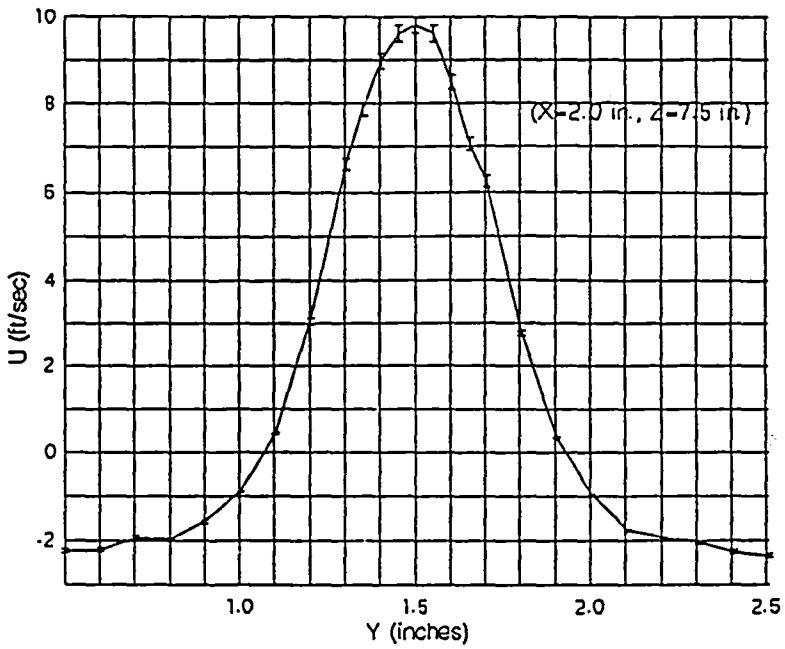

Figure B1 $\bar{U}$ Velocity Error Due to Uncertainty in Beam Angle

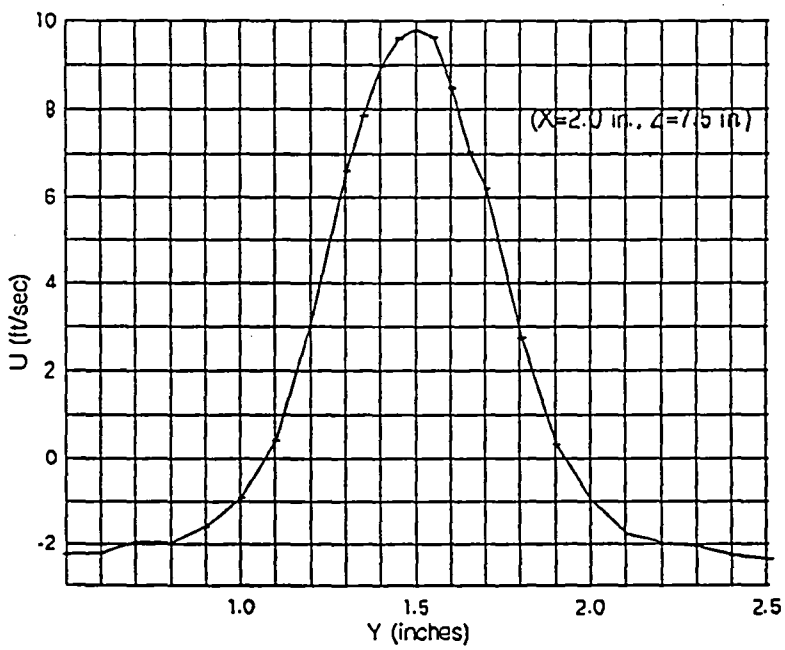

Figure B2 $\bar{U}$ Velocity Error Due to Frequency Resolution

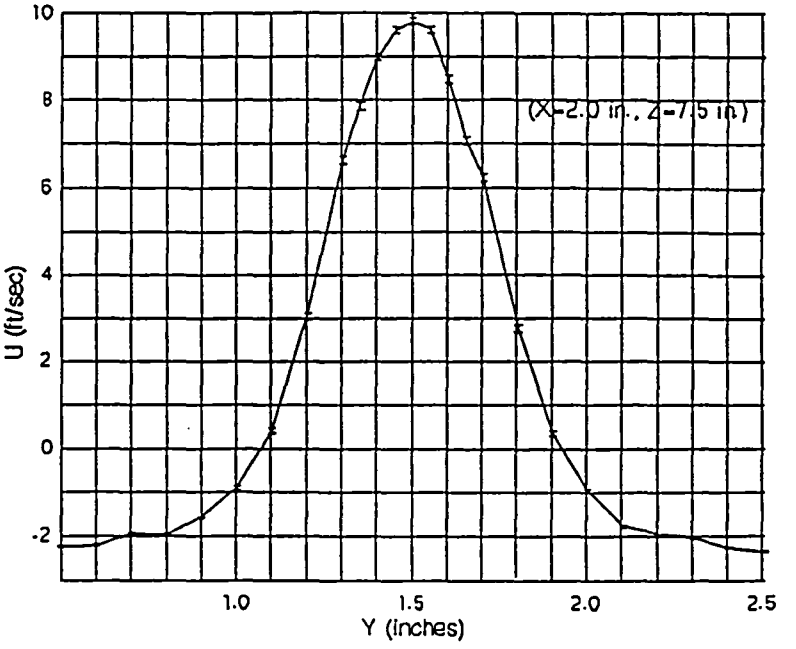

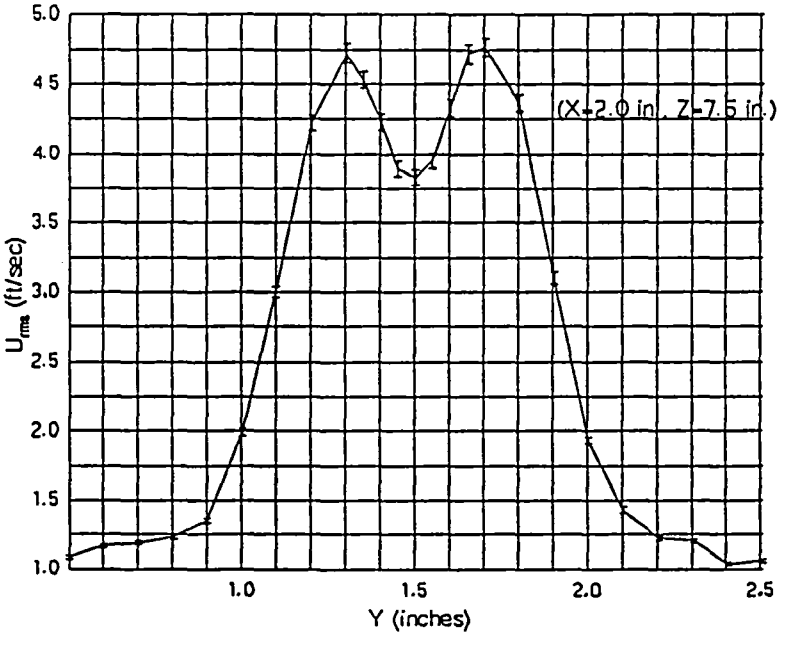

Figure B3 $\bar{U}$ and U_{rms} Velocity Error Due to Sampling Uncertainty

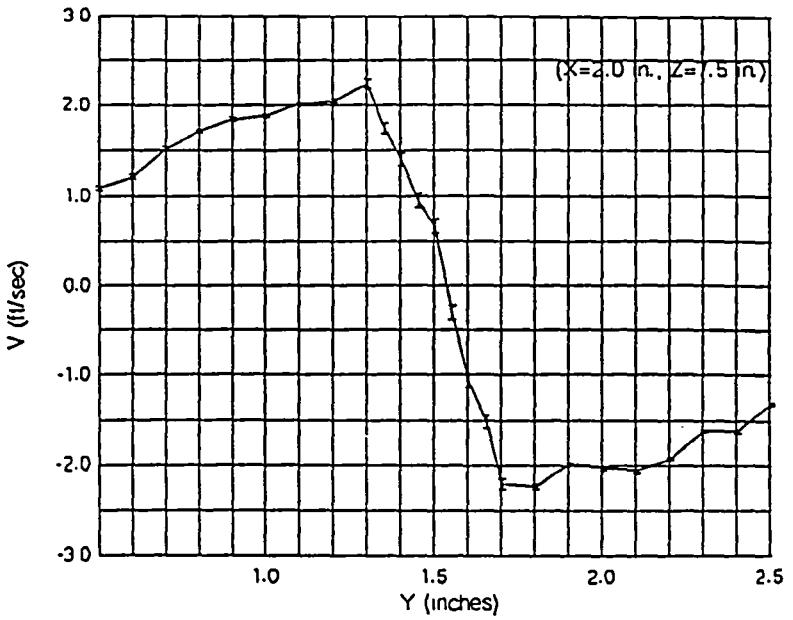

Figure B4 $\bar{V}$ Error Due to Rotation of Optics

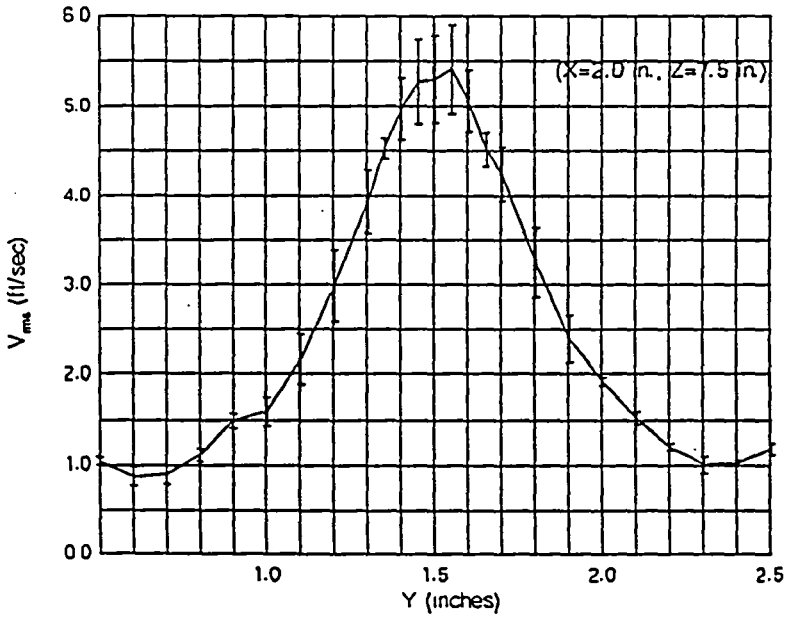

Figure B5 V_{rms} Velocity Error Due to Rotation of Optics

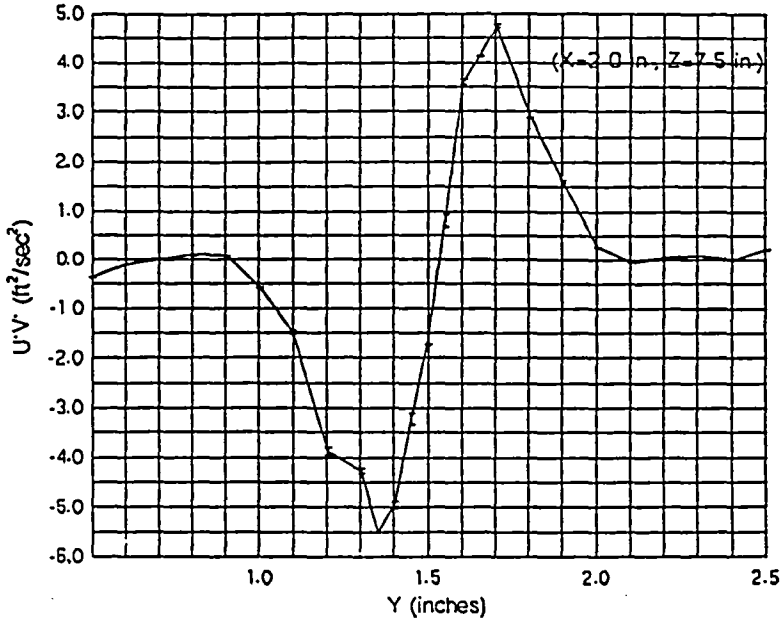

Figure B6 U'V' Error Due to Rotation of Optics

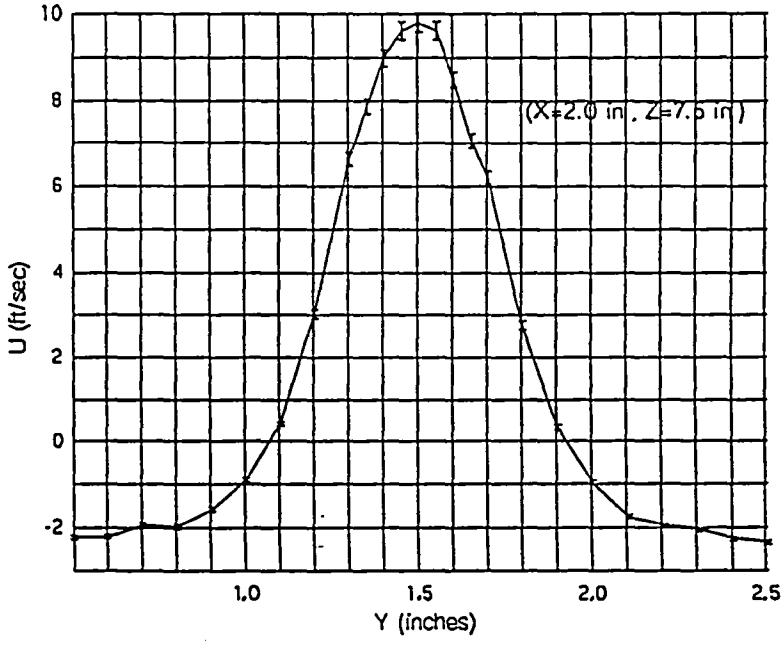

Figure B7 Total $\bar{U}$ Velocity Error

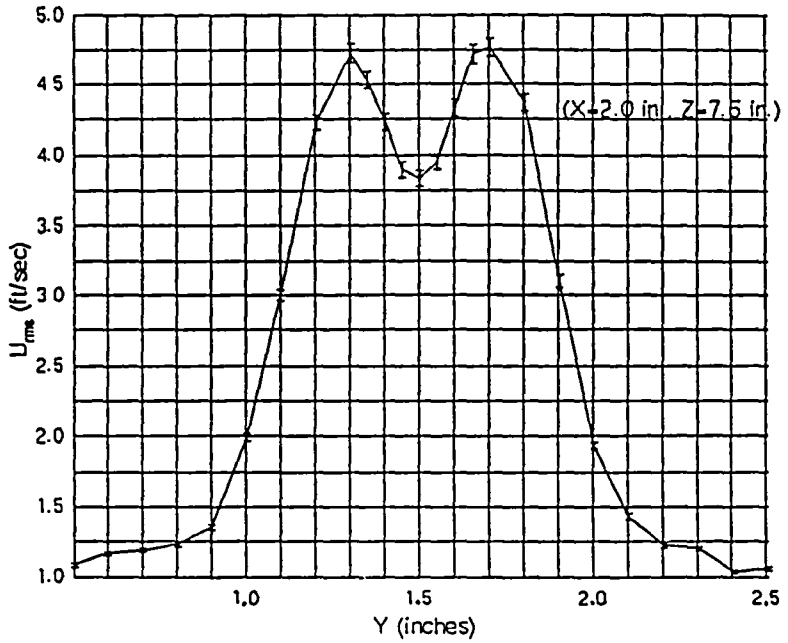

Figure B8 Total U_{rms} Velocity Error

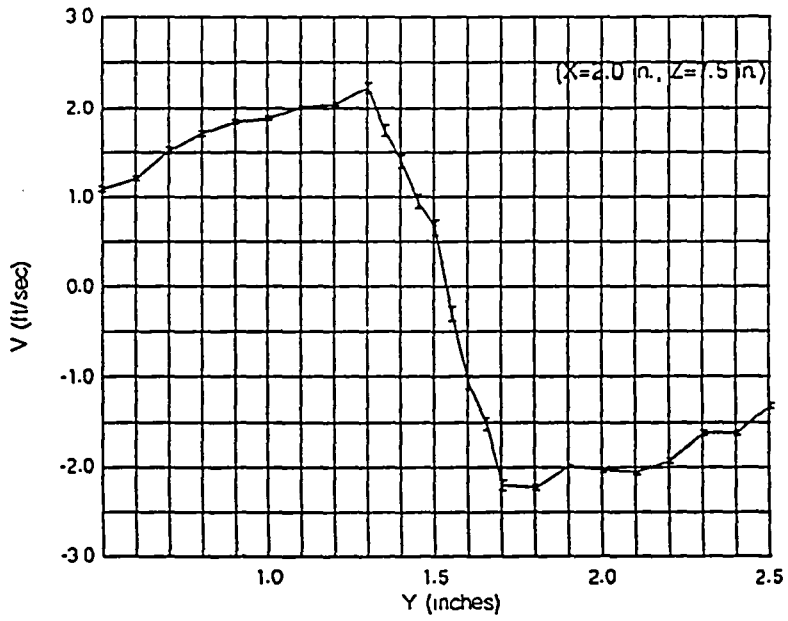

Figure B9 Total $\bar{V}$ Velocity Error

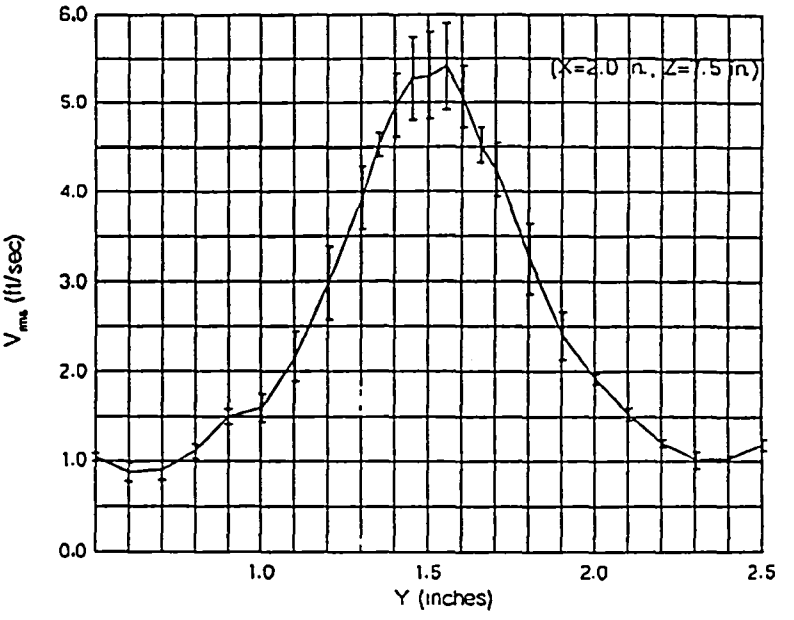

Figure B10 Total V_{rms} Velocity Error

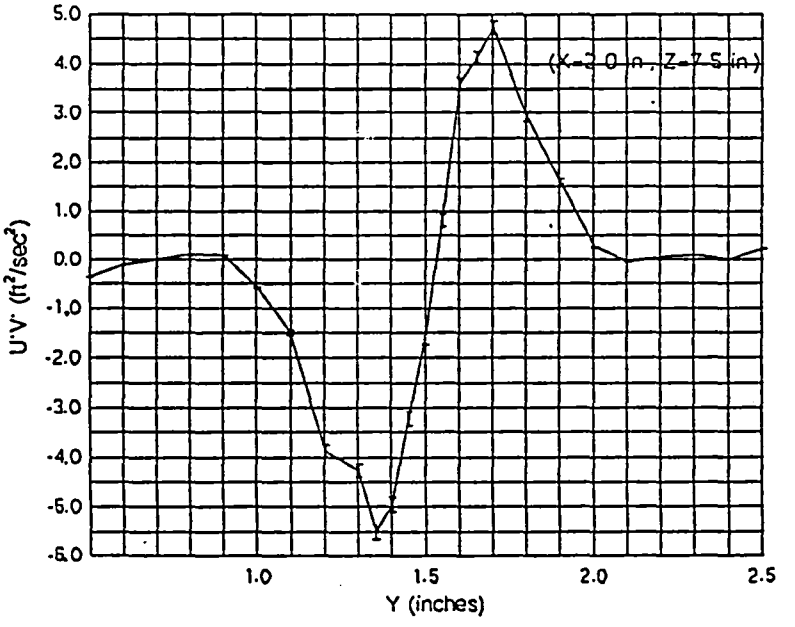

Figure B11 Total U'V' Error

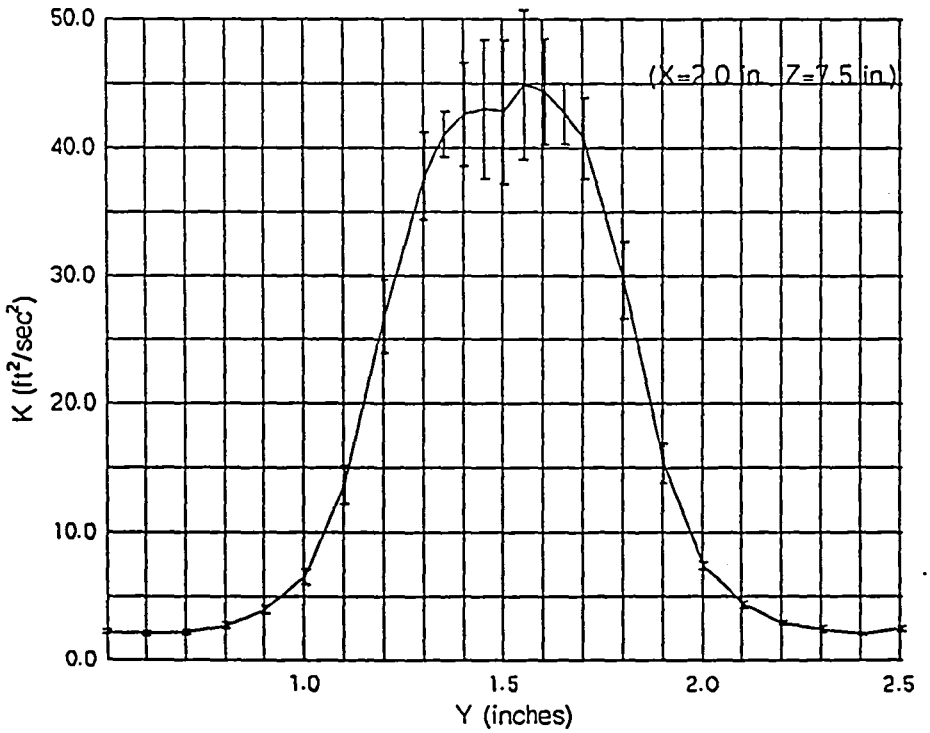

Figure B12 Total Turbulent Kinetic Energy Error

Appendix C

Additional Plots

Additional vector plots, contour plots, and line plots are contained in this appendix for the three different configurations on the combustor investigated.

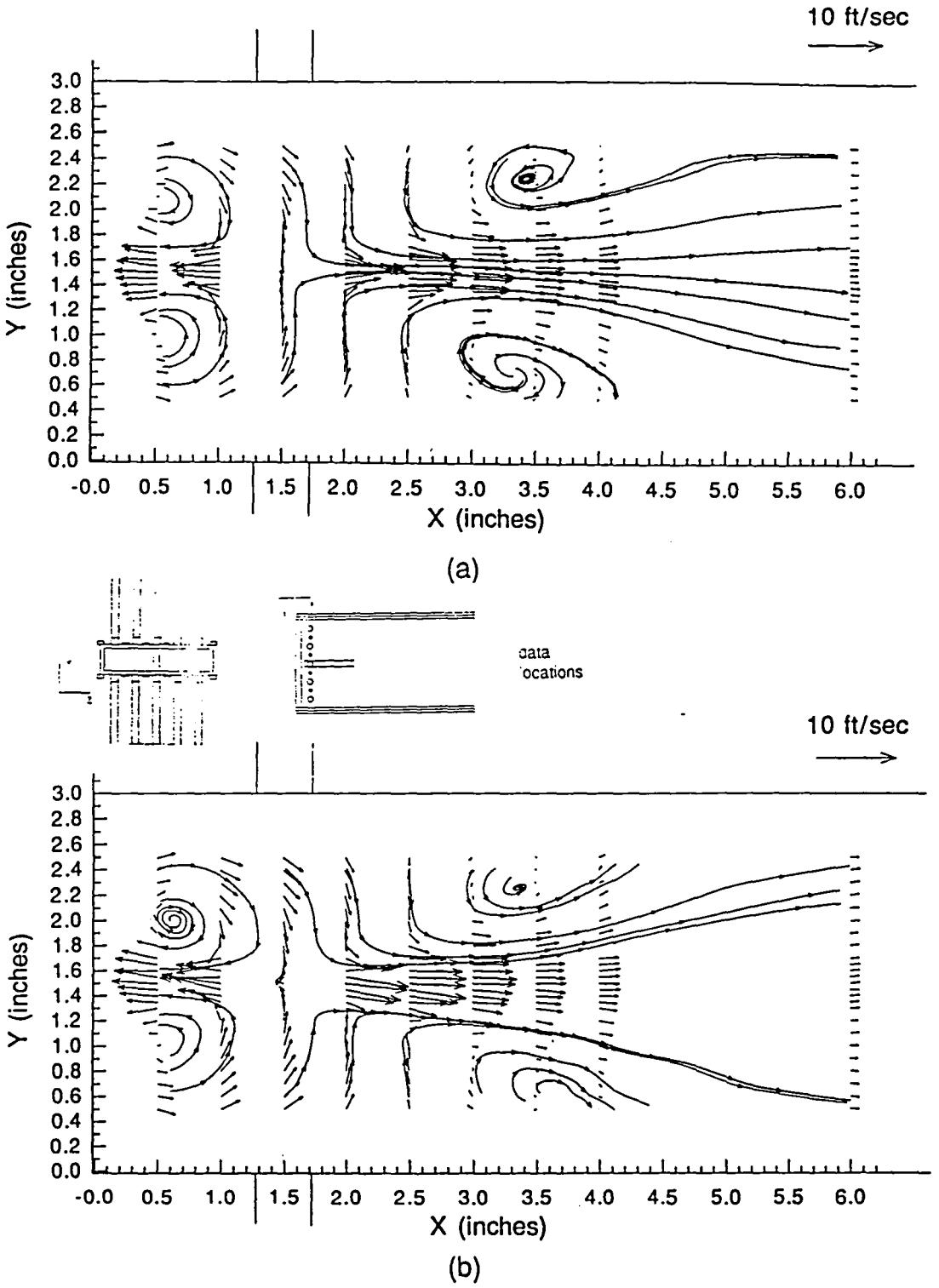

Figure C1 Primary Jets Only Mean Velocity Vector Plots
a) Z=7.0 in.; b) Z=8.0 in.

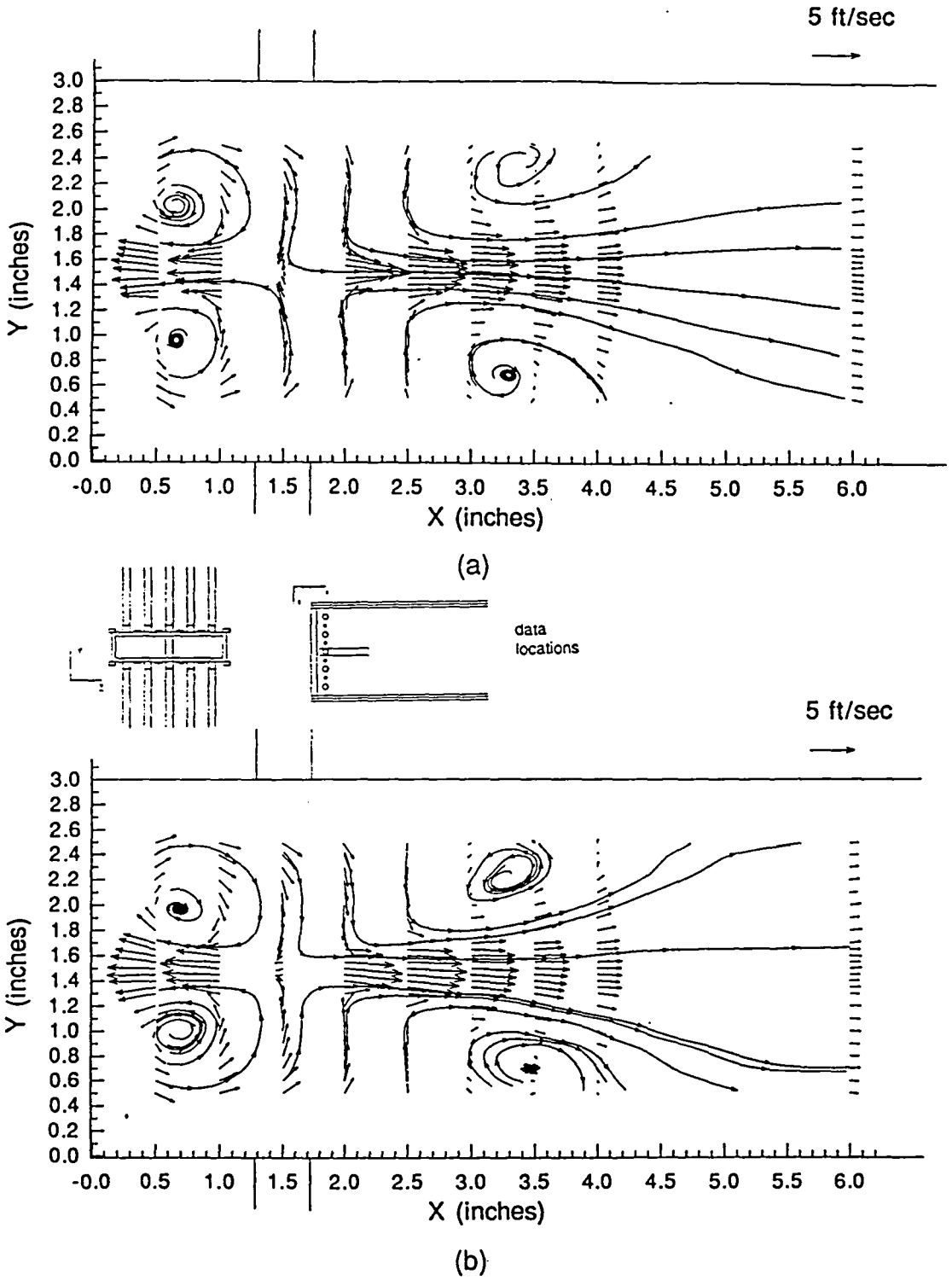

Figure C2 Primary Jets Only Mean Velocity Vector Plots
a) Z=6.9 in.; b) Z=8.1 in.

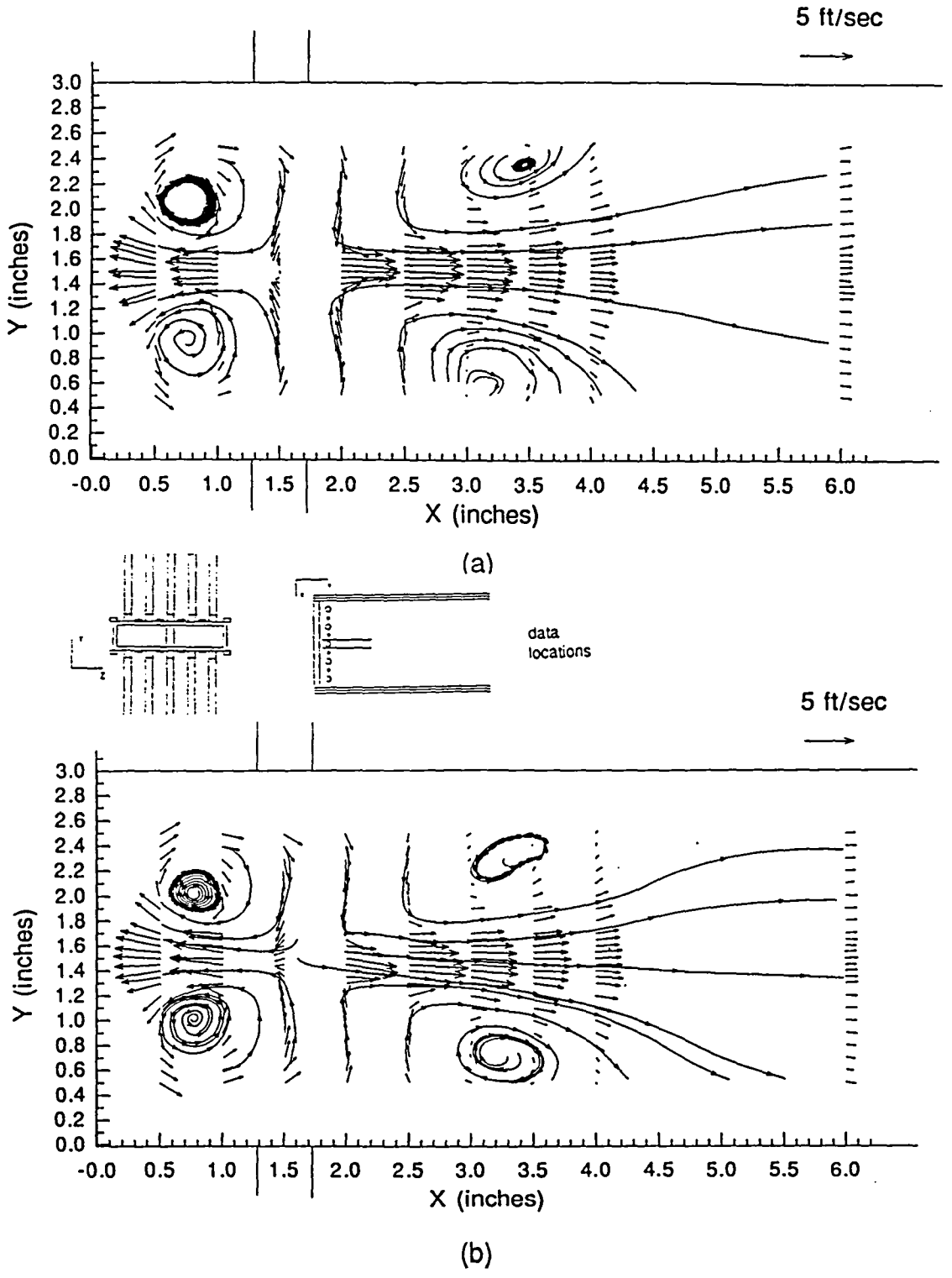

Figure C3 Primary Jets Only Mean Velocity Vector Plots
a) Z=6.8 in.; b) Z=8.2 in.

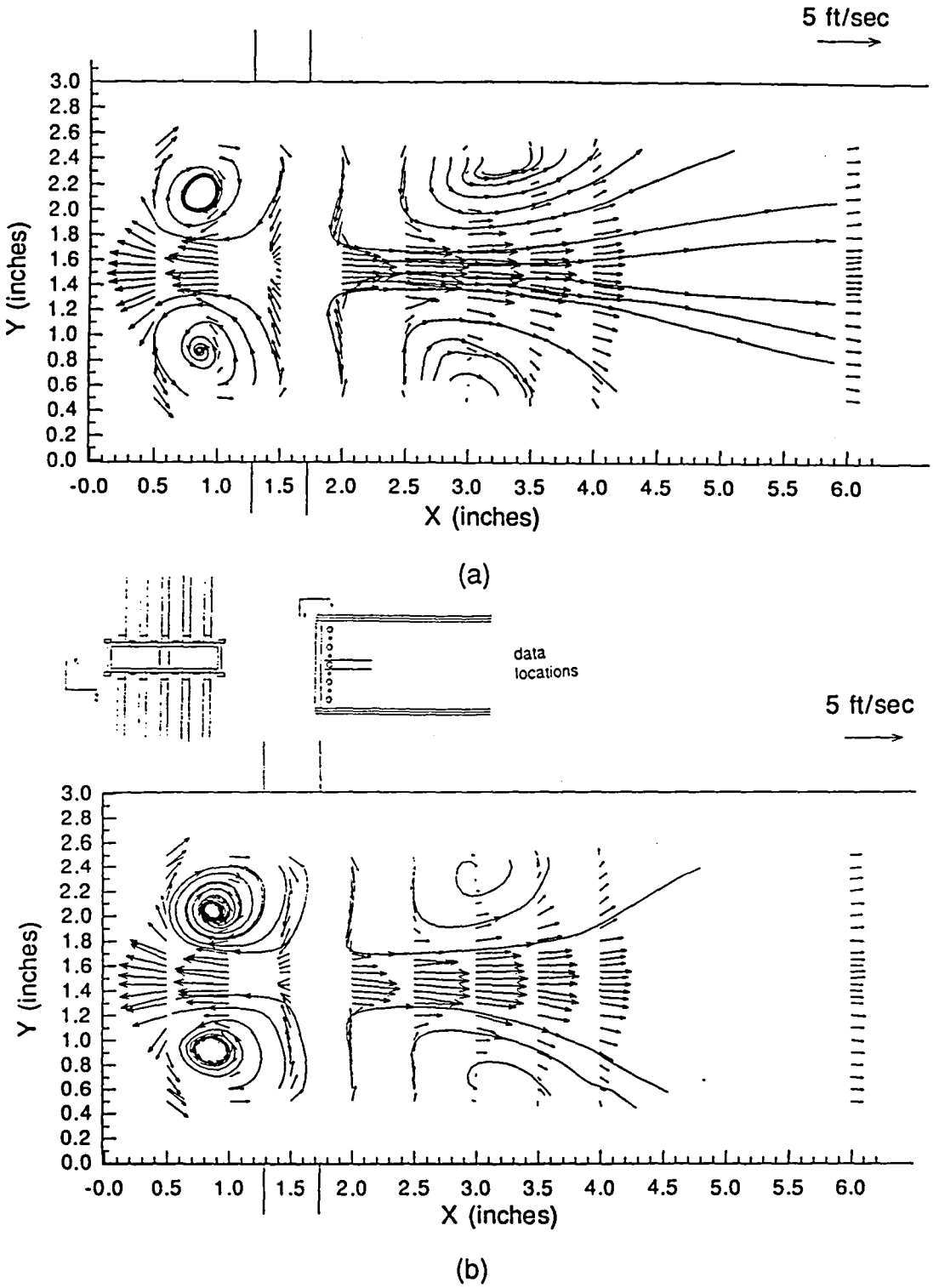

Figure C4 Primary Jets Only Mean Velocity Vector Plots
a) Z=6.7 in.; b) Z=8.3 in.

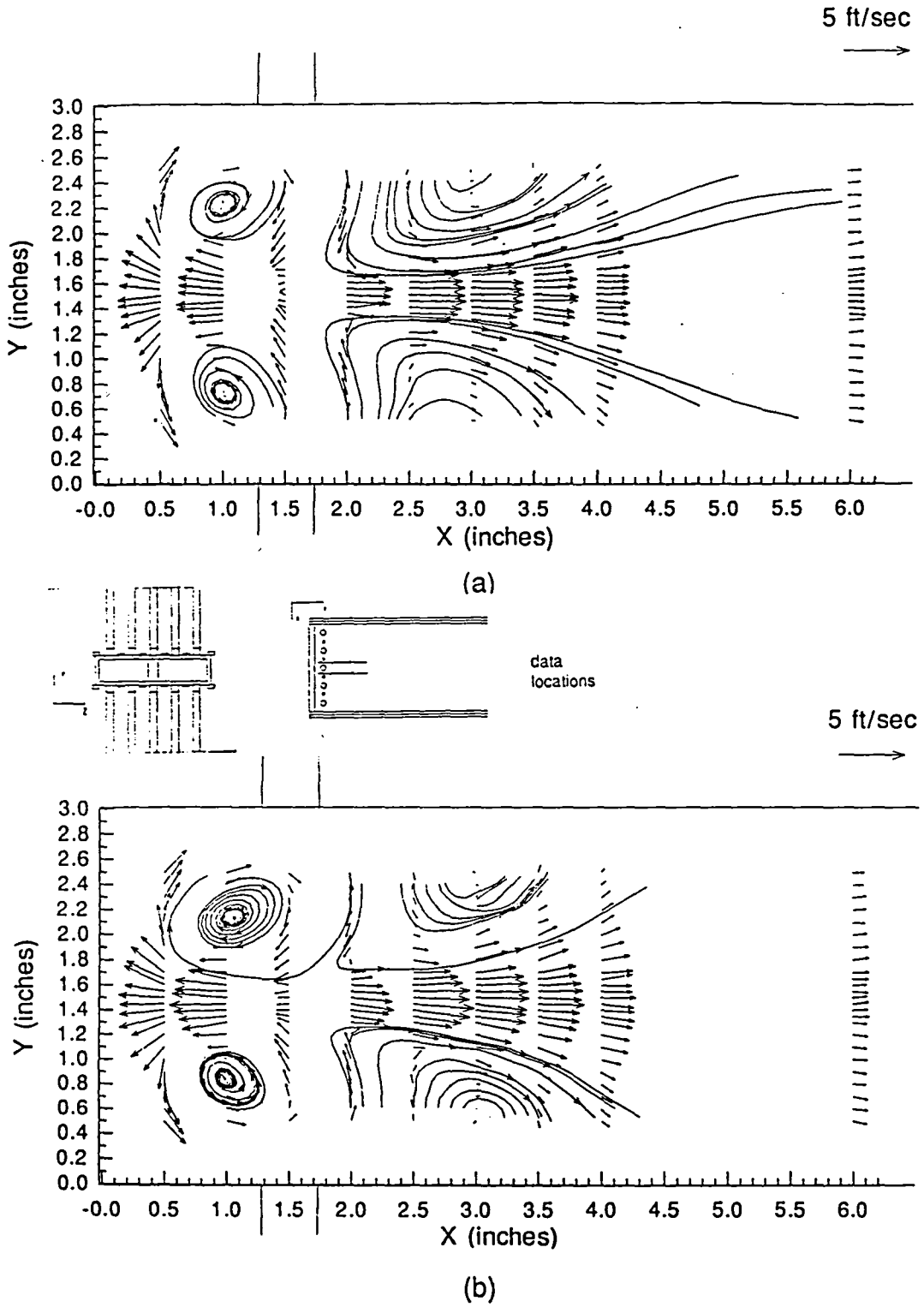

Figure C5 Primary Jets Only Mean Velocity Vector Plots
a) Z=6.6 in.; b) Z=8.4 in.

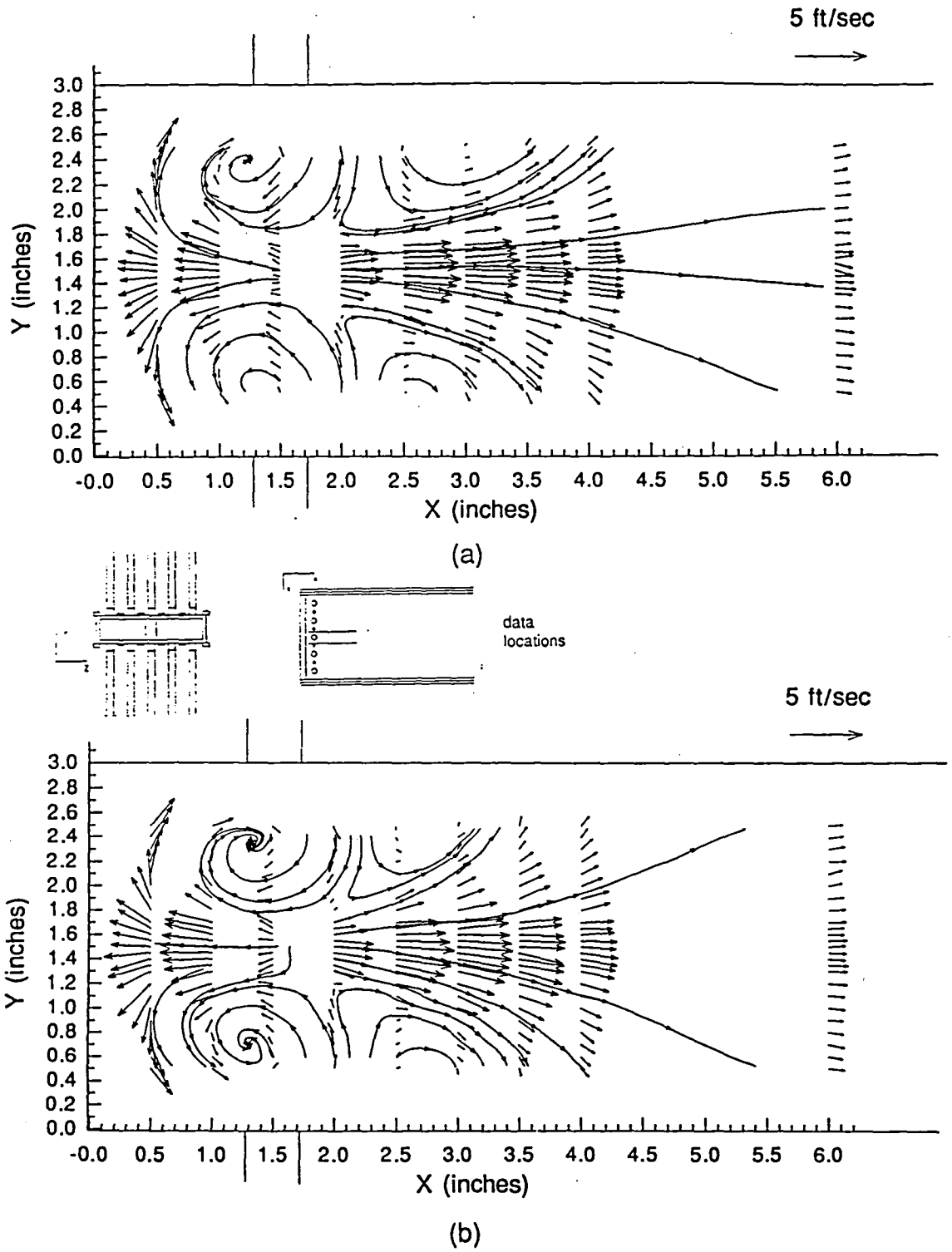

Figure C6 Primary Jets Only Mean Velocity Vector Plots
a) Z=6.5 in.; b) Z=8.5 in.

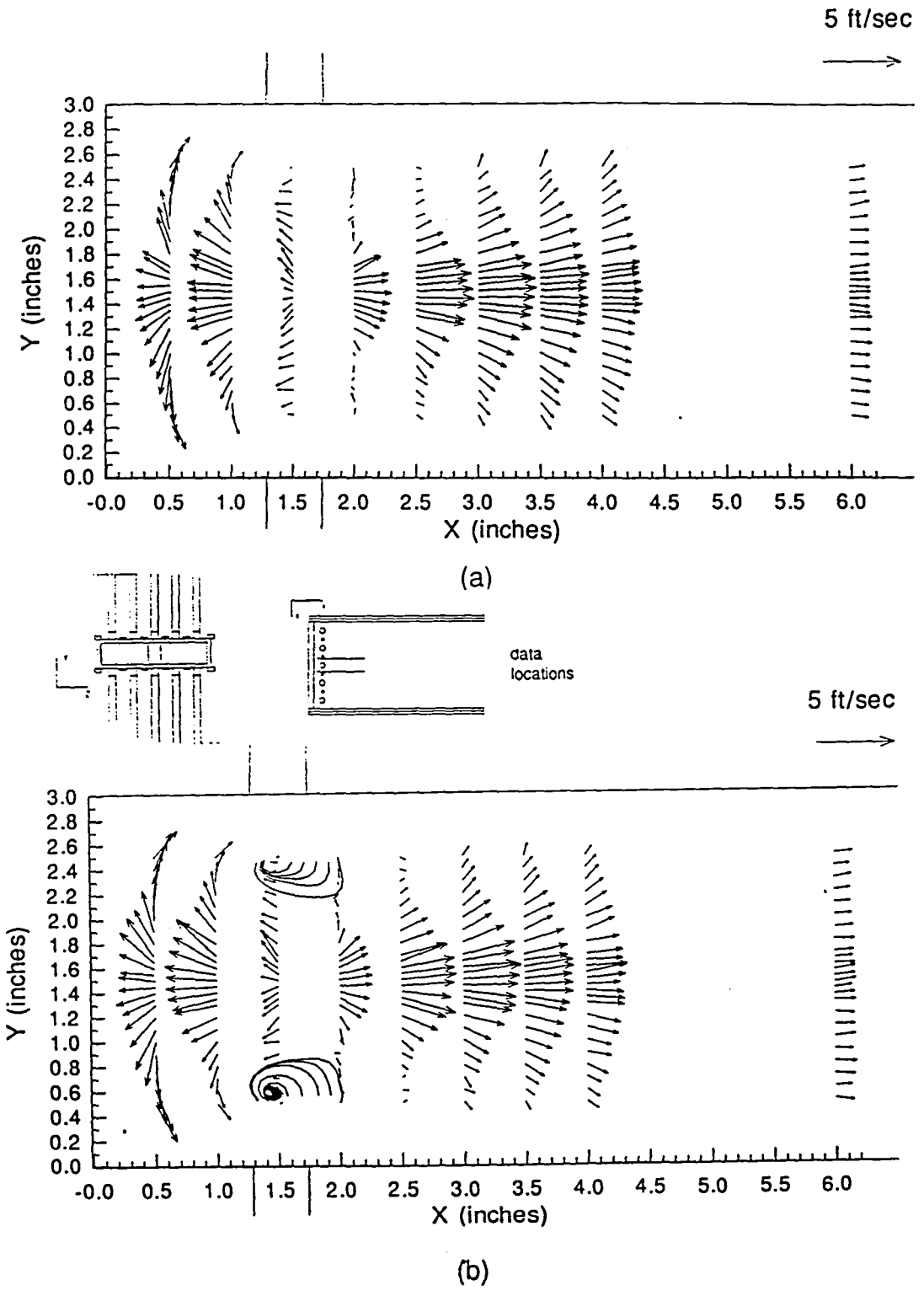

Figure C7 Primary Jets Only Mean Velocity Vector Plots
a) Z=6.4 in.; b) Z=8.6 in.

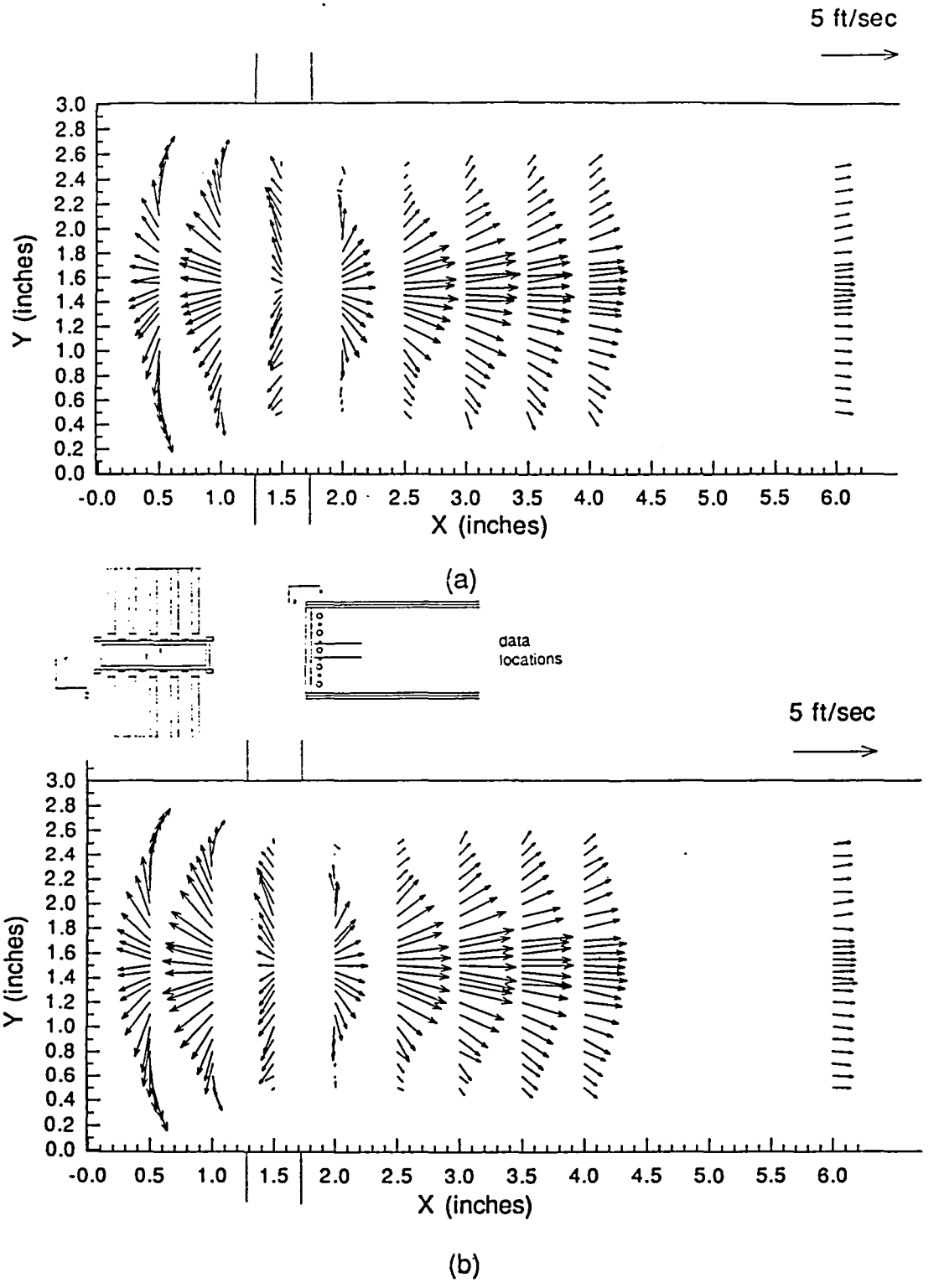

Figure C8 Primary Jets Only Mean Velocity Vector Plots
a) Z=6.3 in.; b) Z=8.7 in.

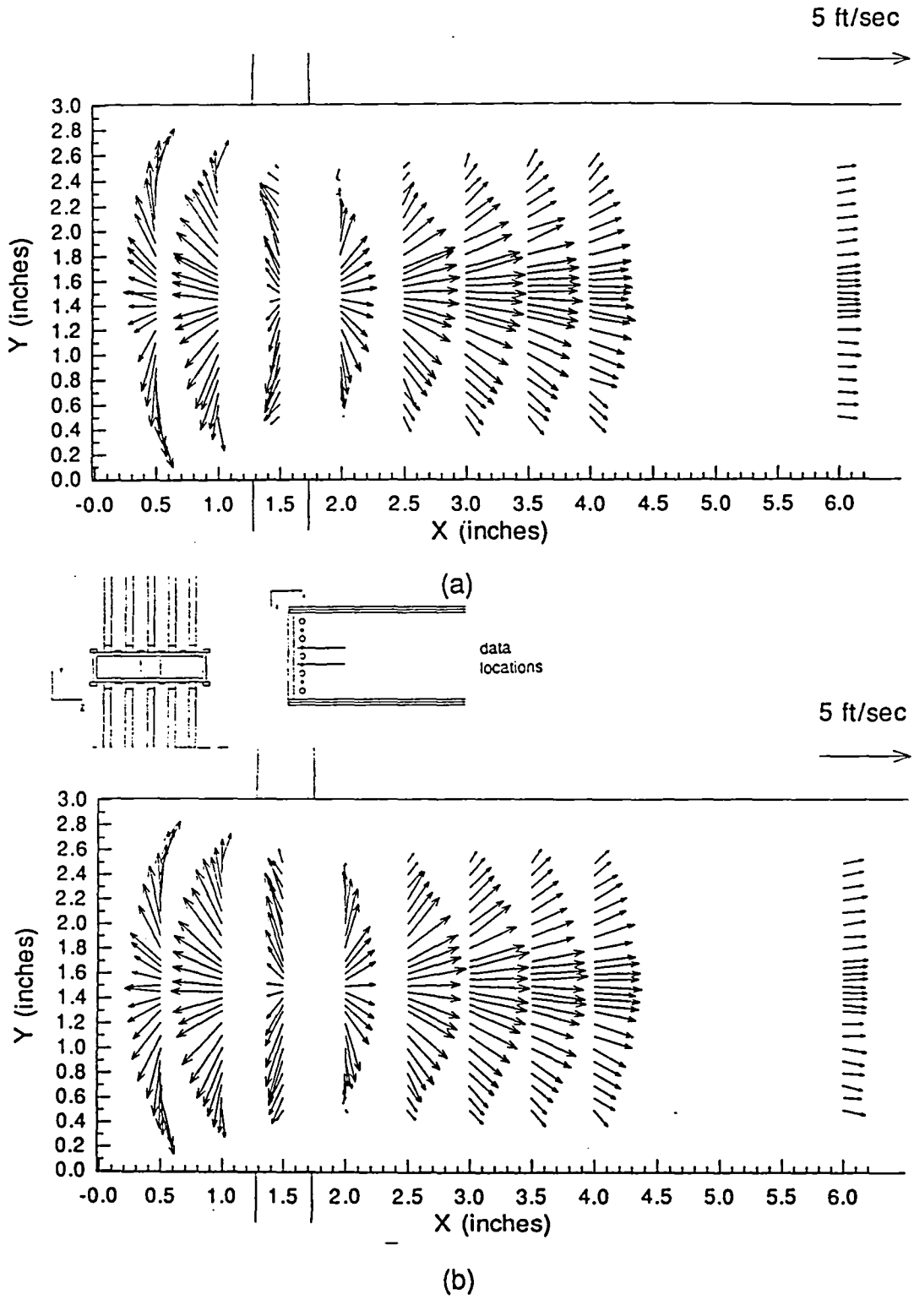

Figure C9 Primary Jets Only Mean Velocity Vector Plots
a) Z=6.2 in.; b) Z=8.8 in.

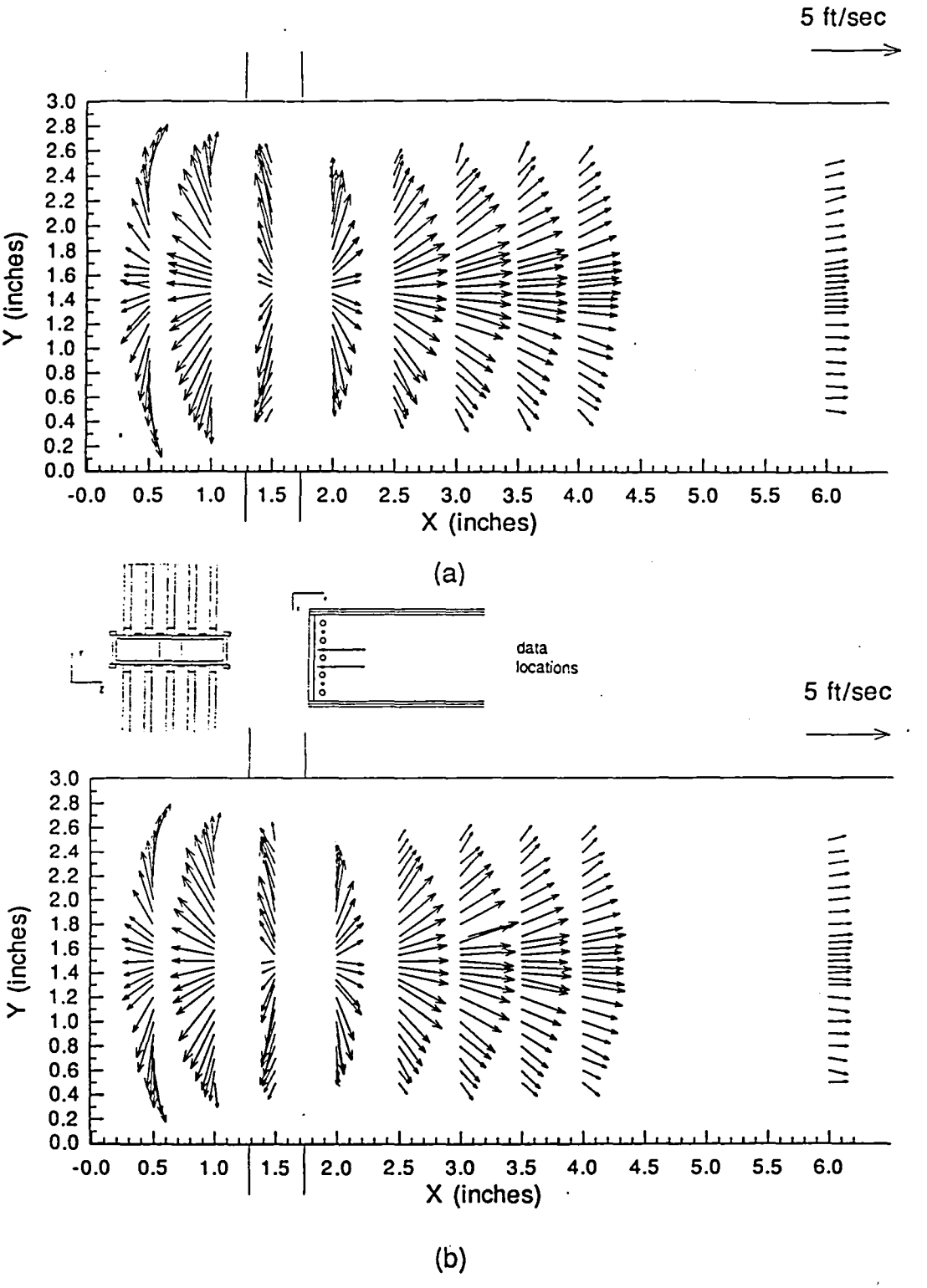

Figure C10 Primary Jets Only Mean Velocity Vector Plots
a) Z=6.1 in.; b) Z=8.9 in.

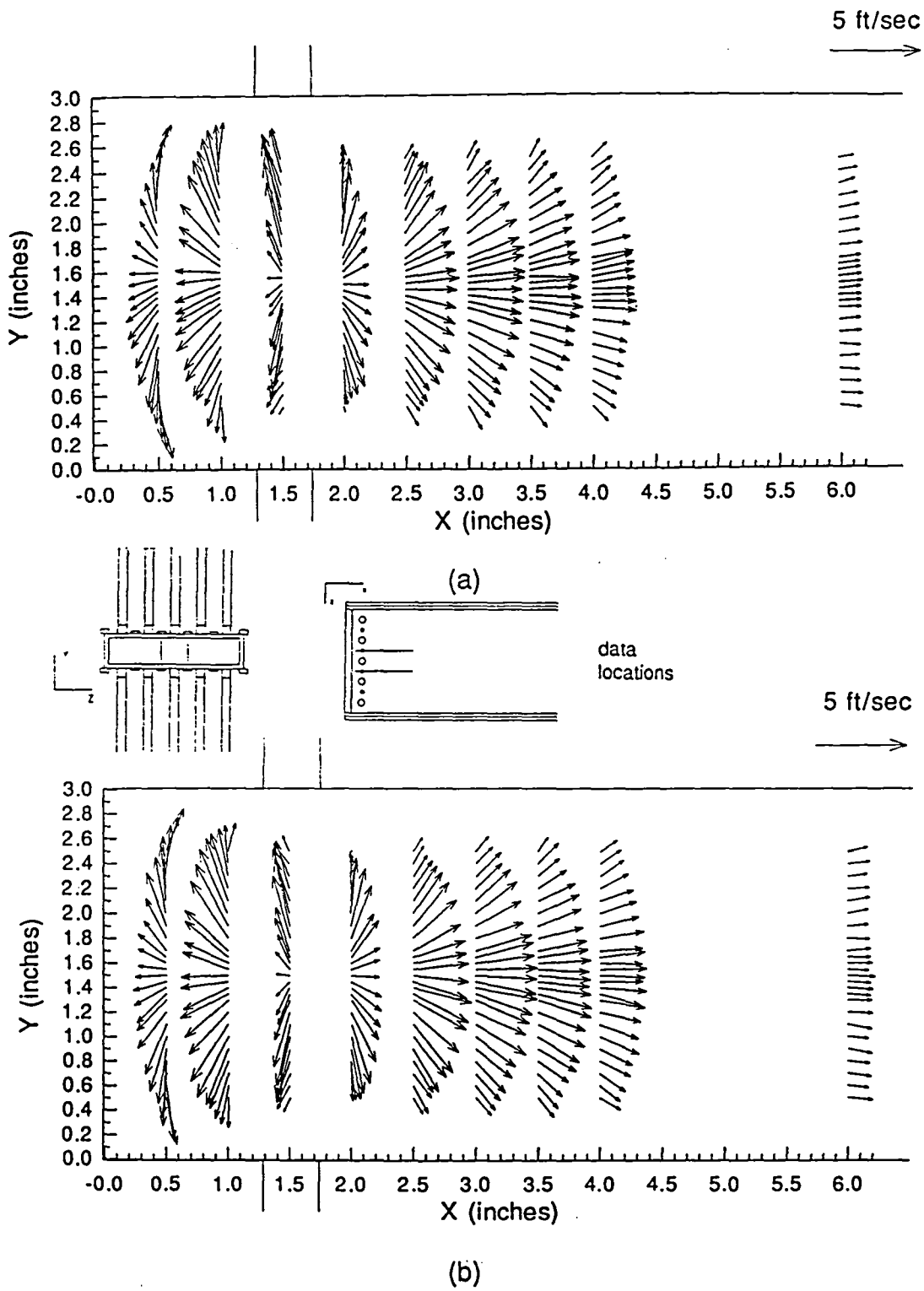

Figure C11 Primary Jets Only Mean Velocity Vector Plots
a) Z=6.0 in.; b) Z=9.0 in.

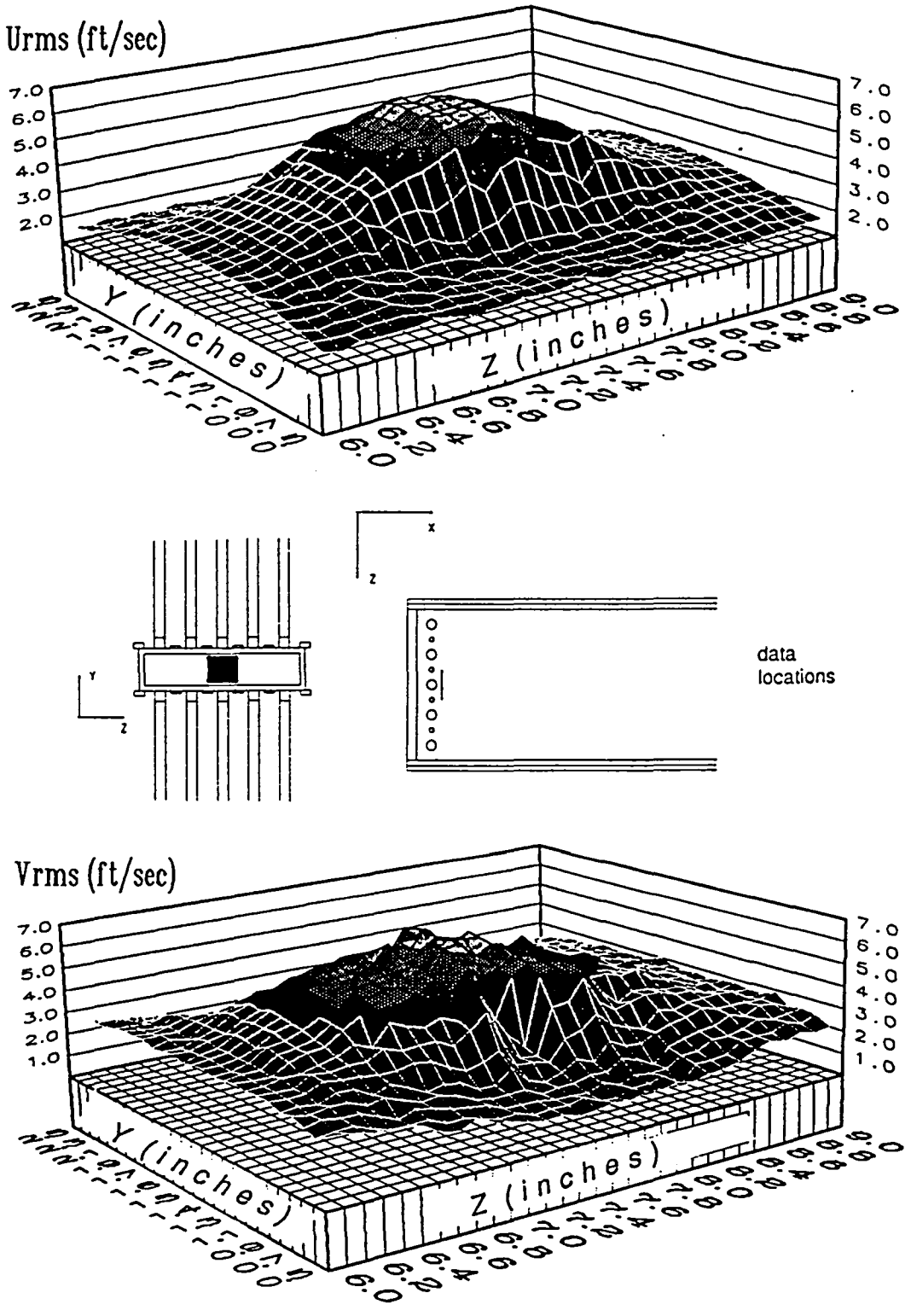

Figure C12 Primary Jets Only Contour Plot of U_{rms} and V_{rms} at X=2.5 in.

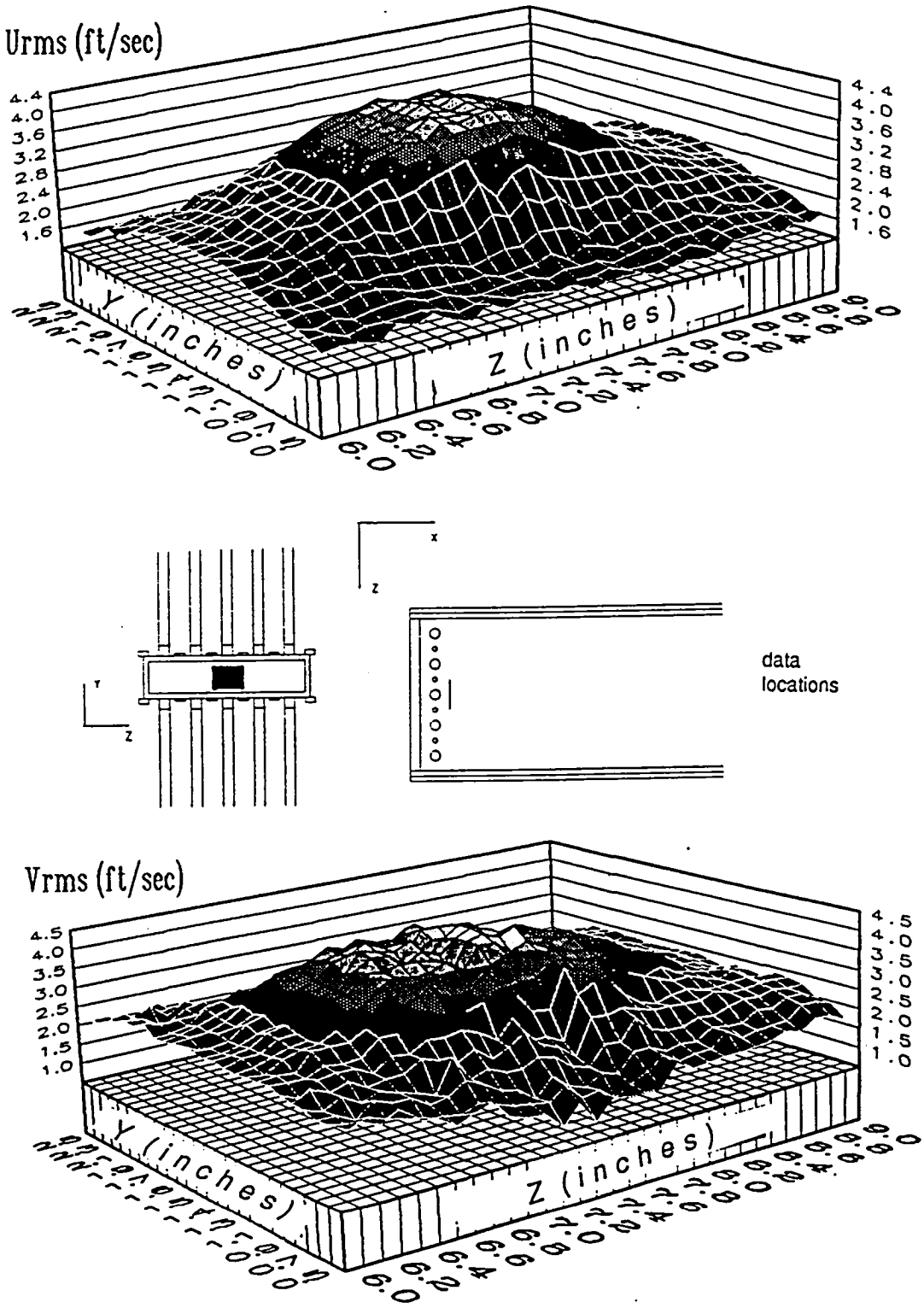

Figure C13 Primary Jets Only Contour Plot of U_{rms} and V_{rms} at X=3.0 in.

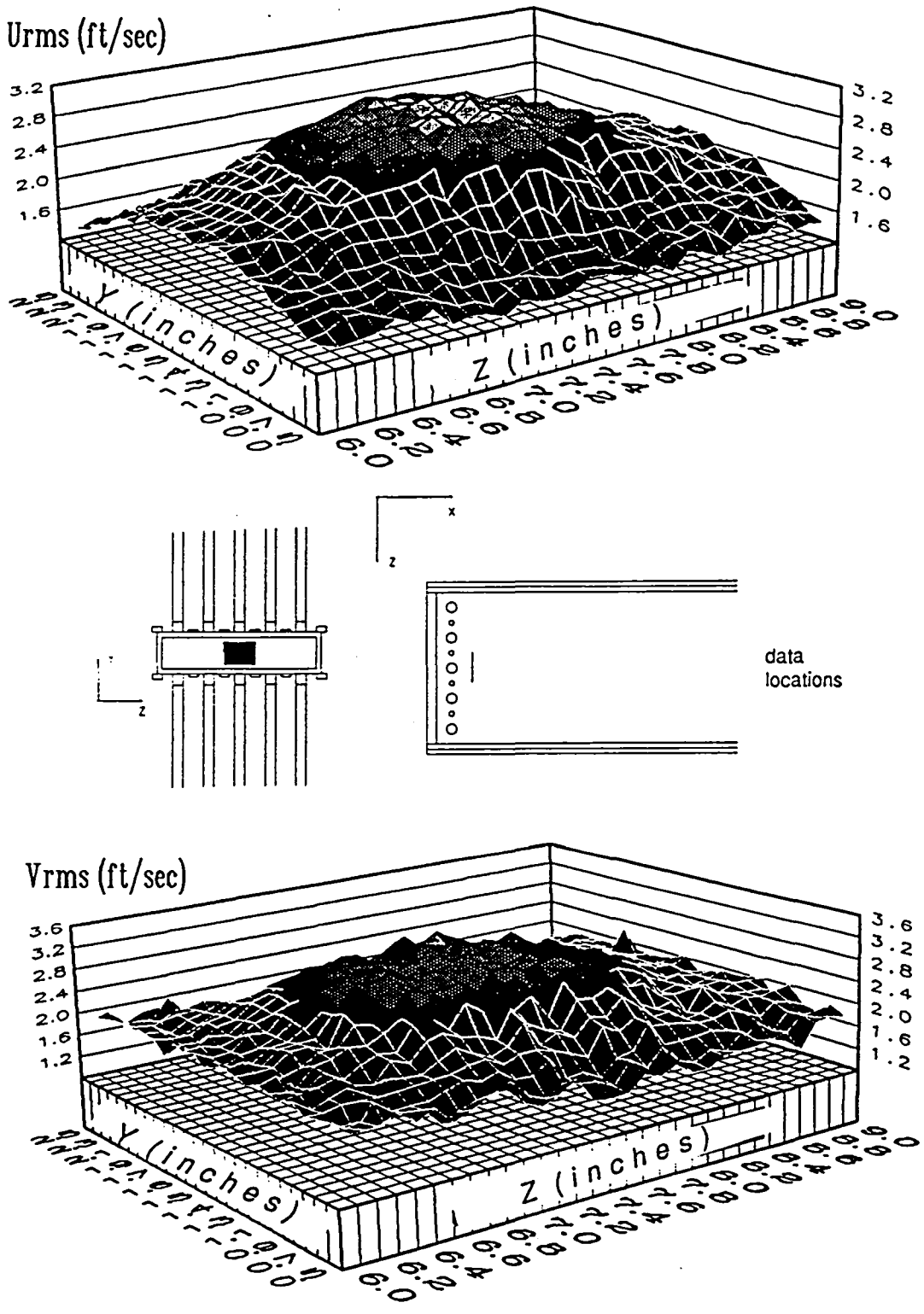

Figure C14 Primary Jets Only Contour Plot of U_{rms} and V_{rms} at X=3.5 in.

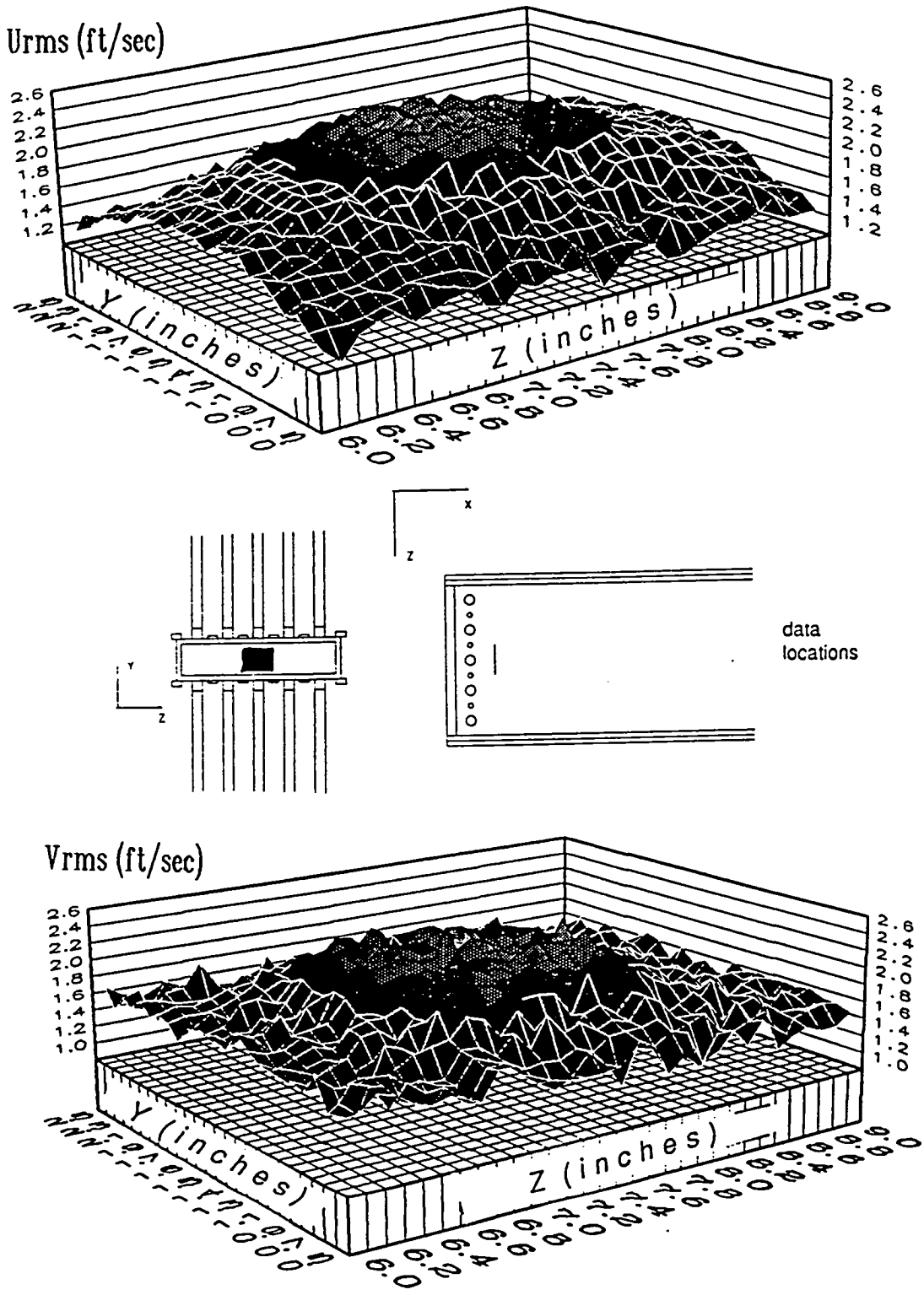

Figure C15 Primary Jets Only Contour Plot of U_{rms} and V_{rms} at X=4.0 in.

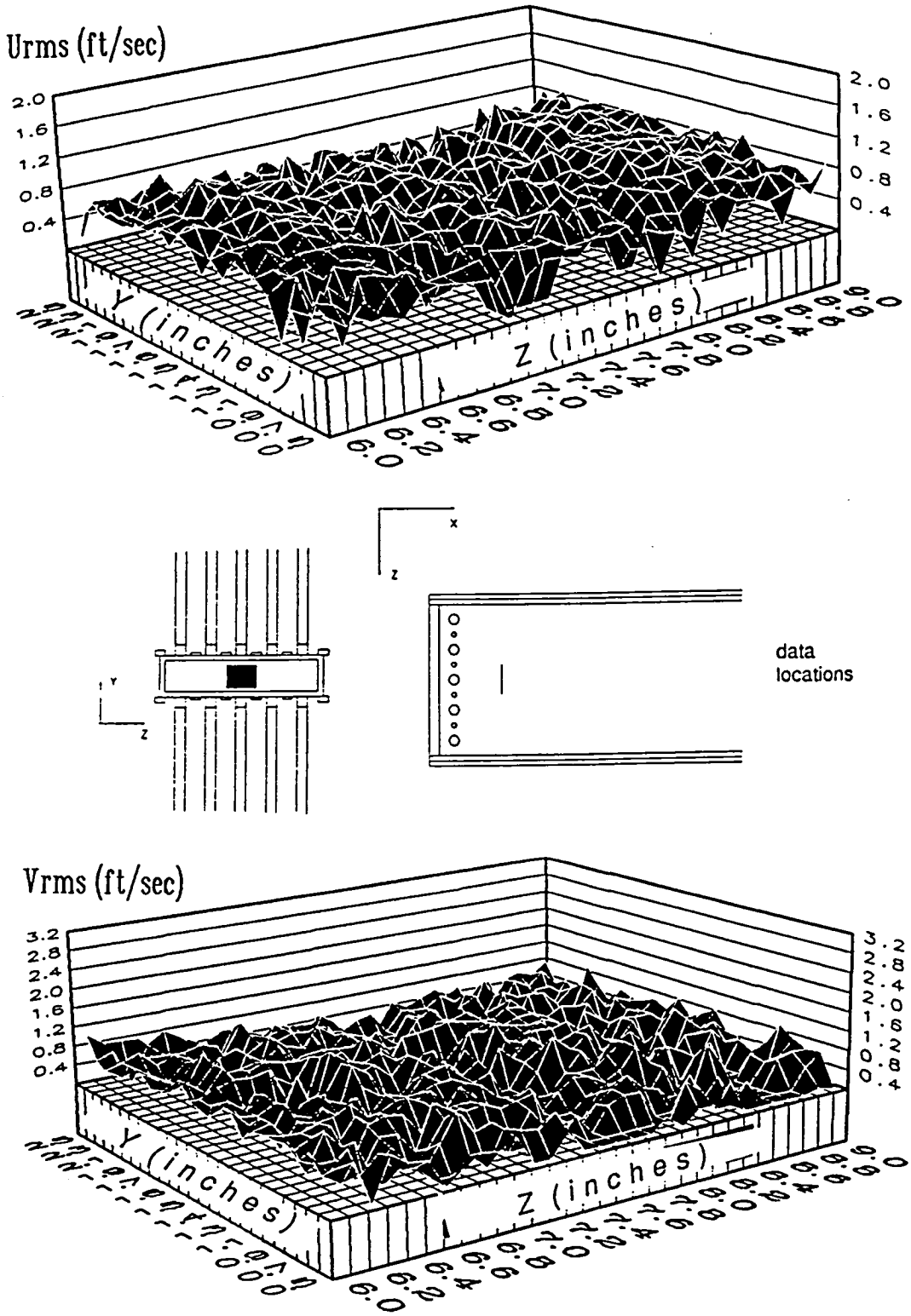

Figure C16 Primary Jets Only Contour Plot of U_{rms} and V_{rms} at X=6.0 in.

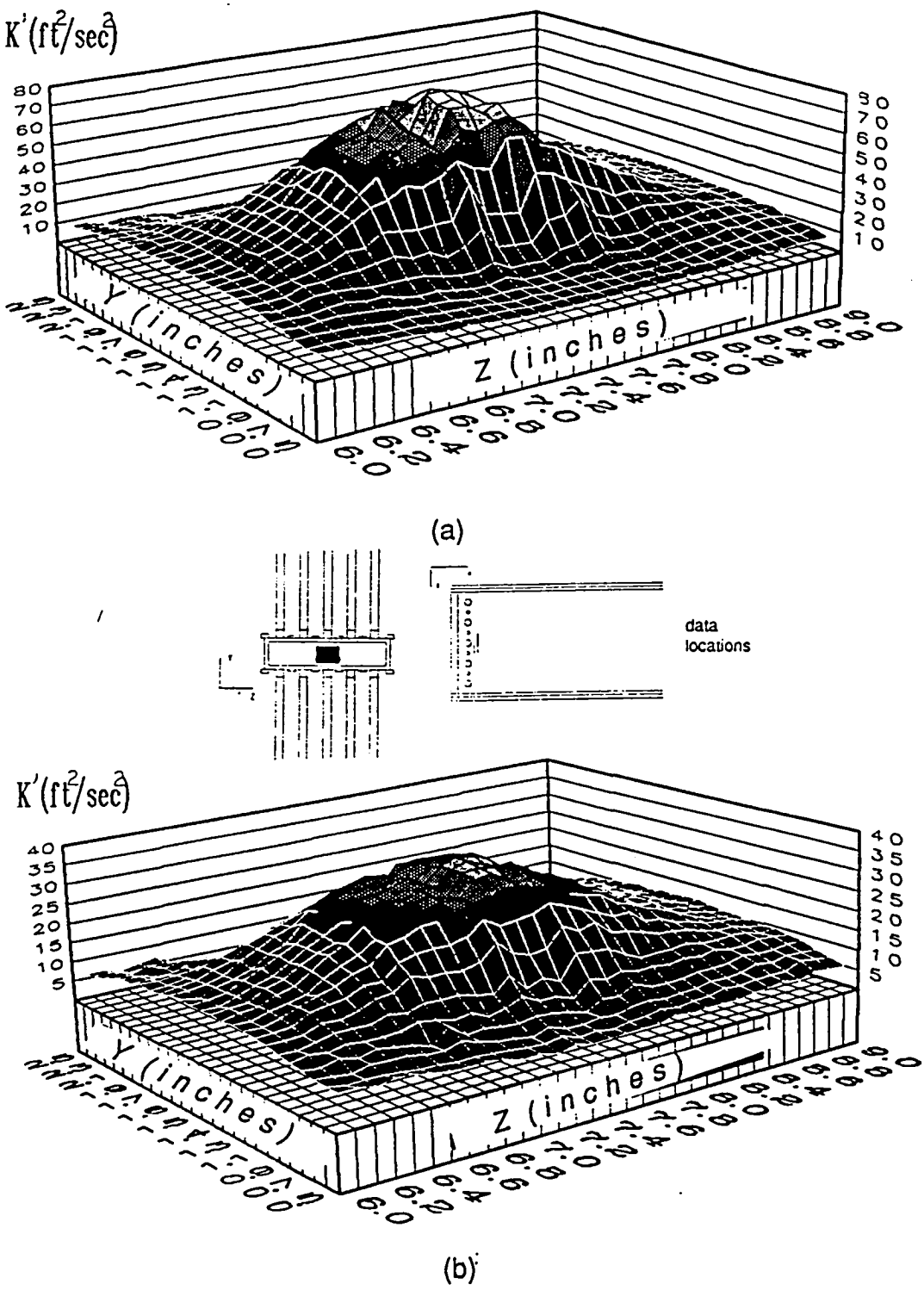

Figure C17 Primary Jets Only Contour Plot of K' at
a) X=2.5 in.; b) X=3.0 in.

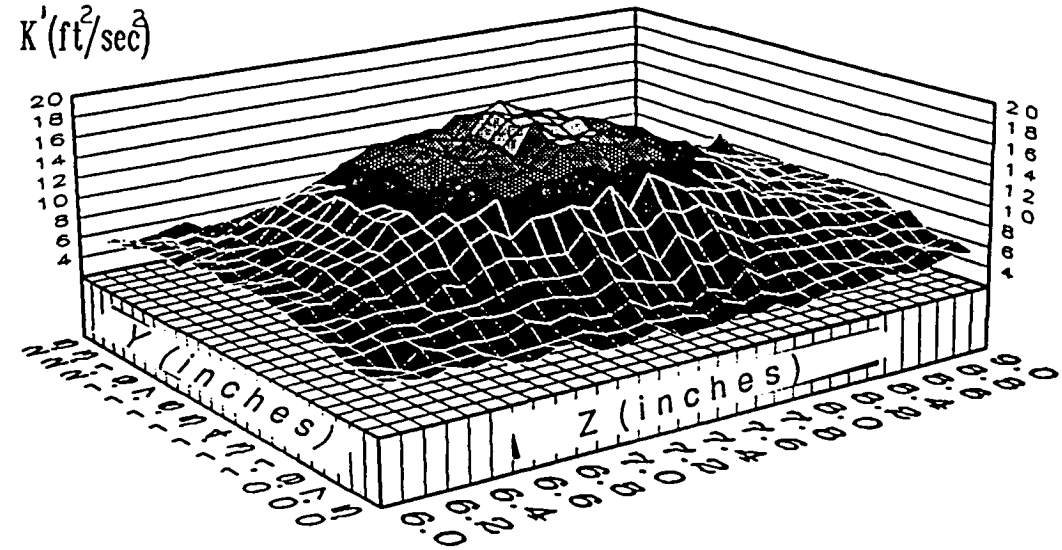

(a)

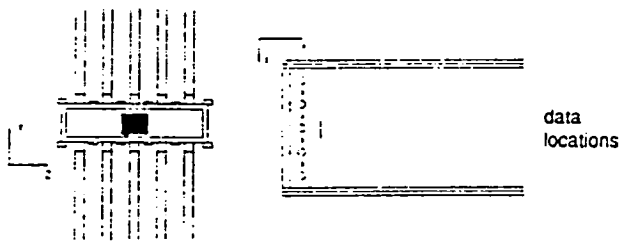

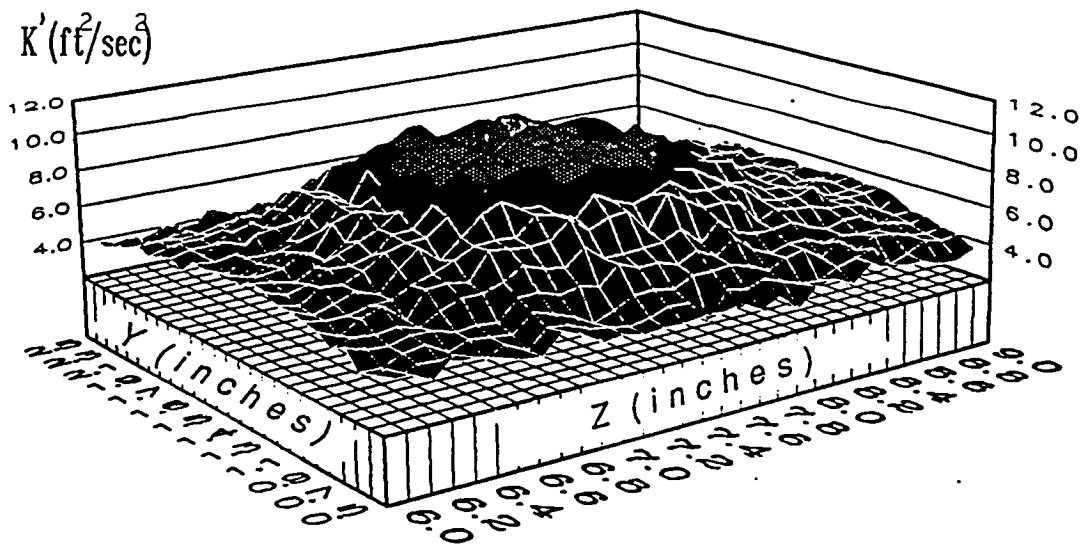

(b)

Figure C18 Primary Jets Only Contour Plot of K' at
a) X=3.5 in.; b) X=4.0 in.

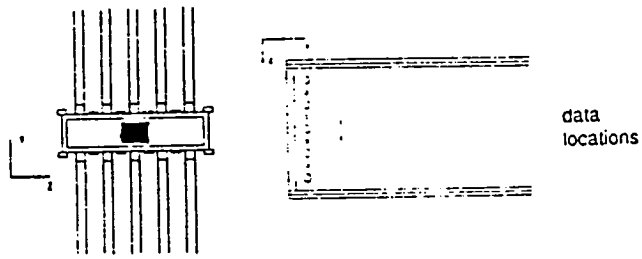

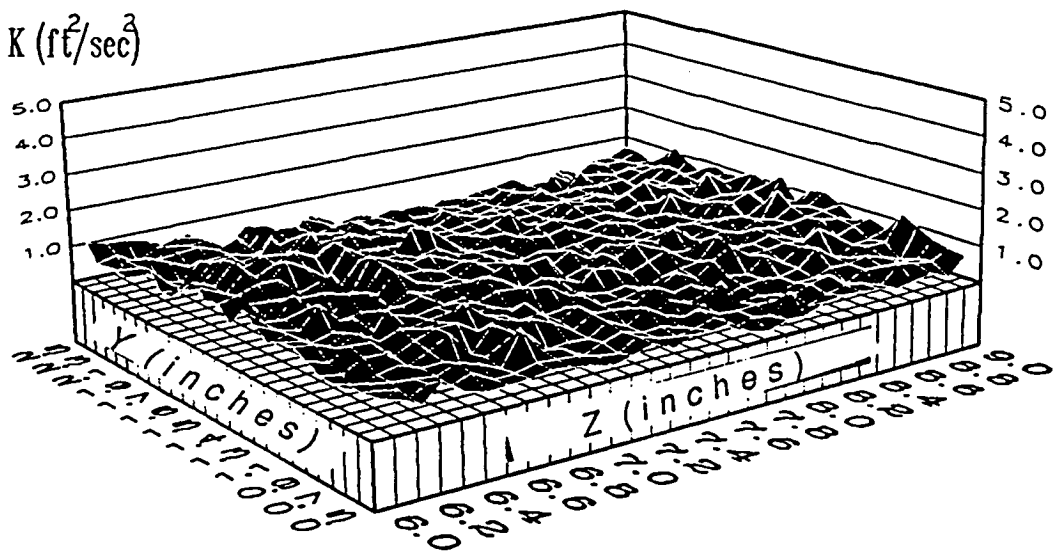

Figure C19 Primary Jets Only Contour Plot of K' at X=6.0 in.

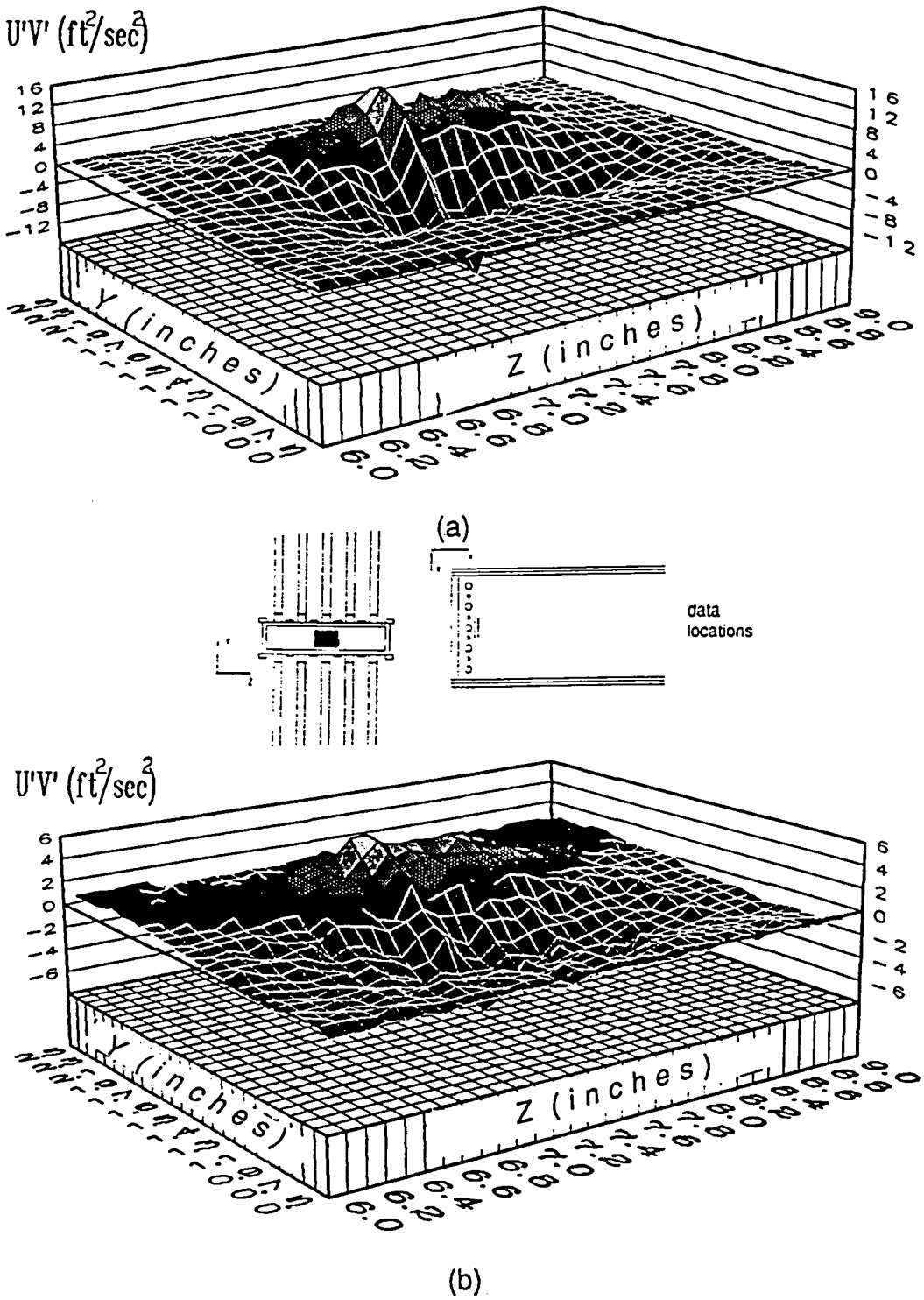

Figure C20 Primary Jets Only Contour Plot of U'V' at
a) X=2.5 in.; b) X=3.0 in.

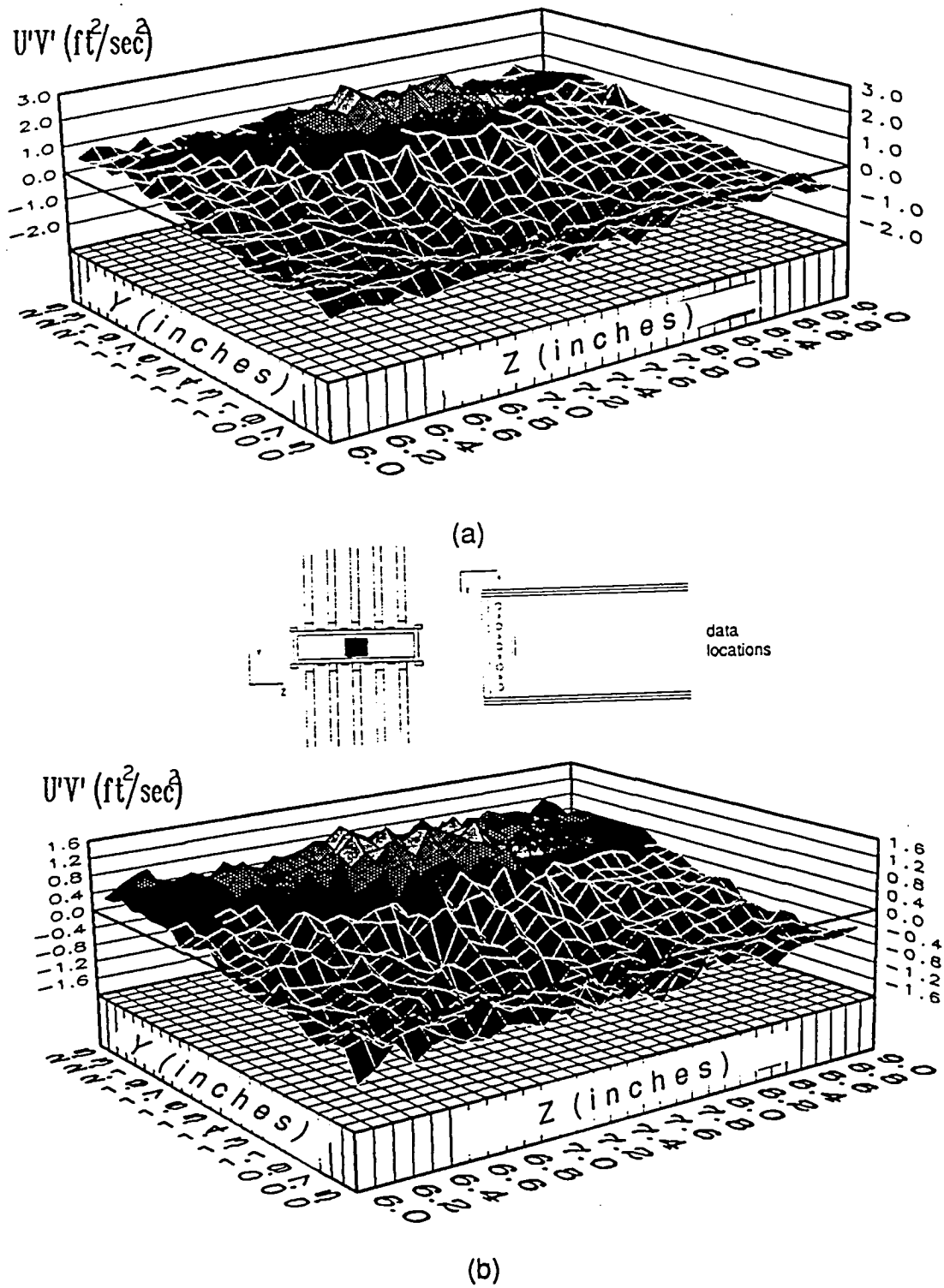

Figure C21 Primary Jets Only Contour Plot of U'V' at
a) X=3.5 in.; b) X=4.0 in.

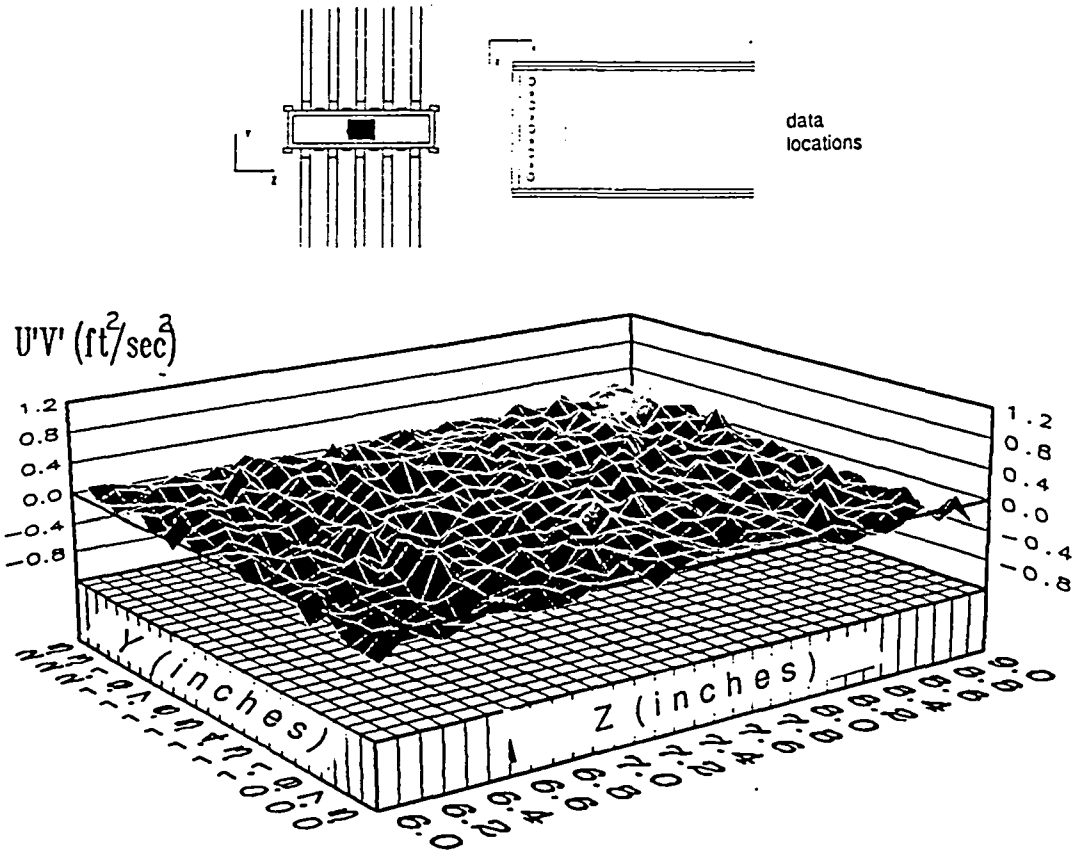

Figure C22 Primary Jets Only Contour Plot of U'V' at X=6.0 in.

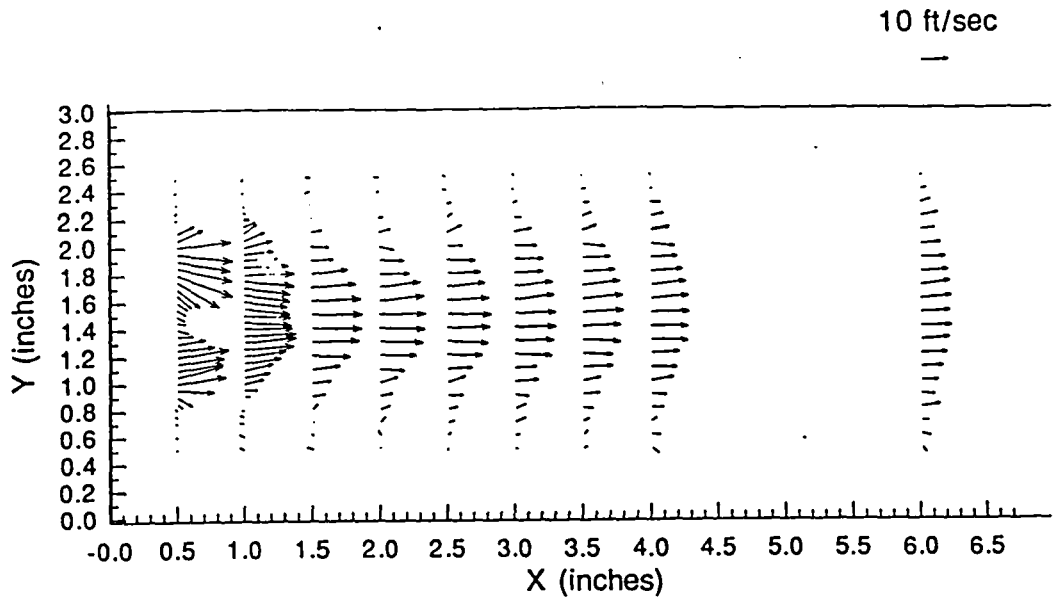

(a)

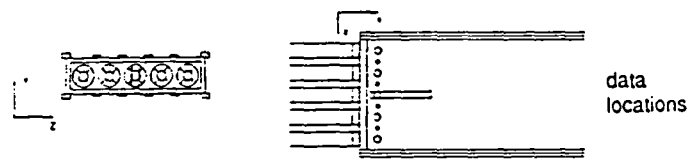

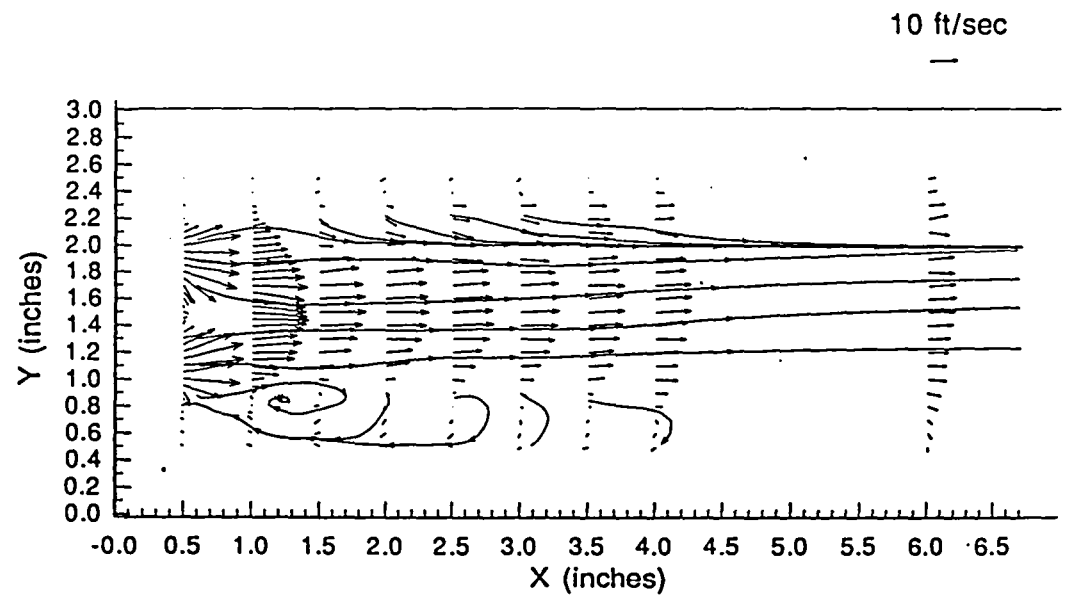

(b)

Figure C23 Annular Jets Only Mean Velocity Vector Plots
a) Z=7.1 in.; b) Z=7.9 in.

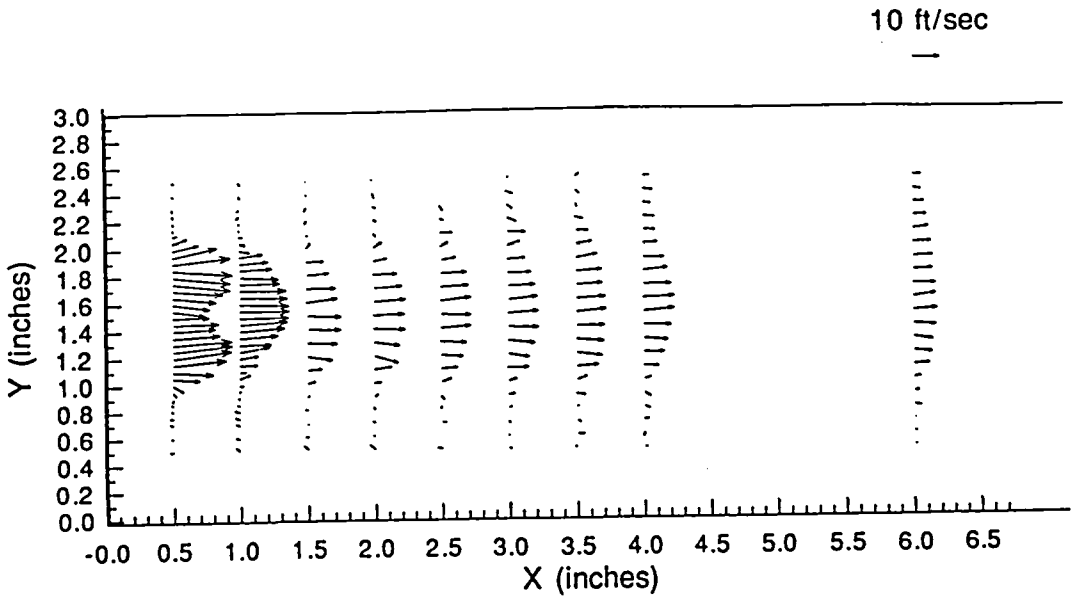

(a)

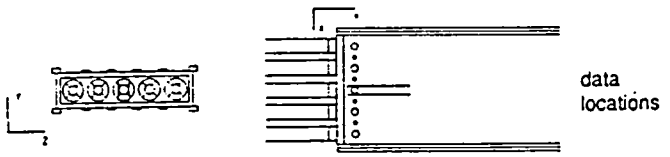

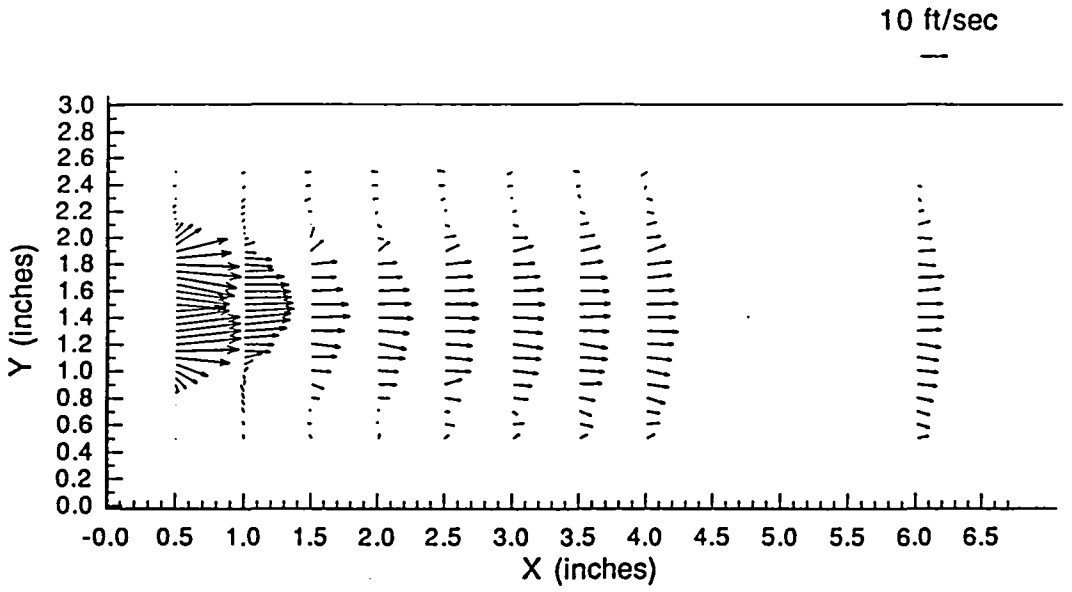

(b)

Figure C24 Annular Jets Only Mean Velocity Vector Plots
a) Z=7.0 in.; b) Z=8.0 in.

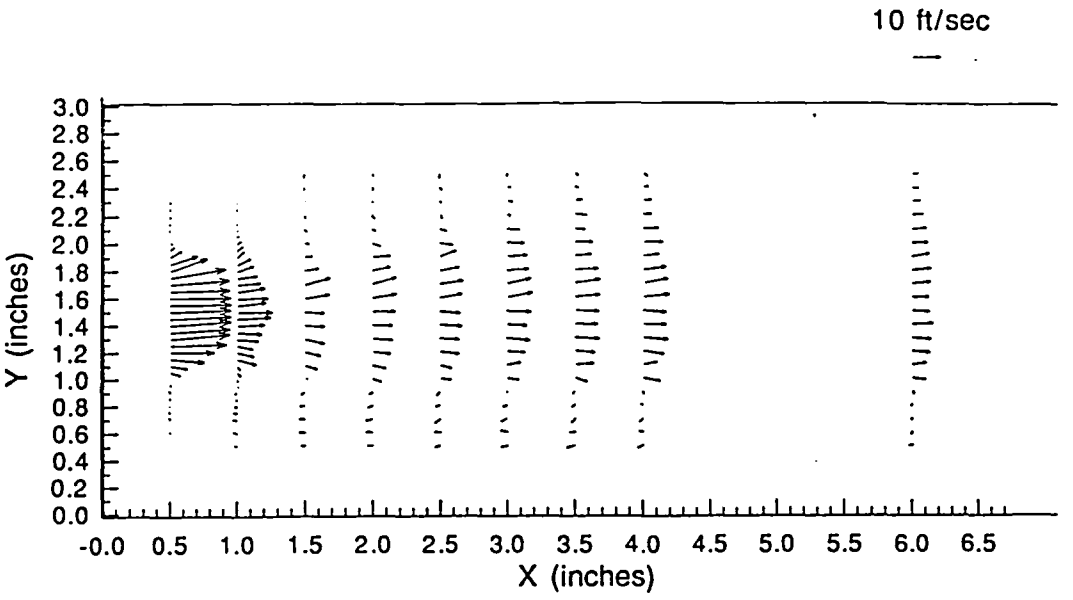

(a)

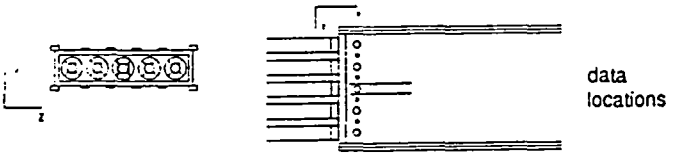

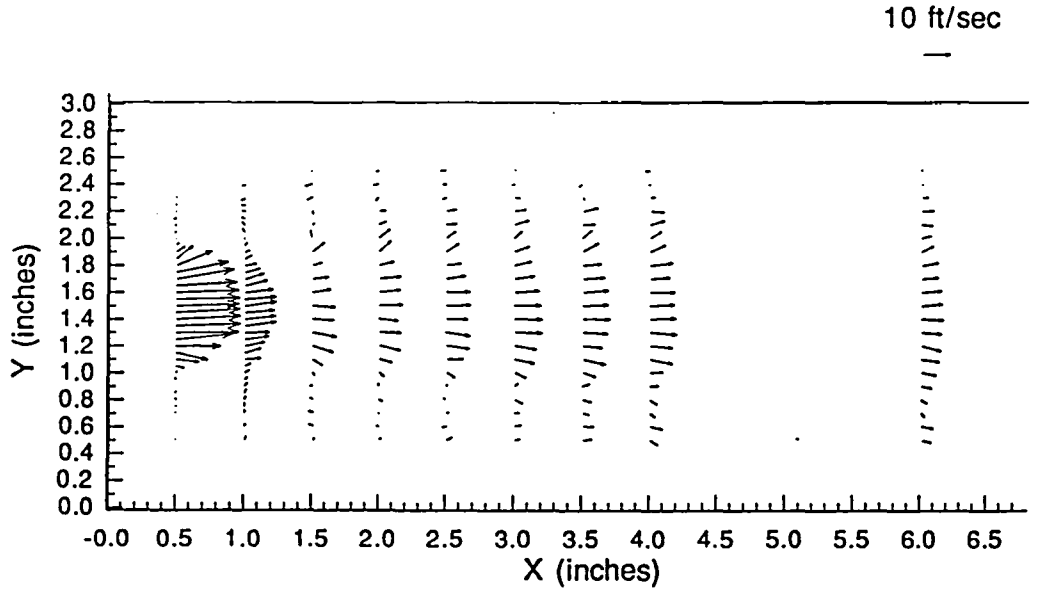

(b)

Figure C25 Annular Jets Only Mean Velocity Vector Plots
a) Z=6.9 in.; b) Z=8.1 in.

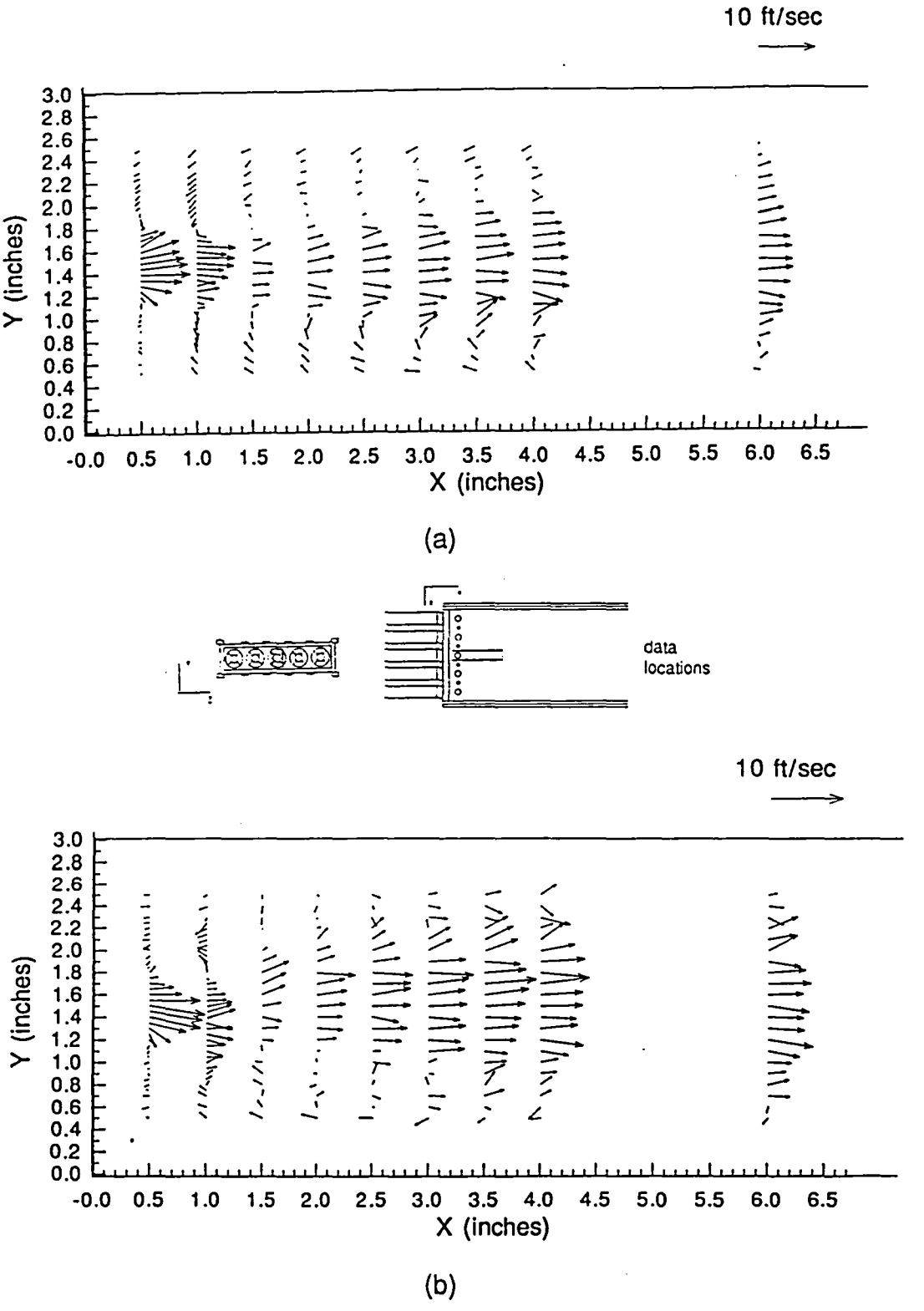

Figure C26 Annular Jets Only Mean Velocity Vector Plots
a) Z=6.8 in.; b) Z=8.2 in.

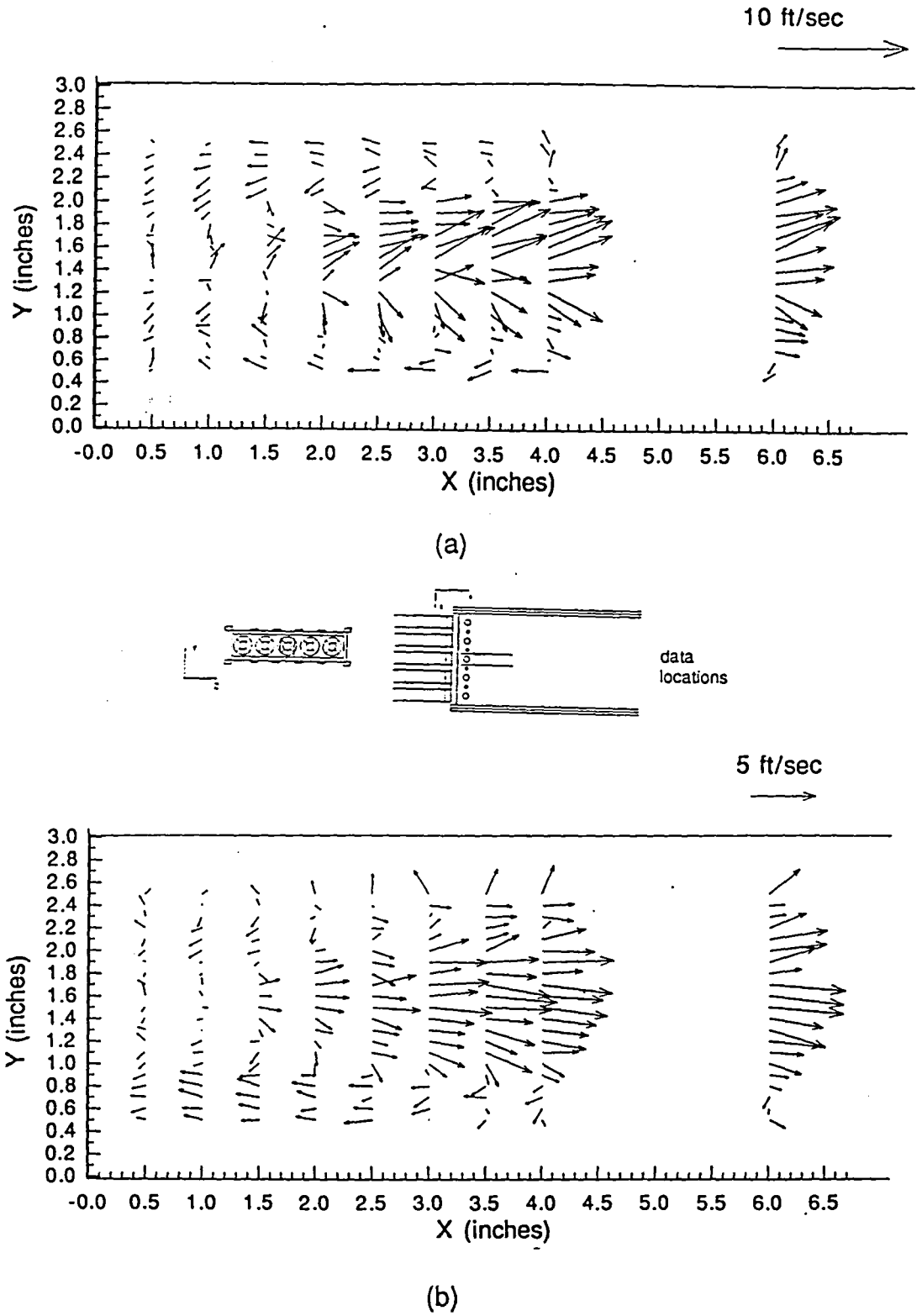

Figure C27 Annular Jets Only Mean Velocity Vector Plots
a) Z=6.7 in.; b) Z=8.3 in.

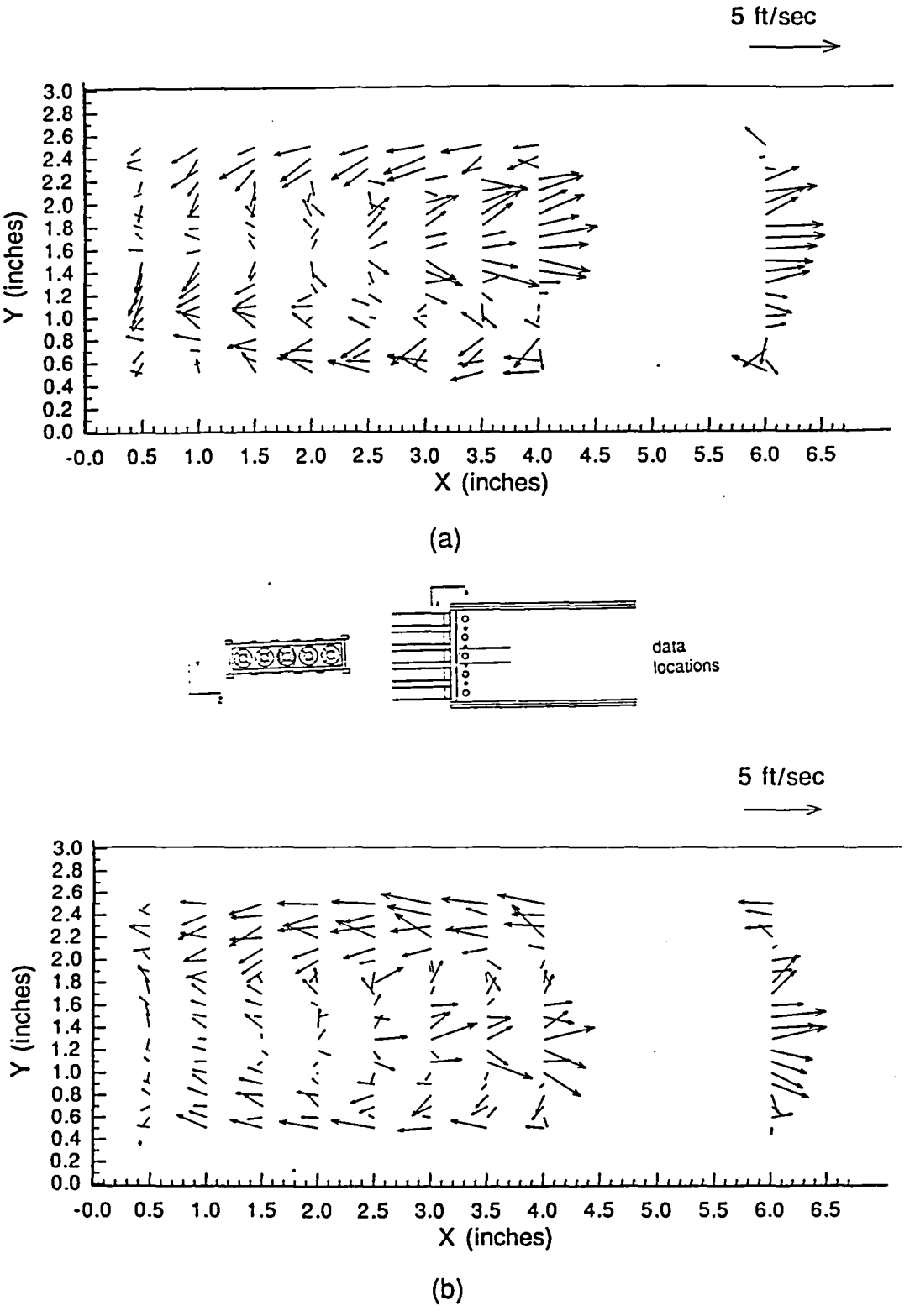

Figure C28 Annular Jets Only Mean Velocity Vector Plots
a) Z=6.6 in.; b) Z=8.4 in.

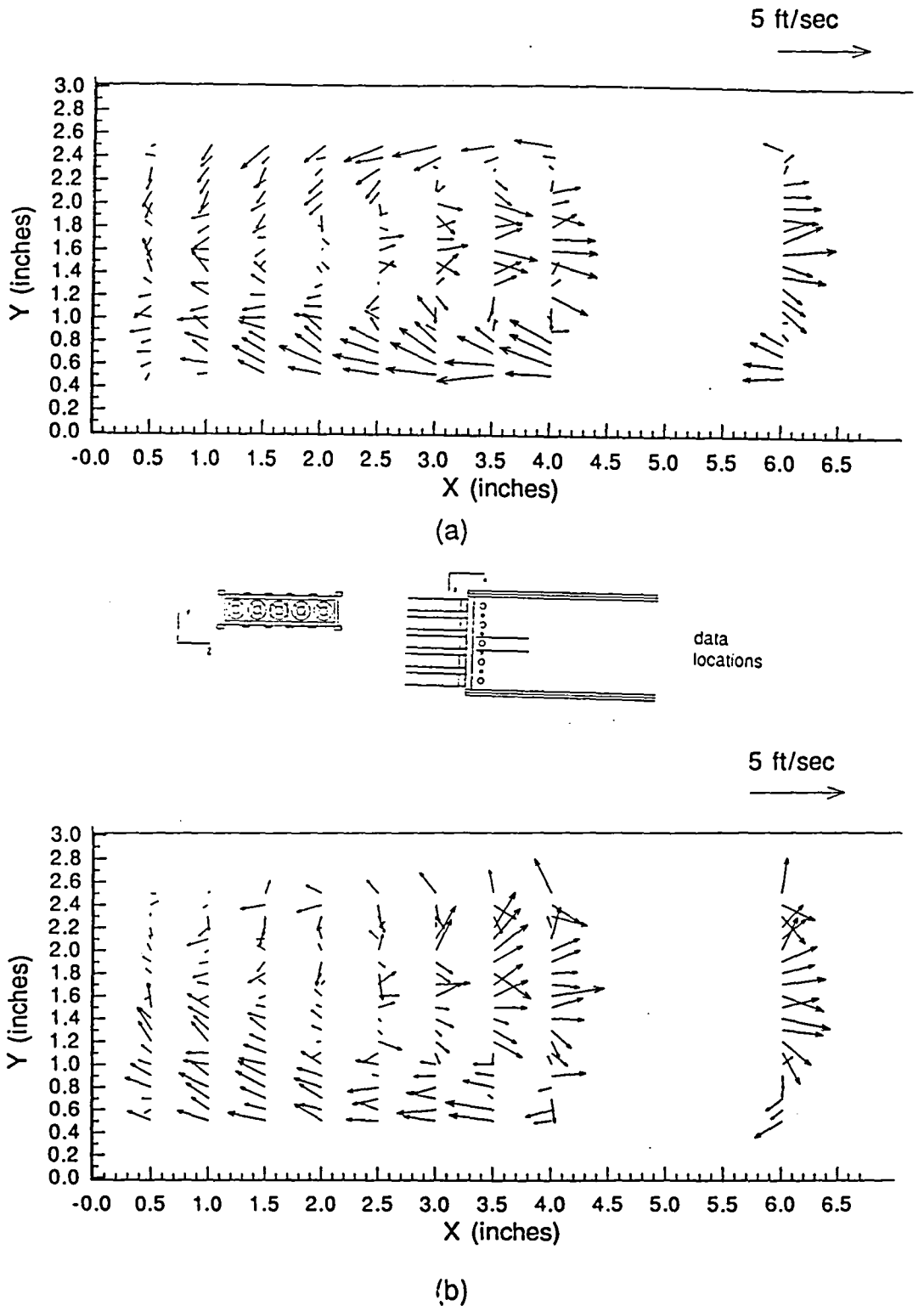

Figure C29 Annular Jets Only Mean Velocity Vector Plots
a) Z=6.5 in.; b) Z=8.5 in.

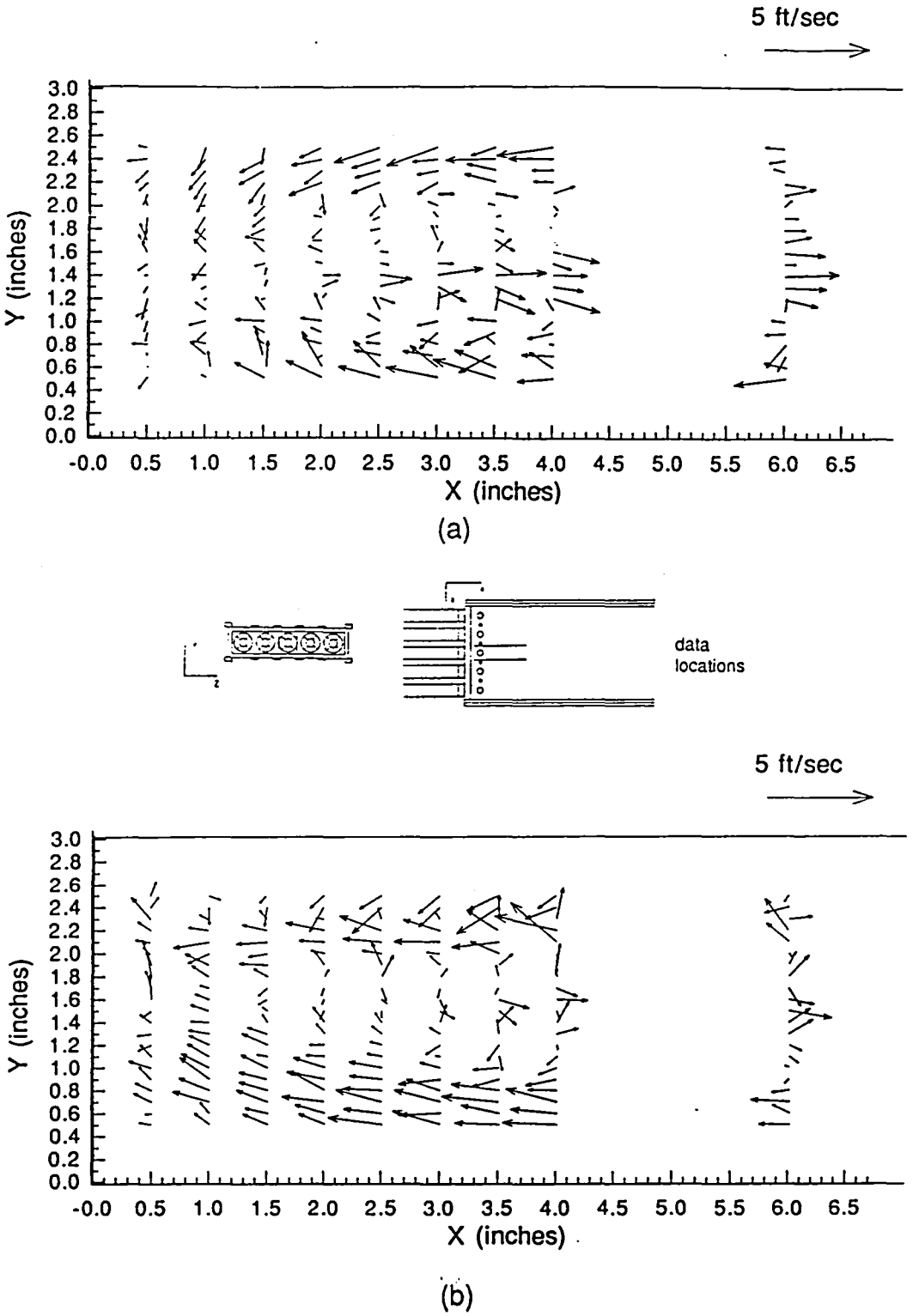

Figure C30 Annular Jets Only Mean Velocity Vector Plots
a) Z=6.4 in.; b) Z=8.6 in.

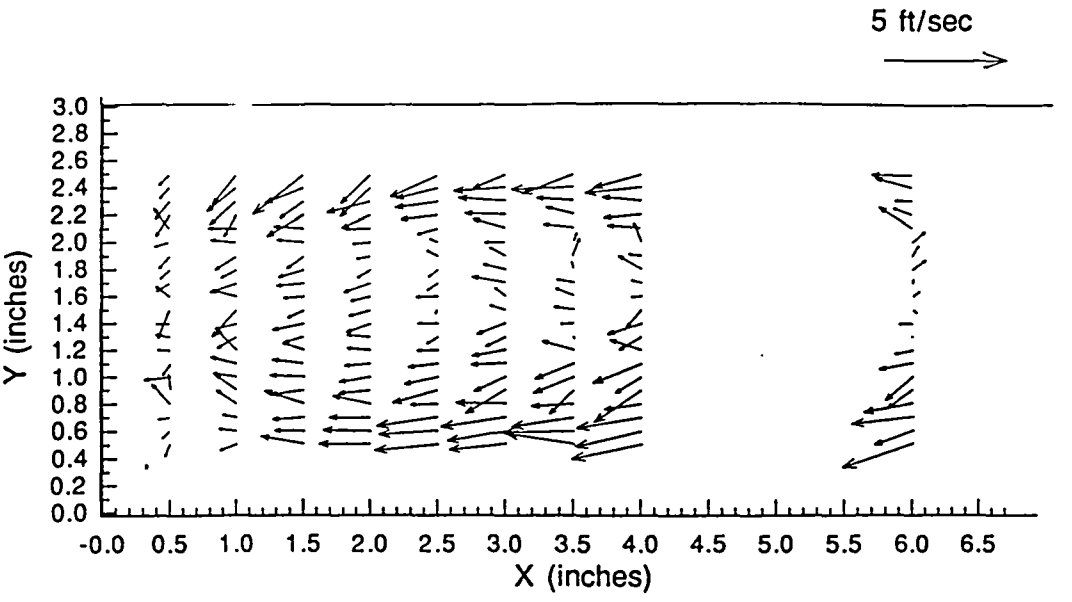

(a)

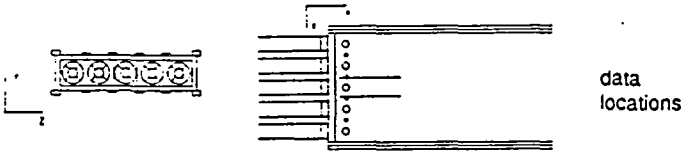

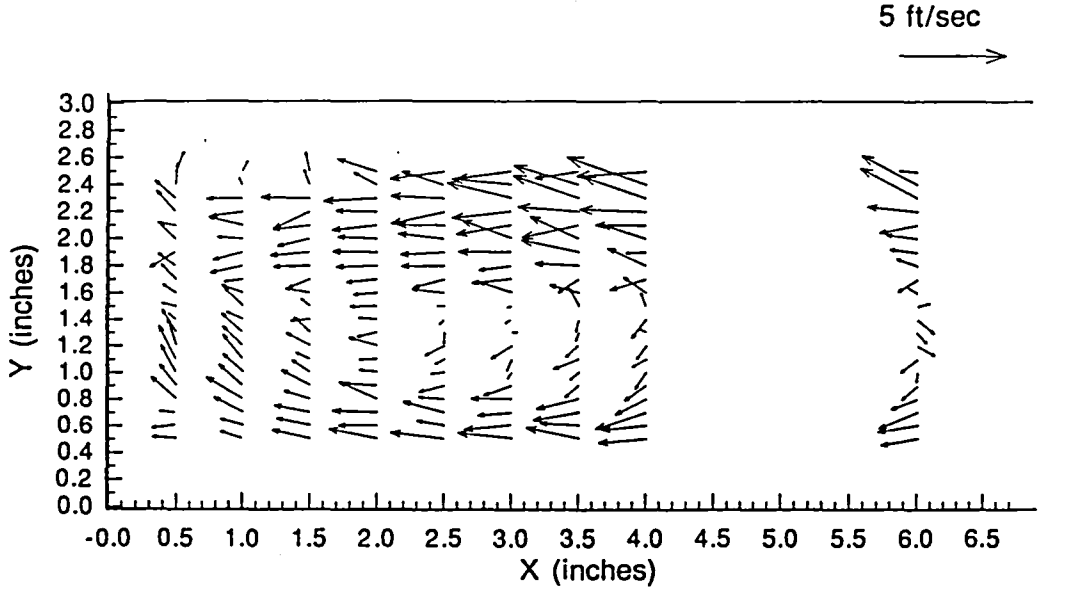

(b)

Figure C31 Annular Jets Only Mean Velocity Vector Plots
a) Z=6.3 in.; b) Z=8.7 in.

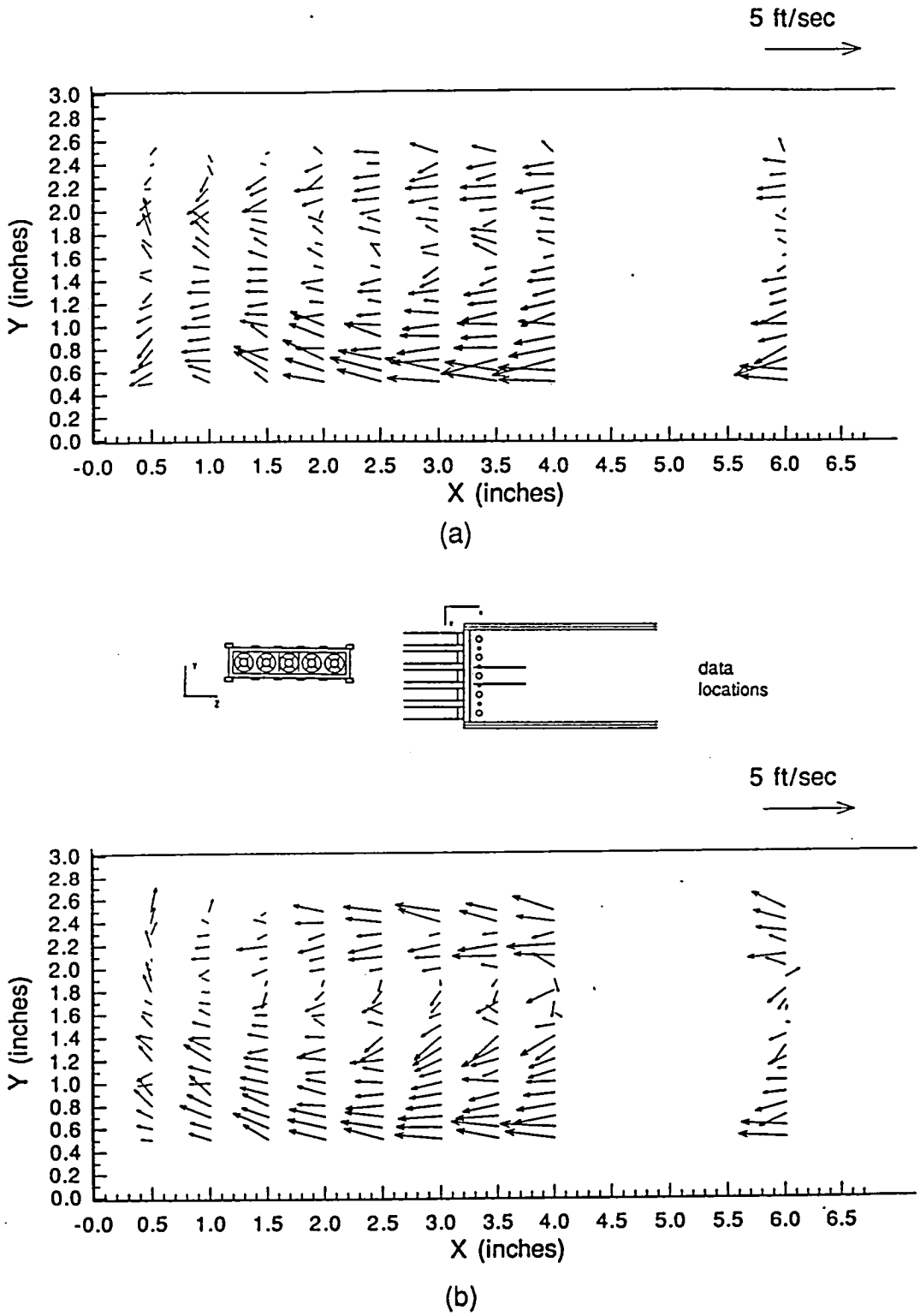

Figure C32 Annular Jets Only Mean Velocity Vector Plots
a) Z=6.2 in.; b) Z=8.8 in.

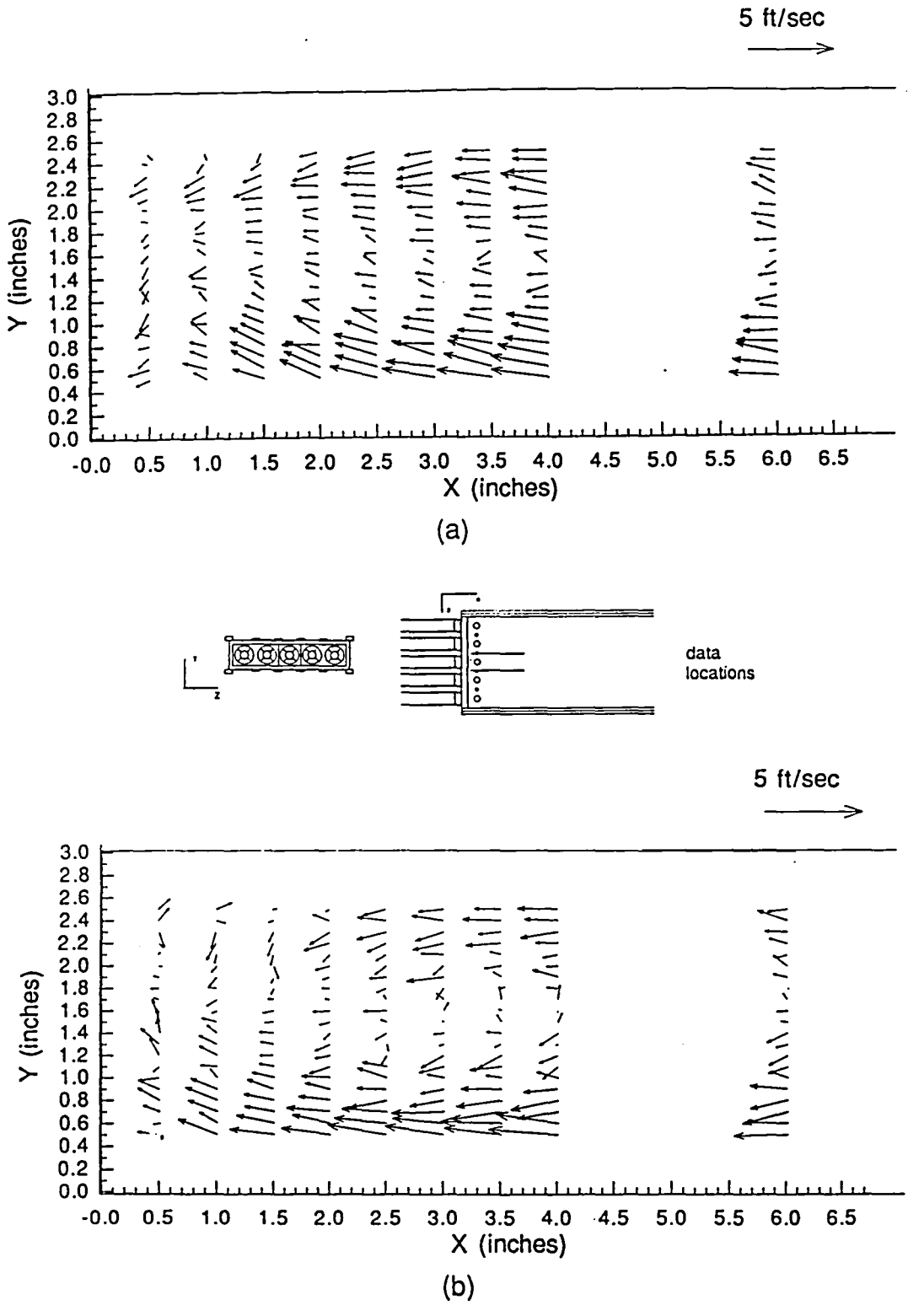

Figure C33 Annular Jets Only Mean Velocity Vector Plots
a) Z=6.1 in.; b) Z=8.9 in.

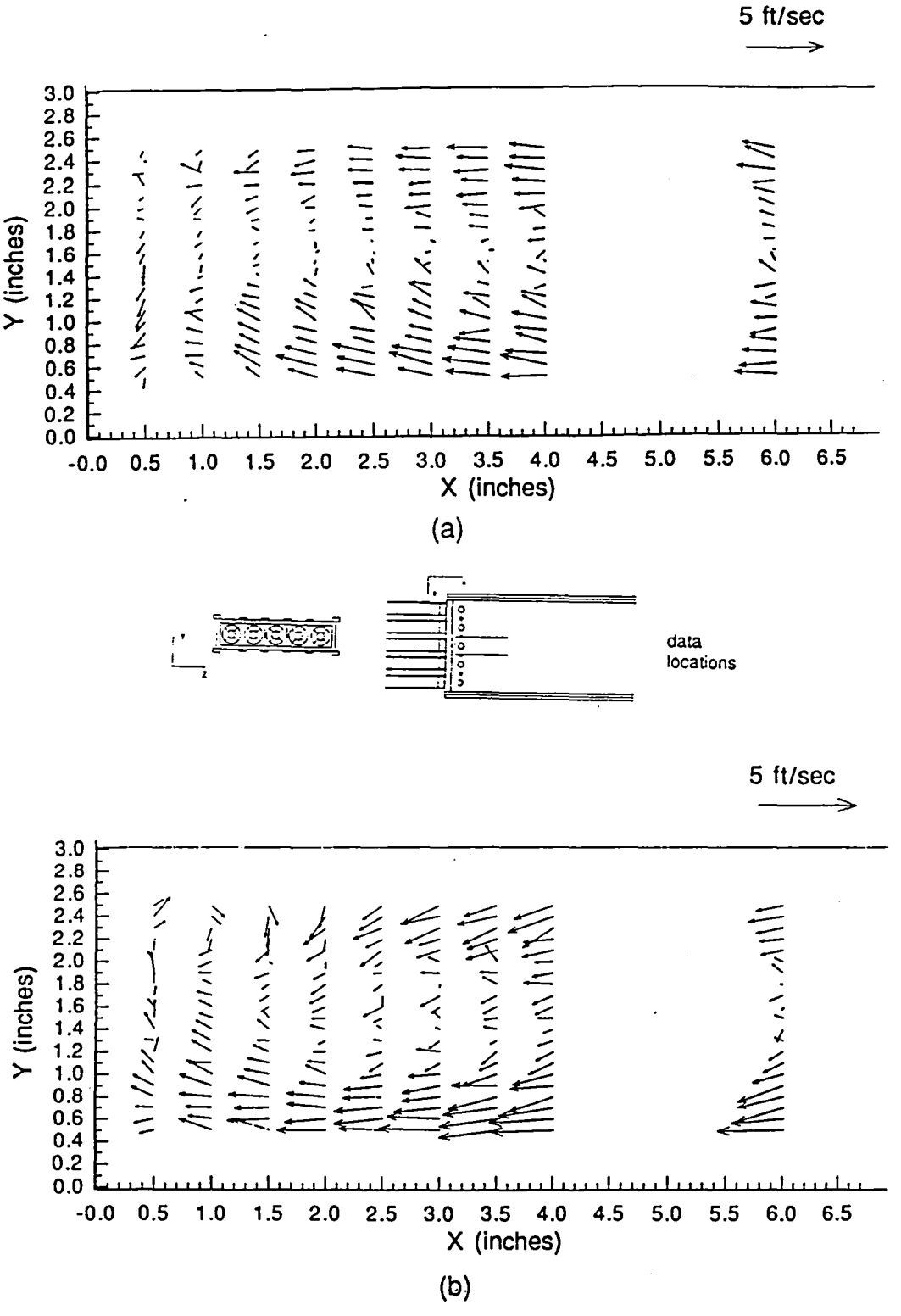

Figure C34 Annular Jets Only XY Plane Mean Velocity Vector Plots
a) Z=6.0 in.; b) Z=9.0 in.

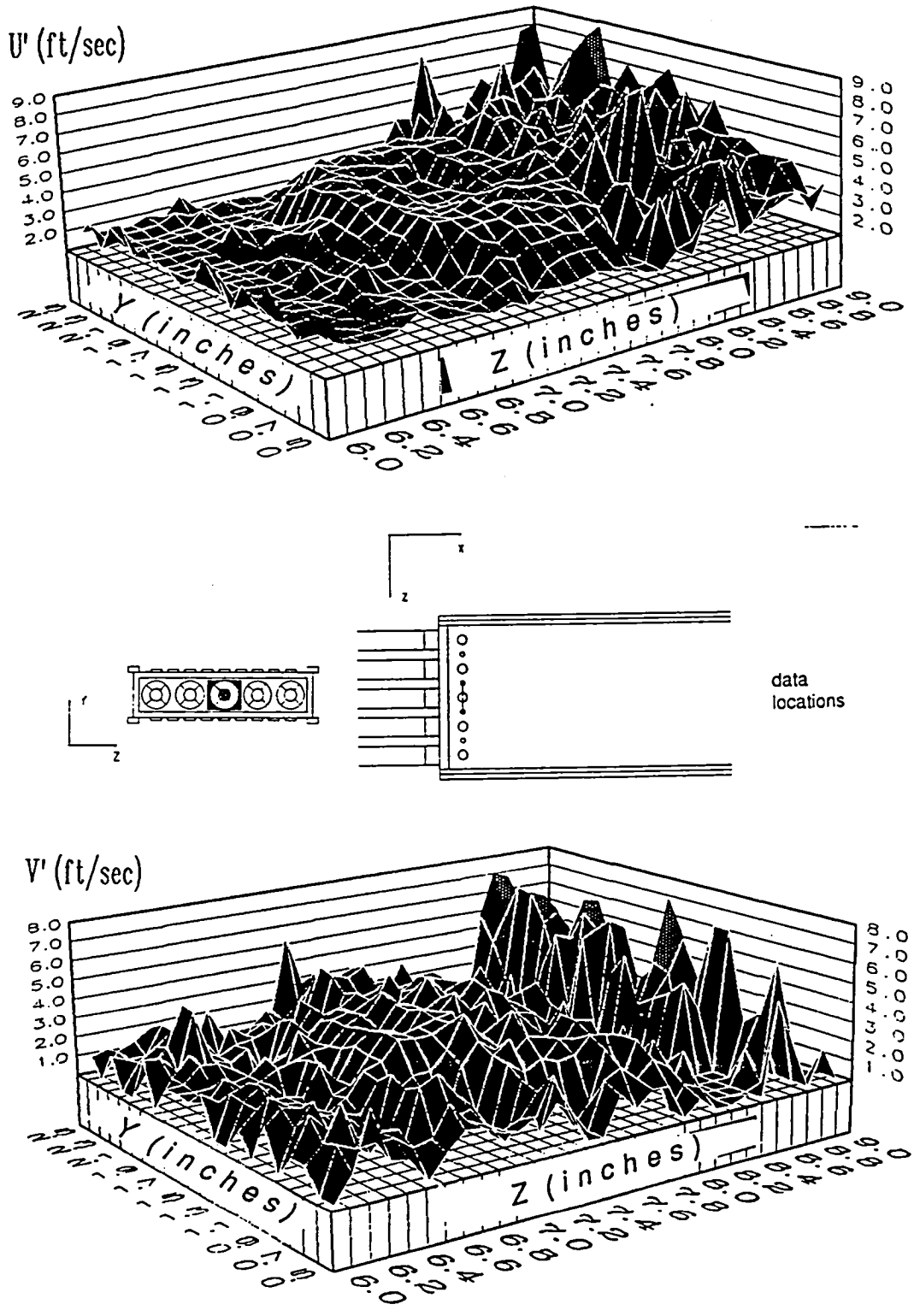

Figure C35 Annular Jets Only Contour Plot of U_{rms} and V_{rms} at X=1.5 in.

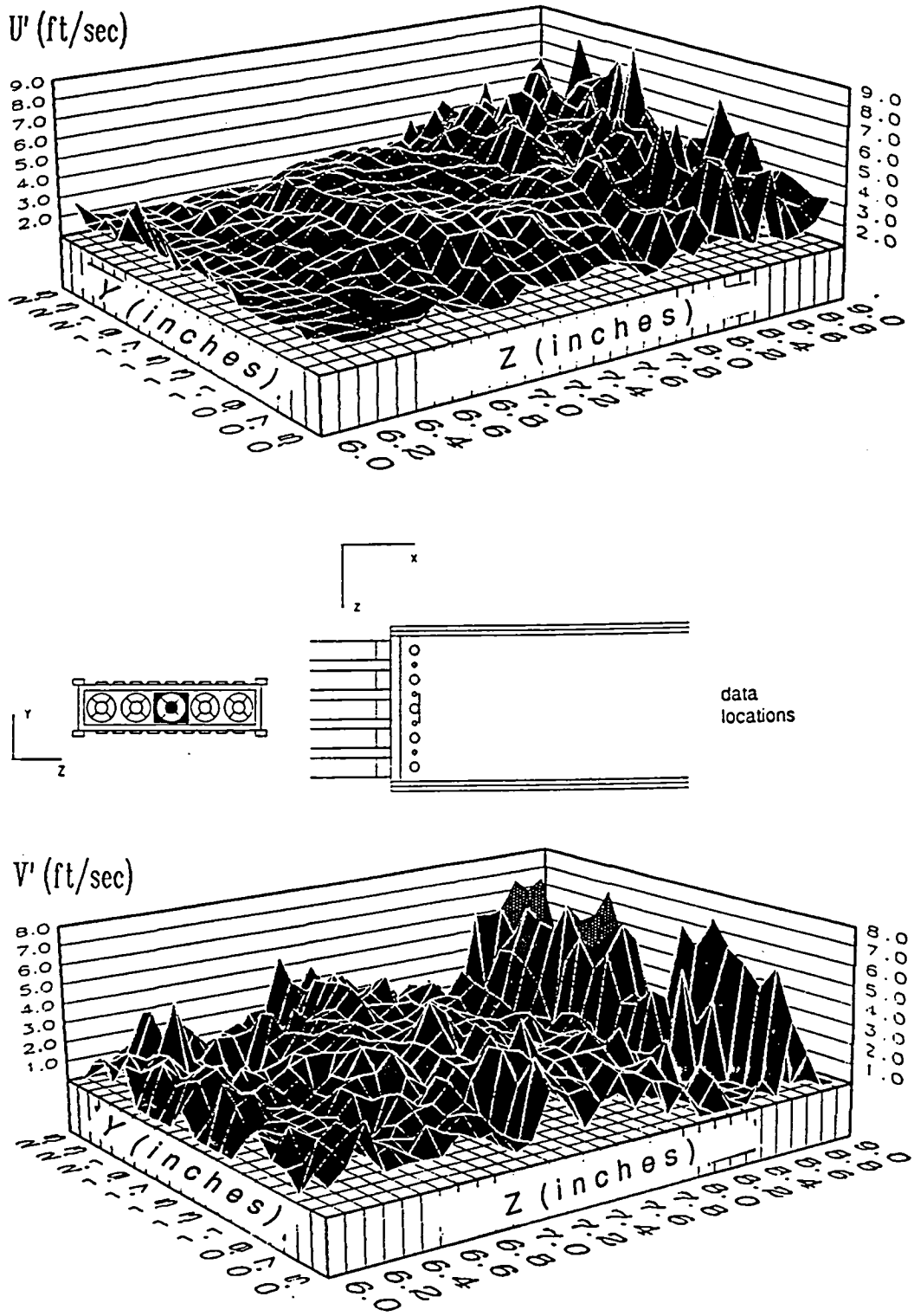

Figure C36 Annular Jets Only Contour Plot of U_{rms} and V_{rms} at X=2.0 in.

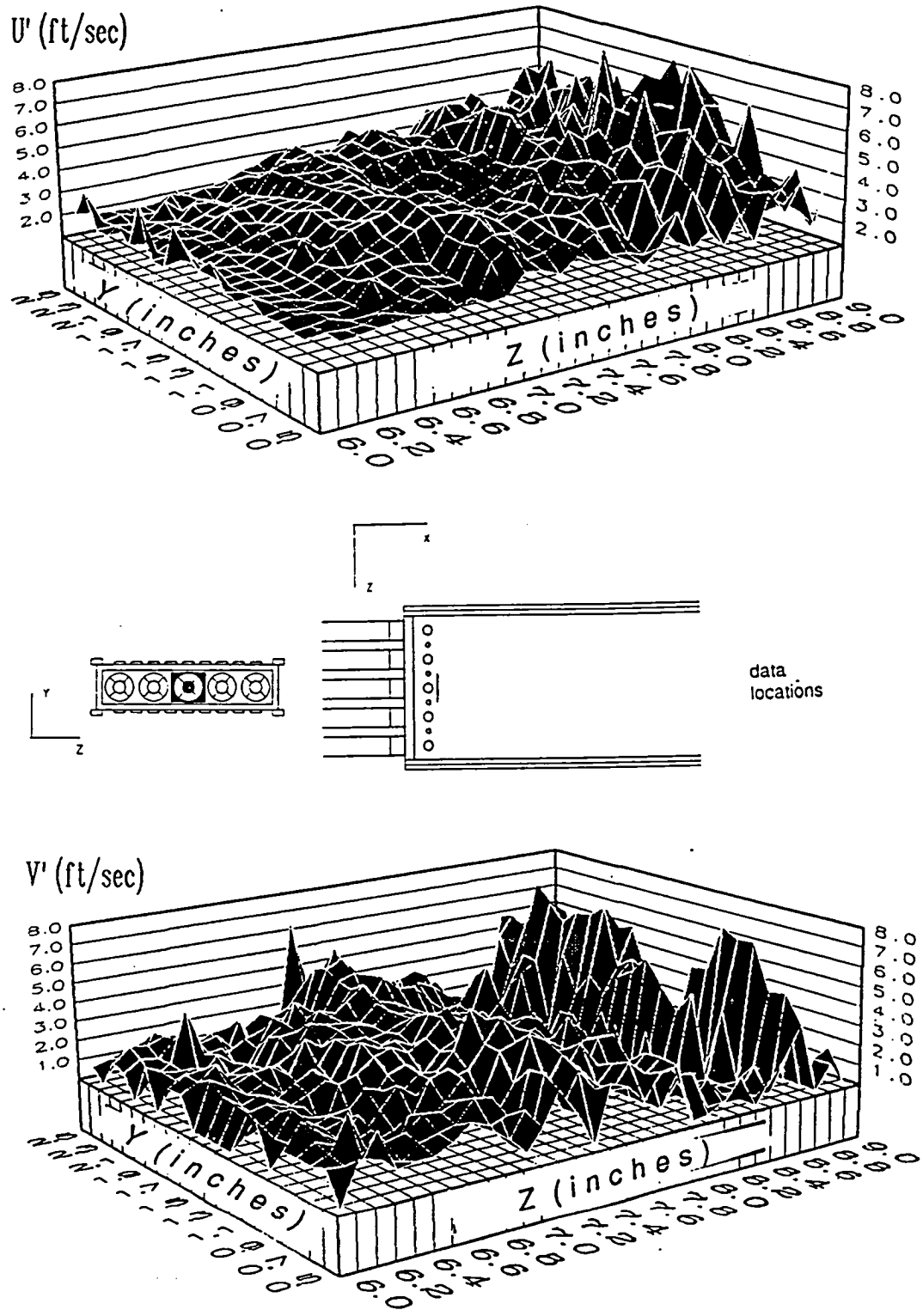

Figure C37 Annular Jets Only Contour Plot of U_{rms} and V_{rms} at X=2.5 in.

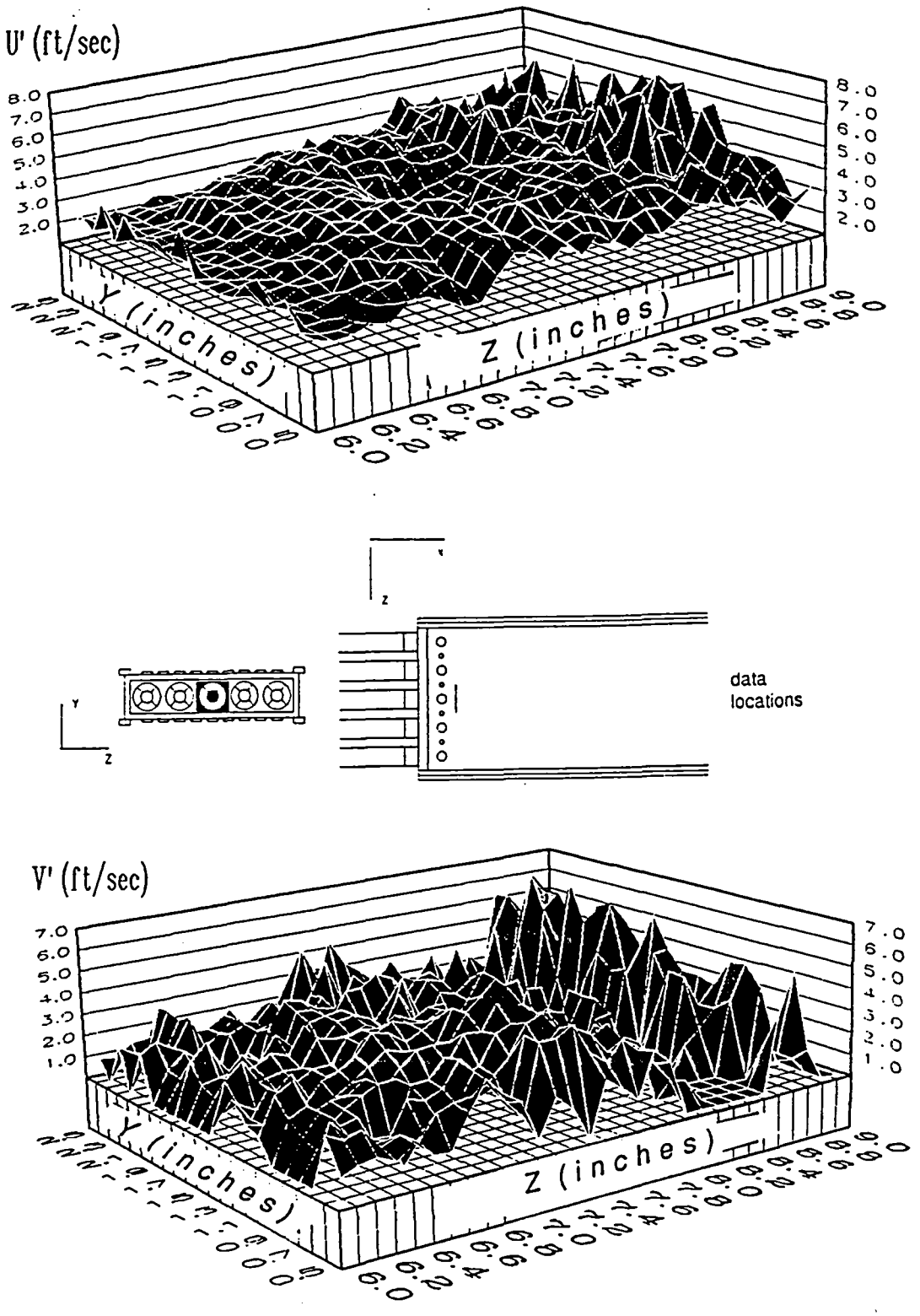

Figure C38 Annular Jets Only Contour Plot of U_{rms} and V_{rms} at X=3.0 in.

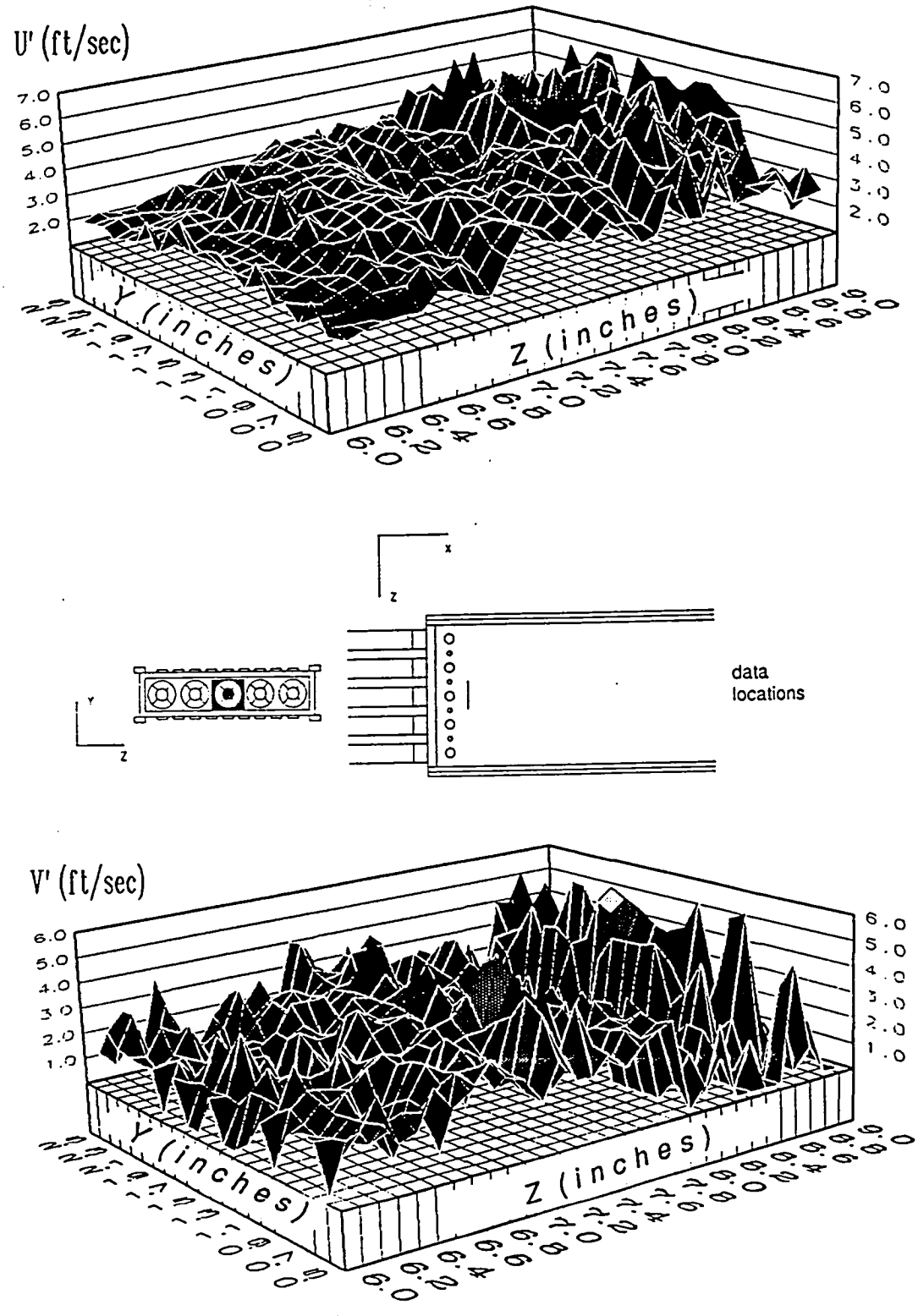

Figure C39 Annular Jets Only Contour Plot of U_{rms} and V_{rms} at X=3.5 in.

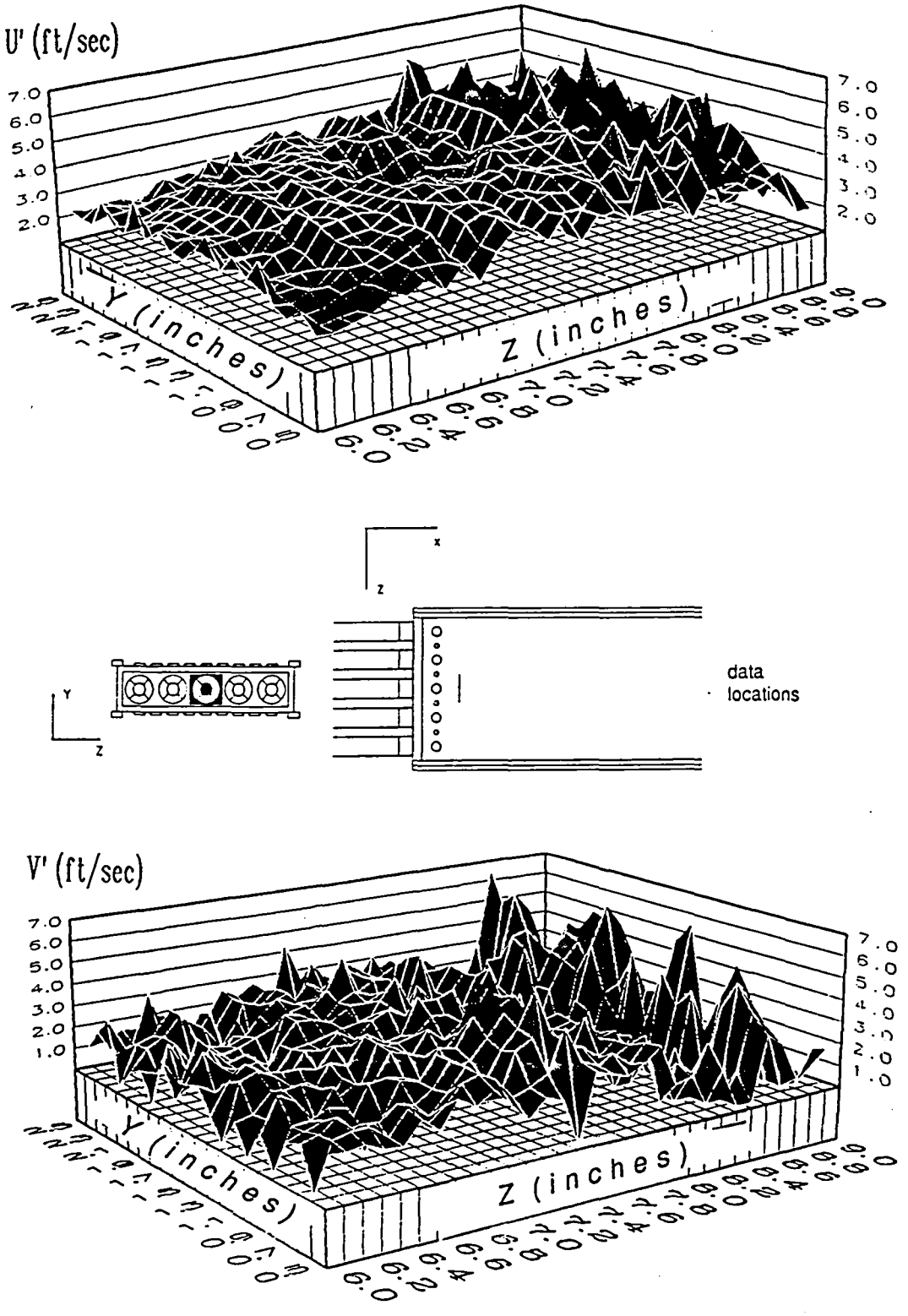

Figure C40 Annular Jets Only Contour Plot of U_{rms} and V_{rms} at X=4.0 in.

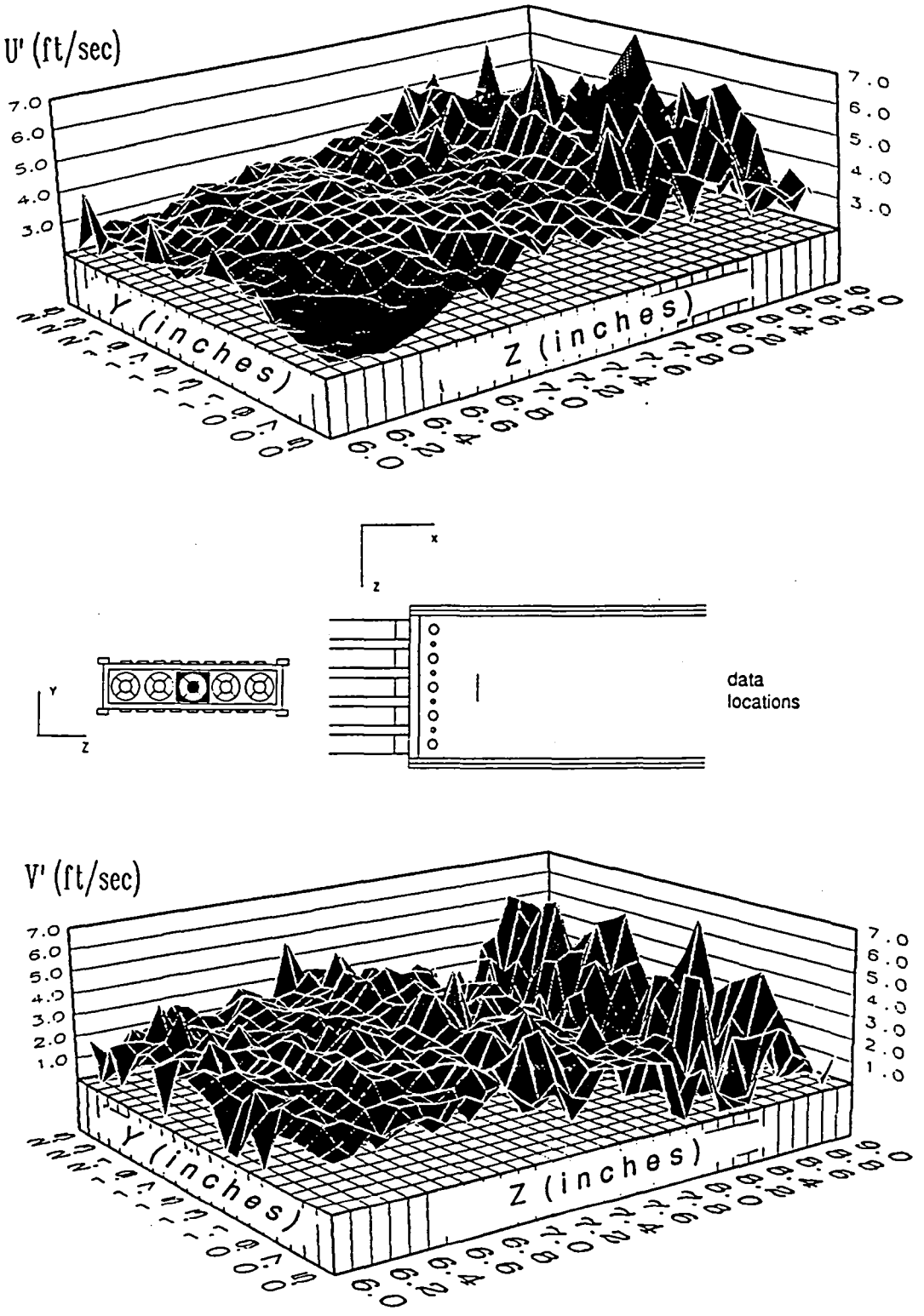

Figure C41 Annular Jets Only Contour Plot of U_{rms} and V_{rms} at X=6.0 in.

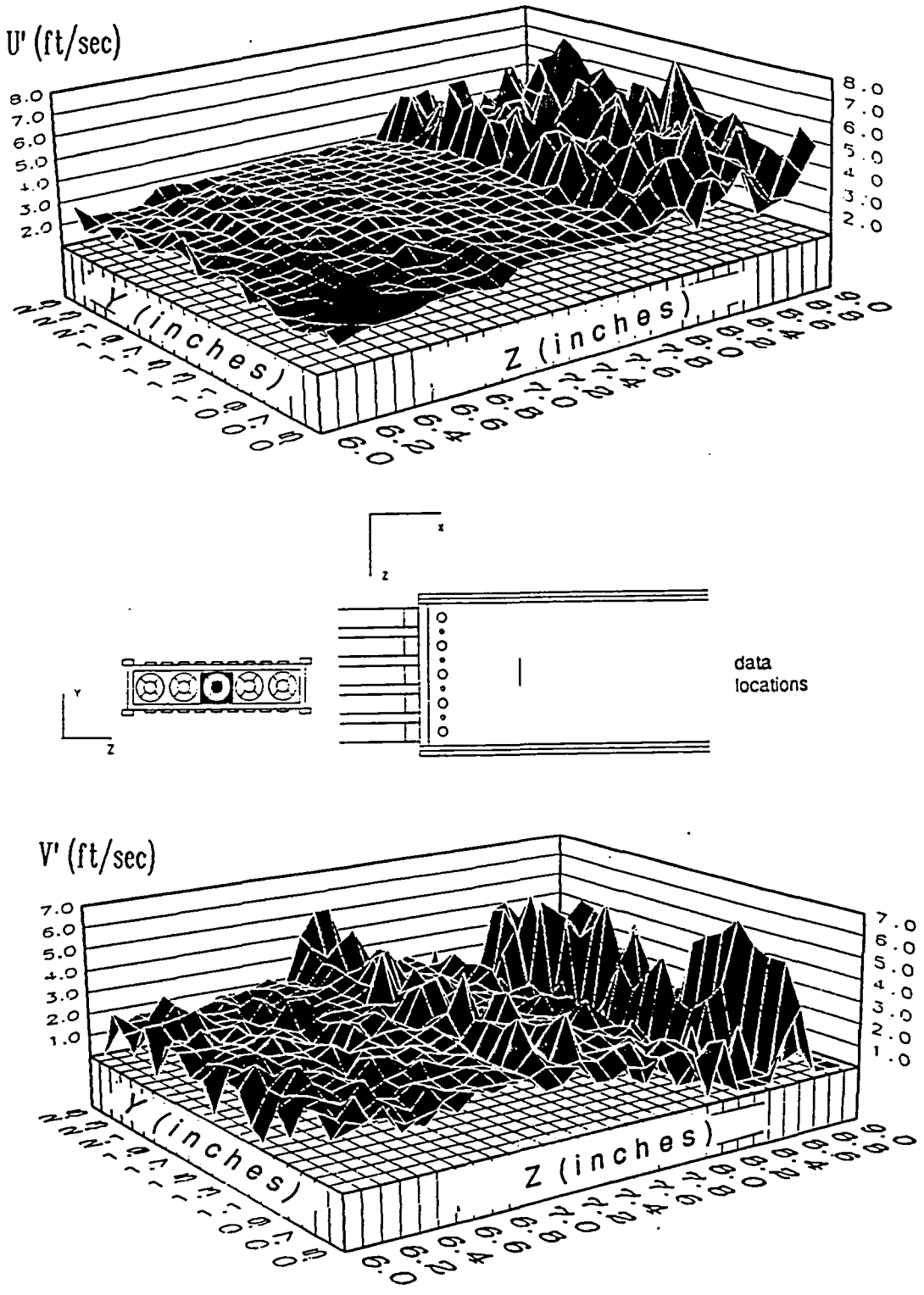

Figure C42 Annular Jets Only Contour Plot of U_{rms} and V_{rms} at X=9.0 in.

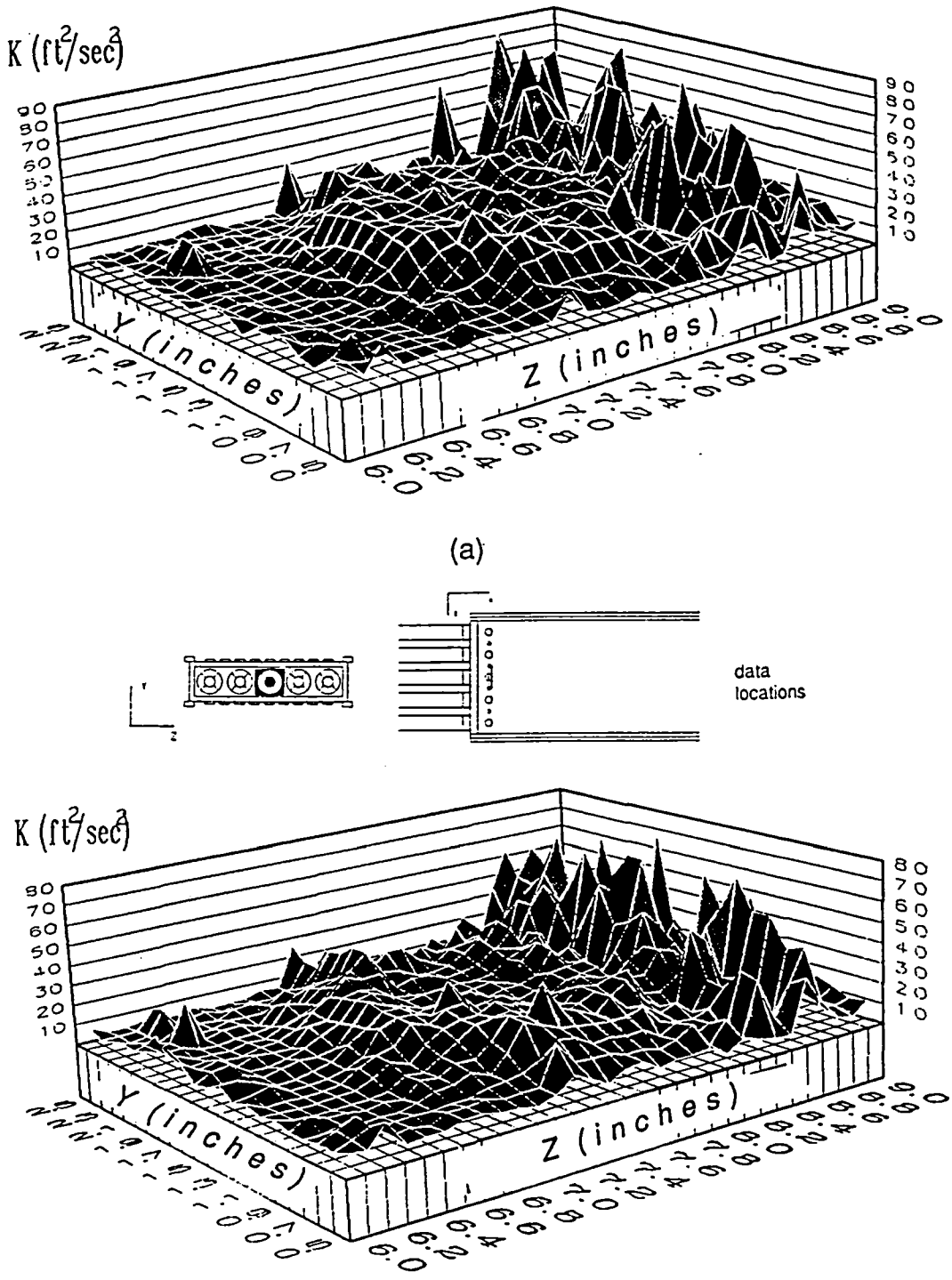

Figure C43 Annular Jets Only Contour Plot of K' at
a) X=1.5 in.; b) X=2.0 in.

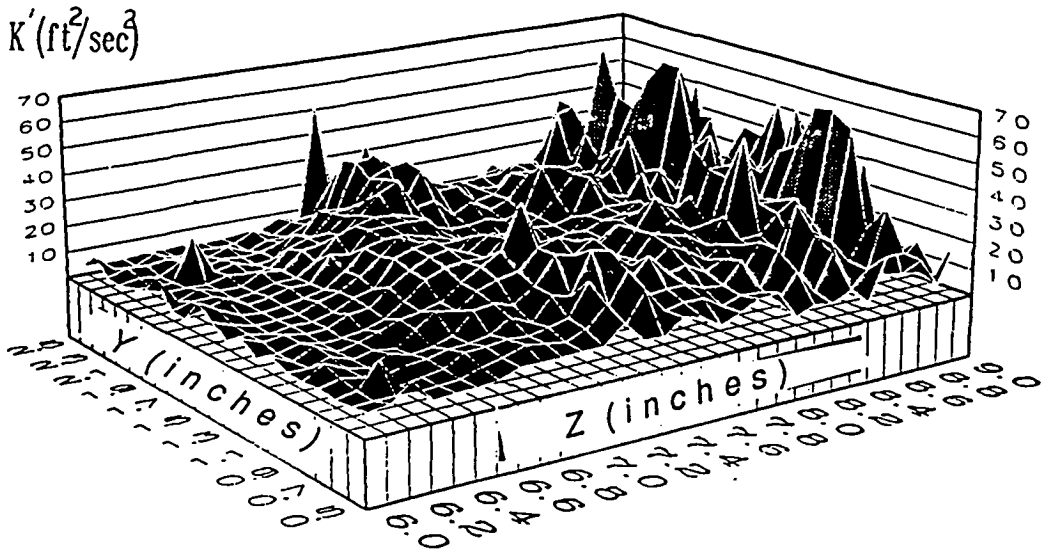

(a)

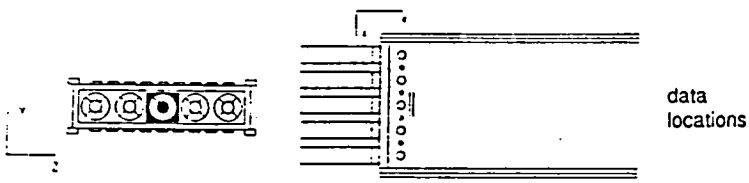

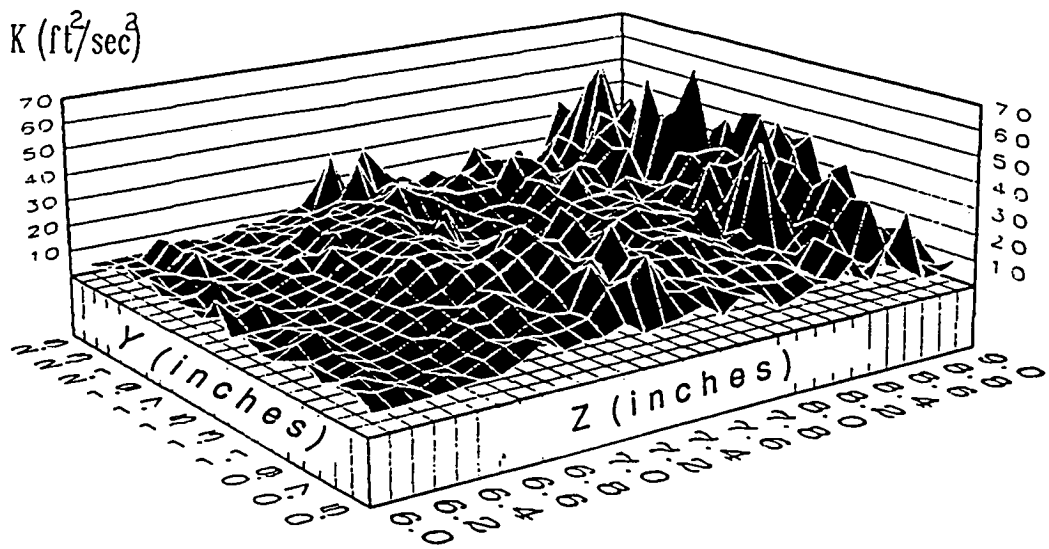

(b)

Figure C44 Annular Jets Only Contour Plot of K' at
a) X=2.5 in.; b) X=3.0 in.

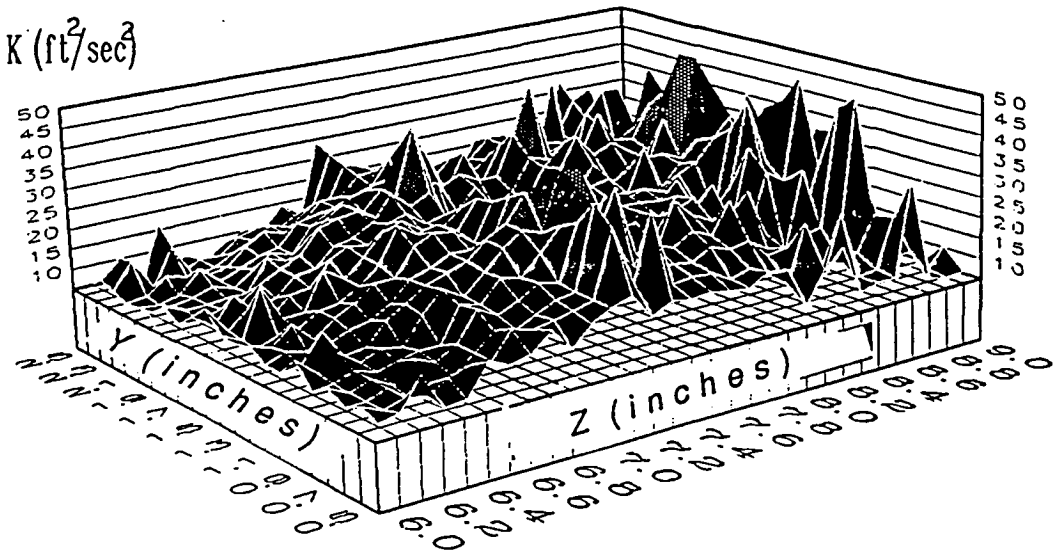

(a)

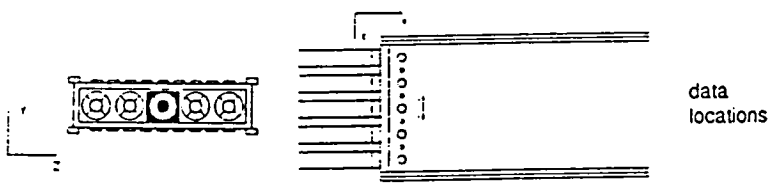

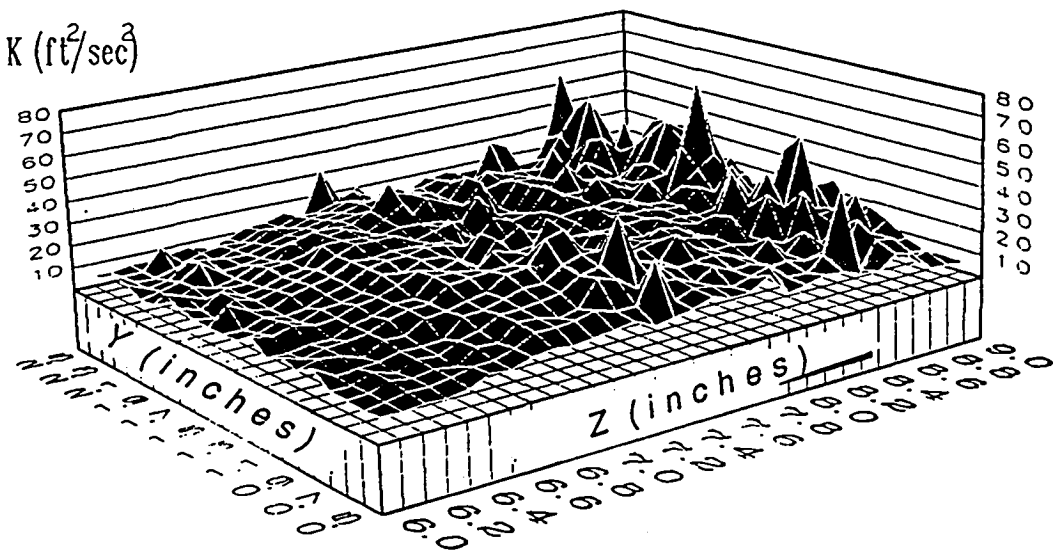

(b)

Figure C45 Annular Jets Only Contour Plot of K' at
a) X=3.5 in.; b) X=4.0 in.

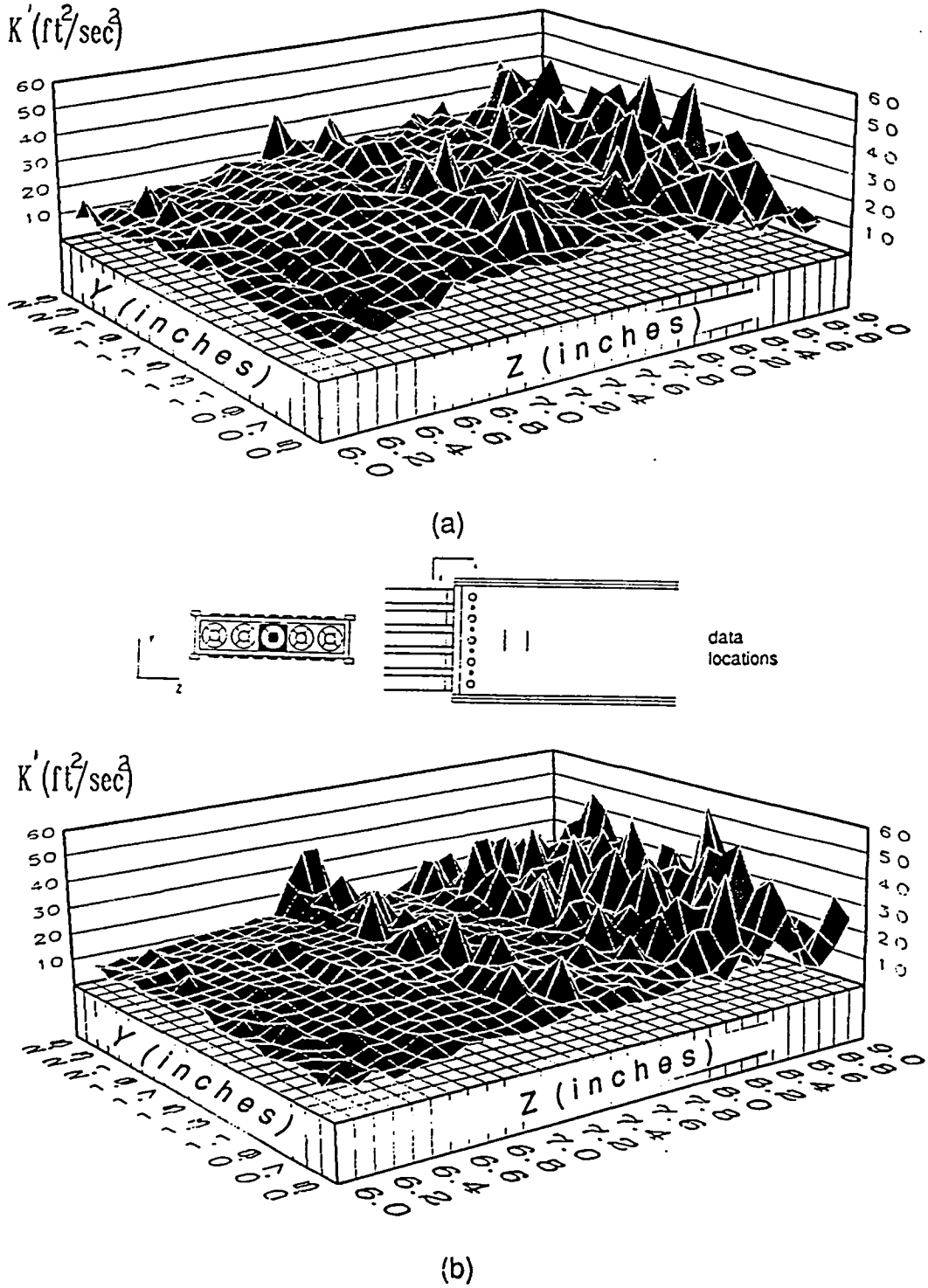

Figure C46 Annular Jets Only Contour Plot of K'at
a) X=6.0 in.; b) X=9.0 in.

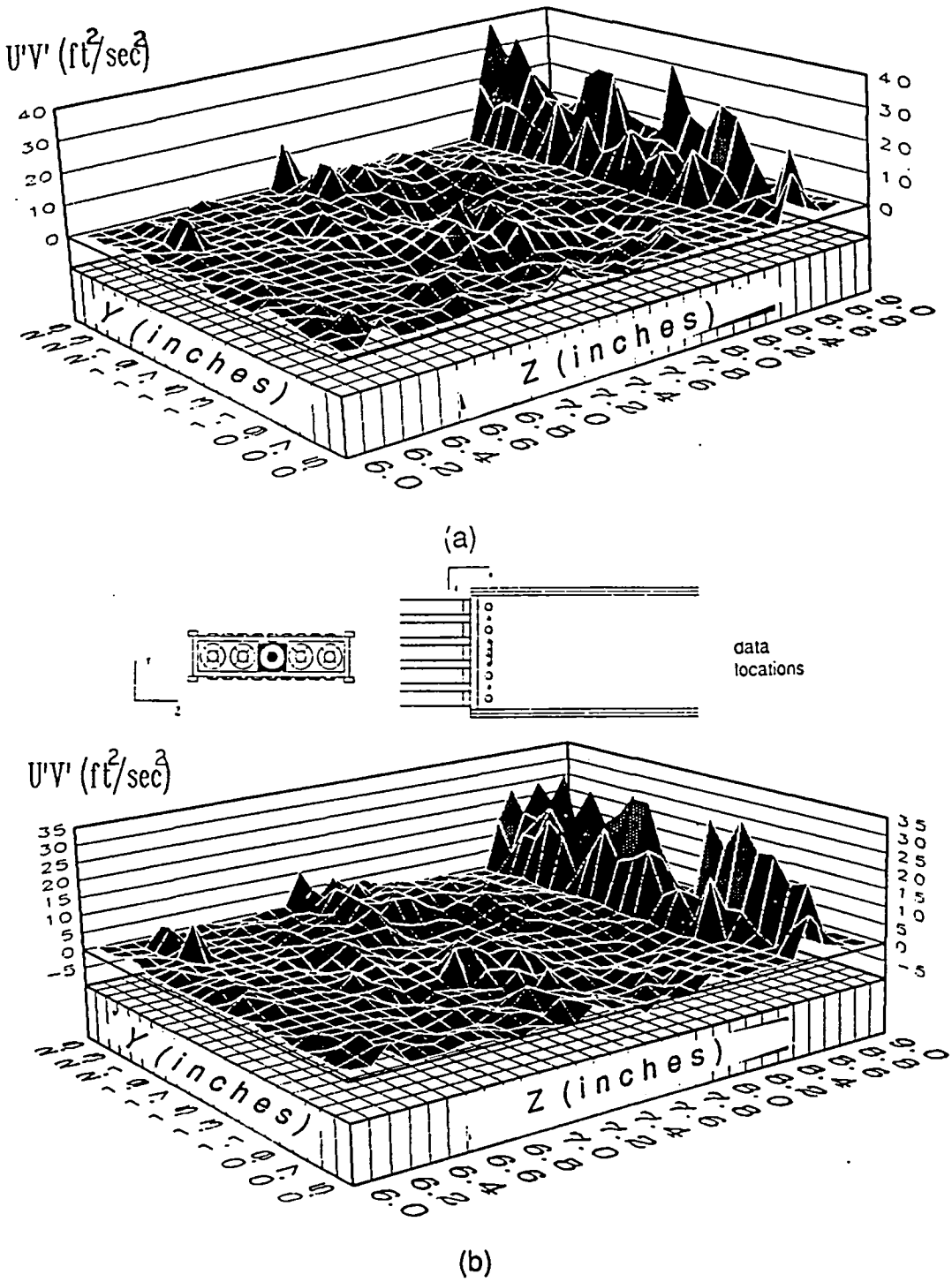

Figure C47 Annular Jets Only Contour Plot of U'V' at
a) X=1.5 in.; b) X=2.0 in.

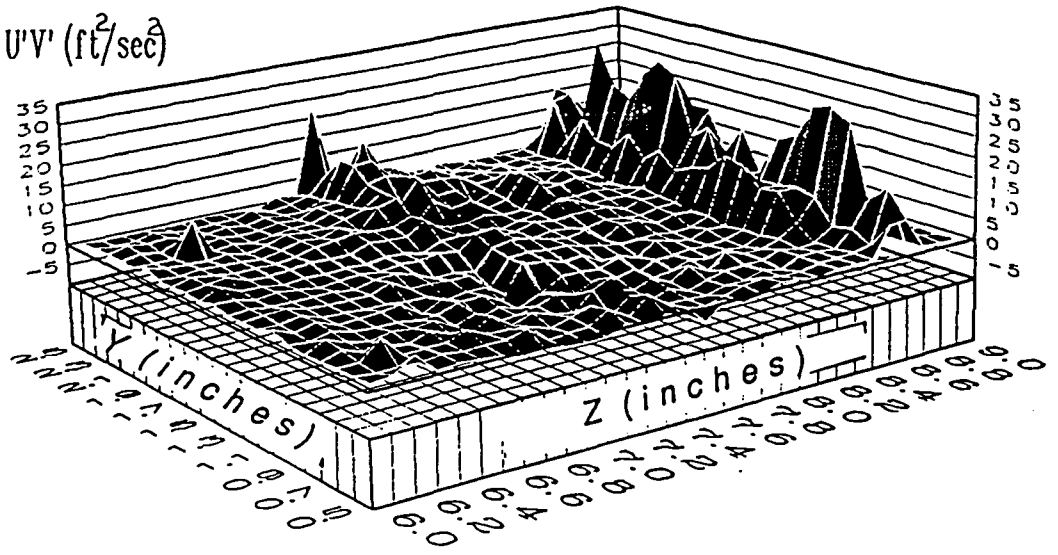

(a)

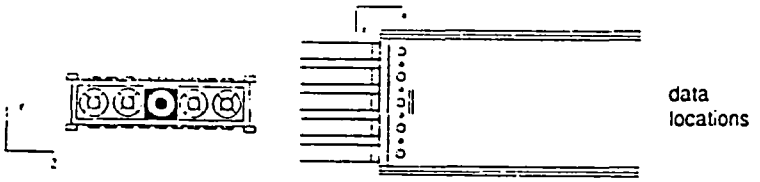

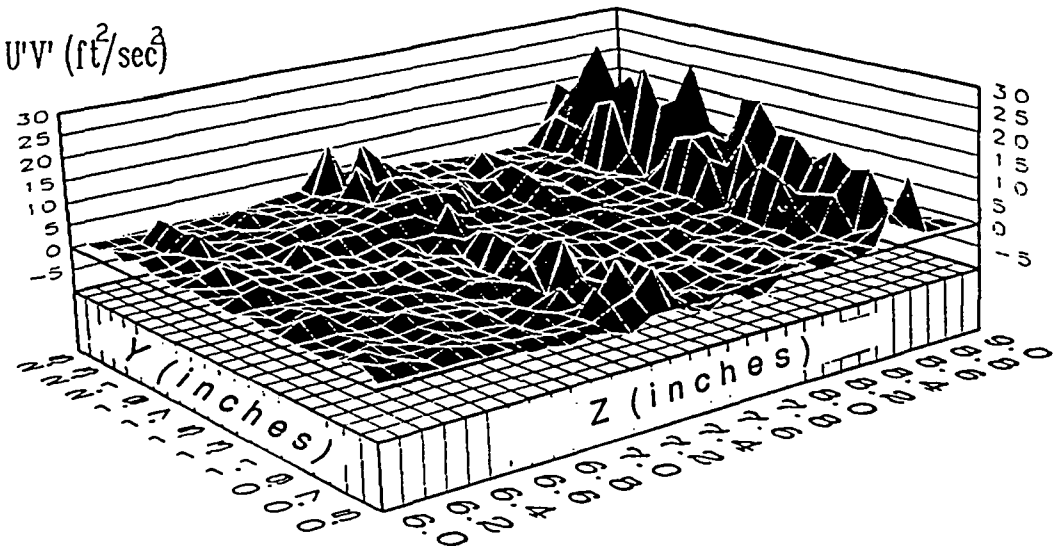

(b)

Figure C48 Annular Jets Only Contour Plot of U'V' at
a) X=2.5 in.; b) X=3.0 in.

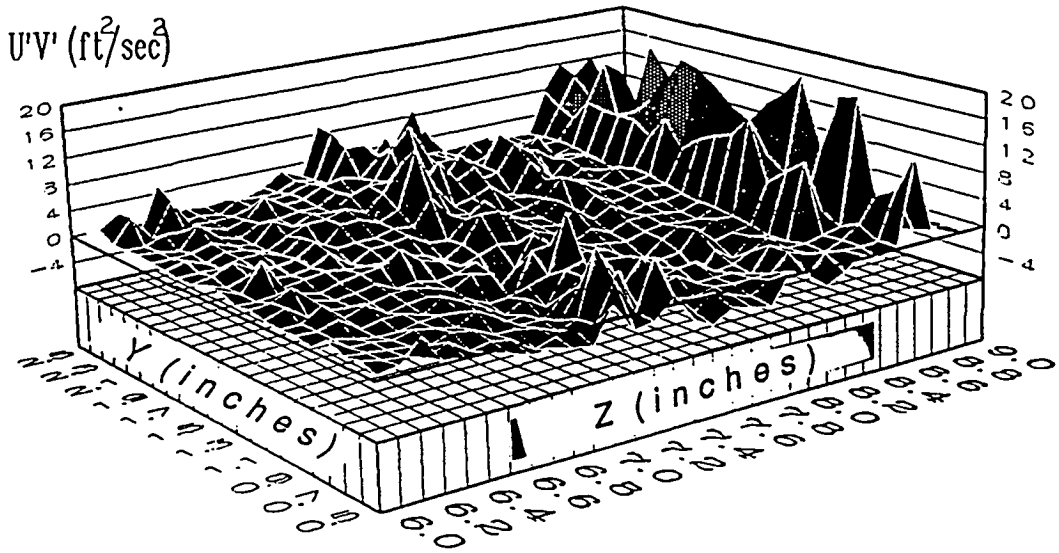

(a)

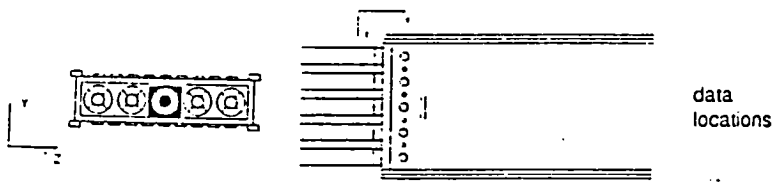

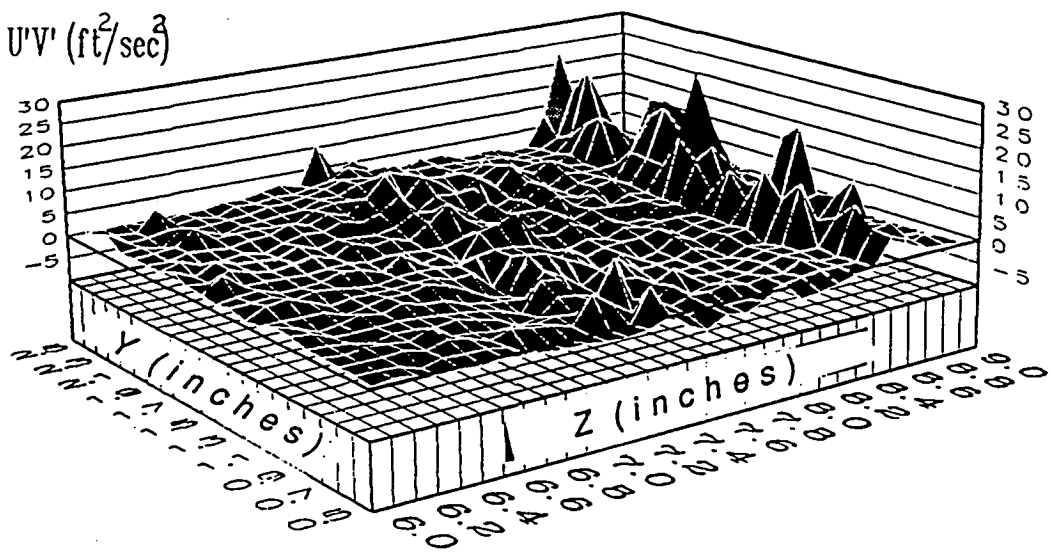

(b)

Figure C49 Annular Jets Only Contour Plot of U'V' at
a) X=3.5 in.; b) X=4.0 in.

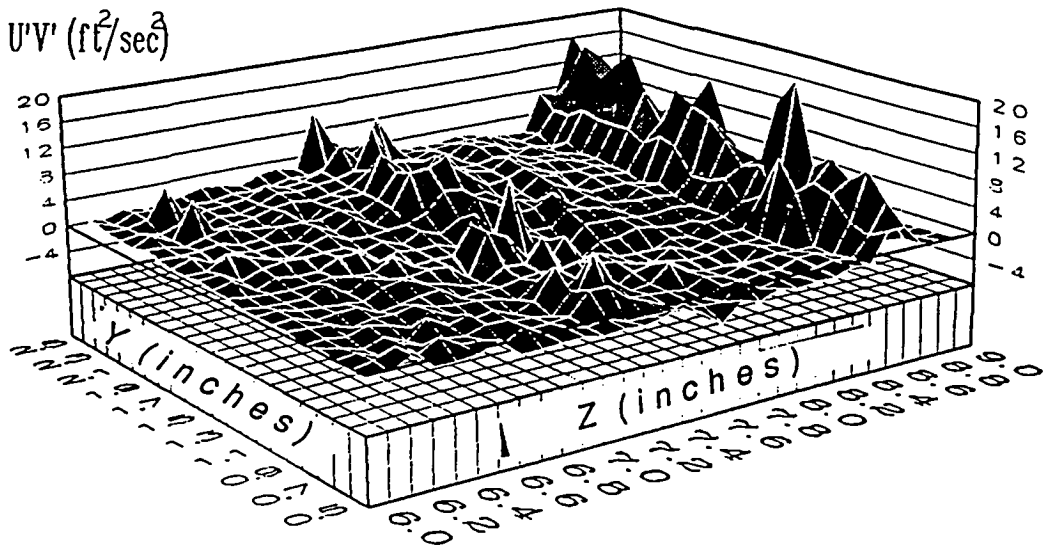

(a)

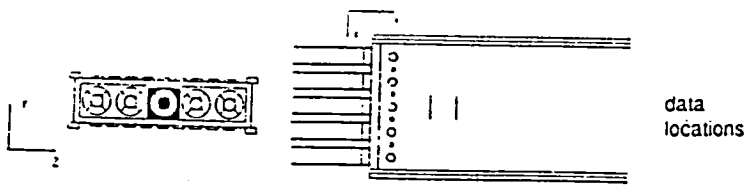

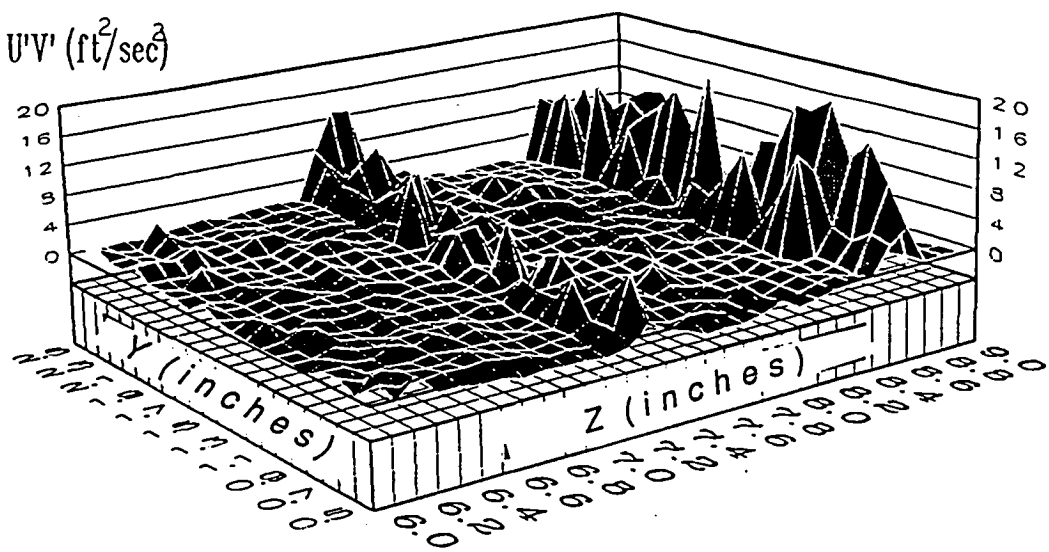

(b)

Figure C50 Annular Jets Only Contour Plot of U'V' at
a) X=6.0 in.; b) X=9.0 in.

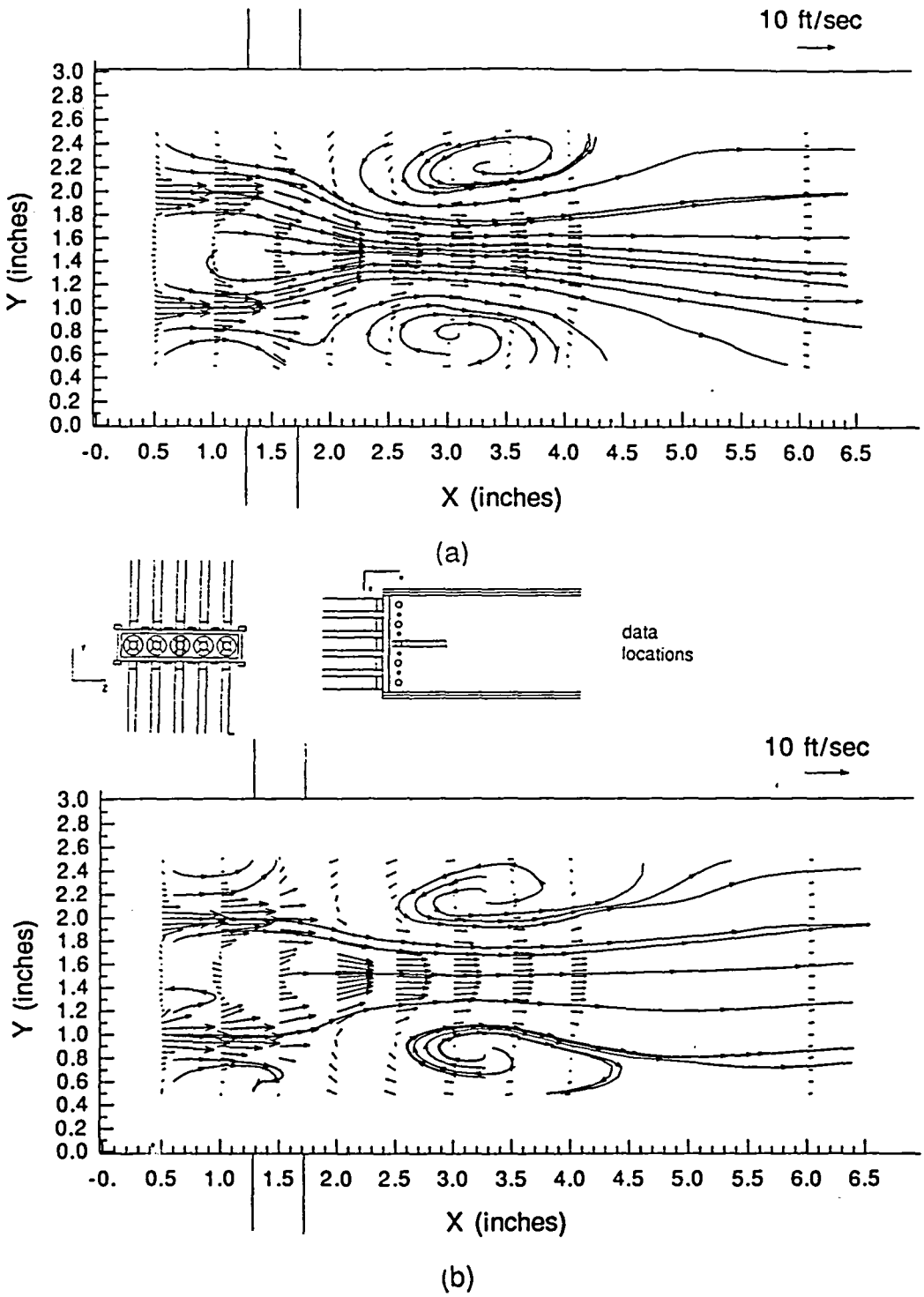

Figure C51 Annular and Primary Jets Mean Velocity Vector plots at a) Z=7.1 in.; b) Z=7.9 in.

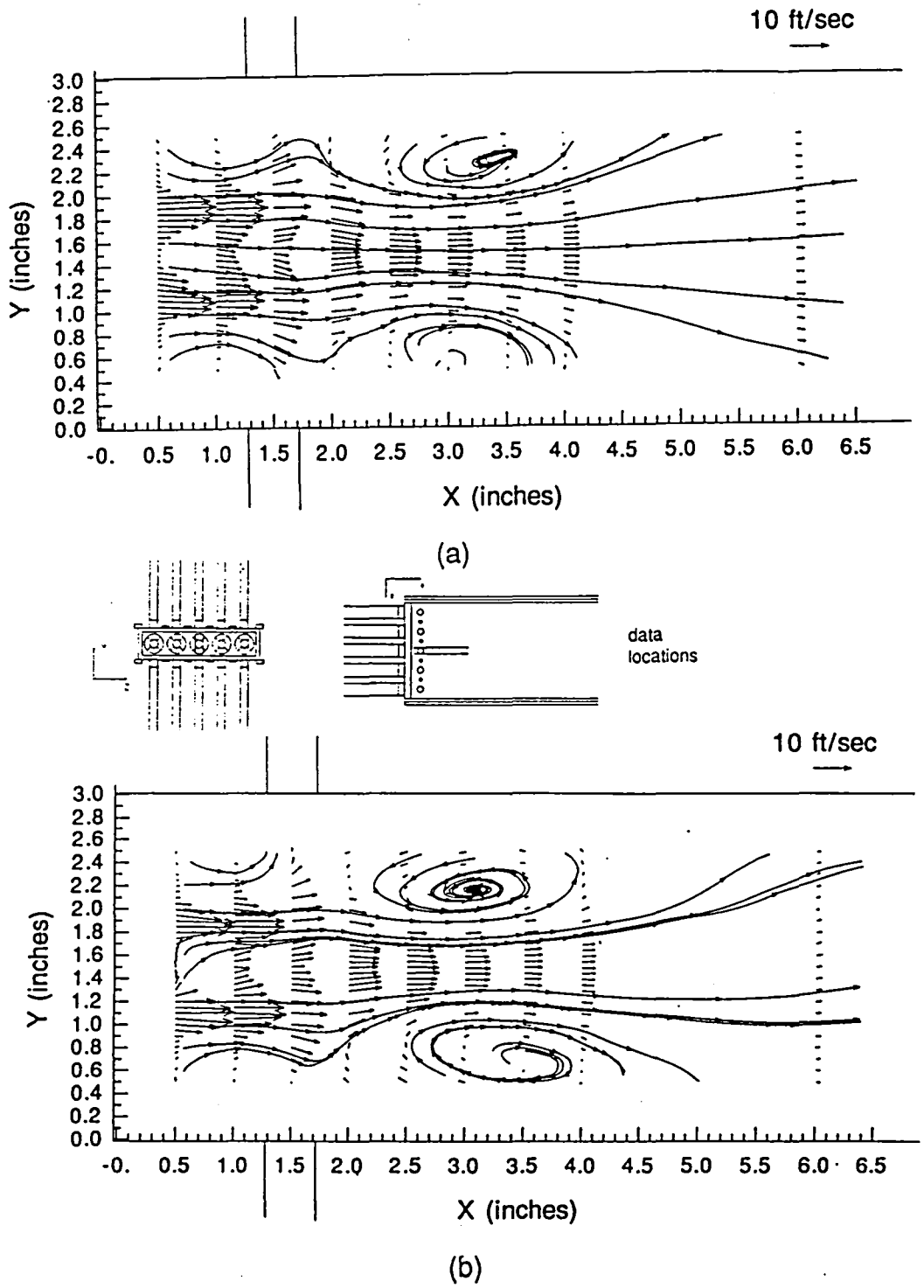

Figure C52 Annular and Primary Jets Mean Velocity Vector plots at a) Z=7.0 in.; b) Z=8.0 in.

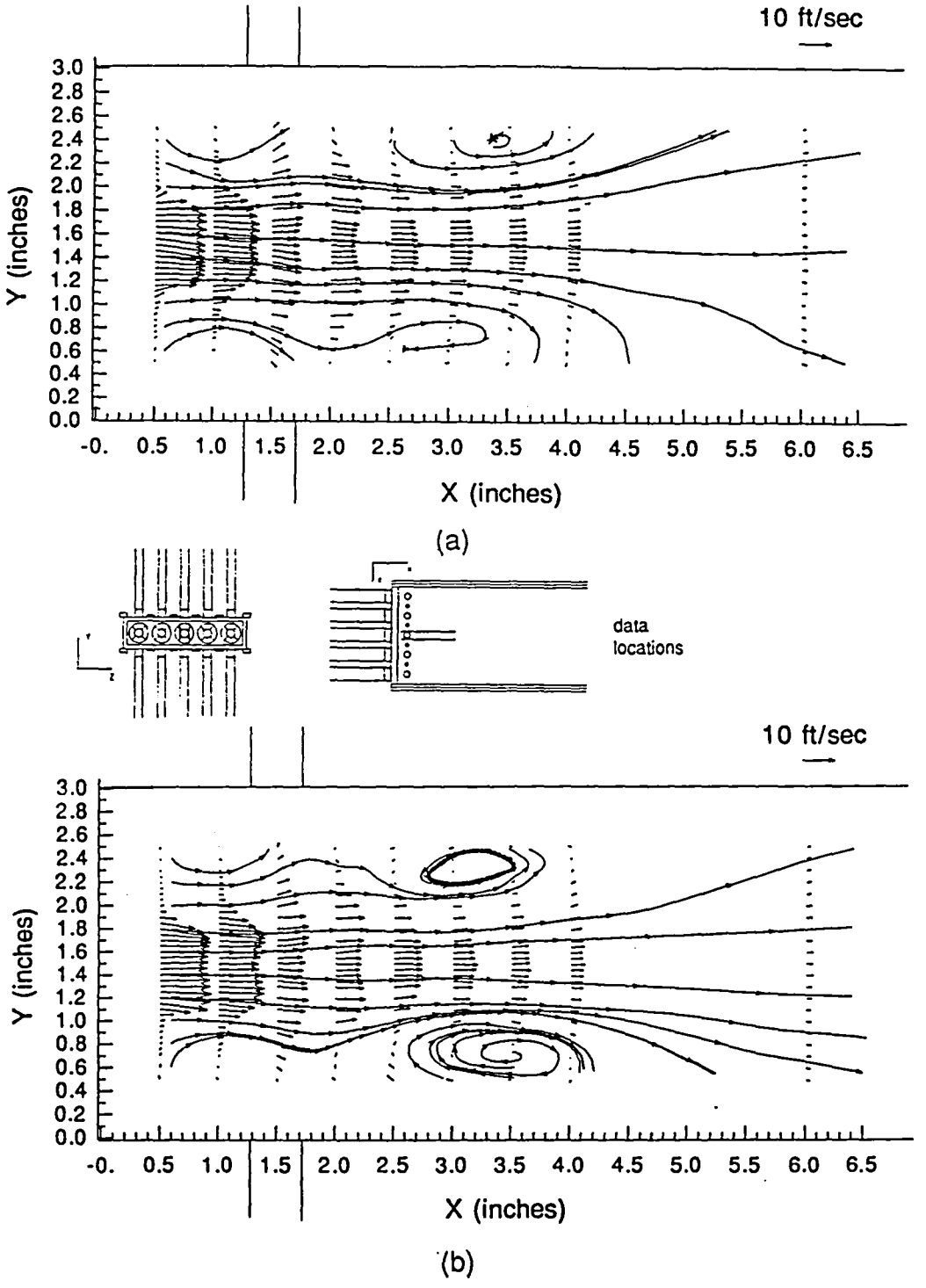

Figure C53 Annular and Primary Jets Mean Velocity Vector plots at a) Z=6.9 ir..; b) Z=8.1 in.

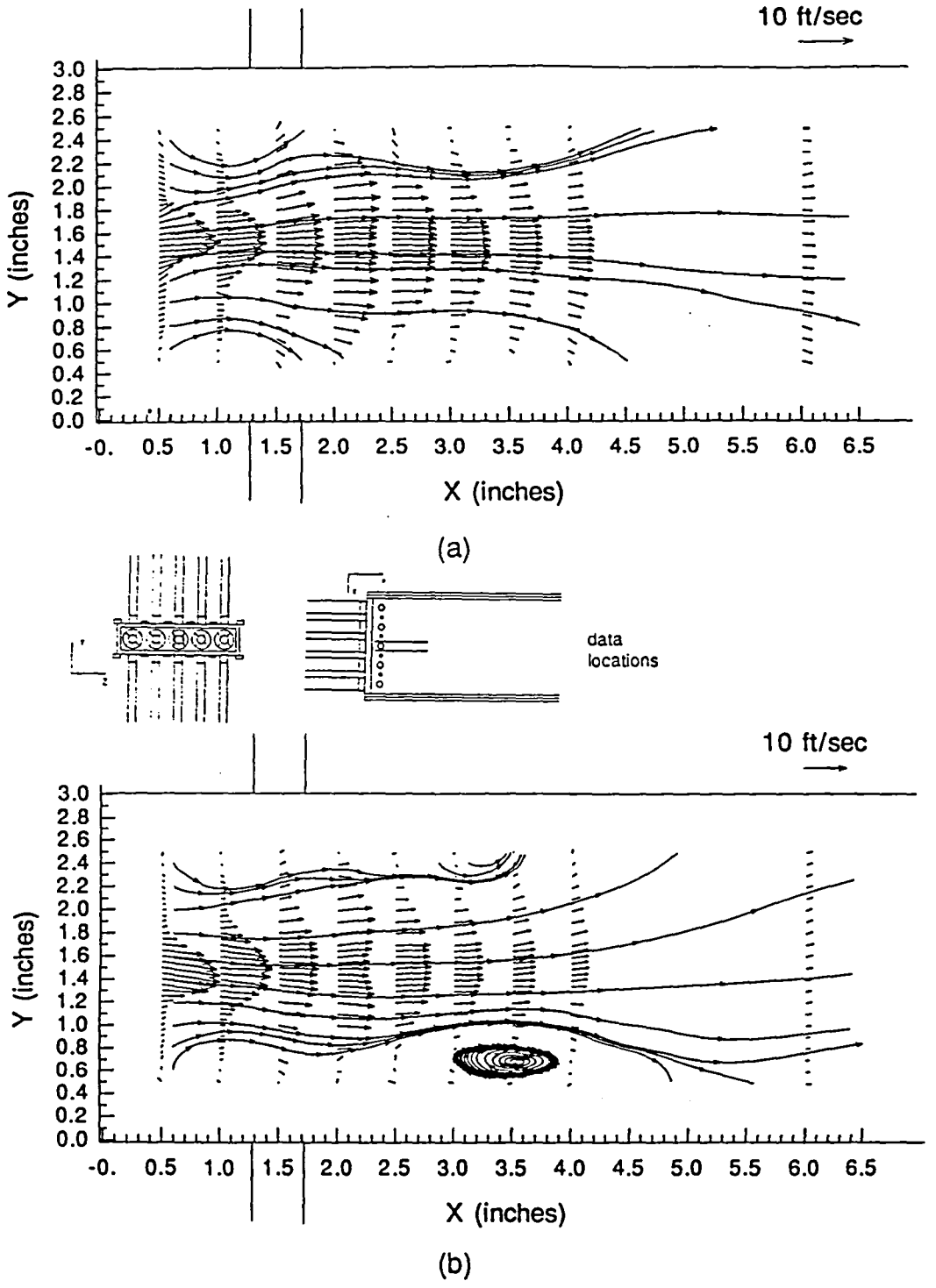

Figure C54 Annular and Primary Jets Mean Velocity Vector plots at a) Z=6.8 in.; b) Z=8.2 in.

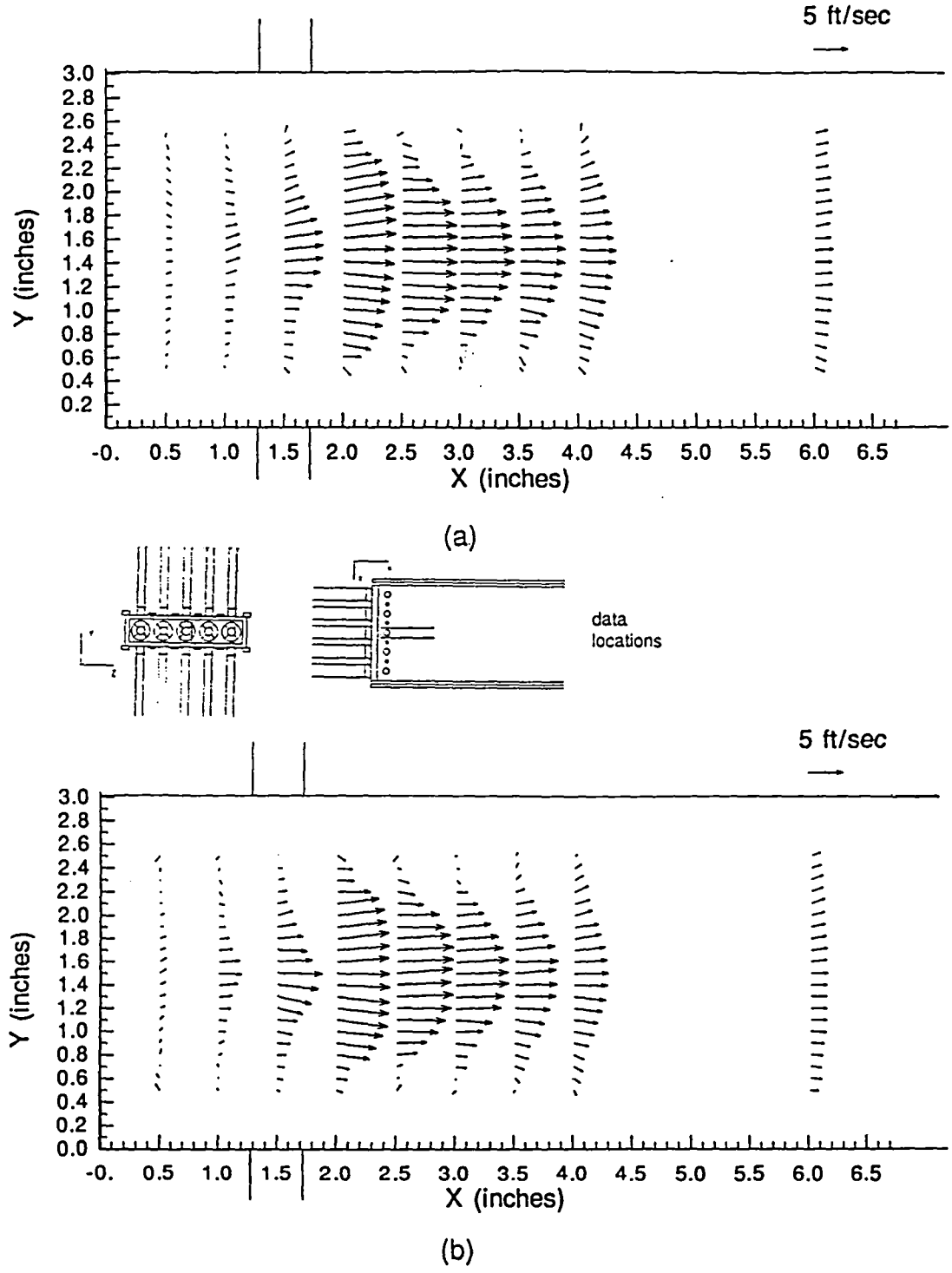

Figure C55 Annular and Primary Jets Mean Velocity Vector plots at a) Z=6.7 in.; b) Z=8.3 in.

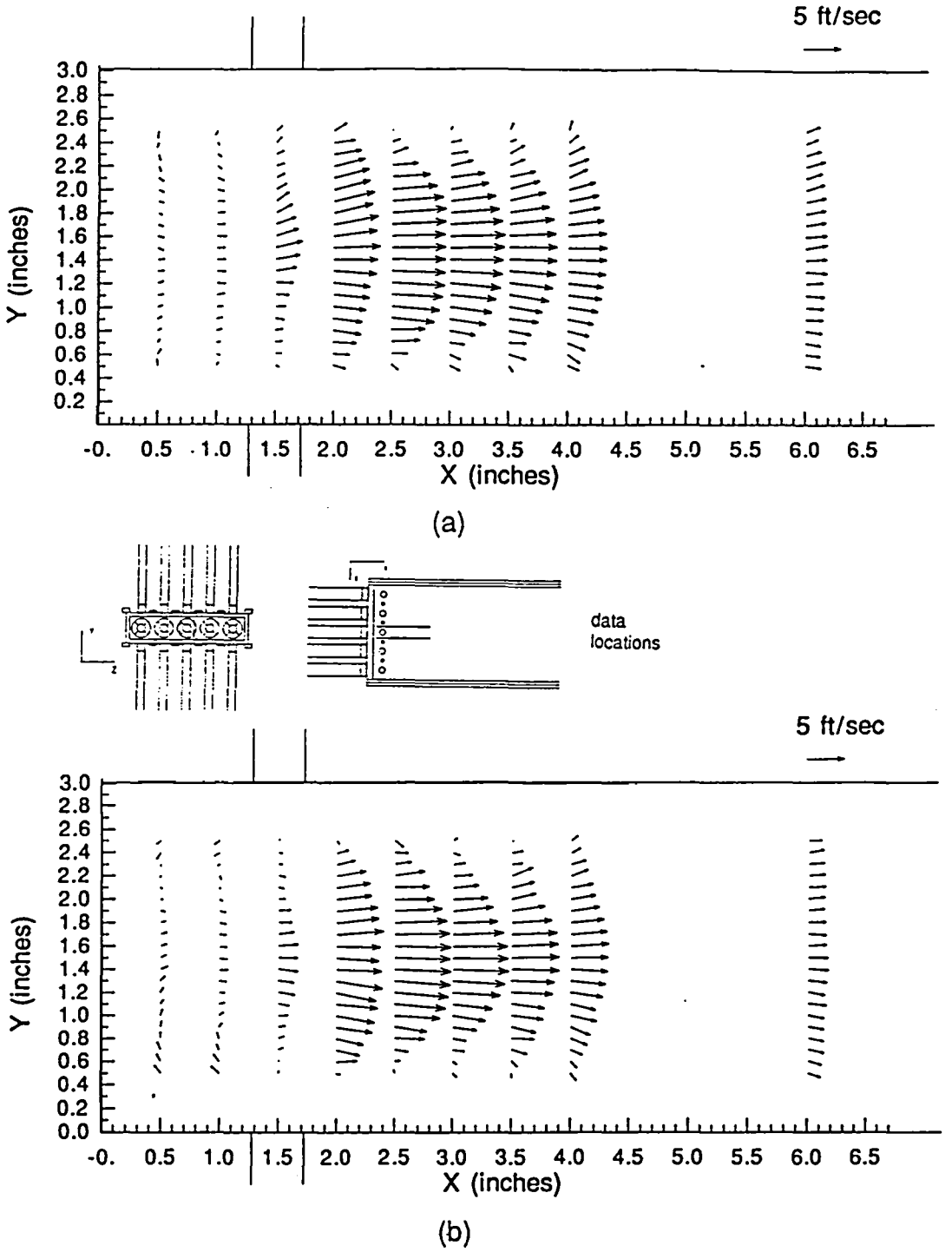

Figure C56 Annular and Primary Jets Mean Velocity Vector plots at a) Z=6.6 in.; b) Z=8.4 in.

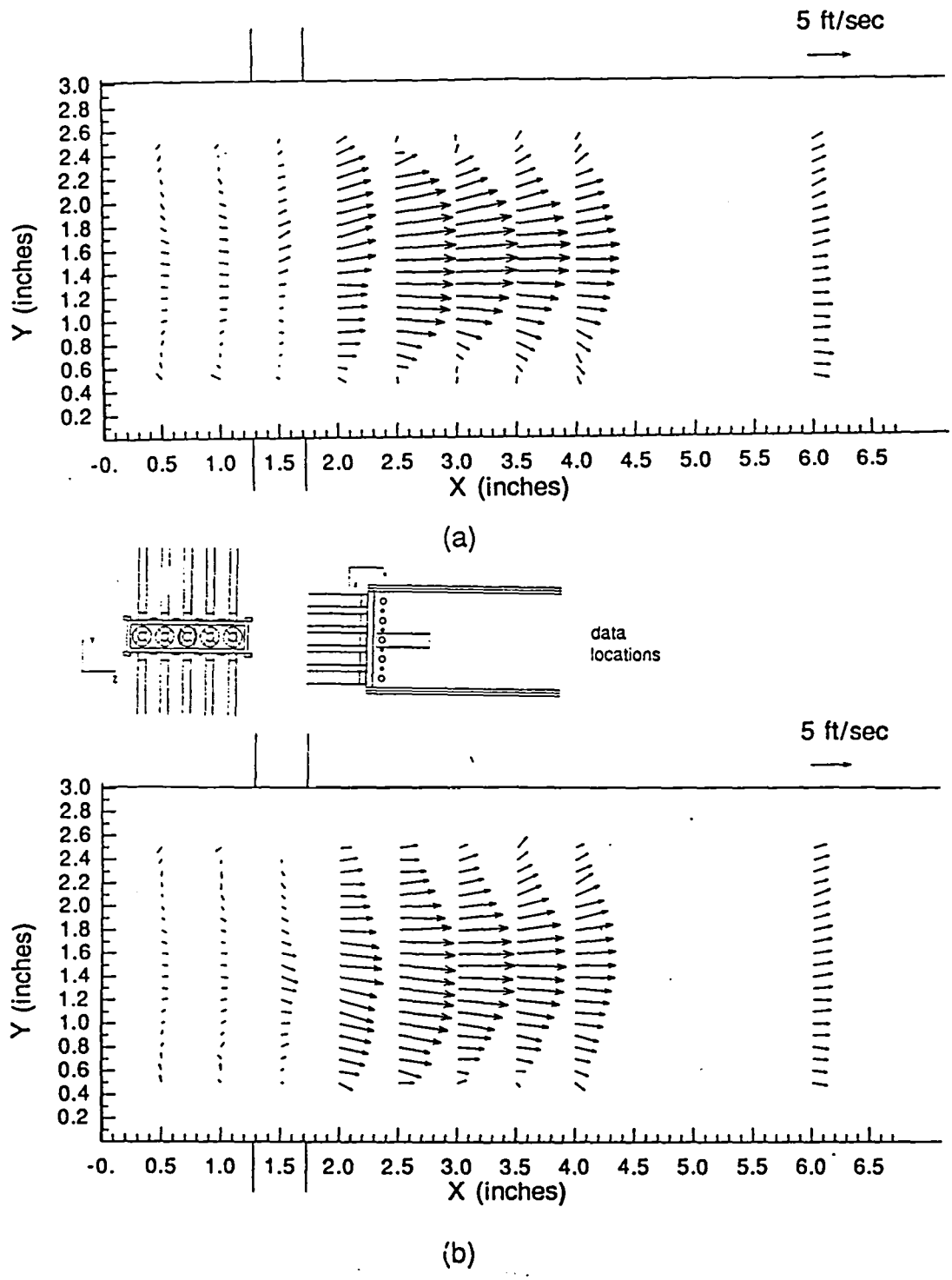

Figure C57 Annular and Primary Jets Mean Velocity Vector plots at a) Z=6.5 in.; b) Z=8.5 in.

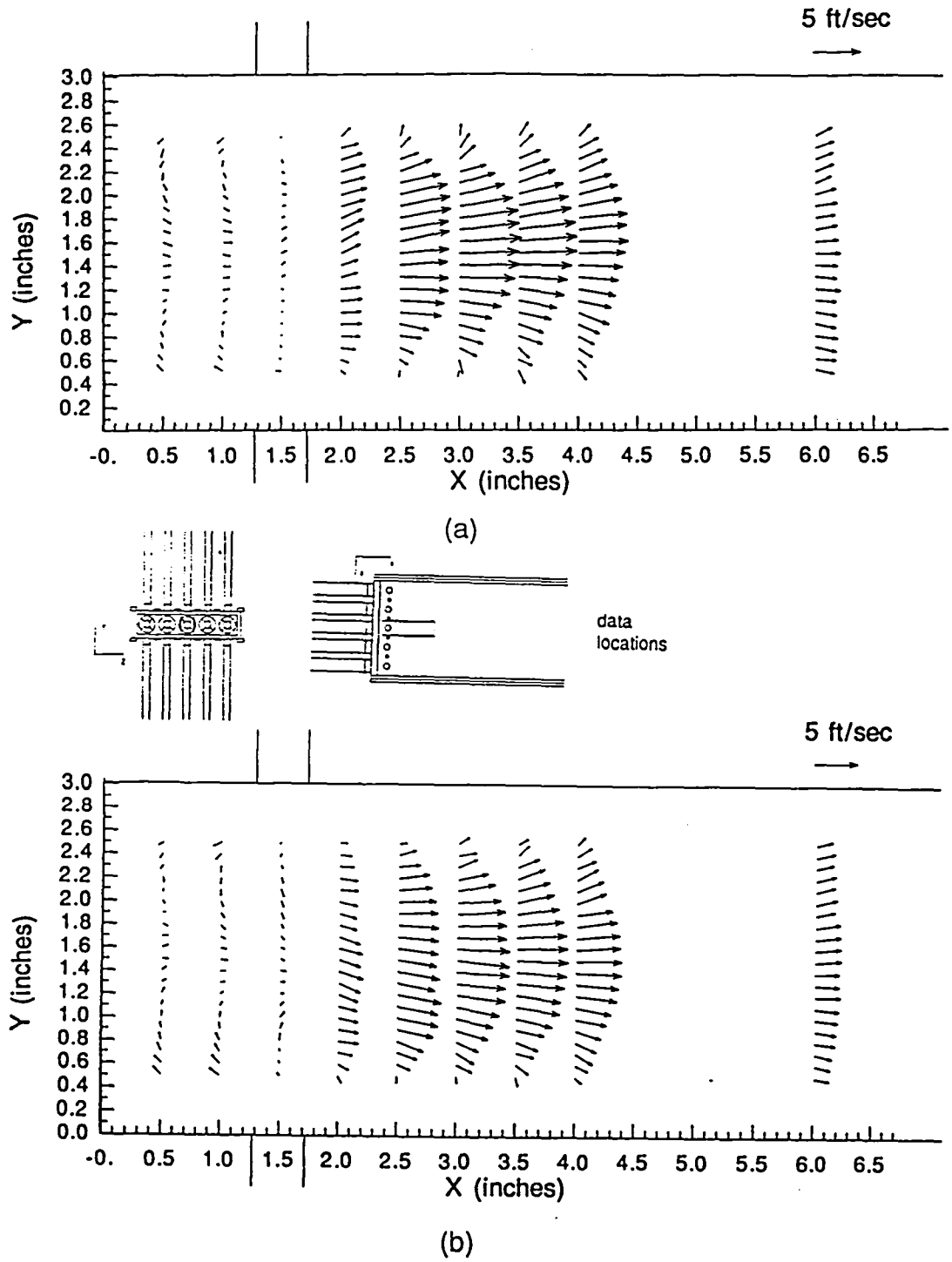

Figure C58 Annular and Primary Jets Mean Velocity Vector plots at a) Z=6.4 in.; b) Z=8.6 in.

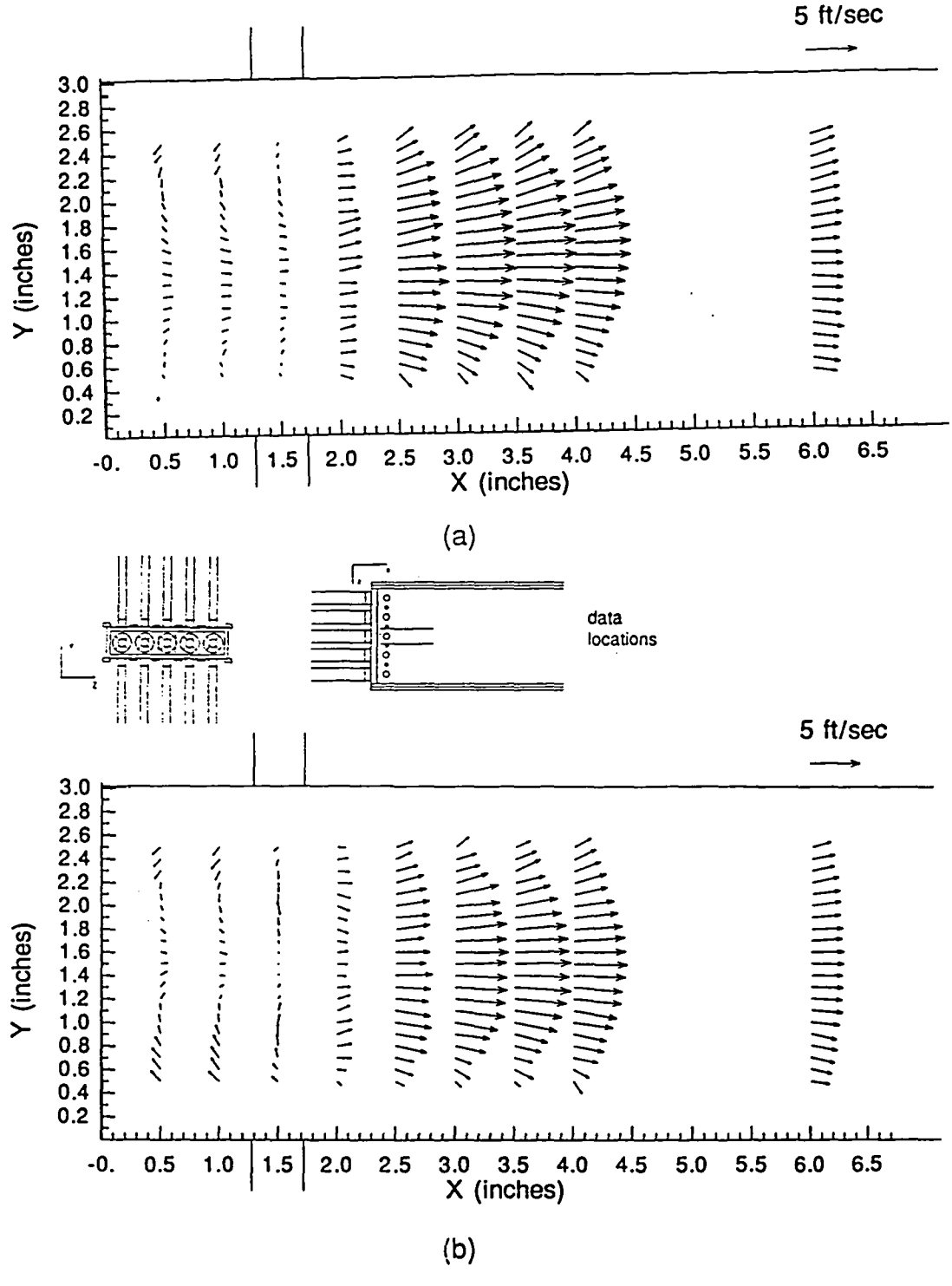

Figure C59 Annular and Primary Jets Mean Velocity Vector plots at a) Z=6.3 in.; b) Z=8.7 in.

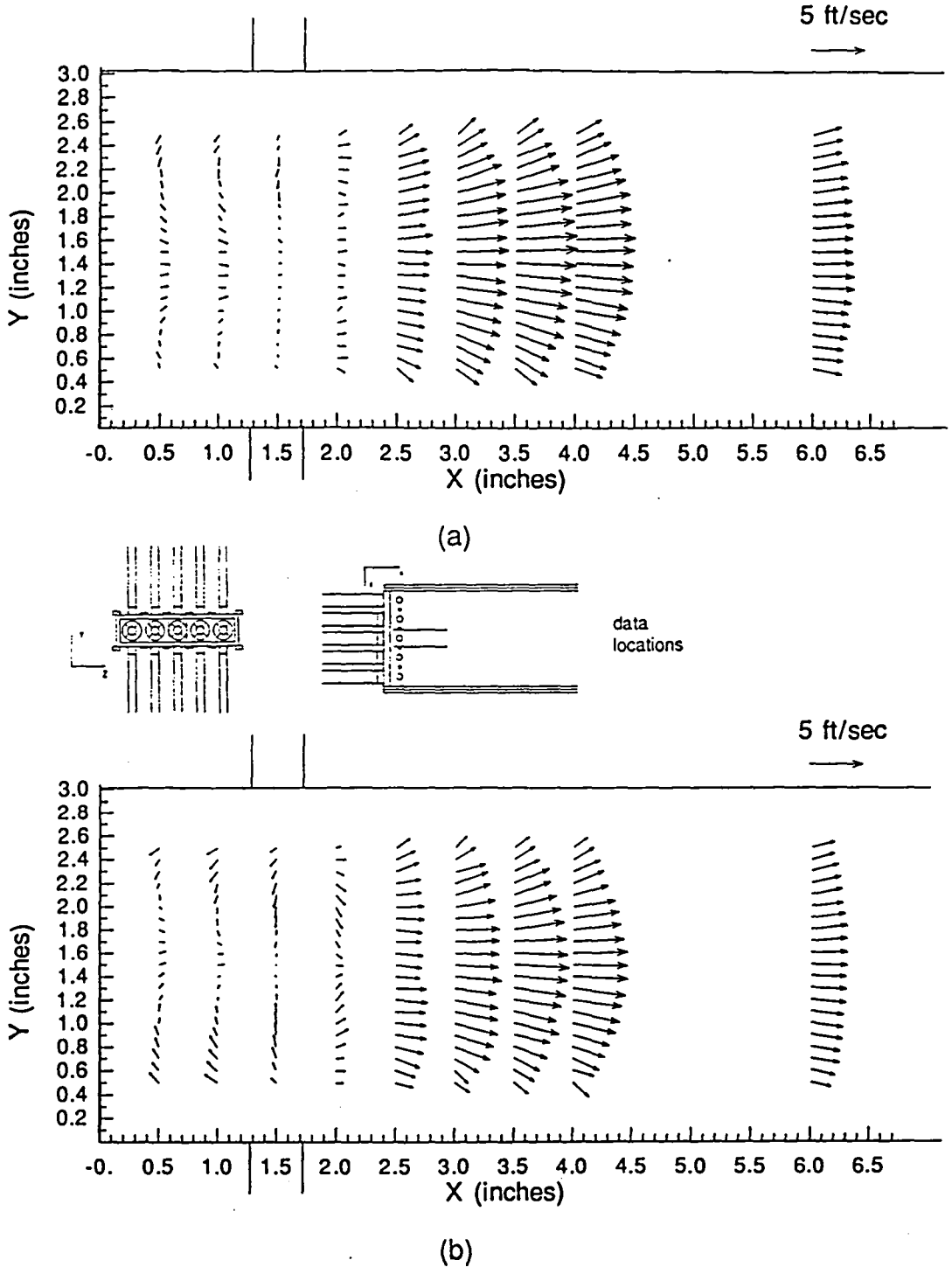

Figure C60 Annular and Primary Jets Mean Velocity Vector plots at a) Z=6.2 in.; b) Z=8.8 in.

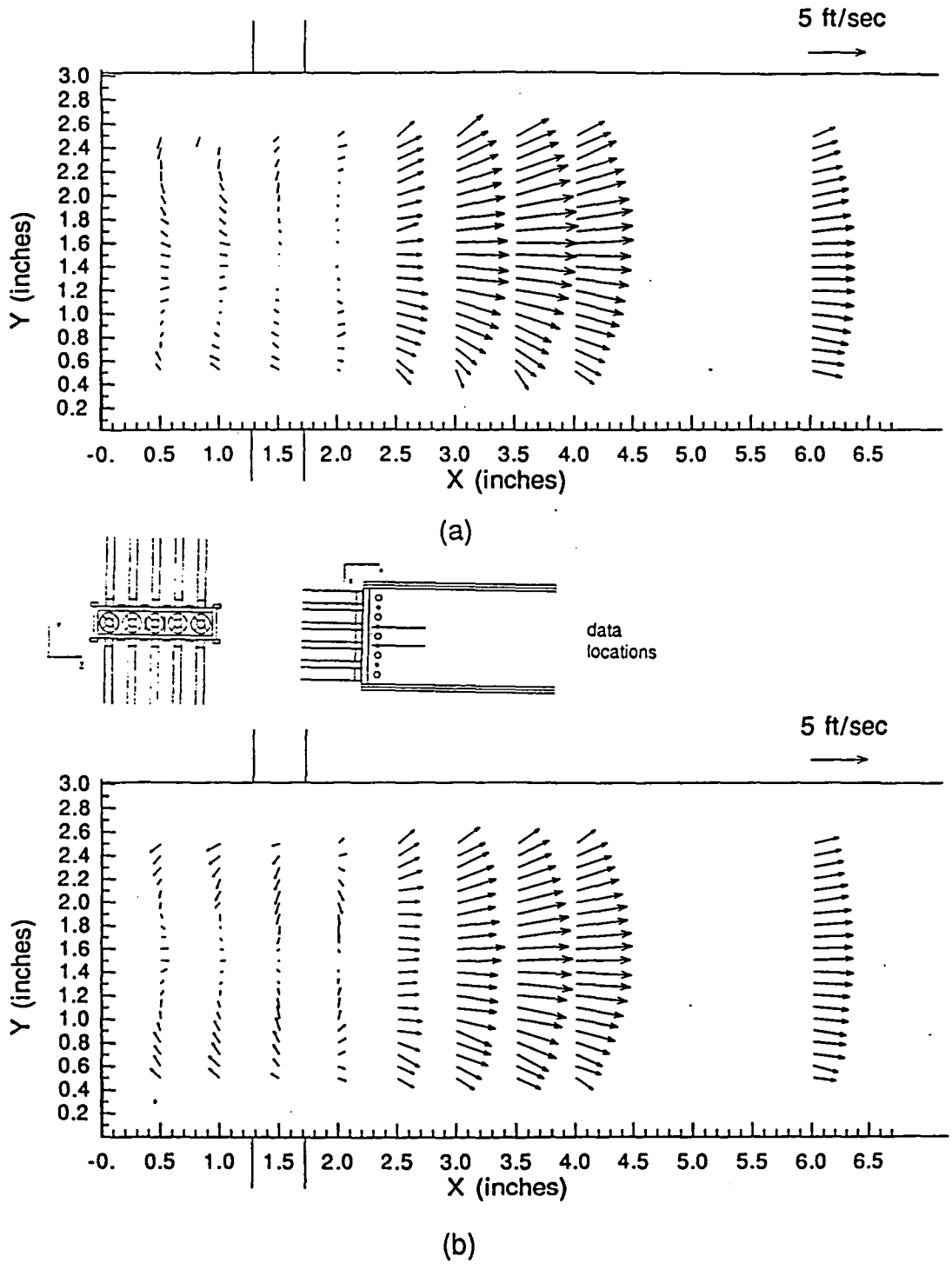

Figure C61 Annular and Primary Jets Mean Velocity Vector plots at a) Z=6.1 in.; b) Z=8.9 in.

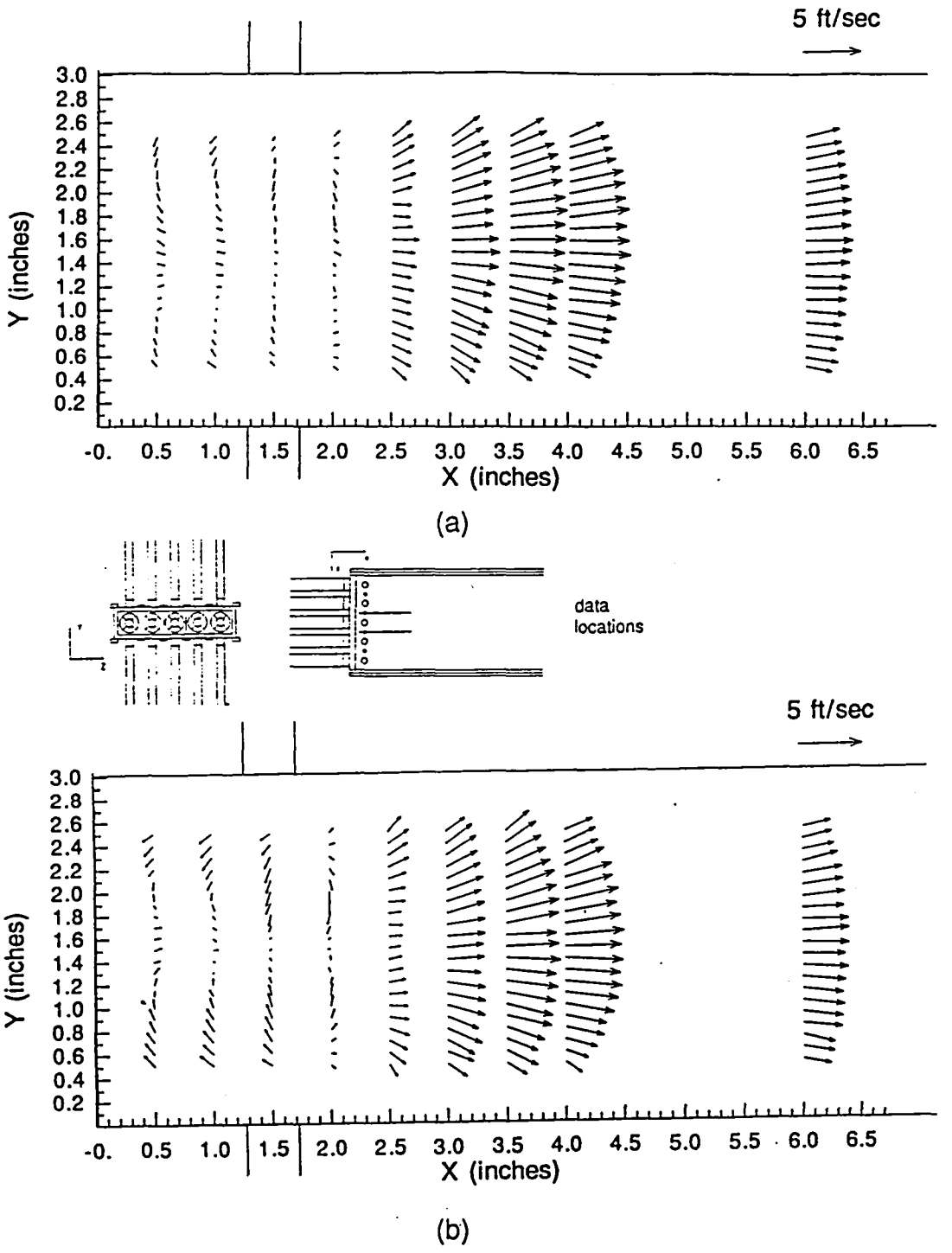

Figure C62 Annular and Primary Jets Mean Velocity Vector plots at a) Z=6.0 in.; b) Z=9.0 in.

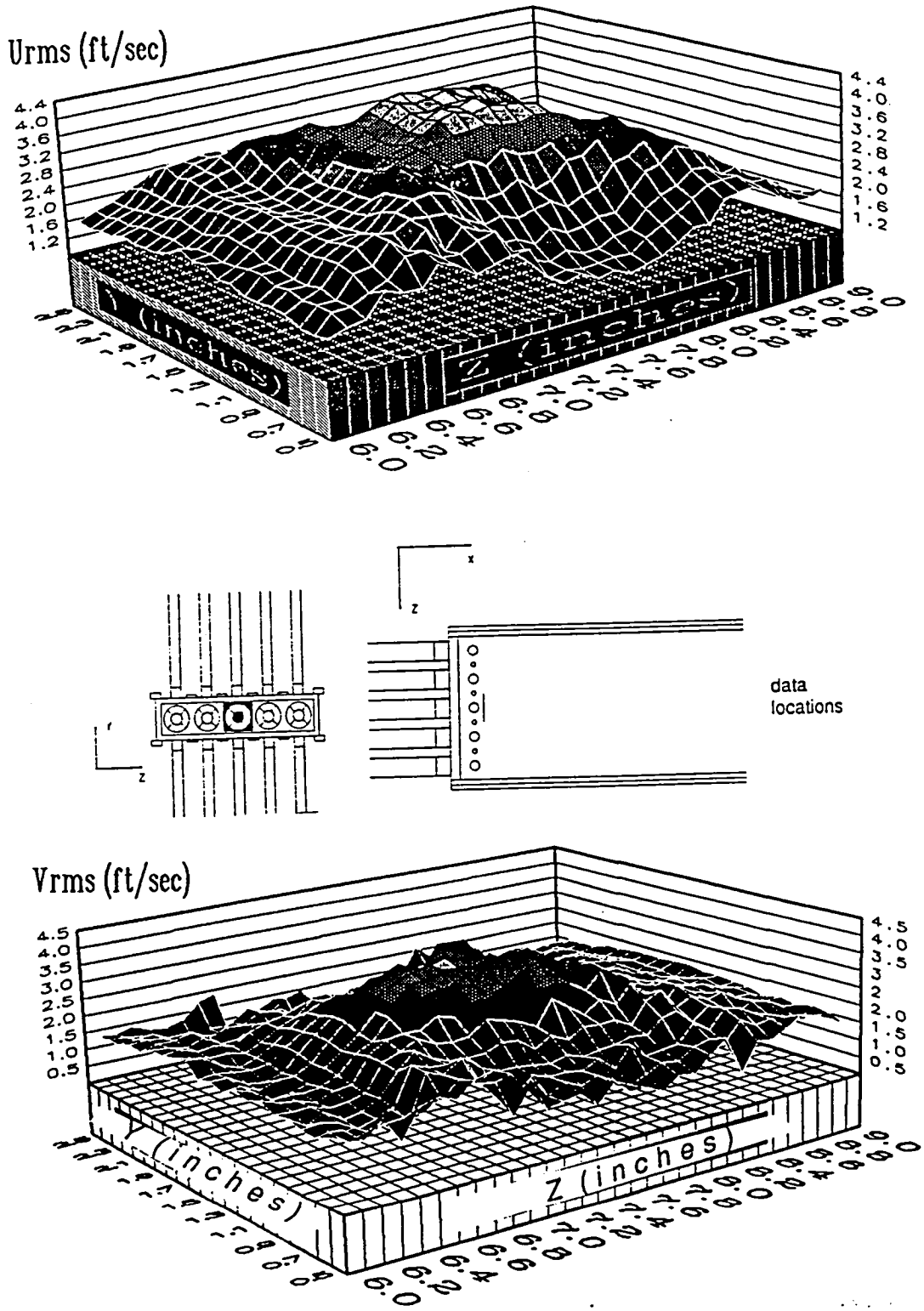

Figure C63 Annular and Primary Jets Contour Plot of U_{rms} and V_{rms} at X=2.5 in.

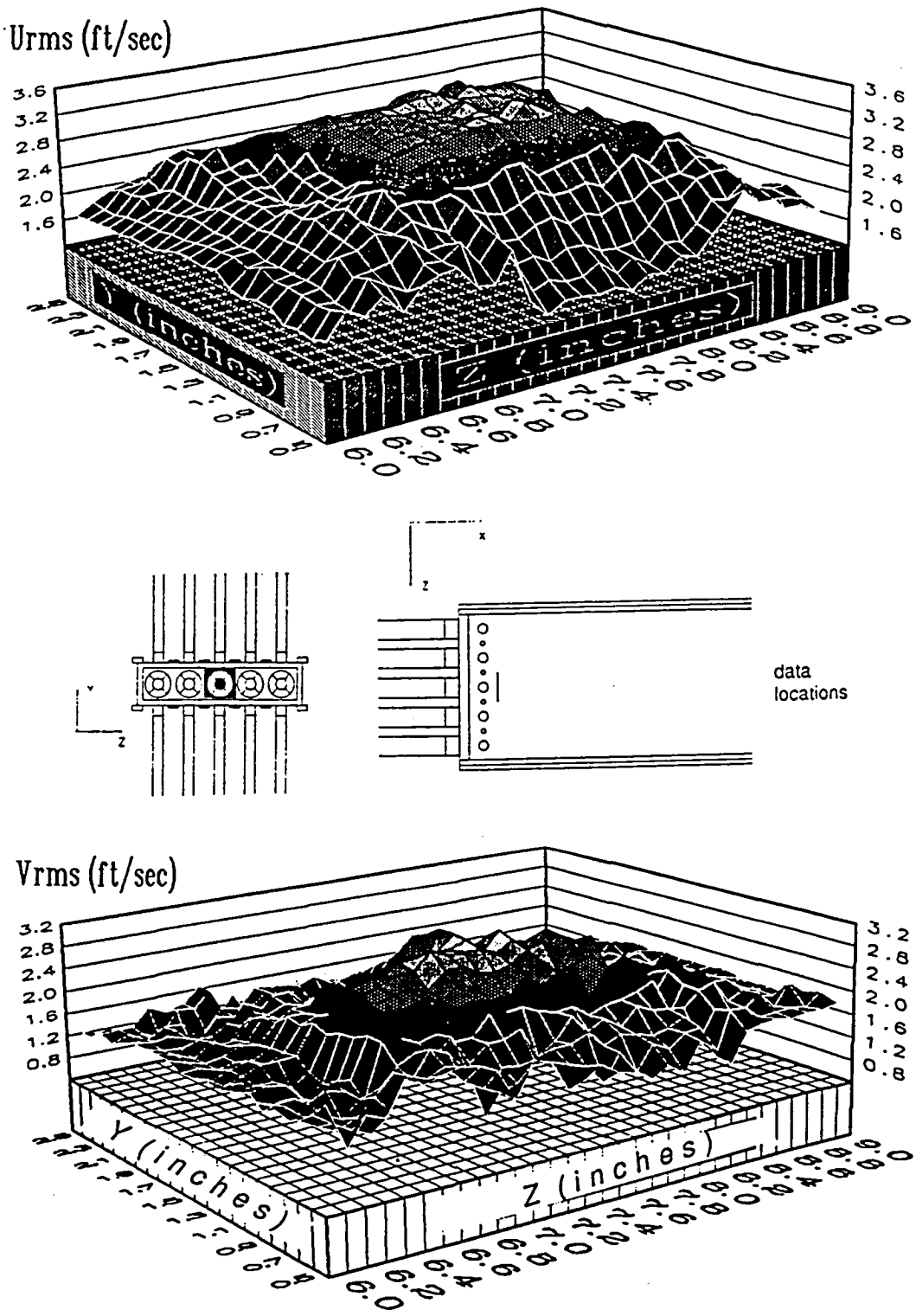

Figure C64 Annular and Primary Jets Contour Plot of U_{rms} and V_{rms} at X=3.0 in.

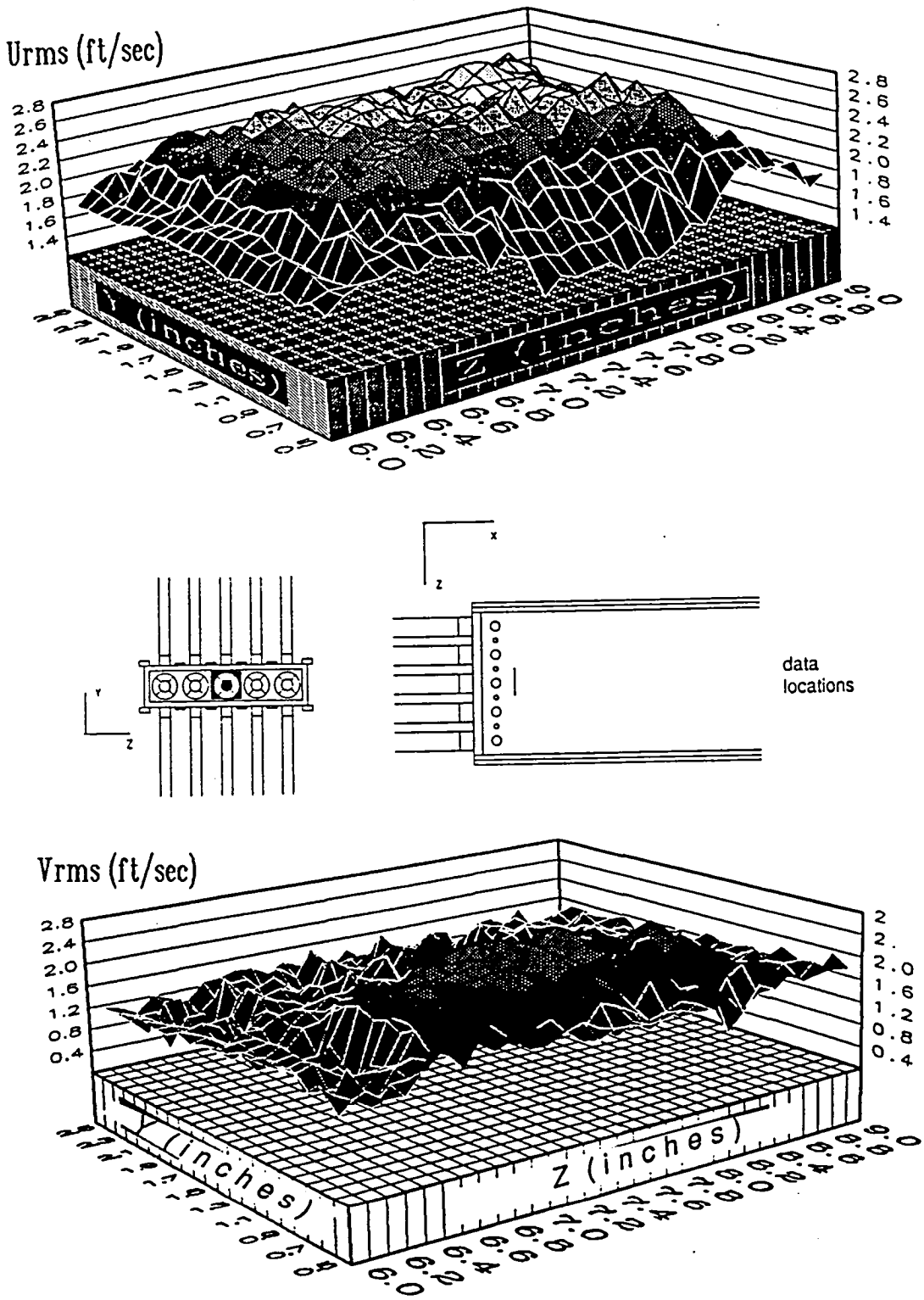

Figure C65 Annular and Primary Jets Contour Plot of U_{rms} and V_{rms} at X=3.5 in.

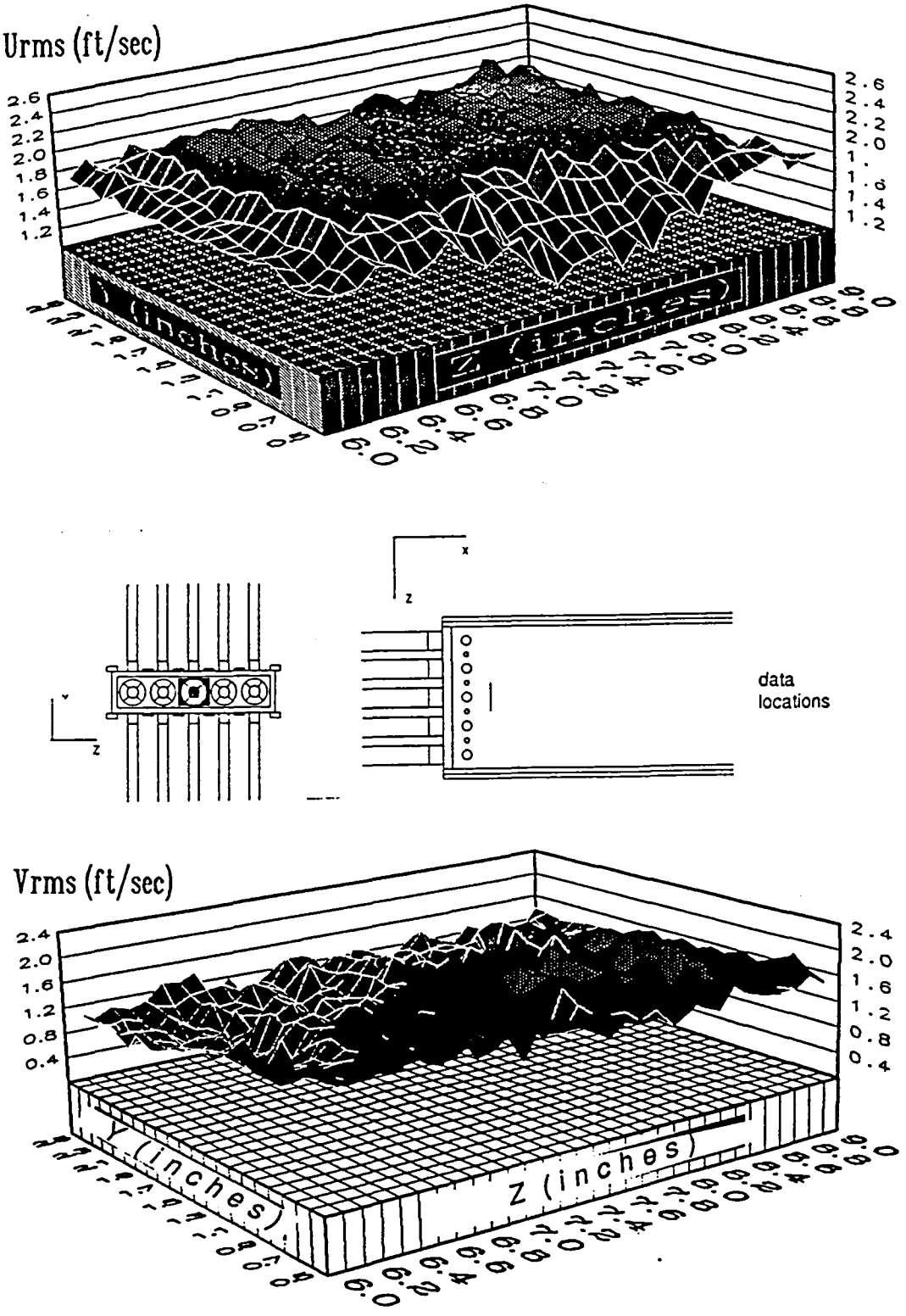

Figure C66 Annular and Primary Jets Contour Plot of U_{rms} and V_{rms} at X=4.0 in.

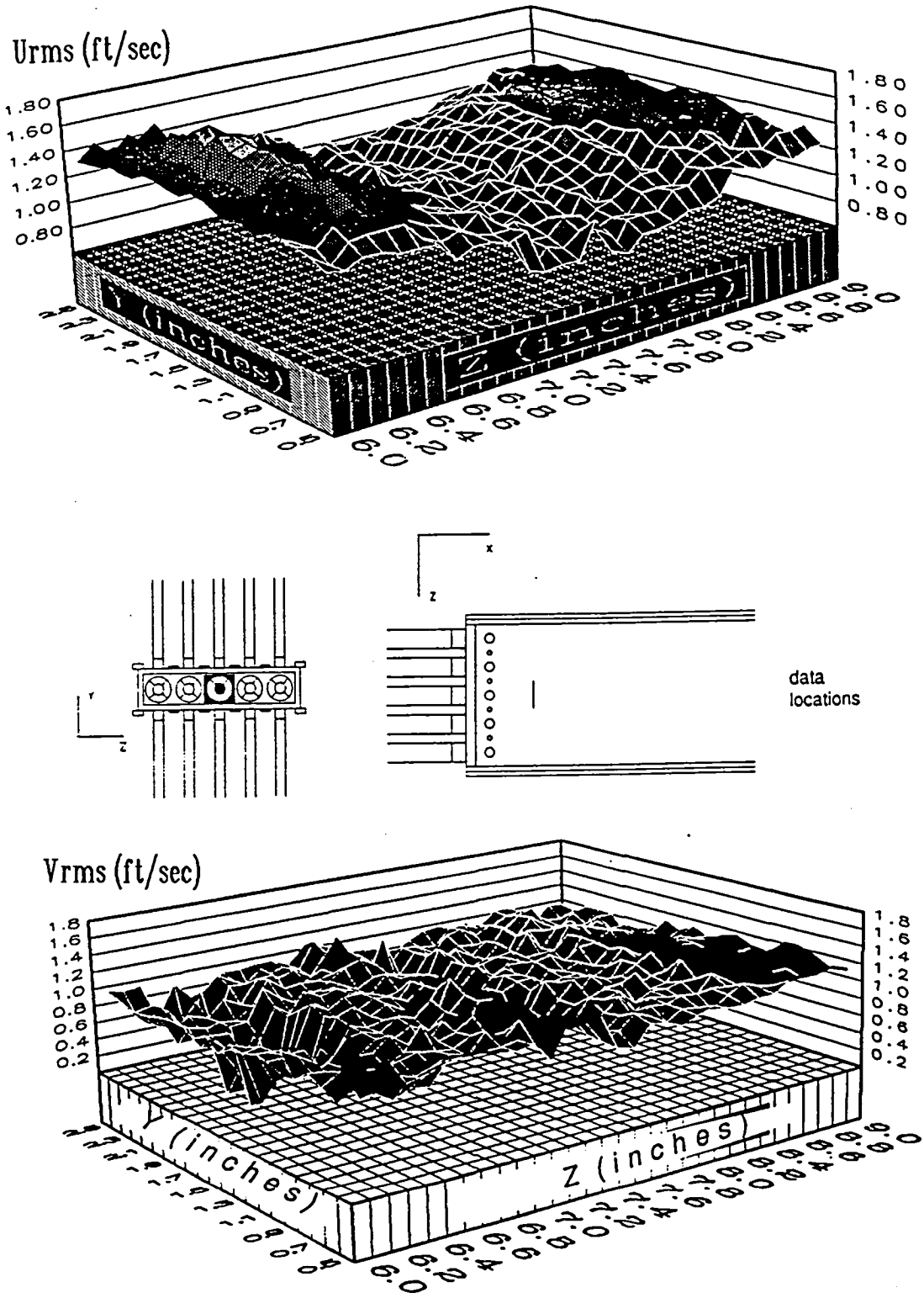

Figure C67 Annular and Primary Jets Contour Plot of U_{rms} and V_{rms} at X=6.0 in.

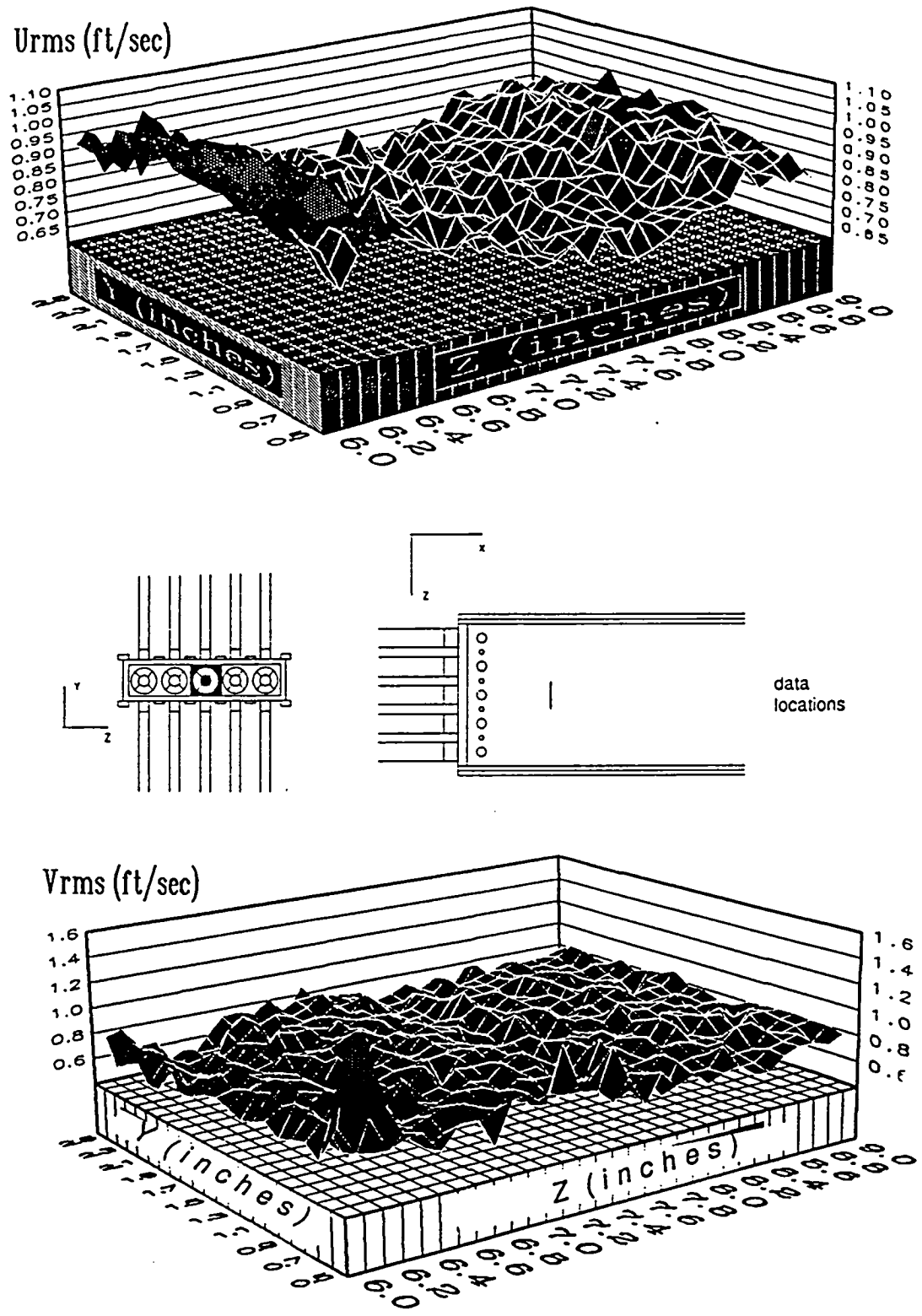

Figure C68 Annular and Primary Jets Contour Plot of U_{rms} and V_{rms} at X=9.0 in.

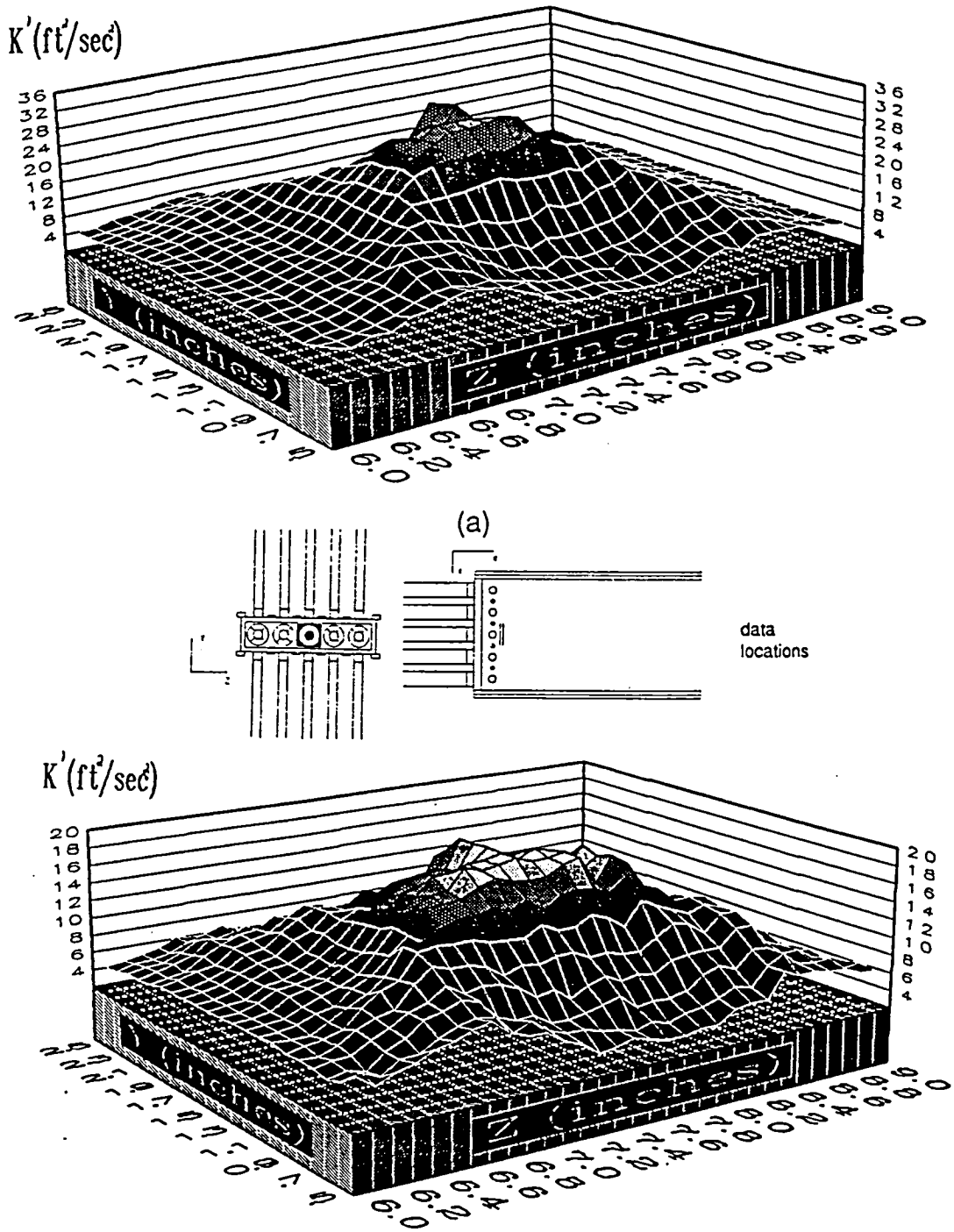

Figure C69 Annular and Primary Jets Contour Plot of K at
a) X=2.5 in.; b) X=3.0 in.

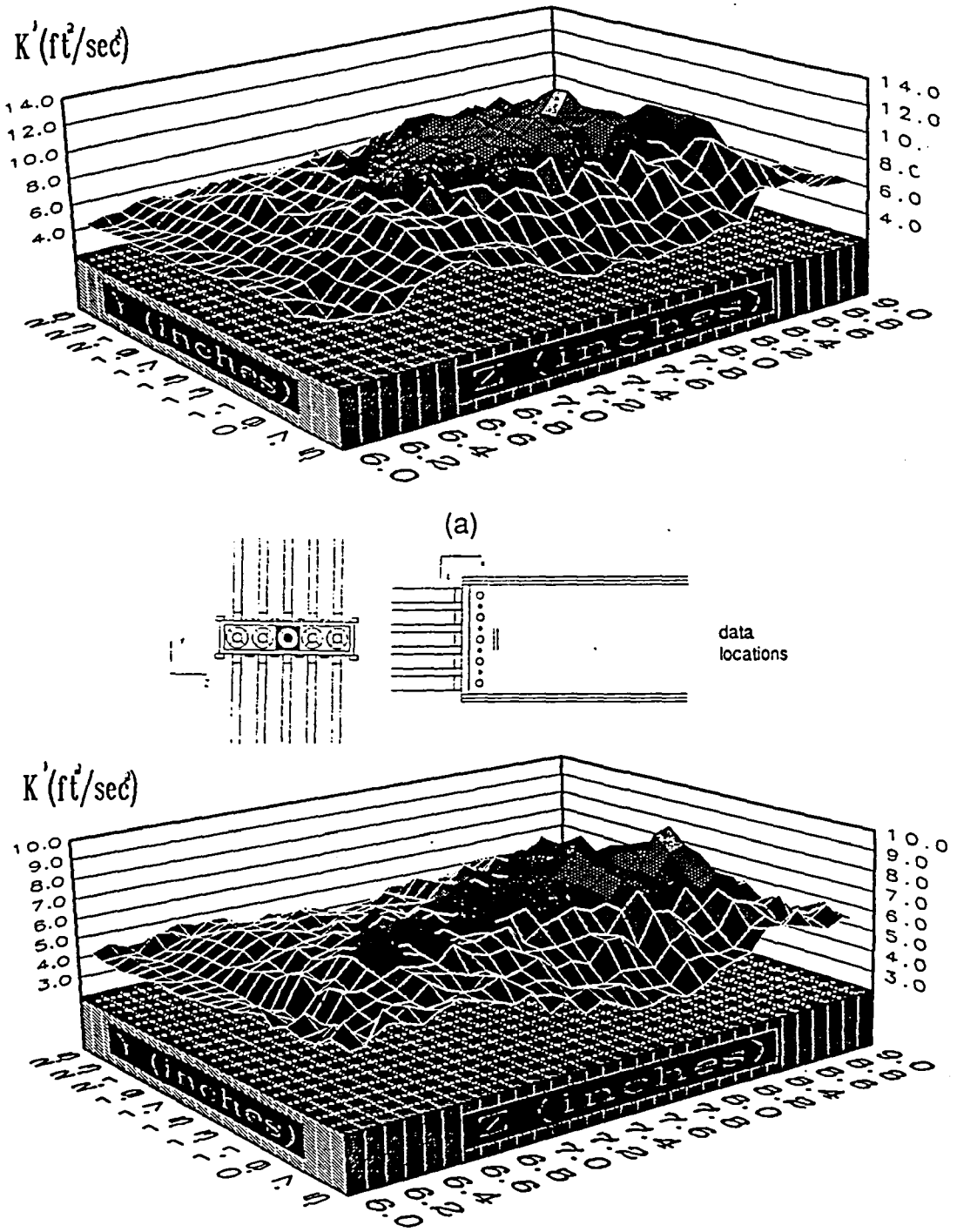

Figure C70 Annular and Primary Jets Contour Plot of K′ at
a) X=3.5 in.; b) X=4.0 in.

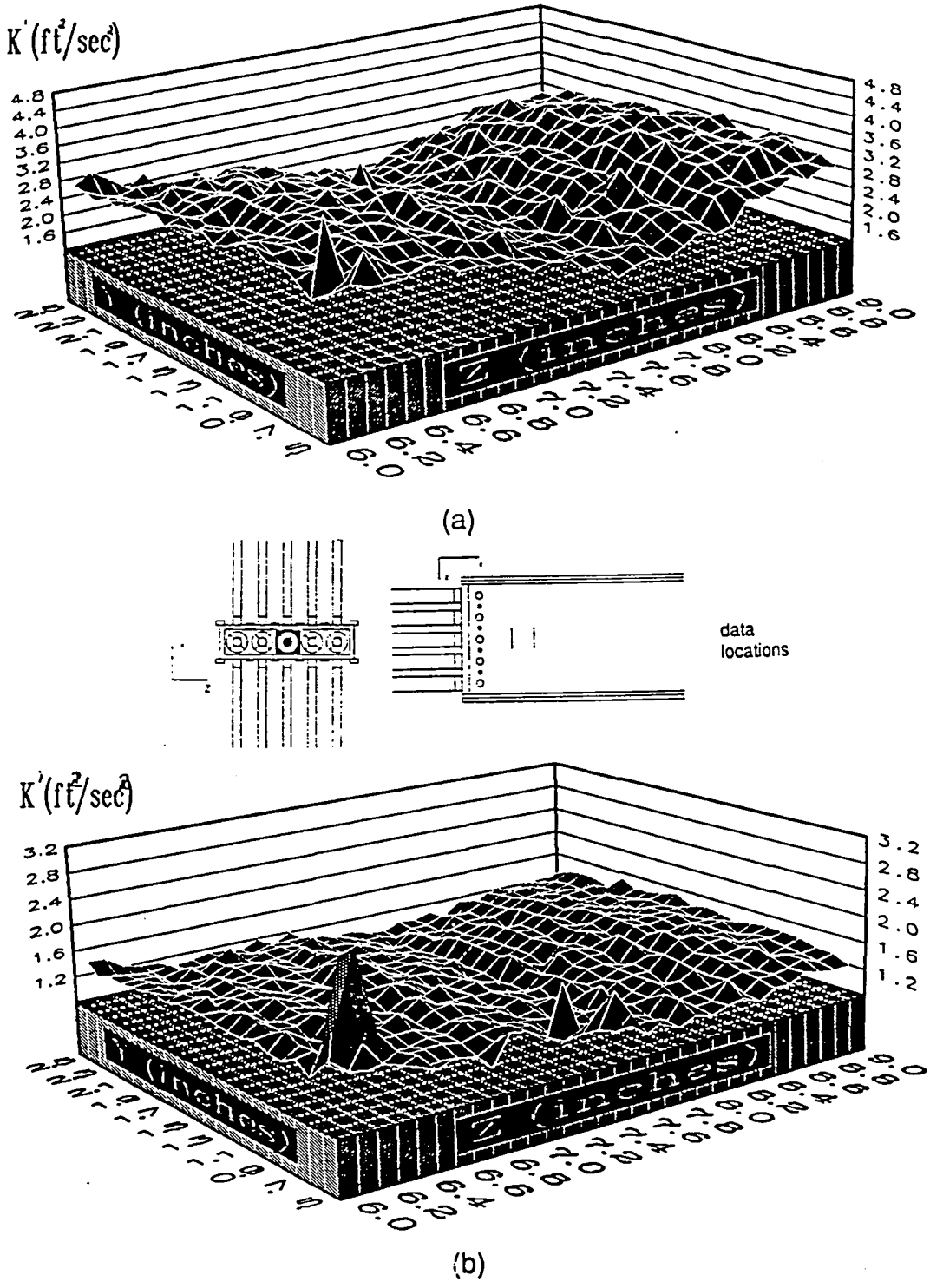

Figure C71 Annular and Primary Jets Contour Plot of K' at
a) X=6.0 in.; b) X=9.0 in.

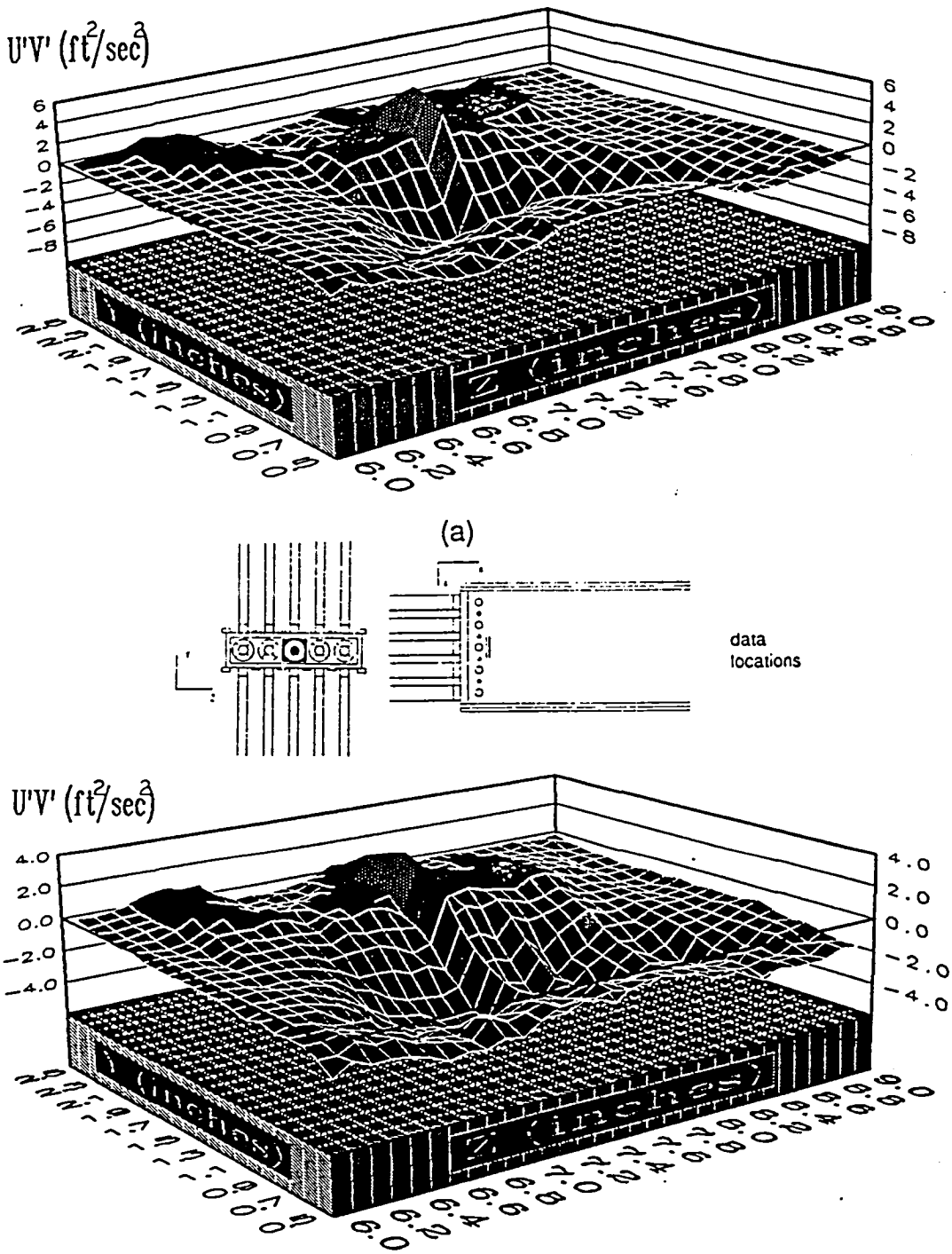

Figure C72 Annular and Primary Jets Contour Plot of U'V' at
a) X=2.5 in. b) X=3.0 in.

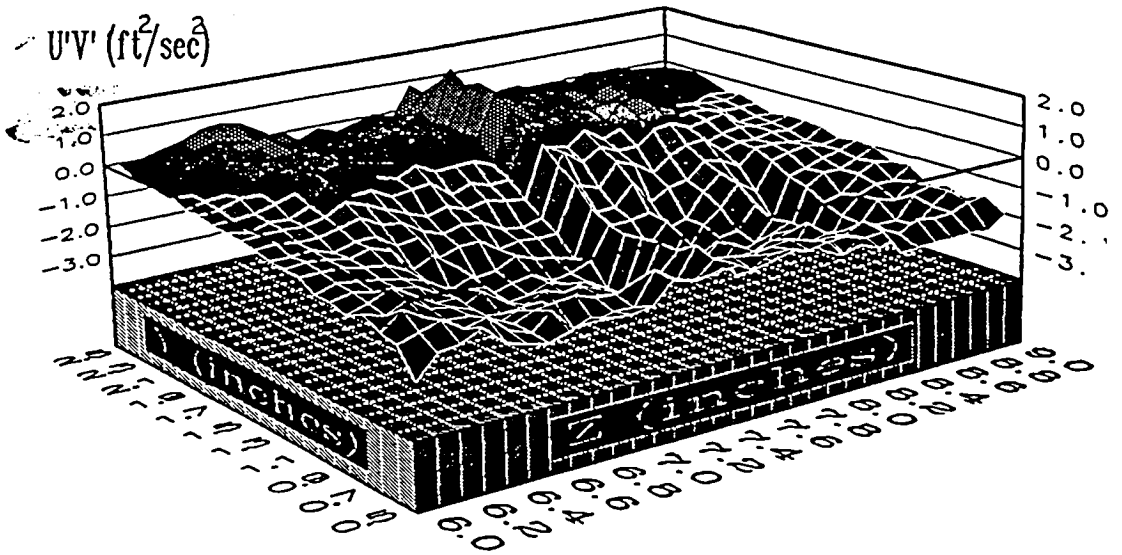

(a)

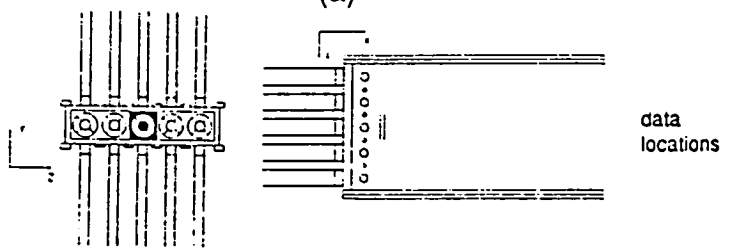

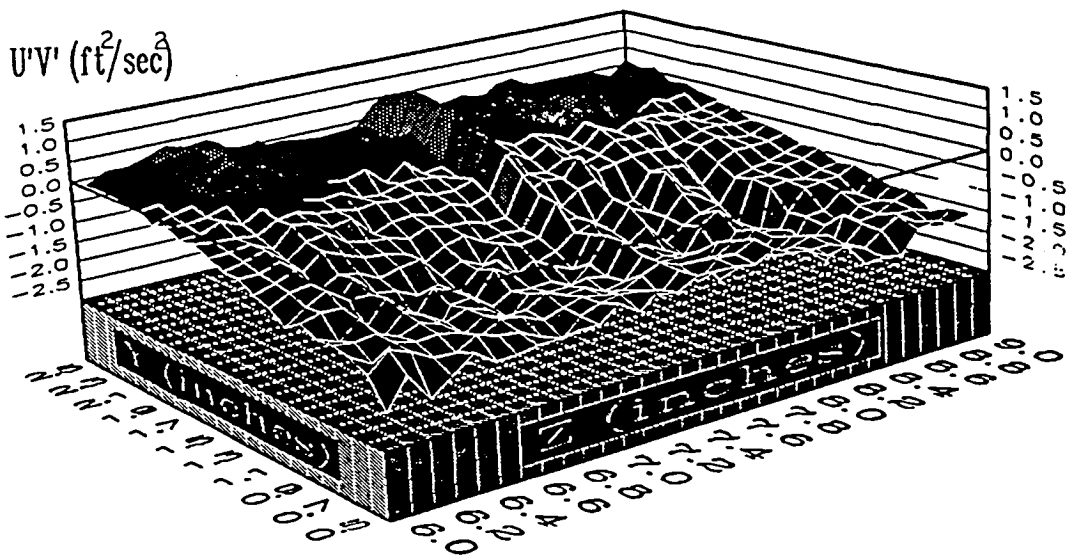

(b)

Figure C73 Annular and Primary Jets Contour Plot of U'V' at
a) X=3.5 in.; b) X=4.0 in.

REPORT DOCUMENTATION PAGE

Form Approved
OMB No. 0704-0188

1. AGENCY USE ONLY (*Leave blank*)	2. REPORT DATE	3. REPORT TYPE AND DATES COVERED
	December 1995	Final Contractor Report

4. TITLE AND SUBTITLE

Laser Doppler Velocimeter Measurements and Laser Sheet Imaging in an Annular Combustor Model

5. FUNDING NUMBERS

WU-537-02-21
C-NAS3-24350

6. AUTHOR(S)

Richard Dale Dwenger

7. PERFORMING ORGANIZATION NAME(S) AND ADDRESS(ES)

Purdue University
West Lafayette, Indiana 47907

8. PERFORMING ORGANIZATION REPORT NUMBER

E-9866

9. SPONSORING/MONITORING AGENCY NAME(S) AND ADDRESS(ES)

National Aeronautics and Space Administration
Lewis Research Center
Cleveland, Ohio 44135-3191

10. SPONSORING/MONITORING AGENCY REPORT NUMBER

NASA CR-191060

11. SUPPLEMENTARY NOTES

This report was submitted as a thesis in partial fulfillment of the requirements for the degree Master of Science in Aeronautics and Astronautics to Purdue University, West Lafayette, Indiana in August 1990. Project Manager, J. Holdeman, Internal Fluid Mechanics Division, NASA Lewis Research Center, organization code 2650, (216) 433-5846.

12a. DISTRIBUTION/AVAILABILITY STATEMENT

Unclassified - Unlimited
Subject Category 07

This publication is available from the NASA Center for Aerospace Information, (301) 621-0390.

12b. DISTRIBUTION CODE

13. ABSTRACT (*Maximum 200 words*)

An experimental study was conducted in an annular combustor model to provide a better understanding of the flowfield. Combustor model configurations consisting of primary jets only, annular jets only, and a combination of annular and primary jets were investigated. The purpose of this research was to provide a better understanding of combustor flows and to provide a data base for comparison with computational models. The first part of this research used a laser Doppler velocimeter to measure mean velocity and statistically calculate root-mean-square velocity in two coordinate directions. From this data, one Reynolds shear stress component and a two-dimensional turbulent kinetic energy term was determined. Major features of the flowfield included recirculating flow, primary and annular jet interaction, and high turbulence. The most pronounced result from this data was the effect the primary jets had on the flowfield. The primary jets were seen to reduce flow asymmetries, create larger recirculation zones, and higher turbulence levels. The second part of this research used a technique called marker nephelometry to provide mean concentration values in the combustor. Results showed the flow to be very turbulent and unsteady. All configurations investigated were highly sensitive to alignment of the primary and annular jets in the model and inlet conditions. Any imbalance between primary jets or misalignment of the annular jets caused severe flow asymmetries.

14. SUBJECT TERMS

Turbulence modeling; Jet-in-cross flow; Three-dimensional flow; Gas turbine combustion; Experimental data; Turbulent flow model validation

15. NUMBER OF PAGES

284

16. PRICE CODE

A13

17. SECURITY CLASSIFICATION OF REPORT	18. SECURITY CLASSIFICATION OF THIS PAGE	19. SECURITY CLASSIFICATION OF ABSTRACT	20. LIMITATION OF ABSTRACT
Unclassified	Unclassified	Unclassified	

National Aeronautics and
Space Administration
Lewis Research Center
21000 Brookpark Rd.
Cleveland, OH 44135-3191